

Development and Application of MRI Methods to Assess Coronary Microvascular Disease

A

Dissertation

Presented to

The Faculty of the School of Engineering and Applied Science

University of Virginia

In partial fulfillment

of the requirements for the degree

Doctor of Philosophy

by

Soham Shah

May 2022

APPROVAL SHEET

This
Dissertation
is submitted in partial fulfillment of the requirements
for the degree of
Doctor of Philosophy

Author Signature: *Seham Shah*

This Dissertation has been read and approved by the examining committee

Advisor: Dr. Frederick Epstein

Committee Member: Dr. Brent French

Committee Member: Dr. Shayn Peirce-Cottler

Committee Member: Dr. Craig Meyer

Committee Member: Dr. Matthew Wolf

Accepted for the School of Engineering and Applied Science:



Jennifer L. West, School of Engineering and Applied Science

May 2022

Abstract

Every year, over eight million patients in the US visit the emergency department for angina with the most common cause being myocardial ischemia. Traditionally, treatment for myocardial ischemia has focused on the evaluation of obstructed coronary arteries via angiography for coronary artery disease (CAD). However, a considerable proportion of these patients have a normal coronary angiogram. In presentations of ischemia with no obstructive CAD (NOCAD), current evidence has shown that the primary cause may be coronary microvascular disease (CMD), defined as an impairment to the coronary microcirculation and assessed by an inadequate vasodilatory response to physiological or pharmacological stress. Patients with CMD are at a high risk of major adverse cardiovascular events, and emerging evidence links CMD with NOCAD to heart failure with preserved ejection fraction (HFpEF), the most common form of heart disease in the US. However, the mechanisms underlying CMD are not fully understood, and there are no established treatments for CMD.

Mouse models of heart disease are commonly used to study explore disease processes, mechanisms, and therapies; magnetic resonance imaging (MRI) in mice enables noninvasive and serial assessment of cardiovascular structure, function, and disease. The overall goal of this dissertation is to a) develop MRI methods for the assessment of CMD, and b) use these novel methods along with traditional imaging methods to study the underlying mechanisms and potential therapies for CMD using mouse models of high-fat high-sucrose diet (HFHSD) induced CMD.

Oxidative stress, defined as the imbalance of the generation and biotransformation of reactive oxygen species (ROS), has a potential central role in altering microvascular function and exacerbating CMD. In Specific Aim 1, we developed a dynamic nitroxide-enhanced MRI method for the quantification of cardiovascular oxidative stress to facilitate future investigations of the role of oxidative stress in CMD. The development of the technique is summarized in [Chapter 2](#).

Epicardial adipose tissue (EAT), in pathological conditions, has been described as a transducer metabolic inflammation to the myocardium and coronary microvasculature. Recent studies have linked the EAT fatty acid composition (FAC) to its proinflammatory state. In Specific Aim 2, we developed an accelerated FAC MRI method for the mouse EAT and assessed the role of EAT FAC on HFHSD-induced CMD. The development and assessment of this technique is summarized in [Chapter 3](#).

Lastly, mineralocorticoid receptor (MLR) activation has many downstream mechanisms, including vascular oxidative stress and a proinflammatory EAT, and may contribute to the development of CMD. In Specific Aim 3, we utilized multiparametric preclinical MRI to test the hypotheses that MLR antagonism with eplerenone and cell-specific MLR deletion protects against microvascular impairment in a mouse model of HFHSD-induced CMD. The results of these experiments are summarized in [Chapter 4](#).

Table of Contents

ABSTRACT	3
TABLE OF CONTENTS.....	4
CHAPTER 1 – INTRODUCTION	7
1.1 CORONARY MICROVASCULAR DISEASE (CMD)	8
1.1.1 Relevance of CMD in HFpEF	8
1.1.2 Coronary microvasculature	9
1.1.3 Assessment of CMD	10
1.1.4 Current treatments for CMD	10
1.1.5 Mouse models of CMD/HFpEF	11
1.2 GOAL.....	12
1.3 OXIDATIVE STRESS.....	13
1.3.1 Relevance of oxidative stress in CMD	13
1.3.2 Assessment of cardiovascular oxidative stress in-vivo	13
1.4 EPICARDIAL ADIPOSE TISSUE	15
1.4.1 Relevance of epicardial adipose tissue in CMD	15
1.4.2 MRI assessment of epicardial adipose tissue	16
1.5 MINERALOCORTICOID RECEPTORS.....	17
1.5.1 Mineralocorticoid receptors in cardiovascular diseases and CMD	17
1.5.2 Mineralocorticoid receptor antagonism in cardiovascular disease and CMD	20
CHAPTER 2 – NITROXIDE ENHANCED MRI OF CARDIOVASCULAR OXIDATIVE STRESS.....	22
2.1 ABSTRACT	23
2.2 INTRODUCTION	24
2.3 METHODS	26
2.4 RESULTS	31
2.5 DISCUSSION AND CONCLUSIONS	36
2.6 APPENDIX 1.....	38
2.7 APPENDIX 2.....	39
CHAPTER 3 – ACCELERATED FATTY ACID COMPOSITION MRI OF EPICARDIAL ADIPOSE TISSUE: DEVELOPMENT AND APPLICATION TO EPLERENONE TREATMENT IN A MOUSE MODEL OF OBESITY-INDUCED CORONARY MICROVASCULAR DISEASE.....	41
3.1 ABSTRACT	42
3.2 INTRODUCTION	43
3.3 METHODS	44
3.4 RESULTS	53

3.5	DISCUSSION AND CONCLUSIONS	61
CHAPTER 4 – ROLE OF MINERALOCORTICOID RECEPTOR BLOCKADE AND CELL SPECIFIC DELETION ON THE PREVENTION OF DIET-INDUCED CORONARY MICROVASCULAR DISEASE..... 65		
4.1	ABSTRACT	66
4.2	INTRODUCTION	67
4.3	METHODS	69
4.4	RESULTS	73
4.5	DISCUSSION AND CONCLUSIONS	82
CHAPTER 5 – CONCLUSIONS AND FUTURE DIRECTIONS 85		
5.1	CONCLUSIONS.....	86
5.1.1	Nitroxide-enhanced MRI of cardiovascular oxidative stress.....	86
5.1.2	Accelerated fatty acid composition MRI of epicardial adipose tissue	86
5.1.3	Role of mineralocorticoid receptors in CMD.....	86
5.2	FUTURE DIRECTIONS	87
5.2.1	Nitroxide-enhanced MRI	87
5.2.2	MRI of epicardial adipose tissue	87
5.2.3	Mechanisms and treatments for CMD.....	88
APPENDIX A – ROLE OF INOS IN PREVENTING AND REVERSING CORONARY MICROVASCULAR DISEASE DUE TO A HIGH-FAT HIGH-SUCROSE DIET..... 90		
A.1	ABSTRACT	91
A.2	CLINICAL PERSPECTIVE.....	92
A.3	INTRODUCTION	93
A.4	METHODS	94
A.5	RESULTS	98
A.6	DISCUSSION AND CONCLUSIONS	109
APPENDIX B – MOLECULAR MECHANISMS OF ADENOSINE STRESS T1 MAPPING 111		
B.1	ABSTRACT	112
B.2	CLINICAL PERSPECTIVE.....	113
B.3	INTRODUCTION	114
B.4	METHODS	116
B.5	RESULTS	119
B.6	DISCUSSION AND CONCLUSIONS	127
B.7	DATA SUPPLEMENT	130
APPENDIX C – AWARDS AND PUBLICATIONS..... 132		
C.1	AWARDS.....	133
C.2	FIRST AUTHOR MANUSCRIPTS	134
C.3	OTHER MANUSCRIPTS	134

C.4	FIRST AUTHOR ORAL ABSTRACTS.....	135
C.5	FIRST AUTHOR POSTER PRESENTATIONS.....	135
	ACKNOWLEDGEMENTS.....	136
	REFERENCES.....	137

Chapter 1 – Introduction

1.1 Coronary Microvascular Disease (CMD)

Every year, over eight million patients in the US visit the emergency department for angina or chest pain, with the most common cause being myocardial ischemia¹. Traditionally, the prevailing practice for the treatment of myocardial ischemia has focused on the evaluation of obstructed coronary arteries via angiography for coronary artery disease (CAD)²; however, a significant portion of these patients have a normal coronary angiogram³⁻⁶. In these presentations of ischemia with no obstructive CAD (NOCAD), current evidence has shown an emerging paradigm shift where coronary microvascular disease (CMD) is considered the primary cause⁷⁻⁹. CMD, also known as cardiac syndrome X, is defined as an impairment to the coronary microcirculation (architectural or sub-cellular) which leads to an inadequate vasodilatory response to physiological or pharmacological stress¹⁰. This can cause a supply-demand mismatch of blood-oxygen resulting in myocardial ischemia. Patients with CMD are at a high risk of major adverse cardiovascular events (MACE) including stroke, heart failure, myocardial infarction, and cardiovascular death^{7,11-13}. In addition, patients with CMD generally exhibit recurrent angina, shortness of breath, trouble sleeping, fatigue, and a lower quality of life^{9,12,14,15}. Risk factors for CMD include aging, smoking, obesity, diabetes, hypertension, hyperlipidemia, chronic inflammation, and a family history of heart disease^{16,17}. There may also be a sex-specific risk of CMD; women with signs and symptoms of myocardial ischemia and myocardial infarction are more likely than men to have NOCAD¹⁷, and women comprise of nearly 70% of patients with CMD¹⁸.

1.1.1 Relevance of CMD in HFpEF

CMD with NOCAD is not only an important cause of ischemic heart disease, but recent evidence links CMD to heart failure with preserved ejection fraction (HFpEF) (Figure 1), which is emerging as most common form of heart failure in the United States¹⁹, with up to 75% of patients with HFpEF suffering from CMD²⁰⁻²². Patients with CMD and diastolic dysfunction, a hallmark of HFpEF, have a 5-fold greater risk of HFpEF hospitalization compared to diastolic dysfunction alone²³. In general, patients with CMD tend to simultaneously develop risk factors for HFpEF²⁴⁻²⁶. More specifically, comorbidities such as obesity and type II diabetes induce a systemic proinflammatory state causing coronary microvascular oxidative stress, inflammation, and eventually CMD²⁷. Concurrently, a systemic proinflammatory state also promotes left ventricular cardiomyocyte hypertrophy, remodeling, fibrosis, stiffness causing diastolic left ventricular dysfunction and HFpEF²⁷. Furthermore, both CMD and HFpEF may initiate and exacerbate each other as both share common pathophysiological pathways involving primary or secondary changes in the coronary microcirculation^{28,29}.

Myocardial Remodeling in HFPEF

Importance of Comorbidities

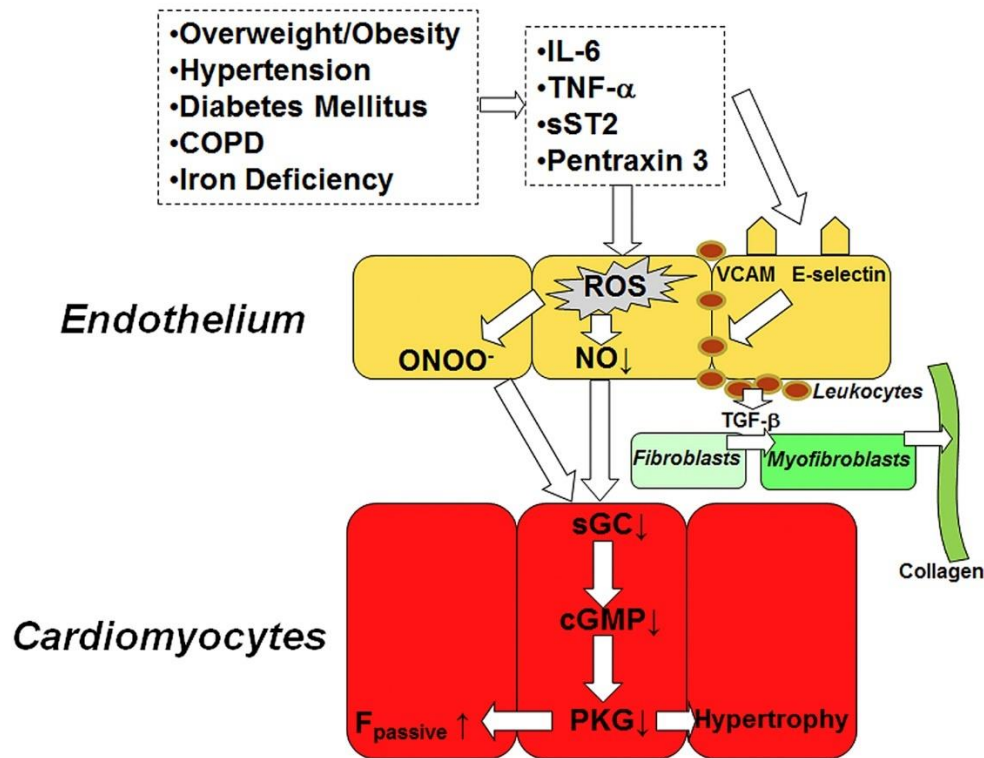


Figure 1. Relationship between obesity, CMD, and HFpEF.

Figure source: Paulus, W. J., & Tschoepe, C. (2013). A novel paradigm for heart failure with preserved ejection fraction: comorbidities drive myocardial dysfunction and remodeling through coronary microvascular endothelial inflammation. *Journal of the American College of Cardiology*, 62(4), 263-271.

1.1.2 Coronary microvasculature

The coronary arterial system is a continuous network of anatomically and functionally distinct vessels, generally broken down to four subtypes: the large epicardial coronary arteries (>400µm), small pre-arterioles (100 to 400 µm), intramural arterioles (<100 µm), and the coronary capillary bed (<10 µm)^{8,30,31}. Under normal physiological conditions, the large coronary arteries primarily exhibit conductance functions and provide minimal resistance to coronary blood flow. In contrast, the pre-arterioles and arterioles are responsible for the bulk of the cardiovascular resistance circuit of the heart and are responsible for the regulation of blood flow to match the metabolic demand of the heart. Blood is ultimately distributed to the tissues via the capillary beds^{8,30,31}. In a pathophysiological state, the inadequate relaxation of the resistance vessels in response to an increase in metabolic demand denotes an impairment in microvascular function and can cause signs and symptoms of CMD, including angina and ischemia, with NOCAD.

1.1.3 Assessment of CMD

Since the coronary microcirculation cannot be resolved by coronary angiography, a direct interrogation of the coronary microvascular function is necessary to diagnose CMD³². Several invasive and noninvasive techniques have been developed for the evaluation of CMD, each with advantages and limitations.

Invasive techniques for CMD diagnosis include measurement of coronary flow reserve (CFR), index of microvascular resistance (IMR), and fractional flow reserve (FFR). CFR is typically assessed using an intracoronary Doppler-tipped guidewire or thermodilution techniques to measure blood flow at rest and pharmacological-induced hyperemia in response to adenosine (endothelial-independent) and acetylcholine (endothelial-dependent) vasodilation^{8,33}. IMR is measured using a pressure-temperature sensor-tipped coronary guidewire which measures the mean transit time of an intracoronary injection of room temperature saline and allows for simultaneous measurements of coronary pressure and hyperemic flow^{8,34}. FFR, while not primarily used to measure CMD, provides a surrogate measure of flow limitation calculated as a ratio between coronary pressure distal to a stenosis and aortic pressure during hyperemia⁸.

Noninvasive methods for CMD diagnosis typically assess the myocardial perfusion reserve (MPR), which is the ratio of myocardial perfusion at stress over rest, using positron emission tomography (PET), cardiac magnetic resonance (CMR), or dynamic computerized tomography (CT) and are well correlated with results from invasive measurements^{35,36}. Patients with angina, reduced MPR, and a normal coronary angiogram are at risk or are diagnosed with CMD. Typically, for each modality, myocardial perfusion is determined after injection of a tracer (PET: radiotracers, CMR: gadolinium, CT: ionized contrast agent) to capture the first pass of the contrast medium through the heart³⁷. More recently, gadolinium-free CMR approaches using T1 mapping³⁸ and arterial spin labeling³⁹ have been proposed and developed^{40,41}. For both contrast and non-contrast methods, stress perfusion is measured during maximal hyperemia induced either by exercise or endothelial-independent vasodilators including adenosine and regadenoson. Endothelial-dependent vasodilators, such as acetylcholine, are not used because systemic administration may cause severe drops in blood pressure. In general, advantages of CMR are high spatial temporal resolution, a lack of ionizing radiation, and the ability to concurrently perform a comprehensive assessment of cardiovascular structure and function^{8,42}. Other noninvasive methods include Doppler echocardiography and contrast echocardiography, however, these methods are highly operator-dependent and suffer from inter-user variability^{43,44}.

1.1.4 Current treatments for CMD

Currently there are no effective therapies specifically targeting CMD. Unfortunately, the pathophysiology of CMD is multifactorial with multiple overlapping phenotypes, and while CMD may be a primary abnormality in some patients, it may be secondary or tertiary in other. Current approaches to CMD treatment have been empirical and largely based on reducing comorbidities, reducing angina, and incorporating treatments developed for CAD (beta-blockers, nitrates, antiplatelets),

however, there is little evidence to support the effectiveness of these treatment for specifically CMD⁴⁵.

Many therapeutic trials have shown promise for CMD treatment; however, they have been largely inconclusive⁴⁵. Mineralocorticoid receptor antagonists, such as eplerenone and spironolactone, have shown promise in improving MPR in patients with CMD^{46,47}. In contrast, a study in women exhibiting signs and symptoms of CMD showed that eplerenone did not improve CFR⁴⁸. However, all these studies suffered from variable patient selection and a limited sample size. Other studies have tested nitric oxide modulators, statins, alpha-blockers, beta-blockers, and nitrates, but the improvements in CFR and MPR are not always significant^{49–55}. Most recently, a combination therapy of potent statins + ACE-inhibitors at the maximum tolerated dose appears effective in improving angina, myocardial perfusion, and CMD^{56,57}. In addition, an ongoing WARRIOR trial is testing the efficacy of high-intensity statin + ACE-inhibitors + aspirin for long term CMD treatment and management^{56,57}.

Overall, a pinpointed treatment for CMD has yet to be established. A better understanding of the pathophysiology of CMD is needed to facilitate the development of targeted therapeutic strategies which both treat and improve the long-term outcomes of CMD.

1.1.5 Mouse models of CMD/HFpEF

Mouse models of heart disease are commonly used to study explore disease processes, mechanisms, and therapies due to the similarities in cardiovascular biology between mice and humans, low cost, and the relative ease of genetic manipulation in mice^{58,59}. Because of strong correlation between CMD and HFpEF, mouse models of CMD and HFpEF can be used to study microvascular dysfunction, and both can be grouped into two divisions: 1) diet-induced obese mice and 2) transgenic mice.

Mouse models of diet-induced obesity

Obesity is a common comorbidity for CMD and HFpEF, and a variety of mouse models that induce obesity have been developed to study cardiovascular disease including impaired microvascular function.

High-Fat Diet (HFD): In mouse models, unhealthy food consumption and obesity can be mimicked by a HFD. Aouqui et al. and Kwiatkowski et al. showed that mice fed a HFD (51% and 60% fat respectively) for eight weeks develop coronary microvascular dysfunction^{60,61}. Furthermore, Naresh et al. showed that mice fed a HFD (60% fat) for 18–24 weeks have impaired MPR with fibrosis, normal capillary density, and without aortic plaque thus establishing mice fed a HFD as a model of CMD without obstructive CAD⁶².

HFD + Angiotensin II (AngII) infusion: Multiple groups have established a HFD + AngII infusion for 8-16 weeks as a model of HFpEF^{63–65}. Angiotensin II infusion, in addition to a HFD, induces both hypertension and obesity and is regarded as a more severe model of CMD/HFpEF than HFD alone⁶⁶.

HFD + L-NAME: Schiattarella et al. were the first to present a two-hit pre-clinical mouse model resembling human HFpEF. Mice were subjected to an HFD with L-NAME (nitric oxide synthase inhibitor) induced hypertension for 15 weeks. Mice subjected to both stress factors developed a typical HFpEF phenotype, including a reduced exercise tolerance and a reduced CFR⁶⁷.

High-Cholesterol Diet (HCD): Stokes et al. showed that mice fed a HCD (1.25% cholesterol, 15.8% fat) for just three weeks have a significant increase in vessel wall inflammation and develop significant endothelial dysfunction in arterioles measured using intravital microscopy⁶⁸.

High-Fat High-Sucrose Diet (HFHSD): A HFHSD, also known as a western diet (WD), is comprised of 30-40% kcal from fat and 30-40% kcal sucrose. Multiple groups have shown that mice on a HFHSD or WD develop a range of mild to severe symptoms of CMD and HFpEF⁶⁹⁻⁷².

Transgenic models:

Db/db mice: Diabetes mellitus is another comorbidity for CMD and HFpEF, and db/db mice have a mutation in leptin receptor resulting in excessive hunger and obesity and thus is a well-accepted model of type II diabetes. However, the onset of symptoms in db/db mice is severe and early in life, so, it does not directly mirror the human situation⁷³. Nonetheless, db/db mice from as early as 10 weeks old have exhibited CMD-like⁷⁴⁻⁷⁶ and HFpEF-like symptoms⁷⁷.

Ob/ob mice: Ob/ob mice are leptin deficient mice which develop spontaneous obesity and later HFpEF⁷⁸⁻⁸⁰, however, obese patients with HFpEF and leptin deficiency are rare, so the ob/ob mice does not mimic human HFpEF⁸¹.

ApoE^{-/-} mice: Apolipoprotein E knockout mice (ApoE^{-/-}) are commonly used for studies on atherosclerosis, however, at 12 weeks post-WD, they have also displayed coronary endothelial dysfunction in isolated arterioles⁸² and in isolated buffer perfused hearts⁸³.

TRPV1^{-/-} mice: DelloStritto et al. showed that TRPV1 signaling is an important metabolic regulator of coronary blood flow⁷⁶. Contrast echocardiography showed that H₂O₂-induced vasodilation was inhibited in TRPV1^{-/-} mice, and in addition, in wild-type mice, TRPV1 antagonism blocked H₂O₂- induced coronary microvessel dilation⁷⁶.

1.2 Goal

The overall goal of this dissertation is to develop MRI methods to assess the progression of CMD, its underlying mechanisms, and potential therapies in a mouse model of HFHSD-induced CMD. MRI in mice enables noninvasive and serial assessment of cardiovascular physiology and pathophysiology, thus traditional and novel imaging methods combined with a mouse model of HFHSD-induced CMD can provide insight into its underlying mechanisms and potential therapies.

1.3 Oxidative Stress

Oxidative stress can be defined as the imbalance of the generation and biotransformation of reactive oxygen species (ROS), or the inability of antioxidant enzymes and defenses to counteract increases in ROS. The ROS family includes molecules such as superoxide anion ($O_2^{\cdot-}$), hydroxyl radical ($HO\cdot$), lipid radicals ($ROO\cdot$), nitric oxide (NO), hydrogen peroxide (H_2O_2), peroxynitrite ($ONOO^-$) and hypochlorous acid (HOCl). ROS can be generated from the upregulation of NADPH oxidases, involvement of the renin-angiotensin system, xanthine oxidases, respiratory chain of the mitochondria, and nitric oxide synthase (NOS) uncoupling⁸⁴. ROS has been implicated multiple pathophysiological signaling pathways which induce cellular damage, necrosis, and apoptosis, especially in mitochondria, due to its direct oxidizing effects on macromolecules such as lipids, proteins and DNA⁸⁵. Generation of one free radical can lead to a positive feedback loop via sequential chain reactions leading to further formation of ROS⁸⁶. In addition, $O_2^{\cdot-}$ radicals can interact with nitric oxide (NO) resulting in the formation of reactive nitrogen species (RNS) thereby reducing NO bioavailability and causing NO toxicity known as “nitrosative stress”⁸⁷. Like ROS, an increase in RNS results in nitrosylation reactions that alter structure and function of cellular proteins⁸⁸.

1.3.1 Relevance of oxidative stress in CMD

Comorbidities of obesity and diabetes have long been implicated as cardiovascular risk factors which promote oxidative and nitrosative stress⁸⁹. In vascular and microvascular disease, ROS and RNS can contribute to both endothelial-dependent and -independent microvascular dysfunction⁹⁰. ROS and RNS promote endothelial NOS (eNOS) uncoupling, TRPV1 channel dysfunction, and inflammatory cell adhesion which contribute to endothelial dysfunction and endothelial-dependent reductions in coronary blood flow (CBF)^{76,91}. ROS and RNS-mediated K^+ -ATP and voltage-gated K^+ channel dysfunction contribute to smooth muscle cell dysfunction and endothelial-independent reductions in CBF^{91,92}. In general, oxidative and nitrosative stress, due to obesity and diabetes, have an important role in altering microvascular function and the progression of CMD.

1.3.2 Assessment of cardiovascular oxidative stress in-vivo

Although oxidative stress is involved in the development of numerous cardiovascular diseases, there are limited methods to quantify this parameter *in-vivo*. Nitroxide radicals are non-metallic compounds with antioxidant properties which degrade ROS and have been used in biophysics studies to measure oxidative stress levels in cancer⁹³. In addition, nitroxide radicals have a single unpaired electron giving it paramagnetic properties and the ability to be a T1-shortening agent⁹⁴, though they are not commonly used because metal-based contrast agents, such as gadolinium and manganese, have a higher number of unpaired electrons corresponding to a greater T1-shortening effect. Nevertheless, nitroxide contrast agents can and have been used as oxidative-stress-sensitive T1-shortening agents for electron paramagnetic resonance imaging⁹⁵ and dynamic nitroxide-enhanced (DNE) MRI⁹⁶⁻¹⁰¹ where the reduction of the nitroxide to a non-T1-shortening compound, due to ROS, decreases the overall T1-shortening effect. DNE-MRI methods have been developed to assess relative levels of oxidative stress between tissues (Figure 2), but DNE-MRI methods have neither been

developed for total quantification of oxidative stress nor have they been developed for the cardiovascular system. Thus, this dissertation seeks to address this opportunity and through the following specific aim:

Specific Aim 1 is to develop a DNE-MRI for the quantification of cardiovascular oxidative stress to facilitate future investigations of the role of oxidative stress in CMD. Here, we sought to a) develop and combine DNE-MRI with tracer kinetic modeling which can account for cellular nitroxide reduction, a surrogate of oxidative stress levels, and b) use this method to quantify oxidative stress in mouse models of heart disease. The design and evaluation of this technique is summarized in [Chapter 2](#).

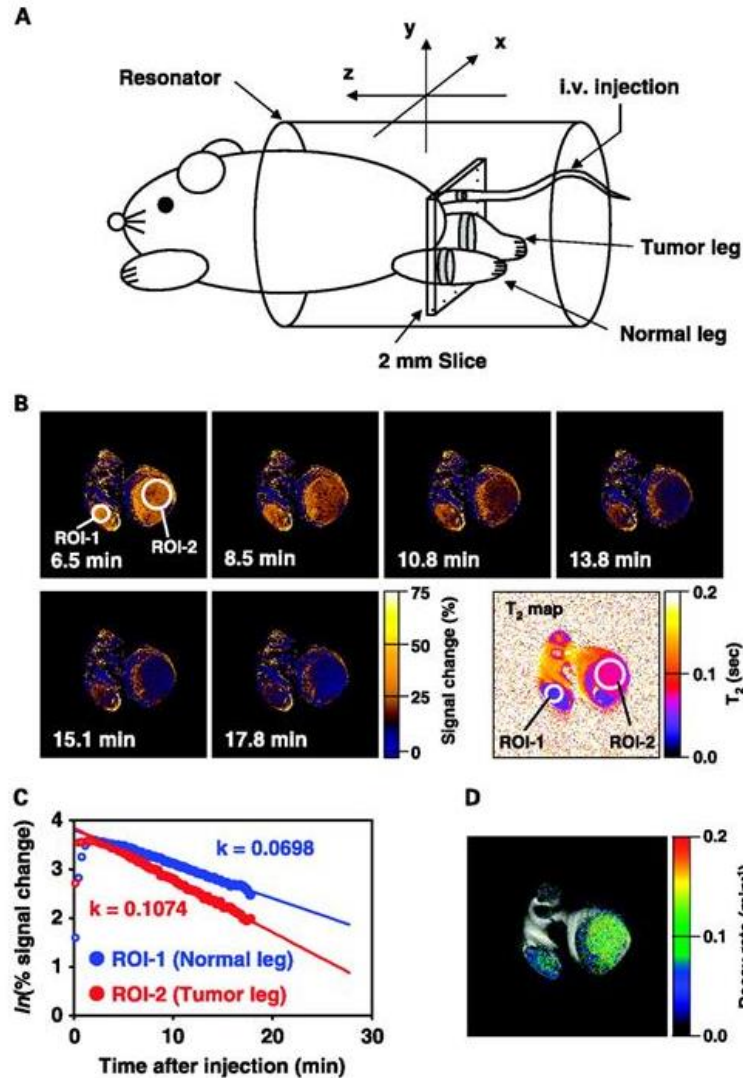


Figure 2. Nitroxide enhanced MRI for the assessment of tissue redox status

Figure Source: Matsumoto, K. I., Hyodo, F., Matsumoto, A., Koretsky, A. P., Sowers, A. L., Mitchell, J. B., & Krishna, M. C. (2006). High-resolution mapping of tumor redox status by magnetic resonance imaging using nitroxides as redox-sensitive contrast agents. *Clinical cancer research*, 12(8), 2455-2462.

1.4 Epicardial Adipose Tissue

A second driver of the chronic systemic inflammatory state seen in obesity and diabetes is the significant accumulation of epicardial adipose tissue (EAT)¹⁰². EAT can be defined as the fat depot surrounding the myocardium consisting of both adipocytes and immune cells and uniquely sharing an obstructed microcirculation with the adjacent myocardial tissue. In normal conditions, EAT has a cardioprotective role in which it buffers the heart against inflammation, fibrosis, and excessively high circulating levels of fatty acids by its ability to rapidly take up and incorporate fatty acids^{103–105}. However, during pathological conditions such as obesity and diabetes, EAT can become a major source of proinflammatory hormones, cytokines, fatty acids, and biomolecules, and it has been described as a transducer metabolic inflammation to the myocardium and coronary vasculature^{102,106}.

EAT also functions as an energy storage source, specifically triglycerides, for cardiac muscle in times of high demand¹⁰⁷. Triglycerides are composed of a carbon backbone and three fatty acid chains which are categorized into three groups: saturated fatty acids (SFAs), mono-unsaturated fatty acids (MUFAs) and poly-unsaturated fatty acids (PUFAs)¹⁰⁸. Fatty acids are a major energy source for a healthy heart to maintain contractile function¹⁰⁹. However, in pathological conditions, the increased demand and oxidation of fatty acids by the myocardium may contribute to cardiac lipotoxicity¹¹⁰. In addition, an increased incorporation of SFAs in EAT, due to obesity, promotes macrophage M1 polarization and inflammasome activation through toll-like receptor-2 and -4 signaling resulting in an increased proinflammatory cytokine secretion^{111,112}. In contrast, studies have shown that decreasing SFAs and increasing MUFA and PUFA incorporation impedes inflammasome activation and promotes cardioprotection^{113–115}. Thus, both EAT accumulation and its fatty acid composition (FAC) have key roles in the development of cardiovascular diseases.

1.4.1 Relevance of epicardial adipose tissue in CMD

In general, a proinflammatory EAT due to obesity and diabetes greatly enhances the risk of developing CMD and HFpEF (Figure 3)^{116–122}. EAT mediates microvascular inflammation that promotes endothelial-independent and -dependent dysfunction and a reduced CBF^{106,123,124}. In HFpEF patients, EAT may have a vasocrine effect by directly releasing vasoconstrictive molecules into the coronary microvasculature¹²⁵. Briefly, proinflammatory cytokines (e.g., IL-1 β , IL-6, TNF α , MCP-1), from EAT either diffuse or are directly released into the coronary microvessels, including coronary arterioles and capillaries, and interact with endothelial and vascular smooth muscle cells^{106,126}. These cytokines upregulate expression of monocyte adhesion molecules (e.g. ICAMs and VCAMs) on the endothelial surface and promote both endothelial and smooth muscle cell proliferation, migration, and apoptosis generally resulting in microvascular dysfunction^{102,106,126}.

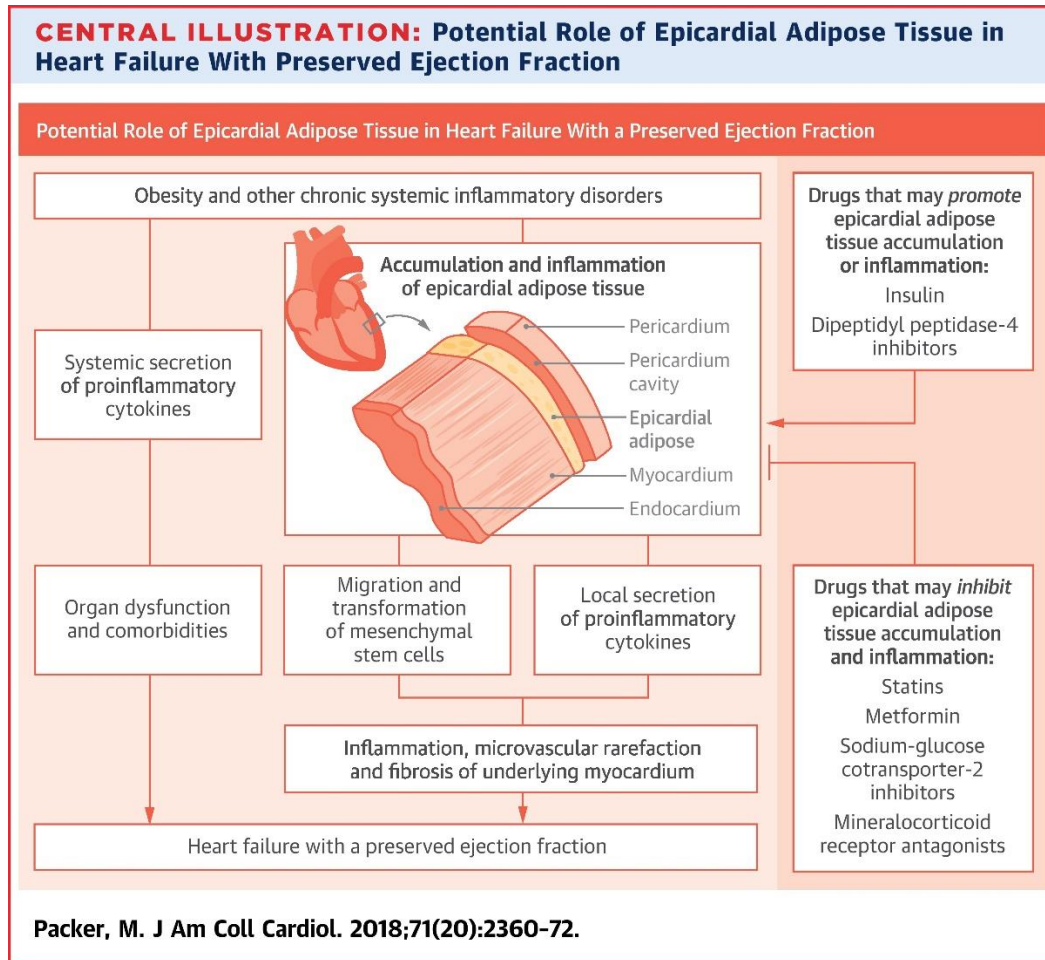


Figure 3. Role of EAT in CMD and HFpEF

Figure Source: Packer, M. (2018). Epicardial adipose tissue may mediate deleterious effects of obesity and inflammation on the myocardium. *Journal of the American College of Cardiology*, 71(20), 2360-2372.

1.4.2 MRI assessment of epicardial adipose tissue

MRI methods for the quantification of EAT volume have long been developed. The earliest methods, commonly known as “Dixon water-fat separation” utilized the idea that the protons of fat molecules have different resonant frequencies than those of water, the largest of which is shifted 3.5 parts per million (ppm) from water, corresponding to an ~1000 Hz shift at 7T¹²⁷. By acquiring images at strategic echo times (TEs) where water and fat protons are either in-phase or out-of-phase, the combined signal from a voxel can be decomposed into water-fraction and fat-fraction images¹²⁷. To account for B₀ inhomogeneities and R₂^{*} effects, a three-point method was developed which acquired images at TE_s that generated phase shifts of -π, 0, and +π between water and fat¹²⁸. These methods have been extensively developed, optimized, and utilized preclinical for clinical imaging to quantify EAT volumes^{122,126,129}.

Unlike fat volume, FAC MRI methods have only been recently developed in the last 15 years. Similar to nuclear magnetic resonance and spectroscopic techniques¹³⁰, rather than focusing on the single most-abundant proton resonant frequency of fat, methods such as variable projection (VARPRO)¹³¹ and iterative decomposition with echo asymmetry and least-squares (IDEAL)^{132,133} simultaneously estimate the signal from water and all 10 triglyceride proton resonances as well as B_0 , and R_2^* within each voxel of an image. By comparing the amounts of each proton resonance in a voxel, the signal can be further decomposed into water, SFA, MUFA, and PUFA components¹³⁴. These methods have been used to calculate FAC of subcutaneous, visceral, and breast adipose tissue in patients and mice¹³⁵; however, they have not been developed and applied for cardiovascular and EAT imaging. The main challenge of FAC MRI of EAT is that heart motion dictates the need for cardiac-gated segmented acquisitions, greatly lengthening the scan time. Thus, this dissertation seeks to address this opportunity and develop EAT FAC MRI through the following specific aim:

Specific Aim 2 is to develop an accelerated FAC MRI method for the mouse heart and EAT to facilitate investigations of the role EAT FAC on CMD. Here, we sought to a) develop and accelerate standard FAC IDEAL methods using compressed-sensing and signal model-based dictionary reconstruction methods¹³⁶ for efficient FAC quantification of EAT, and b) use this technique to quantify the EAT FAC in a mouse model of HFHSD-induced CMD before and after drug (eplerenone) treatment. The design, validation, and evaluation of this technique is summarized in [Chapter 3](#).

1.5 Mineralocorticoid Receptors

The mineralocorticoid receptor (MLR) is a ligand-dependent cellular transcription factor belonging to the steroid nuclear receptor superfamily, and is it widely expressed in various tissues including heart, kidney, colon, adipose tissue, and brain as well as blood vessels and immune cells. Ligands to MLRs include mineralocorticoids such as aldosterone or glucocorticoids such as cortisol. Activation of a MLR results in its translocation to the cell's nucleus, binding to certain gene promoters, and gene expression¹³⁷. The classical role of MLRs involves activation by aldosterone in the renal tubules to regulate sodium and water retention as well as blood pressure¹³⁸, but more recently, it has become established that MLRs have a more systemic role and regulate multiple diverse function across different tissues¹³⁹. There is also accumulating evidence supporting the pathophysiological role of MLRs in a wide range of diseases, particularly cardiovascular diseases and potentially CMD^{46,140,141}.

1.5.1 Mineralocorticoid receptors in cardiovascular diseases and CMD

In the heart, MLRs are present in cardiomyocytes, vascular smooth muscle cells (SMCs), endothelial cells (ECs), EAT, and immune cells¹⁴². The mechanisms involved in MLR activation within the cardiovascular system are complex and includes oxidative stress, inflammation, and fibrosis – all of which contribute to cardiovascular and microvascular dysfunction¹⁴⁰.

Cardiomyocyte MLRs, in addition to oxidative stress, inflammation, and fibrosis, have also been implicated in dysregulation chronotropic inotropic actions of the heart^{143,144}. Cardiomyocyte MLRs directly regulate trophic factors which control cell growth, L Type/T Type calcium channels, and other calcium and sodium handling proteins to modulate contractile activity and force generation. They also regulate numerous cytokines and oxidative stress generators including NADPH oxidases and p22phox to promote chemoattraction of immune cells and generally tissue inflammation^{144,145}. In a study of cardiomyocyte MLRs in rats, it was shown that MLRs not only promote oxidative stress, but oxidative stress can activate MLR signaling thus demonstrating an amplification loop mediated by ROS¹⁴⁶. These findings suggested that MLR activation can occur in the context of obesity and chronic inflammation in the absence of hyperaldosteronism.

Activation of the SMC and EC MLRs have been implicated in numerous disease processes resulting in coronary vascular and microvascular dysfunction. SMC MLRs are involved in blood pressure regulation¹⁴⁷, vascular stiffening and fibrosis^{147,148}, and coronary dysfunction¹⁴⁹. SMC MLRs act through genomic and non-genomic mechanism such as binding and dysregulation of calcium channels¹⁵⁰. EC MLRs are involved in diet-induced oxidative stress and inflammation, eventually leading to aortic stiffness¹⁵¹⁻¹⁵³. Similar to SMC MLRs, EC MLRs also act through genomic pathways such as upregulating ICAM/VCAM expression, and non-genomic pathways by promoting eNOS uncoupling and ROS expression¹⁵⁴. Davel *et al.* recently demonstrated that EC MLRs are a key factor in the sex dimorphism related to obesity-induced microvascular dysfunction by showing that only female mice were sensitive to obesity-induced MLR-mediated endothelial dysfunction¹⁴¹. Taken together, these findings suggest an important role for SMC and EC MLRs in CMD due to obesity and diabetes.

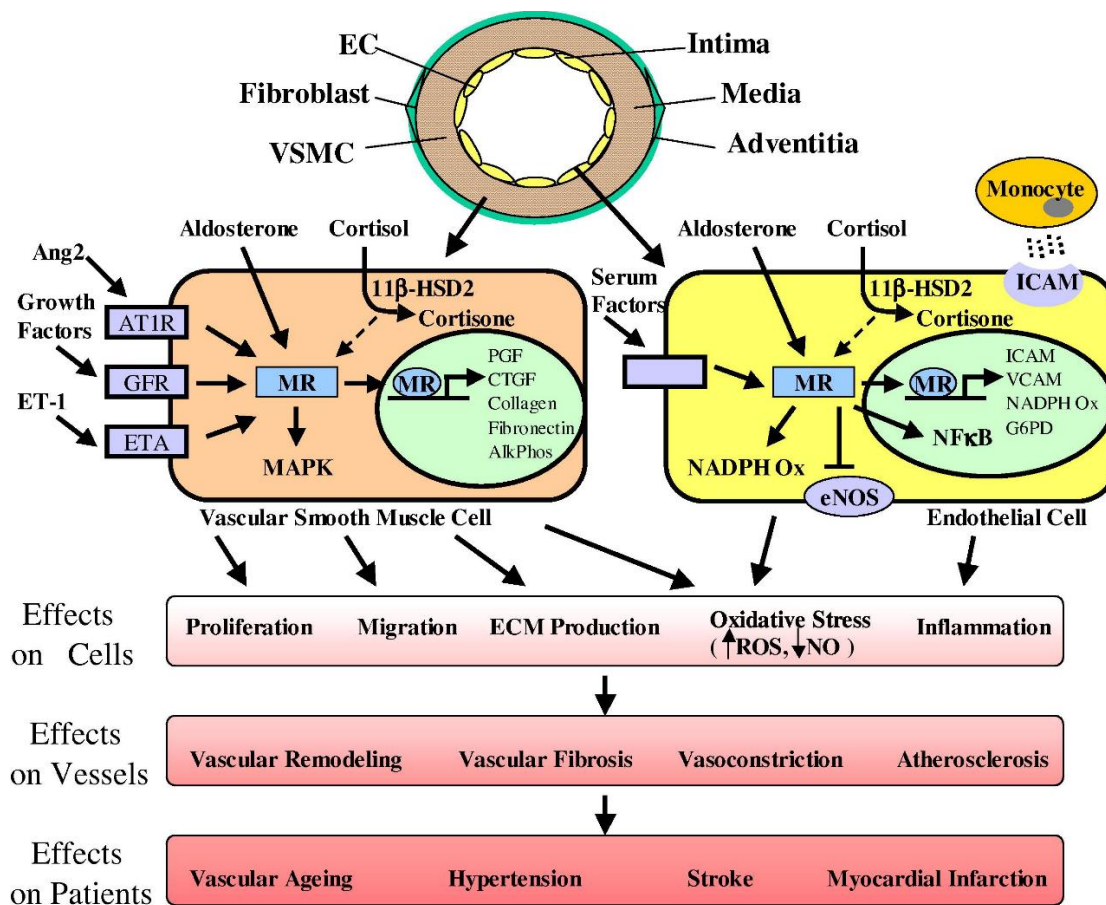


Figure 4. Vascular MLRs in cardiovascular disease and CMD

Figure Source: McCurley, A., & Jaffe, I. Z. (2012). Mineralocorticoid receptors in vascular function and disease. *Molecular and cellular endocrinology*, 350(2), 256-265.

EAT MLRs may have a major impact on exacerbating obesity, the metabolic syndrome, and vascular dysfunction¹⁴⁰. Diet-induced upregulation of EAT MLRs promotes increased lipid storage, weight gain and insulin resistance^{155–157}. In addition, obesity promotes MLR-dependent local production of ROS, local macrophage infiltration, and pro-inflammatory cytokine secretion¹⁵⁸; Because of the cross-talk between EAT and the coronary microvasculature, secretion of immune cells and cytokines can lead to impairments in vascular contractility¹⁵⁹. Altogether, there is sizeable evidence demonstrating the role of EAT MLRs in the transduction of metabolic inflammation to the coronary microvasculature.

Lastly, immune cells MLRs may have a key role in mediating microvascular inflammation. In pro-fibrotic mouse models, activation of MLRs induces M1-polarization of macrophages toward a pro-inflammatory phenotype, whereas MLR deletion leads to an anti-inflammatory M2 phenotype and prevents atherosclerosis, inflammation, and cardiovascular fibrosis^{160–164}. In macrophages, MLRs enhance production of ROS in part via inducible NOS (iNOS) activation^{160,161}. MLRs in T-cells and dendritic cells

promote T-cell polarization to pro-inflammatory Th1/Th17 which are associated with hypertension and chronic vascular inflammation^{165,166}.

In summary, systemic MLR activation due to obesity and diabetes promotes a diverse range of pathological mechanisms from oxidative stress to inflammation and fibrosis. Given the central role of these mechanisms in the pathophysiology of cardiovascular diseases, MLRs may represent important therapeutic marker for the treatment of CMD^{140,167}.

1.5.2 Mineralocorticoid receptor antagonism in cardiovascular disease and CMD

Current licensed MLR antagonists (MRAs) for clinical use include spironolactone and eplerenone. While both are steroid-based compounds which competitively bind MLRs, they differ in MLR affinity (spironolactone ↑), MLR selectivity (eplerenone ↑), half-life (eplerenone ↑), and metabolism pathways^{168–170}. More recently, non-steroidal MRAs have been developed, such as finerenone, which have potential to deliver similar efficacy as steroid MRAs, but without the endocrine and estrogenic side effects due to its non-steroidal structure^{168,171,172}. MRAs have been well-established as treatments for patients with hypertension, heart failure, and left ventricular systolic dysfunction post-myocardial infarction¹⁶⁸. Experimental data has also shown the effects of MRAs on reducing vascular inflammation, macrophage activation, oxidative/nitrosative stress, endothelial dysfunction, and myocardial fibrosis, and thus may provide more widespread benefits in multiple other cardiovascular disease states including CMD and HFpEF^{137,168}.

Studies on the impact of MRAs in animal models of heart disease have shown reductions in oxidative stress and inflammation, and an improvement in CBF^{173,174}. In addition, eplerenone has prevented adipose inflammasome activation and dysfunction, thus suppressing chronic vascular inflammation, in mouse models of obesity^{156,175}. Despite the preclinical success of MRAs, clinical studies investigating the role of MRAs on CMD and HFpEF have had mixed results and have altogether been inconclusive. In small clinical studies of patients with CMD, both spironolactone⁴⁶ and eplerenone⁴⁷ improved coronary microvascular function, as indicated by MPR. However, other studies examining MRA treatment in women found that improvements in CFR were lower compared to males¹⁷⁶ or completely absent⁴. In addition, results from a recent MRA-HFpEF trial were negative, though, there were some positive outcomes in specific patient subgroups^{177,178}.

Altogether, systemic MLRs activation due to obesity and diabetes may have a central role in the development of CMD, and MRAs have potential as a treatment for CMD albeit sex differences may have an impact on MRA treatment. This dissertation seeks to address these gaps in knowledge through the following specific aim:

Specific Aim 3 is to utilize multiparametric preclinical MRI and a mouse model of HFHSD-induced CMD to test the hypotheses that: a) MLR inhibition via eplerenone protects against MPR impairment and the development of CMD, b) eplerenone is a more effective treatment for CMD in males vs females, and c) SMC and EC MLRs have key roles in MPR impairment and the progression of CMD. The results of this aim are summarized in [Chapter 4](#).

In addition, recent studies have uncovered the role of iNOS as a central mediator of microvascular oxidative stress and dysfunction^{67,179,180}, so as an extra experiment, using a mouse model of HFHSD-induced CMD, we tested the hypotheses that: a) global iNOS deletion protects against MPR impairment and the development of CMD, and b) iNOS inhibition via 1400W can reverse established MPR impairment and CMD. The results of these experiments are summarized in [Appendix A](#).

Lastly, though both adenosine stress perfusion imaging and adenosine stress T1 mapping can be used to investigate coronary vascular function and myocardial ischemia without application of a contrast agent, other stress agents such as regadenoson can be used, and the receptors through which adenosine and regadenoson impart their effects are incompletely understood. In [Appendix B](#), using gene-modified mice and the two vasodilators, we elucidated and compared the mechanisms of stress myocardial perfusion imaging and stress T1 mapping.

Chapter 2 – Nitroxide Enhanced MRI of Cardiovascular Oxidative Stress

Note: The content in Chapter 2 has formally been published in NMR in Biomedicine

Shah SA, Cui SX, Waters CD, Sano S, Wang Y, Doviak H, Leor J, Walsh K, French BA, Epstein FH. Nitroxide-enhanced MRI of cardiovascular oxidative stress. NMR in Biomedicine. 2020 Sep;33(9):e4359.

2.1 Abstract

Background. In vivo imaging of oxidative stress can facilitate the understanding and treatment of cardiovascular diseases. We evaluated nitroxide-enhanced MRI with 3-Carbamoyl-PROXYL (3CP) for the detection of myocardial oxidative stress.

Methods. Three mouse models of cardiac oxidative stress were imaged, namely angiotensin II (ANG II) infusion, myocardial infarction (MI), and high fat high sucrose (HFHS) diet-induced obesity (DIO). For the ANG II model, mice underwent MRI at baseline and after 7 days of ANG II (n=8) or saline infusion (n=8). For the MI model, mice underwent MRI at baseline (n=10) and at 1 (n=8), 4 (n=9), and 21 (n=8) days after MI. For the HFHS-DIO model, mice underwent MRI at baseline (n=20) and 18 weeks (n=13) after diet initiation. The 3CP reduction rate, K_{red} , computed using a tracer kinetic model, was used as a metric of oxidative stress. Dihydroethidium (DHE) staining of tissue sections was performed at day 1 post-MI.

Results. For the ANG II model, K_{red} was higher after 7 days of ANG II vs. other groups ($p<0.05$). For the MI model, K_{red} in the infarct region was significantly elevated on days 1 and 4 post-MI ($p<0.05$), whereas K_{red} in the noninfarcted region did not change after MI. DHE confirmed elevated oxidative stress in the infarct zone at day 1 post-MI. After 18 weeks of HFHS diet, K_{red} was higher in mice post-diet vs. baseline ($p<0.05$)

Conclusions. Nitroxide-enhanced MRI noninvasively quantifies tissue oxidative stress as one component of a multiparametric preclinical MRI exam. These methods may facilitate investigations of oxidative stress in cardiovascular disease and related therapies.

2.2 Introduction

Oxidative stress, an imbalance between the generation and detoxification of reactive oxygen species (ROS), plays a central role in many types of cardiovascular disease. For example, in heart failure (HF) the renin-angiotensin-aldosterone system (RAAS) is activated, leading to the formation of ROS and oxidative stress in cardiovascular tissue¹⁸¹. Under these conditions, a primary pathway involves angiotensin II (Ang II) stimulation of nicotinamide adenine dinucleotide phosphate (NADPH) oxidases, which catalyze the production of superoxide and other ROS in vascular smooth muscle cells, endothelial cells, and cardiomyocytes. In another example, that of reperfused myocardial infarction (MI), infiltrating leukocytes such as neutrophils and macrophages are primary sources of ROS and oxidative stress¹⁸². As a third example, obesity, a condition with epidemic prevalence in Western societies, leads to systemic oxidative stress and contributes to cardiovascular disease¹⁸³. In general, cardiovascular oxidative stress leads to tissue damage by inducing vascular and myocardial inflammation, apoptosis, necrosis, hypertrophy, calcium dysregulation, and fibrosis. Various therapies may reduce oxidative stress and improve cardiovascular health and function¹⁸⁴.

While oxidative stress is an important mechanism underlying many types of cardiovascular disease and is a therapeutic target, there are limited means of measuring this parameter in vivo. Fluorescence methods are commonly used for ex vivo studies, but due to limited penetration depth, these methods are unsuitable for the in vivo assessment of cardiovascular structures. Electron paramagnetic resonance (EPR) imaging that measures the oxidative-stress-dependent decay rate of intravenously-injected exogenous nitroxide stable free radicals is an effective technique, as reviewed recently⁹⁵. In this method, paramagnetic nitroxides with oxygen free radicals undergo reduction reactions within cells where the EPR-visible paramagnetic nitroxide gets reduced to an EPR-invisible non-paramagnetic hydroxylamine, and the rate of reduction is dependent on oxidative stress. However, EPR imaging is not widely available, and EPR imaging has not been developed for human imaging. Alternatively, there is an opportunity to leverage the body of work that has developed oxidative-stress-sensitive nitroxide probes for EPR, and to use these nitroxides as oxidative-stress-sensitive T1-shortening agents for MRI where reduction of the nitroxide due to oxidative stress decreases the nitroxide's T1-shortening effect⁹⁶. This approach has the advantages that (a) MRI is widely available and regularly used preclinically for both small and large animals, (b) MRI can provide better spatial and temporal resolution than EPR imaging, and (c) MRI also provides high-quality anatomical and functional imaging that can be registered with oxidative stress images. These methods have already been developed and demonstrated for preclinical cancer^{97,99} and neurological^{98,185} MRI, but have not been evaluated for MRI of the cardiovascular system. Further, in principle, there are no fundamental obstacles preventing the application of nitroxide-enhanced MRI in humans.

In the present study we sought to demonstrate the utility of dynamic nitroxide-enhanced MRI to detect cardiovascular oxidative stress, and to quantify the nitroxide reduction rate. We investigated the application of dynamic nitroxide-enhanced MRI in three mouse models of cardiovascular oxidative stress: Ang II infusion, reperfused MI, and diet-induced obesity. Ang II infusion mimics many aspects of HF and leads, in the

short term, to an excess of coronary vascular superoxide¹⁸⁶, and in the long term to vascular dysfunction, myocardial fibrosis, hypertrophy and cardiac contractile dysfunction¹⁸⁷. The MI model exhibits oxidative stress due to a well-established time course of infiltrating neutrophils and macrophages in the infarct region providing intra-heart regional differences in oxidative stress as well as time dependent increases and decreases in oxidative stress. The high fat high sucrose diet-induced obesity (HFHS-DIO) model was selected as a third test system as this diet causes elevated levels of cardiac NADPH oxidase expression and superoxide anion production and leads to metabolic heart disease and coronary microvascular dysfunction¹⁸⁸. For a quantitative analysis, while simple exponential models have been used previously to describe the decay rate of nitroxide-enhanced MRI^{96,97}, we modified a two-compartment tracer kinetic model to incorporate intracellular nitroxide reduction and used the modified model to analyze our images.

2.3 Methods

The data that supports the findings of this study are available from the corresponding author upon reasonable request.

Two-compartment exchange and reduction tracer kinetic model

Two-compartment exchange models (2CXM) are widely used to describe the kinetics of MRI contrast agents such as gadolinium that exchange between the vascular and extravascular spaces. As shown in Figure 1 and similar to an approach taken for EPR of nitroxides¹⁸⁹, we propose to modify a conventional 2CXM by accounting for chemical reduction of the nitroxide when the nitroxide is in the extravascular space. The rationale for this approach is that the extravascular space includes the intracellular space wherein nitroxides undergo reduction reactions with reactive oxygen species such as superoxides. Mathematically, we define $C_V(t)$ as the vascular nitroxide concentration and $C_{EV}(t)$ as the extravascular nitroxide concentration and we express the two-compartment exchange and reduction model (2CXRM) as

$$\frac{dC_{EV}(t)}{dt} = K_1 \cdot C_V(t) - K_2 \cdot C_{EV}(t) - K_{red} \quad (Eq. 1)$$

$$\frac{dC_V(t)}{dt} = K_2 \cdot C_{EV}(t) - K_1 \cdot C_V(t) \quad (Eq. 2)$$

where K_1 is the vascular to extravascular exchange rate, K_2 is the extravascular to vascular exchange rate, and K_{red} is the nitroxide reduction rate within the extravascular compartment. Justification for the concentration-independent nature of K_{red} is provided in Appendix 1. Using a Laplace transform method to solve Eq. 1, C_{EV} can be expressed as

$$C_{EV}(t) = K_1 \cdot [e^{-(K_2) \cdot t} * C_V(t)] - K_{red} \cdot e^{-(K_2) \cdot t} + B \quad (Eq. 3)$$

where B is a constant. The nitroxide concentration (C_T) in the myocardial tissue, which includes both the vascular and extravascular compartments, is expressed as

$$C_T(t) = v \cdot C_V(t) + (1 - v) \cdot C_{EV}(t) \quad (Eq. 4)$$

where v is the vascular volume fraction of the tissue. In the present study, the signal from the left-ventricular blood pool was used to estimate $C_V(t)$ and the signal from the myocardium was used to estimate $C_T(t)$. We assumed that v is 0.05, consistent with previous studies¹⁹⁰. The nitroxide reduction rate, K_{red} , was used throughout all experiments as the MRI metric of myocardial oxidative stress.

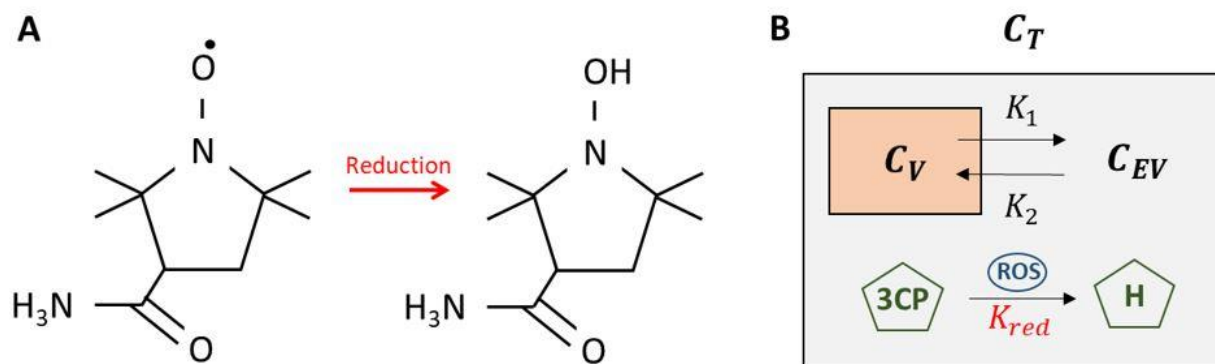


Figure 1. A. Molecular structure of the paramagnetic nitroxide, 3-Carbamoyl-PROXYL (3CP), showing a single unpaired electron, and the molecular structure of 3CP after undergoing a reduction reaction into a diamagnetic hydroxylamine, without an unpaired electron. **B.** The two-compartment exchange and reduction model (2CXRM) which accounts for (1) nitroxide exchange between the vascular and extravascular compartments within the tissue compartment with rate constants K_1 and K_2 , and (2) nitroxide reduction, with rate constant K_{red} , in the extravascular compartment due to intracellular reactions driving 3CP reduction to hydroxylamine via reactive oxygen species (ROS). C_V , C_{EV} , and C_T , are the 3CP concentrations in the vascular, extravascular, and tissue compartments.

Mouse models of oxidative stress

All animal studies were performed in accordance with protocols that conformed to the Declaration of Helsinki as well as the Guide for Care and Use of Laboratory Animals (NIH publication no. 85-23, revised 1996) and were approved by the Animal Care and Use Committee at the University of Virginia. Wild type male C57Bl/6 mice were obtained from Jackson Laboratories (8-10 weeks of age). For the Ang II infusion model, osmotic minipumps (Alzet Model 1002; Durect Corp, Cupertino, CA) loaded with Ang II at the concentration necessary to provide an infusion rate of 0.7 mg/kg body weight per day were implanted in mice ($n=8$) as previously described¹⁸⁶. Ang II was infused for seven days as this duration and dose have been shown previously to induce vascular oxidative stress¹⁸⁶. Control mice ($n=8$) with osmotic minipumps were infused with saline for seven days. Mice underwent MRI before and 7 days after implantation of infusion pumps.

For the model of reperfused MI, a surgical procedure employing a 40-minute occlusion of the left anterior descending (LAD) coronary artery followed by reperfusion was performed as previously described¹⁹¹. The 40-minute occlusion with reperfusion was chosen as this model has been shown to produce a strong inflammatory response 1-4 days post-MI, which largely resolves by 21 days post-MI^{192,193}. This well-characterized time course of inflammatory cell infiltration was used to select the imaging time points for the present nitroxide-enhanced MRI study. To demonstrate the detection of oxidative stress localized to the region of infarction and the effect of the time-varying

process of post-MI leukocyte infiltration, mice underwent nitroxide-enhanced MRI prior to MI (n=10) and at days 1 (n=8), 4 (n=9), and 21 (n=8) after reperfused MI.

Finally, for the HFHS-DIO model, mice were fed a HFHS diet (40% kcal fat, 40% kcal sucrose, Diet 12327, Research Diets Inc., New Brunswick, NJ), which was initiated at 10 weeks of age and was continued for 18 weeks. Mice underwent MRI at baseline (n=20, 8 weeks old) and 18 weeks post-diet (n=13).

Cardiac MRI

We chose the nitroxide 3-Carbamoyl-PROXYL (3CP) (Sigma–Aldrich, St. Louis, MO) for these experiments because it is water soluble, commercially available, generally well tolerated by mice, and it has previously been shown to provide signal enhancement in skeletal muscle and the heart^{94,194}. 3CP (C₉H₁₇N₂O₂) has a molecular weight of 185.24 g/mol, solubility in water of 50 mg/ml, formal charge 0, and a blood half-life of 7-10 minutes. 3CP has relaxation rates R₁ (or 1/T₁) that increase linearly with concentration in the range of 0.5 to 35 mM, and the relaxivity of 3CP in saline solution at 7T was previously measured to be 0.139 mM⁻¹sec⁻¹. To determine the dose of 3CP to use in the experiments aimed at the detection of oxidative stress in the heart, we performed 3CP-enhanced MRI of three healthy mice with doses of 0.4, 0.8, 1.2, 1.6 and 2.0 mmol/kg body weight. We used a 3CP concentration of 50 mg/mL, as this was the highest concentration of 3CP that would dissolve in saline. At this concentration and considering that the highest well-tolerated injection volume for mice weighing approximately 25 g is approximately 200 μL, 2.0 mmol/kg body weight is approximately the highest dose of 3CP that can be delivered. For each dose, we measured myocardial and blood signal-to-noise ratio. A saturation-recovery gradient echo MRI protocol, as described below, was used for 3CP-enhanced imaging.

All MRI studies were performed using a 7T system (Clinscan, Bruker, Ettlingen, Germany) and a 30-mm-diameter birdcage radiofrequency coil. An indwelling tail vein catheter was inserted for the injection of contrast agent during MRI. The electrocardiogram, body temperature, and respiration were monitored during imaging (SA Instruments, Stony Brook, NY). During MRI, mice were anesthetized with 1.25% isoflurane and maintained at 36 ± 0.5°C using circulating warm water, as previously described¹⁹⁵. Localizer imaging was performed to establish cardiac short- and long-axis views. Subsequently, dynamic T₁-weighted MRI was performed in a mid-ventricular short-axis slice before and consecutively after 3CP injection for 10 minutes. For the Ang II and reperfused-MI experiments, 3CP at a dose of 2.0 mmol/kg body weight was injected over 3 to 4 seconds. Over the course of these studies, approximately 10% of the mice died after 3CP-enhanced imaging. Accordingly, we reduced the 3CP dose in the HFHS DIO experiments to 1.2 mmol/kg body weight. For T₁-weighted imaging, an ECG-gated saturation-recovery segmented gradient echo sequence was used with field-of-view = 34 x 24 mm², matrix size = 128 x 104, TE = 1 ms, TR = 1.8 ms, flip angle = 15 degrees, slice thickness = 1 mm, saturation recovery time = 40 ms, number of segments = 8 and number of averages = 16, resulting in a total scan time of approximately 20 seconds per image, depending on heart rate. Consecutive T₁-weighted images were acquired for 12 minutes, beginning before injection of 3CP and

continuing for 10 minutes after the injection. In addition, proton-density-weighted images, similar to the T1-weighted images but without the saturation pulse and using flip angle = 5 degrees, were acquired prior to 3CP injection for myocardial segmentation and, with correction for flip angle differences, were used for normalization of signal intensities. In the MI mice, cine DENSE myocardial strain imaging¹⁹⁶ was performed in a matched short-axis slice prior to 3CP injection, as previously described^{197,198}.

Image analysis

For the MI mice, to distinguish the locations of infarcted and noninfarcted (remote) myocardium, strain maps were computed from the DENSE images acquired in a plane matched to that of the nitroxide-enhanced images, and thresholds were applied to circumferential shortening to define the infarcted (circumferential shortening > -0.05) and noninfarcted (circumferential shortening < -0.08) regions¹⁹⁹, as previously described¹⁹². Strain analysis of cine DENSE images was performed as previously described^{200,201}. The regions identified by strain thresholds were subsequently applied to the nitroxide-enhanced images to measure oxidative stress localized to the infarcted and noninfarcted regions.

The 2CXRm was used to quantify myocardial oxidative stress from the 3CP-enhanced images. The blood pool and the myocardium were manually segmented using a reference proton-density weighted image acquired at a matched location. For each mouse, for the whole slice or for infarcted and noninfarcted regions, the myocardial signal intensities from the dynamic 3CP-enhanced saturation recovery T1-weighted images were normalized to the signal intensities of the proton-density-weighted image. Region-of-interest (ROI) signal intensity was converted to 3CP concentration as previously described²⁰². C_V was estimated by least squares fitting of the [3CP] in the LV blood pool to a gamma-variate function combined with an exponential decay function. In mice that received a dose of 2.0 mmol/kg, C_V was scaled to account for the nonlinearity of signal vs. [3CP] for blood as shown in Figure 2. C_T was estimated by nonlinear regression fitting of the model parameters K_1 , K_2 , K_{red} , and B in Eqs. 3 and 4 to the myocardial ROI [3CP], and v was set to 0.05.

Confocal microscopy of dihydroethidium-stained tissue sections

In addition to MRI, dihydroethidium (DHE) staining of tissue sections was used to verify oxidative stress in the infarct region 1 day after MI. Specifically, following MRI on day 1 post-MI, hearts from 4 mice were explanted, washed with PBS, and sliced into 1 mm sections using a tissue slicer matrix (Zivic Instruments, Pittsburgh, PA). Hearts from 4 noninfarcted control mice also underwent this procedure. Sections were incubated for 20 minutes in DHE diluted to 3.2 μ M in PBS. Next, sections were imaged for the oxidation products of DHE using an excitation wavelength of 488 nm and an emission wavelength of 525 \pm 25nm on an UltraVIEW VoX confocal microscope (PerkinElmer, Waltham, MA)²⁰³. Image analysis was performed using the FIJI distribution of ImageJ²⁰⁴. Due to the localization of the oxidation products of DHE to the nucleus,

nuclei were segmented using localized contrast normalization and global thresholding. For each region (infarct region or noninfarcted region) we measured the mean fluorescence intensity within the nuclei weighted by nuclear count in the analyzed region (nuclear density). Oxidative stress in the infarcted vs. noninfarcted region was quantified as the ratio of the weighted fluorescence intensity of the infarcted vs. noninfarcted region. Use of this ratio controlled for factors that may differ from heart to heart such as photobleaching, dye penetration, and imaging plane depth. For control mice, the ratio between the lateral wall and septum was computed, as in the LAD coronary artery occlusion model the lateral wall is generally infarcted and the septum is not.

Effect of increasing perfusion on 3CP kinetics

Myocardial perfusion is another factor, in addition to oxidative stress, that would affect 3CP kinetics. To investigate the effect of perfusion on 2CXRM parameters, including K_{Red} , we performed dynamic 3CP-enhanced MRI in five mice after the intraperitoneal (IP) infusion of adenosine at a dose sufficient to maximally increase myocardial blood flow²⁰⁵. Specifically, we administered adenosine as a 300 $\mu\text{g}/\text{kg}/\text{min}$ IP infusion at a rate 5 $\mu\text{l}/\text{min}$ for 10 minutes²⁰⁵ prior to dynamic 3CP-enhanced MRI and it was continuously infused during imaging. We waited for 10 minutes after the start of the infusion for the heart rate to stabilize before performing 3CP-enhanced MRI. Five additional mice that did not receive adenosine were used as controls.

Statistics

For the Ang II infusion mice, two-way ANOVA was used to test for significant differences in K_{red} between the Ang II mice and control mice imaged prior to and 7 days post-infusion. For the MI mice, two-way ANOVA was used to test for significant differences in K_{red} between the infarct and noninfarcted regions and between measurements prior to and at days 1, 4, and 21 post-MI. For the HFHS DIO mice, a t-test was used to compare K_{red} between measurement at baseline and 18 weeks post-diet. Also, a t-test was used to compare K_{red} values between control and adenosine-infusion mice. A log-ratio t-test was used to compare ratio-based DHE measurements of oxidative stress in day-1 post-MI hearts vs. controls.

2.4 Results

MRI dose response

Example T1-weighted saturation-recovery gradient-echo short-axis images of the heart acquired before and after the injection of various doses of 3CP are shown in Figure 2A. Substantial enhancement of the blood and myocardial signals are readily observed. As shown in Figure 2B, the signal-to-noise ratio (SNR) of the myocardium linearly increased with dose for the full range of doses that were injected, whereas for the left-ventricular blood pool the SNR increased linearly with dose for the lower doses but started to plateau at doses above 1.2 mmol/kg. All of the injections were well tolerated by the mice. Based on these results, for subsequent experiments we initially chose to use the highest dose to achieve the highest myocardial SNR while maintaining myocardial signal linearity with dose.

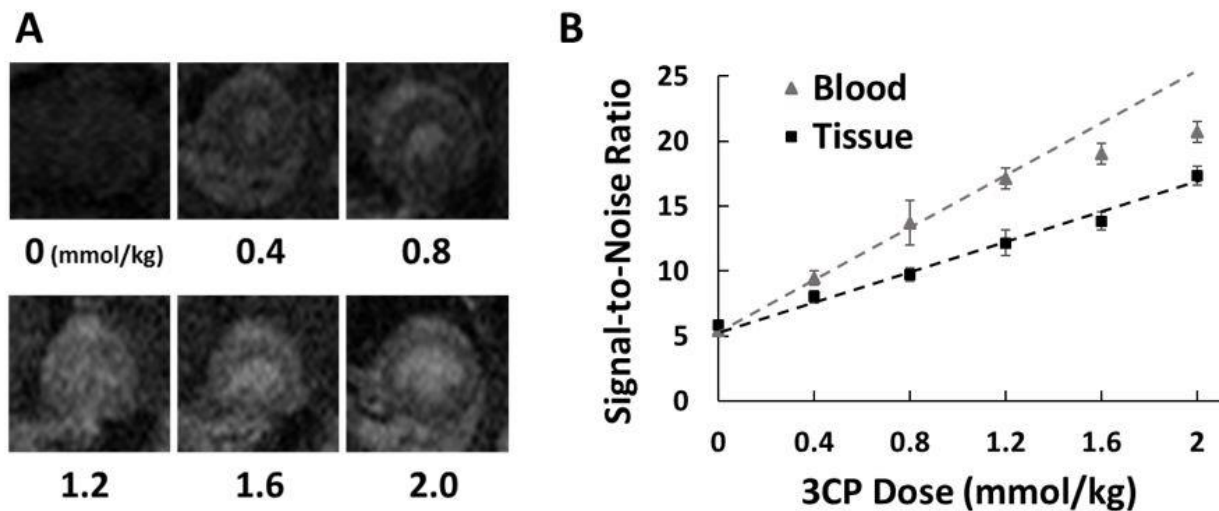


Figure 2. A. Example T1-weighted saturation-recovery gradient-echo short-axis images of the mouse heart acquired before and after the injection of 3CP at doses of 0.4, 0.8, 1.2, 1.6, 2.0 mmol/kg body weight. **B.** Signal-to-noise ratios (mean \pm standard error, $n=3$) are shown for each 3CP dose from regions of interest in the left ventricle blood pool and myocardial tissue.

Angiotensin II infusion

Example dynamic 3CP-enhanced saturation-recovery gradient-echo images of the heart are shown in Figure 3A demonstrating initial signal enhancement followed by decay over time. Figure 3B shows example manually-drawn ROIs for the blood pool and myocardial tissue, and Figure 3C shows example [3CP] data for the blood pool and myocardium and the associated 2CXR fits of $C_V(t)$ and $C_T(t)$. The results of the Ang II infusion experiments are shown in Figure 3D, where it is seen that after 1 week of Ang II infusion $K_{red} = 0.0405 \pm 0.0156$ [3CP]/min, which was approximately 8-fold higher than

the values 0.0051 ± 0.026 [3CP]/min, 0.0039 ± 0.0021 [3CP]/min, 0.0055 ± 0.0024 [3CP]/min for control mice at baseline, Ang II mice at baseline, and control mice at 1 week, respectively ($p < 0.05$). The 2CXRM had excellent goodness of fit, with R^2 values of 0.98 ± 0.2 (average \pm stdev).

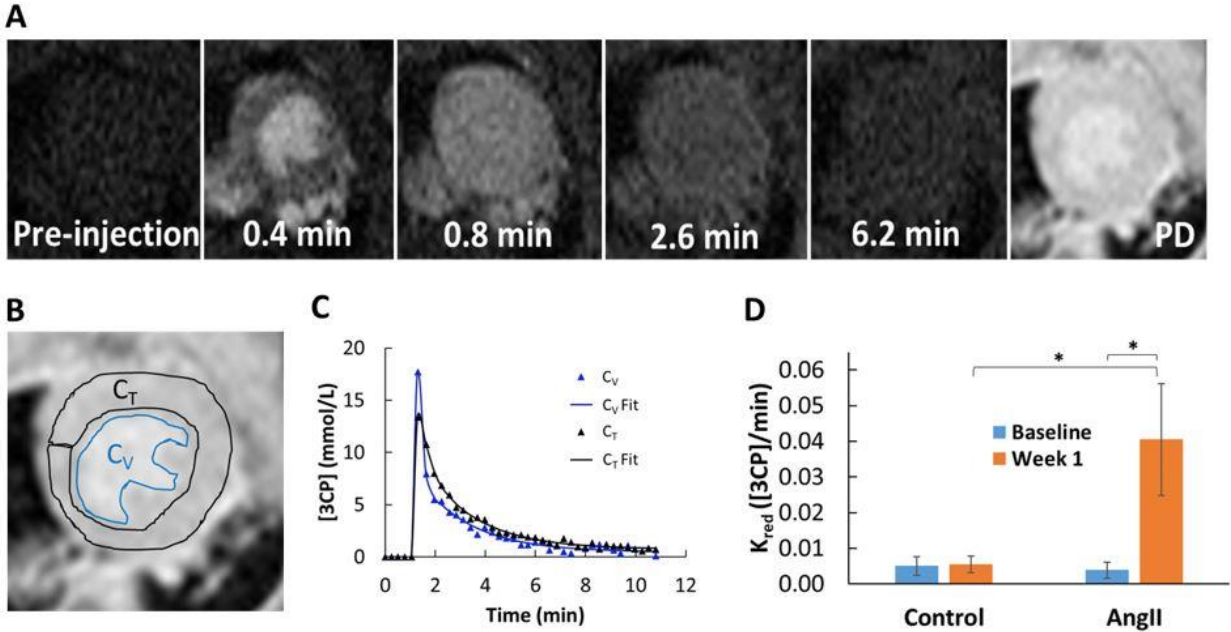


Figure 3. A. Example dynamic nitroxide-enhanced MR images before and after injection of 3CP demonstrate signal enhancement kinetics. A proton-density (PD) weighted image is used to visualize myocardial borders. **B.** Example ROIs of the LV blood pool and myocardium used to estimate vascular and tissue 3CP concentrations, C_V and C_T , respectively. **C.** Example $C_V(t)$ fit and 2CXRM fitting of $C_T(t)$ of a control mouse. The nitroxide reduction rate (K_{red}) was 0.0019 [3CP]/min and the R^2 was 0.99 . **D.** The 3CP reduction rate, K_{red} , was significantly elevated at week 1 in ANG II mice vs. ANG II mice at baseline and control mice at week 1. * $p < 0.05$ using a two-way ANOVA.

Myocardial Infarction

Figure 4 shows the results of the experiments in mice that underwent MRI after reperfused MI. Figure 4A demonstrates the use of a co-registered myocardial strain map to define infarcted and noninfarcted remote regions and shows the application of these regions to a 3CP-enhanced image. Figure 4B shows examples 2CXRM fits for infarcted and remote regions for a mouse scanned day 4 post-MI. K_{red} data summarizing all of the post-MI data are shown in Figure 4C, and show that K_{red} in the infarct zone is elevated on day 1 and day 4 post-MI ($p < 0.05$), and approximately returns to the baseline value on day 21 post-MI. In contrast, K_{red} in the remote region does not change significantly as a function of time post-MI. R^2 values for the 2CXRM were 0.97 ± 0.02 (average \pm stdev), demonstrating excellent goodness of fit. Representative confocal microscopy images from a day-1 post-MI DHE-stained mouse heart taken from remote and infarct regions of the same histological section are shown

in Figure 4D, demonstrating increased oxidative stress in the infarct regions compared to the remote region. Figure 4E shows that the mean infarct/noninfarct DHE ratio from 4 day-1 post-MI mice was 1.49 ± 0.25 as compared to the mean lateral wall/septum DHE ratio of 0.99 ± 0.24 from 4 control mice ($p < 0.01$). Thus, both nitroxide-enhanced MRI and DHE detect oxidative stress in the infarct zone compared to the remote zone one day after MI.

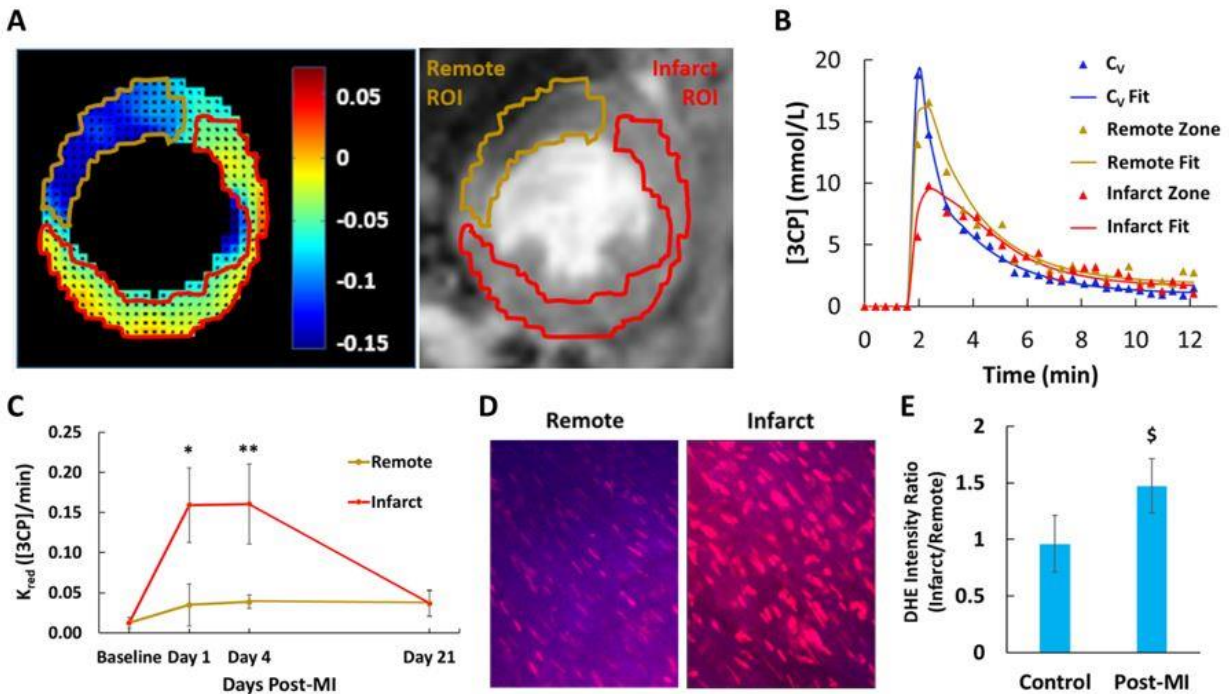


Figure 4: **A.** An example DENSE circumferential strain map was used to identify infarcted and noninfarcted remote regions of the myocardium in post-MI mice, and these regions were applied to nitroxide-enhanced images acquired at matched locations. **B.** Example vascular (C_V) and 2CXR remote zone and infarct zone C_T fits in a mouse one day post-infarction. **C.** Time courses of mean K_{red} for infarct and remote regions from mice before and during 21 days after MI demonstrate the rise and decline of oxidative stress in the infarct region. **D.** Example confocal images of DHE-stained myocardium obtained on day 1 post-MI. Specifically, overlays of 488 nm (for oxidation products of DHE) and 405 nm (for DHE) are shown for remote and infarct regions. **E.** DHE fluorescence in the infarct zone is elevated compared to the remote zone in one day post-MI mice, indicative of oxidative stress in infarcted myocardium. In contrast, in control mice DHE fluorescence was equivalent in the septal and lateral walls.

* $p < 0.05$ compared to Baseline and Day 21 infarct, and Day 1 remote using a two-way ANOVA.

** $p < 0.05$ compared to Baseline and Day 21 infarct, and Day 4 remote using a two-way ANOVA.

\$ $p < 0.05$ compared to Control using a log ratio t test.

High fat high sucrose diet-induced obesity (HFHS-DIO) model

The results of the experiments investigating the detection of oxidative stress after 18 weeks of HFHS diet are shown in Figure 5. K_{red} at 18 weeks post-diet was elevated compared to baseline (0.0327 ± 0.0102 vs 0.0014 ± 0.0009 , $p < 0.05$). R^2 values for the 2CXRM fits were 0.97 ± 0.01 (average \pm stdev).

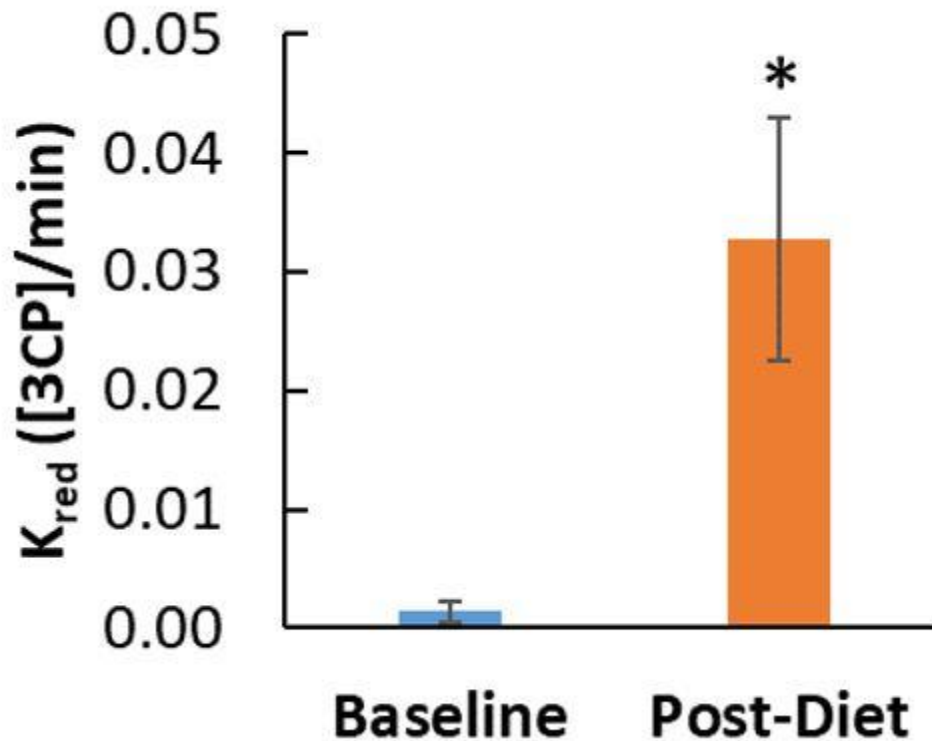


Figure 5: The myocardial 3CP reduction rate, K_{red} , was increased in mice fed a high fat high sucrose diet for 18 weeks compared to baseline (0.0327 ± 0.0102 vs 0.0014 ± 0.0009). * $p < 0.05$ compared to Baseline using a t test.

Adenosine-mediated perfusion

We observed no difference in K_{red} between mice with maximal perfusion due to adenosine injection and control mice without adenosine (0.0046 ± 0.0032 vs 0.0051 ± 0.0020). R^2 values for the 2CXRM fits were 0.98 ± 0.01 (average \pm stdev). This experiment showed that K_{red} is insensitive to changes in myocardial perfusion. Instead, adenosine infusion led to a significant increase in K_2 , and the complete 2CXRM results for adenosine infusion are provided in Appendix 1.

Toleration of 3CP

Overall, the injection of 3CP at a dose of 2.0 mmol/kg body weight was moderately tolerated by the mice. We performed a total of 67 injections of 3CP at this dose and within 1-2 days after 3CP injections 6 mice died, resulting in a 91% toleration rate. All of the mice that died were in the post-ANGII or post-MI groups, suggesting that 3CP at this dose and injection volume is not very well tolerated in mice at a weakened state. However, sixty-one mice had no observable adverse effects of 3CP at a dose of 2.0 mmol/kg with an injection volume of 200 μ L. For mice in the HFHS-DIO study, the injection of 3CP at a dose of 1.2 mmol/kg body weight and an injection volume of 120 μ L was well tolerated. Out of the 33 injections at this dose, only 1 mouse died, resulting in a toleration rate of 97%. Thirty-two mice had no observable adverse response.

2.5 Discussion and Conclusions

The major finding of this study is that the nitroxide reduction rate computed from 2CXRM-analysis of 3CP-enhanced MRI provides a metric of cardiac oxidative stress in preclinical models of heart disease, such as Ang II infusion, reperfused MI, and HFHS DIO. To our knowledge, no other MRI methods have been shown to assess oxidative stress in the heart. The nitroxide used in these studies, 3CP, is inexpensive, commercially available, and fairly well tolerated by mice, and a straightforward MRI method such as saturation-recovery gradient-echo imaging is sufficient for image acquisition, making MRI of cardiac oxidative stress easy to perform. As oxidative stress plays an important role in heart failure²⁰⁶, MI, obesity¹⁸³, coronary microvascular disease²⁷, hypertrophy²⁰⁷, cardiac arrhythmias²⁰⁸, cardiotoxicity due to chemotherapy²⁰⁹, and other types of heart disease, nitroxide-enhanced cardiac MRI may be a broadly applicable method for preclinical studies in many or all of these areas.

We chose to use 3CP because it has previously been shown to enhance skeletal muscle and myocardium^{94,194}, adverse reactions have not previously been reported in the literature, it is commercially available, and it has been shown to detect oxidative stress in tissue using EPR imaging²¹⁰. However, there are other nitroxides that might also be well-suited for MRI of oxidative stress in the heart²¹¹. For example, the nitroxide, 4-(N-methyl piperidine)-2,2,5,5-tetramethylpyrroline-1-oxyl (23c), has been shown to provide strong myocardial signal enhancement and may have a signal decay rate faster than that of 3CP¹⁸⁵. Future work may compare various nitroxides for detecting oxidative stress in the heart using MRI.

In our experiments, we gained experience with two doses of 3CP. For a dose of 2.0 mmol/kg body weight, no adverse events were observed in 91% of the 67 injections that were performed; however, 9% of the mice receiving this dose died. All of the mice that died had been treated with ANG II or underwent MI surgery. We used a lower 3CP dose in the HFHS-DIO experiments, where 33 3CP injections were performed using a dose of 1.2 mmol/kg body weight, and, under those conditions, only 1 mouse died, providing a tolerance rate of 97%. No adverse reactions whatsoever were observed in the remaining 32 mice. The adverse events that occurred at either dose may have been related to potentially toxic effects of 3CP, especially at higher doses, or to volume overload related to the relatively large volume of fluid injected. Based on the image quality and SNR results shown in Figure 1 as a function of 3CP dose, the high R² values demonstrating excellent goodness of fit for the 2CXRM at both doses, and the adverse event data, we advise that future studies should use a 3CP dose of 1.2 mmol/kg body weight.

For the analysis of tissue nitroxide kinetics, we developed a 2CXRM that accounts for exchange of 3CP between the vascular and extravascular spaces as well as 3CP reduction within the extravascular space. With a 3CP dose of 2.0 mmol/kg body weight and the pulse sequence used in this study, the signal intensity in the LV blood pool was nonlinear with the 3CP concentration, as shown in our dosing studies, and a manual adjustment to the arterial 3CP concentration was necessary. With the lower 3CP dose of 1.2 mmol/kg body weight, the blood-pool signal intensity remained in the linear range and no adjustment was used. Using adenosine, we showed that a large

increase in tissue perfusion did not affect the 3CP reduction rate, demonstrating, in conjunction with the oxidative stress models, that the K_{red} parameter is sensitive to changes in oxidative stress and insensitive to changes in perfusion. The overall R^2 values for the 2CXRM fits of 3CP tissue concentration were 0.97 ± 0.02 (average \pm stdev), and we did not observe significantly lower R^2 values when using a 3CP dose of 1.2 mmol/kg.

Confocal microscopy of DHE-stained myocardium was used to confirm oxidative stress in infarcted myocardium 1 day after MI. Quantitative analysis of these images indicated a 49% increase in oxidative stress in infarcted relative to noninfarcted tissue. This value is consistent with previous reports that used DHE histochemistry to assess oxidative stress in rat²¹² and mouse²¹³ models of MI. Non-invasive MRI of K_{red} on day 1 post-MI showed a 355% increase in the nitroxide reduction rate in infarcted vs noninfarcted myocardium. While the percent increase in the assessment of oxidative stress is different between 3CP-enhanced MRI and confocal microscopy after DHE staining, it should be noted that the two methods are performed under different conditions, do not reflect identical underlying tissue distributions of the tracers or their biochemistry, and the two metrics are computed differently.

While the MI studies detected oxidative stress at days 1 and 4 post-infarction, by day 21 post-infarction we detected a reduction of oxidative stress to baseline levels. This result is entirely consistent with prior pathology data showing resolution of the immune cell response by day 21¹⁹³. The clinical significance of this finding is that any potential future therapy that may target these immune cells and/or the associated oxidative stress may be effective at days 1 and 4 post-MI, but not at day 21.

Nitroxide-enhanced imaging can be one component of a multiparametric preclinical cardiac MRI protocol that assesses a number of parameters including cardiac structure, function, strain, perfusion, contractile reserve, perfusion reserve, and other tissue properties²¹⁴. For example, in our MI studies, we used cine DENSE myocardial strain imaging to identify distinct infarct and noninfarct zones, and we demonstrated that oxidative stress is localized to the infarct zone²¹⁵. Similarly, future studies may use nitroxide-enhanced MRI in combination with arterial spin labeling to study the relationship between oxidative stress and coronary vascular function or may use nitroxide-enhanced MRI in combination with T1 mapping to study inflammation or T2 mapping to study iron deposition. Using oxidative stress imaging as part of a comprehensive MRI protocol is a major advantage of nitroxide-enhanced MRI compared to EPR methods.

In summary, nitroxide-enhanced MRI of the heart is a simple and easy-to-use method to quantify tissue oxidative stress as one component of a multiparametric preclinical cardiac MRI exam.

2.6 Appendix 1 - Justification that K_{red} is a concentration-independent rate constant

We determined that the nitroxide reduction parameter, K_{red} , in the 2CXR of Eqs. 1-4 is concentration independent based on experiments relating the signal reduction rate to the nitroxide dose. Prior methods to quantify nitroxide reduction used a simple exponential model to determine the nitroxide signal intensity decay rate as described^{96,97}. Fig. A1A shows that the nitroxide decay rate, using a simple exponential model, stays constant as we increase the dosage of 3CP. Fig. A1B also shows that K_{red} remains fairly constant as the 3CP dose is increased. These results provide justification that K_{red} is a concentration independent rate constant for the doses studied.

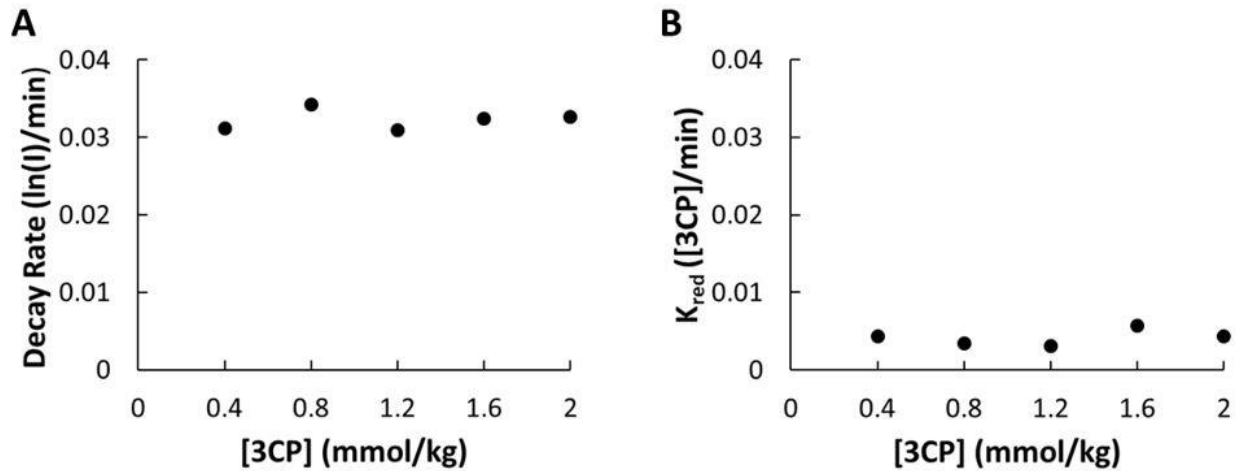


Figure A1: A. The myocardial 3CP decay rate quantified by linear fitting of the natural log of signal intensity (I) decay as a function of the 3CP dose. **B.** The 2CXR myocardial 3CP reduction rate, K_{red} , as a function of the 3CP dose.

2.7 Appendix 2 - K_1 , K_2 , and K_{red} results of 2CXRM analyses of all studies

While the main manuscript focused on K_{red} results, the 2CXRM also generated K_1 and K_2 results for each of the mouse models. Table A1 summarizes K_1 , K_2 , and K_{red} values computed using the 2CXRM for all mice in all studies. In the infarct region of post-MI mice, there was a significant reduction in K_1 and K_2 at day 1 and day 4 post-MI and a recovery to baseline at day 21 consistent with the time course of microvascular damage and revascularization following reperfused MI^{193,215}. In AngII mice, there was a reduction in K_2 post AngII infusion, and in the HFHS DIO mice there were significant reductions in both K_1 and K_2 post-diet. These results suggest that the 2CXRM analysis of 3CP detects compartmental exchange rate changes reflecting alterations of the microvasculature that occur in these disease models^{181,183}. In mice with maximal vasodilation via adenosine, no changes in K_1 were detected; however, the increase in tissue perfusion that occurs with this adenosine dose resulted in a large increase in K_2 , the parameter describing the exchange rate of 3CP from the extravascular to the vascular space.

	K_1	K_2	K_{red}
Saline Pre	2.36 ± 0.30	4.20 ± 0.53	0.0051 ± 0.0026
Saline Post	2.24 ± 0.32	4.14 ± 0.55	0.0055 ± 0.0024
ANGII Pre	2.33 ± 0.17	4.73 ± 0.94	0.0039 ± 0.0023
ANGII Post	2.16 ± 0.25	3.24 ± 0.27	0.0405 ± 0.0156*
Remote Baseline	2.08 ± 0.22	3.49 ± 0.31	0.0126 ± 0.0064
Remote Day 1	1.89 ± 0.15	3.15 ± 0.47	0.0350 ± 0.0261
Remote Day 4	1.88 ± 0.10	2.50 ± 0.12	0.0387 ± 0.0084
Remote Day 21	1.78 ± 0.10	3.04 ± 0.42	0.0370 ± 0.0163
Infarct Baseline	2.05 ± 0.23	3.60 ± 0.38	0.0134 ± 0.0083
Infarct Day 1	1.14 ± 0.08**	1.84 ± 0.17 #	0.1592 ± 0.0464 #
Infarct Day 4	1.52 ± 0.14**	1.97 ± 0.19 #	0.1606 ± 0.0497 #
Infarct Day 21	1.91 ± 0.10	3.07 ± 0.36	0.0369 ± 0.0155
HFHS Baseline	2.18 ± 0.08	4.56 ± 0.39	0.0014 ± 0.0009
HFHS Post-Diet	1.79 ± 0.14 \$	2.86 ± 0.20 \$	0.0327 ± 0.0102 \$
Adenosine Control	2.24 ± 0.32	3.86 ± 0.38	0.0051 ± 0.0020
Adenosine Post	2.34 ± 0.13	5.97 ± 1.24 &	0.0046 ± 0.0032

Table A1: Summary of 2CXRM parameter values obtained from all DNE-MRI experiments performed in this study.

* $p < 0.05$ vs ANGII Pre and Saline Pre using a two-way ANOVA.

** $p < 0.05$ vs all Infarct time points and same day Remote using a two-way ANOVA.

$p < 0.05$ vs Infarct Baseline, Infarct Day 21, and same day Remote using a two-way ANOVA.

\$ $p < 0.05$ vs HFHS baseline using a t test.

Chapter 3 – Accelerated Fatty Acid Composition MRI of Epicardial Adipose Tissue: Development and Application to Eplerenone Treatment in a Mouse Model of Obesity-induced Coronary Microvascular Disease

3.1 Abstract

Purpose: To develop an accelerated MRI method to quantify the epicardial adipose tissue (EAT) fatty acid composition (FAC) and test the hypothesis that eplerenone (EPL) shifts the EAT FAC towards unsaturation in obese mice.

Methods: Undersampled multi-echo gradient-echo imaging employing a dictionary-based compressed-sensing reconstruction and IDEAL-based mapping was developed, validated, and used to study EAT in obese mice scanned at 7T. Fully sampled and rate-2, 2.5, 3, and 3.5 undersampled image data were acquired, reconstructed, and assessed using root mean square error (RMSE) and structural similarity (SSIM). Two groups of mice were studied: untreated (CTRL, n=10) and EPL-treated (n=10) mice fed a high-fat high-sucrose diet. MRI included imaging of EAT FAC, EAT volume, and myocardial perfusion reserve.

Results: Rate-3 acceleration provided RMSE < 5% and SSIM > 0.85 for FAC MRI. After six weeks of diet, EPL-treated compared to untreated mice had a reduced EAT saturated fatty acid fraction (0.27 ± 0.09 vs 0.39 ± 0.07 , $p < 0.05$) and increased EAT unsaturation degree (4.37 ± 0.32 vs 3.69 ± 0.58 , $p < 0.05$). Also, EAT volume in EPL-treated compared to untreated mice was reduced (8.1 ± 0.6 mg vs 11.4 ± 0.7 mg, $p < 0.01$) and myocardial perfusion reserve was improved (1.83 ± 0.15 vs 1.61 ± 0.17 , $p < 0.05$).

Conclusion: Rate-3 accelerated FAC MRI enabled accurate quantification of EAT FAC in mice. EPL-treatment shifted the EAT FAC toward increased unsaturation and was associated with improvement of coronary microvascular function.

3.2 Introduction

In recent years there has been growing interest in the role of epicardial adipose tissue (EAT) in various types of heart disease including coronary microvascular disease and heart failure with preserved ejection fraction^{102,126,216,217}. EAT is an active endocrine organ located directly on the heart's surface with an extensive secretome and it shares an unobstructed microcirculation with the underlying myocardial tissue²¹⁸. In normal conditions, EAT protects the coronary arteries and myocardium from inflammation and fibrosis¹⁰³⁻¹⁰⁵; however, in pathological conditions such as obesity, the EAT has been described as a transducer of metabolic inflammation to the coronary vasculature^{102,106}. Specifically, in obesity the EAT volume increases and a phenotypic shift occurs where M1-polarized macrophages accumulate and the EAT secretes proinflammatory cytokines that promote vascular and myocardial dysfunction²¹⁹⁻²²². In this condition the EAT fatty acid composition (FAC) is thought to contribute to its proinflammatory state^{223,224}, as saturated fatty acids (SFAs), through toll-like receptor-4 signaling, promote macrophage M1 polarization and inflammasome activation¹¹¹. Alternatively, decreasing SFAs and increasing the degree of unsaturation promotes cardioprotection¹¹³⁻¹¹⁵. These points suggest that while imaging EAT volume provides one important metric describing the EAT^{225,226}, imaging EAT FAC may provide additional important information regarding its inflammatory or proinflammatory state.

FAC MRI techniques have recently been developed and validated in phantoms^{134,227,228} and applied in the abdomen^{134,229,230}, liver²³¹, and bone marrow^{232,233} to quantify adipose tissue FAC; however, these methods have not yet been applied to EAT. Generally, by using prior knowledge of the ¹H triglyceride spectrum¹³⁰, the multi-echo gradient-echo signal from adipose tissue is represented using a multi-resonance signal model. After fitting the model to acquired multi-echo gradient-echo data using a method such as iterative decomposition with echo asymmetry and least-squares (IDEAL), physiologically meaningful parameters such as SFA fraction, polyunsaturated fatty acid (PUFA) fraction, monounsaturated fatty acid (MUFA) fraction, unsaturated degree (UD), and polyunsaturated degree (PUD) can be computed from the model parameters¹³⁴.

Although standard FAC MRI methods can be applied to EAT, heart motion dictates the need for cardiac-gated segmented acquisitions, lengthening the scan time. Therefore, acceleration techniques are essential to achieve practical scan times. Liu et al. has demonstrated the use of a compressed sensing method utilizing a dictionary based on the multi-resonance ¹H triglyceride spectrum to reconstruct separate fat and water images of the gastrointestinal tract¹³⁶. Here, we extend these methods to accelerate FAC MRI of EAT.

The first goal of the present study was to develop and validate an accelerated multi-echo gradient-echo MRI method to be used with IDEAL mapping to quantify EAT FAC in mice. Next, using MRI applied to a mouse model of diet-induced obesity, we tested the hypothesis that eplerenone (EPL), a mineralocorticoid antagonist shown to reduce obesity-related adipose inflammation^{156,175}, reduces EAT volume, shifts the EAT FAC toward an anti-inflammatory state (with reduced SFAs and increased UD) and reduces coronary microvascular dysfunction.

3.3 Methods

FAC imaging and mapping

As shown by Ren et al, triglycerides contain ten unique ^1H resonances, such that, at a given time after excitation, t , the phase of each resonance is given by $\alpha_m(t) = e^{i\omega_m t}$, where $\omega_m = \gamma B_0(\delta_m - \delta_W)$, B_0 is the main magnetic field strength, and δ_m and δ_W are the chemical shifts of triglyceride proton m and water protons, respectively, in ppm, and γ is the gyromagnetic ratio¹³⁰. An example triglyceride and the corresponding ^1H nuclear magnetic resonance (NMR) spectrum are shown in Figure 1. As shown by Berglund et al.¹³⁴, any “mean triglyceride” can be described by four components, built up from the individual resonances, given by $\alpha_{F1} = 9\alpha_A + 6\alpha_C + 6\alpha_E + 2\alpha_G + 2\alpha_H + \alpha_I$, $\alpha_{F2} = 2\alpha_B$, $\alpha_{F3} = 4\alpha_D + 2\alpha_J$, and $\alpha_{F4} = 2\alpha_F + 2\alpha_J$. In this model, α_{F1} describes the total number of triglycerides, α_{F2} relates to the carbon chain length of bulk methyls, α_{F3} relates to the total number of double bonds, and α_{F4} relates to the total number of poly-double bonds. Using this model, any admixture of triglycerides can be described by a linear combination of the four components. When we also account for B_0 inhomogeneity, ψ , and R_2^* effects, we can write the equation for the gradient-echo signal at the n th echo time, TE_n , as:

$$S(TE_n) = (2W + \sum_{i=1}^4 F_i \alpha_{Fi}) e^{(i2\pi\gamma\psi - R_2^*)TE_n} \quad [1]$$

where W , F_1 , F_2 , F_3 , and F_4 represent the fraction of signal from the water and fat components, respectively.

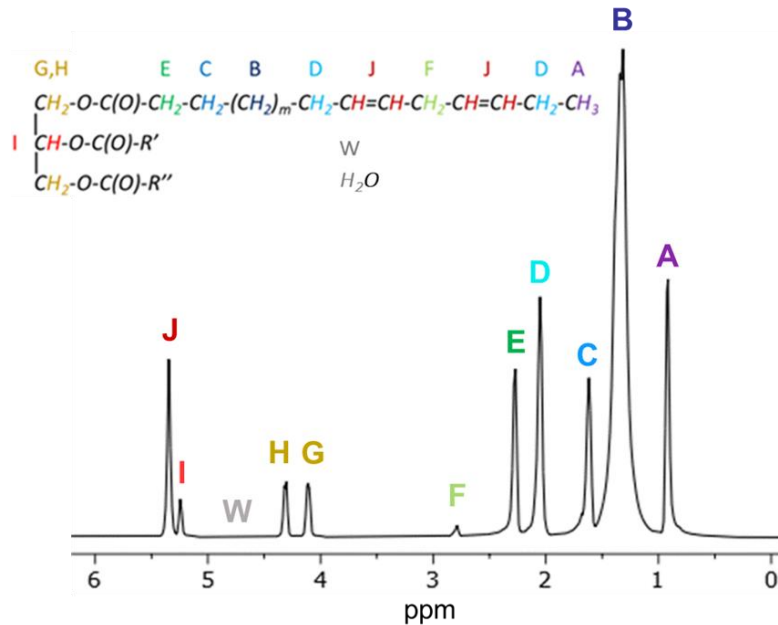


Figure 1: Schematic diagram of a triglyceride showing the 10 different ^1H atoms (A-J) and an example spectrum from olive oil showing the corresponding ^1H NMR resonances. The location of the ^1H resonance of water (W) is shown at its theoretical position of 4.7 ppm.

To calculate the signal fractions, the IDEAL algorithm shown by Yu et al. was extended to incorporate five signal terms²³⁴. If N gradient-echoes are acquired, Eq. 1 can be written in matrix form as $S = PAx$, where $S = [S(TE_1), S(TE_2), \dots, S(TE_N)]^T$ is the complex signal at N echo times, P represents ψ and R_2^* effects and is an $N \times N$ matrix of diagonal elements with values $\Phi_n = e^{(i*2\pi)(\gamma\psi - \frac{R_2^*}{i*2\pi})TE_n}$, $x = [W, F_1, F_2, F_3, F_4]^T$, and $A = [\alpha_{i,j}]$ is an $N \times 5$ matrix with elements $\alpha_{n,1} = 2$, $\alpha_{n,2} = \alpha_{F_1}(TE_n)$, $\alpha_{n,3} = \alpha_{F_2}(TE_n)$, $\alpha_{n,4} = \alpha_{F_3}(TE_n)$, and $\alpha_{n,5} = \alpha_{F_4}(TE_n)$. S is measured at each pixel by acquiring gradient-echo images at N echo times. Assuming that ψ and R_2^* will be estimated for each pixel, then the least-squares solution for x is computed as

$$x = (A^T A)^{-1} \cdot A^T \cdot P^{-1} \cdot S \quad [2].$$

To estimate ψ and R_2^* , following Yu et al., a Taylor series approximation of Eq. 1 is used followed by another least-squares solution²³⁴. Finally, as shown by Berglund et al., the fractional FAC of tissue triglycerides representing SFAs, PUFAs, and MUFAs can be calculated as $SFA = 1 - \frac{F_3}{3F_1}$, $PUFA = \frac{F_4}{3F_1}$, and $MUFA = \frac{F_3 - F_4}{3F_1}$. In addition to fatty acid fractions, the unsaturated degree (UD) and polyunsaturated degree (PUD) can be calculated as $UD = \frac{F_3 + F_4}{F_1}$ and $PUD = \frac{F_4}{F_1}$ which describe the number of double bonds and poly-double bonds, respectively, per triglyceride. An example using this modified IDEAL method to compute FAC maps of a vegetable oil phantom is shown in Figure 2. We refer to these methods as FAC-IDEAL.

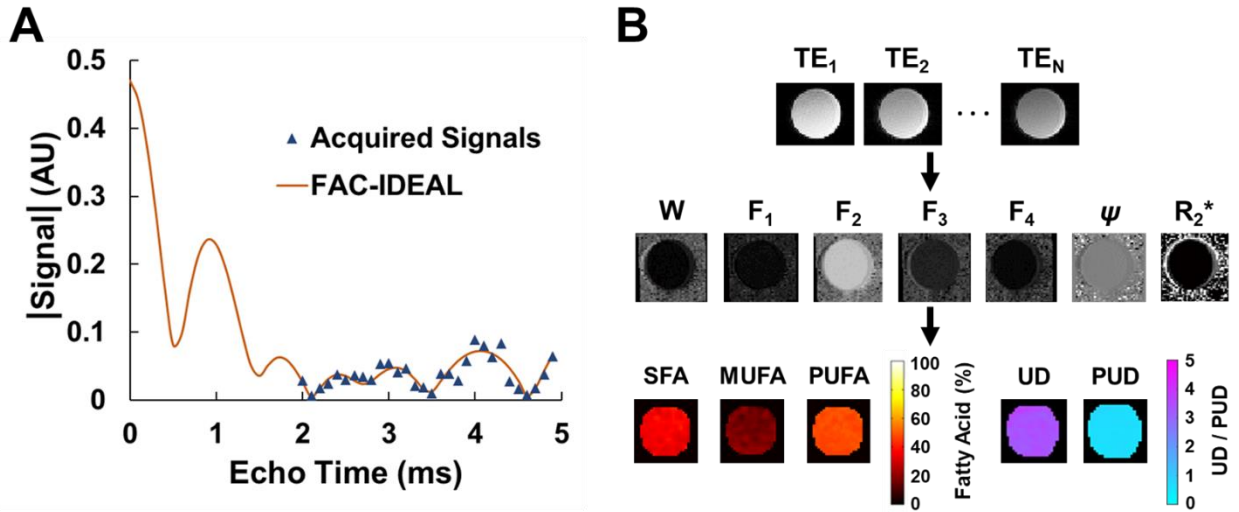


Figure 2: (A) Example FAC-IDEAL least-squares fit of the signal model to the acquired multi-echo gradient-echo data of vegetable oil for one pixel. (B) Flow diagram of FAC-IDEAL showing the process of FAC mapping from N gradient echo images.

Selection of the number of echoes and the echo spacing for FAC MRI at 7T

An important issue for FAC imaging is choosing the number of echoes and interecho spacing required for efficient estimation of SFA, PUFA, MUFA, UD, and PUD. To address this issue, Cramér-Rao lower bound analysis on the variance of the estimates²³⁵ was performed on an oil phantom. The phantom was constructed using separate tubes of water, sesame oil, olive oil, and vegetable oil. Specifically, 1 mL pipette tips were filled with each oil, attached to the lid of an empty 50 mL conical tube, and placed inside the tube. Sesame, olive, and vegetable oils were chosen because they have a FAC similar to that of mammalian adipose tissue. Using a 7T small-animal MRI system (Clinscan, Bruker, Ettlingen, Germany), 30 gradient-echo images were acquired using evenly-spaced TEs ranging from the minimum TE of 2.0 ms to 4.9 ms. Using $TE \geq 5$ ms, due to magnetic field inhomogeneity at 7T around the mouse heart²³⁶, gradient-echo images suffer from $T2^*$ decay and distortion artifacts, thus we constrained our maximum TE to be less than 5ms.. Other acquisition parameters included: slice thickness = 1 mm, TR = 120 ms (approximating the mouse R-R interval), flip angle = 15° , 32 averages, acquisition matrix 128 x 128, and resolution 0.2×0.2 mm². For Cramér-Rao analysis, the number of echoes was retrospectively varied from 6 to 30 and the interecho spacing was retrospectively varied between 0.1 and 0.5 ms. Of note, Berglund et al. demonstrated that the choice of the initial echo time does not have a significant impact on the analysis, so for this analysis, we did not vary the initial echo time¹³⁴.

Figure 3A shows example SFA maps of sesame oil demonstrating changes in parameter map variance with different numbers of echoes and echo spacings. Figure 3B-C shows the average variances for SFA and UD maps from all three oils with various numbers of echoes and interecho spacings. For all parameters, including SFA, PUFA, MUFA, UD, and PUD, the optimal choices for the number of echoes and the interecho spacing were found to be 9 or 10 echoes and 0.3 ms spacing, respectively. Since, in practice for in vivo imaging we will acquire 2 echoes per RF excitation, there is no practical benefit to using 9 vs. 10 echoes.

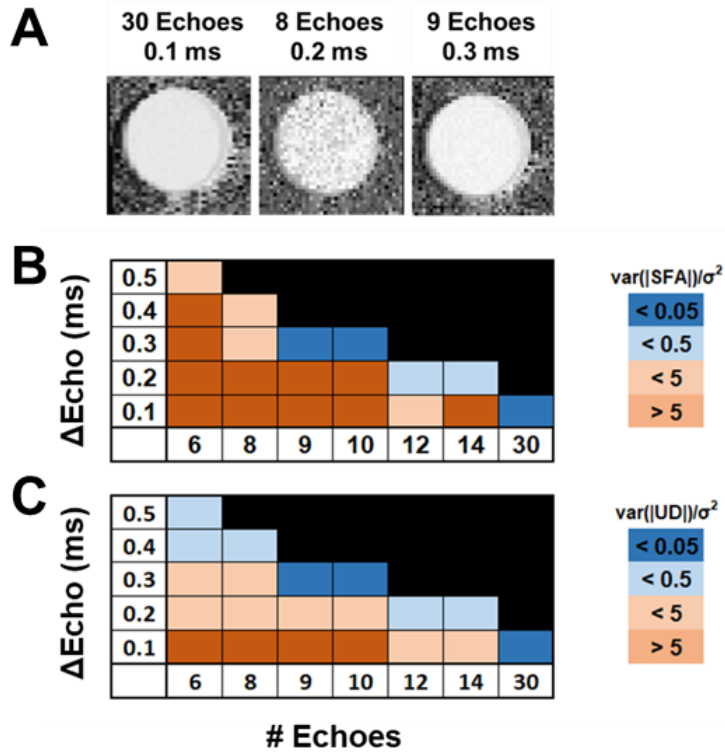


Figure 3: (A) Example grayscale SFA maps of sesame oil from acquisitions with varying numbers of echoes and interecho spacings ($\Delta Echo$) demonstrating differences in signal variance. Cramér-Rao analysis shown for (B) SFA and (C) UD maps indicates that 9 or 10 echoes with 0.3 ms spacing represents the smallest number of echoes that provides a ratio of signal variance / noise variance (σ^2) less than 0.05.

Minimum SNR required for accurate FAC MRI

Because signal-to-noise ratio (SNR) is related to scan time, it is also important to find the minimum SNR that maintains accurate estimation of FAC. Using the oil phantom dataset with 10 echoes and 0.3 ms spacing, we retrospectively varied the number of averages to show that an SNR of 24 (corresponding to 8 signal averages for the in vivo EAT imaging protocol) maintains FAC-IDEAL SFA, PUFA, MUFA, UD, and PUD estimation errors of less than 10% compared to NMR spectroscopy as shown in Figure 4. To measure SNR, regions of interest for signal and noise (~150 pixels per region) were manually contoured on the first echo (TE = 2.0ms) magnitude-reconstructed images, and SNR was calculated as $\text{mean}(\text{signal}) / \text{stdev}(\text{noise})$.

NMR Spectroscopy

As a reference method, NMR spectroscopy was used to characterize the SFA, MUFA, and PUFA fractions and the UD and PUD. Samples were placed in an NMR tube with width of 5 mm and length of 7". A Bruker AVIII-600 spectrometer was used to acquire 1D 1H spectra. Sixteen averages were obtained for each spectrum and the time

between pulses was 10s. Spectral analysis was performed in Mnova v14.2.1 (Mestrelab Research SL, Santiago de Compostela, Spain) and SFA, PUFA, and MUFA fractions as well as UD and PUD were quantified as described^{130,134}.

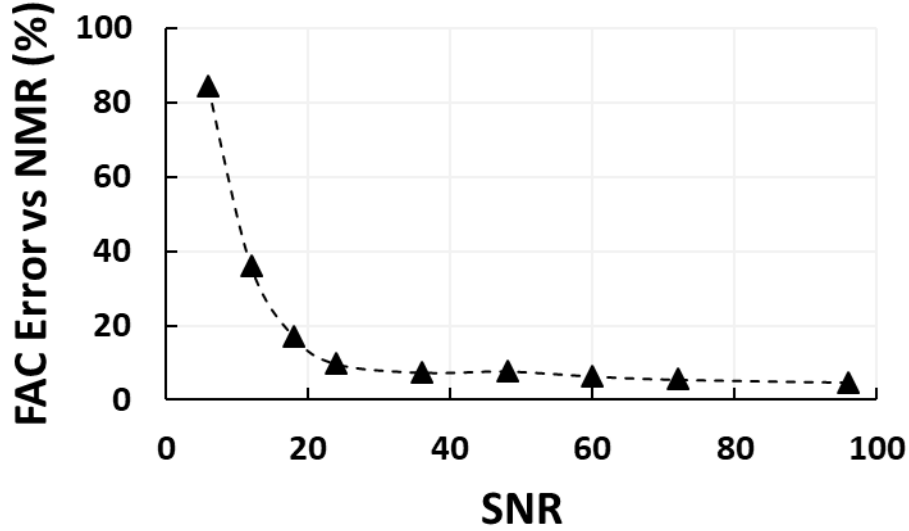


Figure 4: Average FAC-IDEAL error compared to NMR spectroscopy of sesame, olive, and vegetable oils as a function of the SNR of the acquired gradient-echo images.

Accelerated multi-echo gradient-echo FAC MRI

Building upon the work of Liu et al¹³⁶, undersampling masks using a uniform rate-2 undersampling pattern for the center 33% of k-space and a Poisson-Disc undersampling pattern for the outer 66% of k-space along the k_y and echo time dimensions were generated for rate 2, 2.5, 3, and 3.5 acceleration. An example mask is shown in Figure 5A.

Image reconstruction was performed using compressed sensing with a signal model-based dictionary by solving the following minimization Eq:

$$\underset{i, \phi}{\operatorname{argmin}} \|F_U \mathbf{E} \mathbf{i} - \mathbf{d}\|_2^2 + \lambda_T \|\mathbf{i}\|_2 + \lambda_D \|\mathbf{D} \boldsymbol{\phi} - \mathbf{i}\|_2^2 \text{ s. t. } \mathbf{n}(\boldsymbol{\phi}) = \alpha \quad [3]$$

Eq. 3 contains a data fidelity term, Tikhonov regularization to improve stability, and enforces consistency with an overcomplete signal model-based dictionary. In Eq. 3, F_U represents application of the Fourier transform operator after application of the undersampling mask, \mathbf{E} is the coil sensitivities, \mathbf{i} is the reconstructed image, \mathbf{d} is the acquired k-space data, \mathbf{D} is the overcomplete dictionary, $\boldsymbol{\phi}$ is the scaling factor vector for the dictionary related to the signal magnitude, α is the number of non-zero elements in $\boldsymbol{\phi}$, and λ_T and λ_D are weighting factors corresponding to the regularization and dictionary terms.

Eq. 3 was solved using alternating updates of i and ϕ where α elements of ϕ are obtained using orthogonal matching pursuit (OMP) which searches for the entry in D with the highest correlation to i . Subsequently i is updated using M_{GD} steps of gradient descent. After M_{FI} full iterations of OMP and gradient descent, mapping using FAC-IDEAL was performed on the final reconstructed images. Figure 5B shows a flow diagram of the reconstruction, which we refer to as CS-DICT. FAC-IDEAL was applied after using a dictionary-based reconstruction because the resolution of the dictionary was limited in order to achieve a reasonably fast reconstruction time. Use of a dictionary with limited resolution followed by FAC-IDEAL mapping provided a practical combination of computation time and accuracy.

CS-DICT parameter selection

D , α , λ_T , λ_D , M_{GD} , and M_{FI} were optimized to minimize the root mean square error (RMSE) using L-curve analysis²³⁷. The entries to D , potential signal evolutions over N echoes, were created by computing Eq. 1 for all combinations of F_1 , F_2 , F_3 , F_4 , $\gamma\psi$, and R_2^* , given that $W = 1 - F_1 - F_2 - F_3 - F_4$, and using parameter ranges based on FAC-IDEAL mapping of fully-sampled datasets acquired from obese mice scanned at 7T. D was constructed using number of echoes = 10, $0 < F_1 < 0.1$, $0 < F_2 < 0.7$, $0 < F_3 < 0.15$, $0 < F_4 < 0.15$, $-250 \text{ Hz} < \gamma\psi < 250 \text{ Hz}$, and $0 \text{ s}^{-1} < R_2^* < 400 \text{ s}^{-1}$ resulting in a dictionary with size $10 \times 38,016$. Other optimized parameters include: $\alpha = 4$, $\lambda_T = 0.01$, $\lambda_D = 0.1$, $M_{GD} = 12$, and $M_{FI} = 12$.

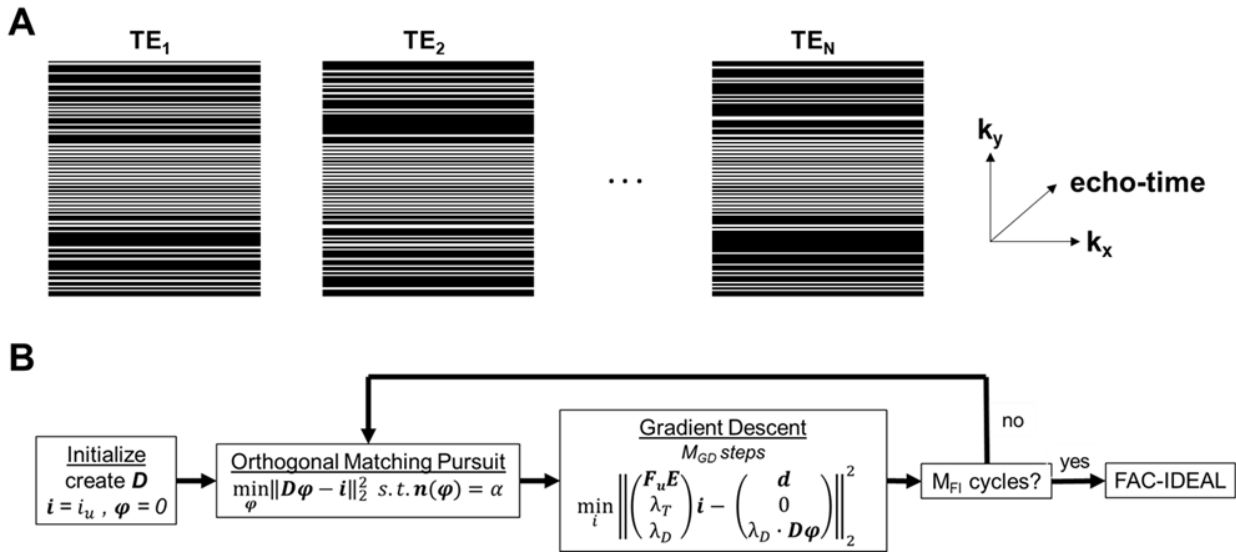


Figure 5: (A) Example rate 2.5 acceleration undersampling masks with uniform undersampling in the center of k-space and Poisson-Disc undersampling in outer k-space and along the echo-time dimension. (B) Flow diagram for CS-DICT reconstruction. First, the image i is initialized to the undersampled image i_u via a 2D inverse Fourier transform. Next, α elements of the dictionary scaling vector ϕ and the image i are alternatively updated by orthogonal matching pursuit and M_{GD} gradient descent steps, respectively, for M_{FI} cycles. Afterward, FAC-IDEAL is performed on the

final image. F_u represents application of the Fourier transform operator after application of the undersampling mask, E is the coil sensitivities, d is the acquired k-space data, D is the overcomplete dictionary, and λ_T and λ_D are weighting factors corresponding to the regularization and dictionary terms, respectively.

FAC MRI protocol for imaging the EAT in mice

All animal studies were performed in accordance with protocols that conformed to the Declaration of Helsinki as well as the Guide for Care and Use of Laboratory Animals (NIH publication no. 85-23, revised 1996) and were approved by the Animal Care and Use Committee at the University of Virginia. Prior to MRI, male C57Bl/6 mice (Jackson Laboratories, Bar Harbor, Maine) were fed a high-fat high-sucrose diet (HFHSD, 40% kcal fat, 40% kcal sucrose, Diet 12327, Research Diets Inc., New Brunswick, NJ) for 6 weeks to induce the development of EAT, which otherwise is inappreciable. MRI was performed using a 7T system and a 4-channel phased-array radiofrequency coil. During imaging, mice were anesthetized with 1.25% isoflurane and their core temperature was maintained at $36 \pm 0.5^\circ\text{C}$ using circulating warm water. Also, the electrocardiogram (ECG), body temperature, and respiration (RESP) were monitored (SA Instruments, Stony Brook, NY). Localizer imaging was performed to establish a short-axis slice positioned toward the base of the left ventricle, where EAT is typically abundant. Fully-sampled and prospectively-undersampled images for FAC-MRI were acquired using an ECG-gated, RESP-gated flyback double-echo gradient-echo sequence with time between echoes of 1.5 ms, TR = R-R interval, flip angle = 15° , averages = 8, bandwidth = 390 Hz/pixel, slice thickness = 1 mm, field of view (FOV) = $25.6 \times 25.6 \text{ mm}^2$, acquisition matrix of 128×128 and resolution of $0.2 \times 0.2 \text{ mm}^2$. Using 5 acquisitions, 10 echoes were acquired with TEs ranging from 2.0ms to 4.7ms with interecho spacings of 0.3ms, corresponding to the optimal values as determined by the Cramér-Rao lower bound analysis. Because fully-sampled images were acquired as a reference for each acquisition, they were also used to generate coil sensitivity maps²³⁸ for the undersampled acquisitions, and autocalibration techniques were not implemented. All post-processing, including computation of coil sensitivity maps, CS-DICT, and FAC-IDEAL, was performed offline using MATLAB r2021a (MathWorks, Natick, Massachusetts, USA).

Selection of acceleration rate

To select an acceleration rate to use for undersampled imaging, fully-sampled EAT FAC MRI datasets were acquired from obese male C57Bl/6 mice (n=12), and images were then retrospectively undersampled at rate-2, 2.5, 5, and 3.5 acceleration and CS-DICT reconstruction was performed. For assessment and error quantification of CS-DICT reconstructed vs. fully-sampled images at various retrospective acceleration rates, RMSE and structural similarity index (SSIM) were computed. Thresholds of $\text{RMSE} < 5\%$ and $\text{SSIM} > 0.85$ were used as criteria to select an undersampling rate for prospectively accelerated imaging.

Phantom and in-vivo validation of FAC parameters

To validate measurements of the FAC parameters, SFA, MUFA, PUFA, UD, and PUD, we performed NMR spectroscopy, fully-sampled FAC-IDEAL, and accelerated FAC-IDEAL on sesame, olive, and vegetable oil phantoms as well as axillary adipose tissue from $n=3$ mice fed 6 weeks of HFHSD. Axillary adipose tissue was chosen instead of EAT because the volume of EAT that could be excised was too small to fill an NMR tube. Mice were euthanized after MRI, and NMR spectroscopy was performed on the excised tissues. For quantification of MRI FAC parameters, adipose depots were manually segmented from F_2 maps for pixels where $F_2 > 0.4$.

Relationship of EAT to coronary microvascular disease - experimental design

Untreated ($n=10$) and EPL-treated ($n=10$) obese wild type male C57Bl/6 mice (Jackson Laboratories, Bar Harbor, Maine) were studied. Untreated mice were fed a HFHSD while treated mice were fed a HFHSD + EPL (100 mg/kg/day, Mylan Pharmaceuticals Inc.). The diets and EPL treatment were initiated at 10 weeks of age and continued for 6 weeks, at which time fully-sampled and rate-3 accelerated EAT FAC MRI was performed. The total scan times for fully-sampled and rate-3 accelerated FAC MRI were ~25 minutes and ~8 minutes, respectively.

The MRI protocol also included multi-slice three-point Dixon imaging of the EAT to quantify EAT volume¹²⁸. An ECG-gated, RESP-gated double-inversion-recovery black-blood cine sequence²³⁹ was used to acquire six short-axis slices covering the left ventricle. Sequence parameters included: $TE_1/TE_2/TE_3 = 2.5/3.0/3.5$ ms, $TR = R-R$ interval, $FOV = 30 \times 30$ mm², matrix size = 128×128 , flip angle = 15° , slice thickness = 1 mm, and number of averages = 3. Water and fat-separated images were computed using the three-point Dixon approach, and EAT volume was manually contoured and calculated from the fat images. The total scan time for EAT volume imaging was ~18 minutes.

Lastly, myocardial perfusion reserve (MPR) imaging of a mid-ventricular short-axis slice was performed at baseline (prior to initiating the HFHSD) and 6 weeks post-diet to assess coronary microvascular function ($n = 8/\text{group}$). Myocardial perfusion was quantified using ECG-gated and RESP-self-gated arterial spin labeling (ASL)^{39,240}. After ASL applied at rest, adenosine was infused i.v. (300 mg/kg/min, 5 μ l/min) and 10 minutes later, perfusion imaging was repeated. ASL parameters included: $TE/TR = 2.5/10.0$ ms, $FOV = 38 \times 38$ mm², matrix size = 128×128 , flip angle = 7° , slice thickness = 1 mm, saturation band thickness = 10 mm, and number of averages = 9. For myocardial perfusion analysis, the myocardium was manually segmented and rest and adenosine stress perfusion were quantified using methods previously described³⁹. Myocardial perfusion reserve (MPR) was calculated as stress perfusion / rest perfusion. The total time for myocardial perfusion reserve imaging including adenosine infusion was ~26 minutes.

Data analysis and statistics

Statistical analysis was performed using IBM SPSS Statistics for Windows v28. All results of RMSE, SSIM, and parametric maps are expressed as mean \pm standard deviation. T-tests were used to test for differences in FAC parameters between untreated and EPL-treated mice. Two-way ANOVA was used to detect differences in rest perfusion, stress perfusion and MPR between groups of mice at baseline and 6 weeks after diet. Bland-Altman analysis was used to compare SFA fractions and UD between fully sampled and CS-DICT reconstructed images.

3.4 Results

CS-DICT reconstructions and FAC-IDEAL mapping of undersampled images

Figure 6A demonstrates CS-DICT reconstructions of retrospectively undersampled images at acceleration rates of 2, 2.5, 3, and 3.5. As expected and shown in Figures 6B and 6C, RMSE and SSIM increase and decrease, respectively, as the acceleration rate increases. At rate-3 acceleration, RMSE was $4.50 \pm 0.61\%$ and SSIM was 0.85 ± 0.02 , which were within our predetermined thresholds for selecting the acceleration rate to use for prospectively-undersampled imaging. Thus, rate-3 acceleration was used for subsequent experiments.

Figure 7 shows example EAT FAC-IDEAL maps computed from fully-sampled, rate-3 retrospectively-undersampled and rate-3 prospectively-accelerated CS-DICT images showing close agreement for all cases. For this example, the mean SFA, PUFA, and MUFA fractions were 0.40, 0.52, and 0.08 for fully-sampled reference maps, 0.41, 0.50, and 0.09 for retrospectively undersampled maps, and 0.40, 0.53, and 0.07 for prospectively-accelerated maps, respectively. Mean UD and PUD were 3.36 and 1.56 for the fully-sampled case, 3.33 and 1.53 for the retrospectively undersampled, and 3.39 and 1.59 for the prospectively-accelerated case, respectively. RMSE and SSIM of the FAC-IDEAL maps were $3.24 \pm 0.26\%$ and 0.90 ± 0.03 for retrospectively undersampled maps and $4.68 \pm 0.37\%$ and 0.86 ± 0.04 for prospectively undersampled maps compared to their fully-sampled counterparts.

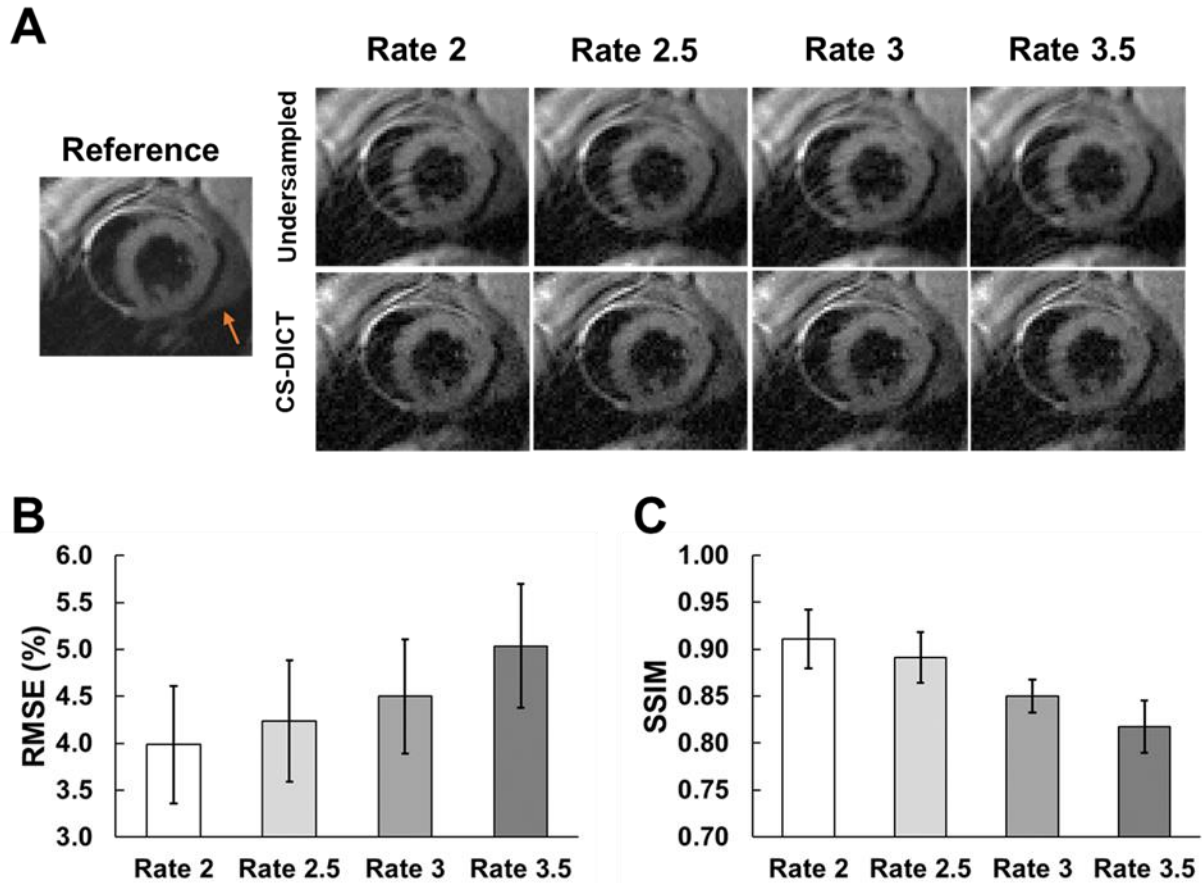


Figure 6: (A) Retrospectively undersampled images reconstructed using CS-DICT for the first echo time at undersampling rates of 2.0, 2.5, 3.0, and 3.5 are shown with the corresponding fully-sampled (reference) image. Orange arrows point towards EAT. Summary of (B) RMSE and (C) SSIM results ($n=12$) shows that rate-3 acceleration provides $RMSE < 5\%$ and $SSIM > 0.85$.

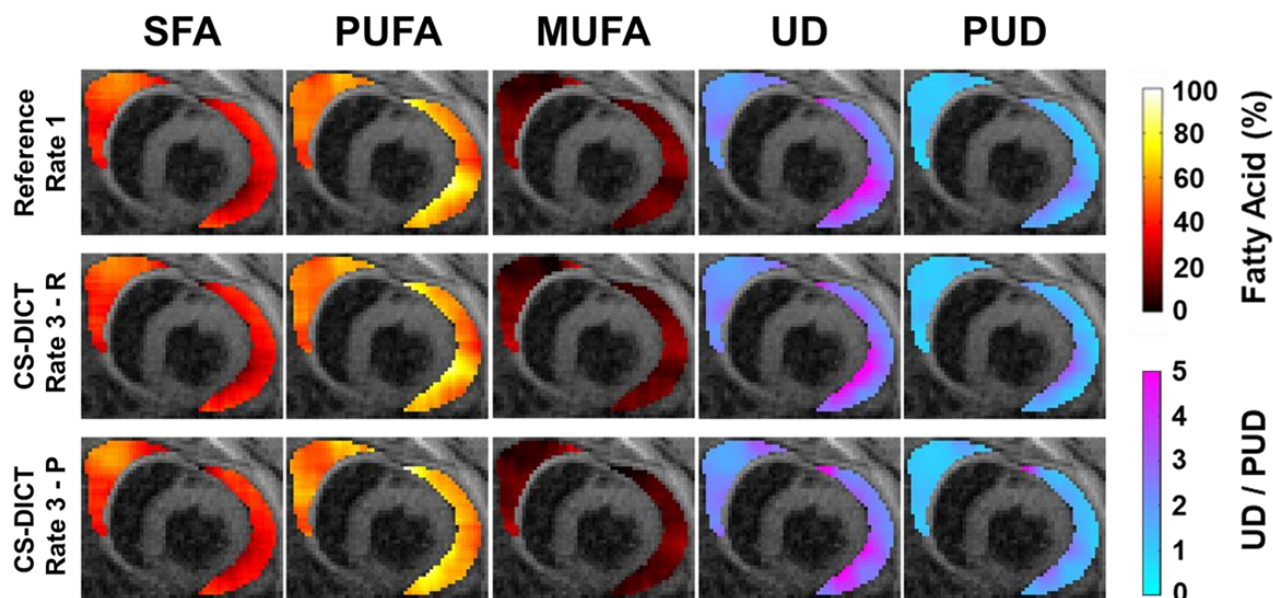


Figure 7: Example EAT SFA, PUFA, MUFA, UD, and PUD maps overlaid on first echo images from mice fed HFHSD. The top row shows fully-sampled images (reference), the middle row shows retrospectively (R) rate-3 undersampled CS-DICT images, and the bottom row shows prospectively (P) rate-3 accelerated CS-DICT images.

Validation of FAC-IDEAL

The measured SFA, PUFA, MUFA, UD, and PUD values of the three oils and axillary adipose tissue from FAC-IDEAL of fully-sampled and rate-3 accelerated CS-DICT images as well as from NMR spectroscopy are summarized in Table 1. As shown, for the oil phantoms, all FAC parameters from fully-sampled and rate-3 accelerated images were within 14% of their corresponding NMR spectroscopy values. For in vivo imaging of axillary adipose tissue in mice, FAC parameters from fully-sampled and rate-3 accelerated images were within 7% of one another, and both were within 7% of NMR spectroscopy values for the measurement of SFAs and UD. However, for PUFAs and PUD, FAC-IDEAL values from fully-sampled and rate-3 accelerated images were 8-24% higher than NMR spectroscopy, and for MUFAs, they were 20-30% lower than NMR spectroscopy. Based on these results, for EAT we had high confidence for estimating SFA and UD, and lower confidence in breaking down the unsaturated fraction into PUFAs and MUFAs or estimating the PUD.

Phantoms		SFA	PUFA	MUFA	UD	PUD
Sesame Oil	<i>NMR</i>	0.25	0.40	0.35	3.45	1.20
	<i>FAC-IDEAL (Ref)</i>	0.23	0.40	0.37	3.50	1.19
	<i>FAC-IDEAL (R=3)</i>	0.22	0.42	0.36	3.58	1.25
Olive Oil	<i>NMR</i>	0.29	0.26	0.45	2.91	0.78
	<i>FAC-IDEAL (Ref)</i>	0.29	0.28	0.44	2.96	0.83
	<i>FAC-IDEAL (R=3)</i>	0.29	0.29	0.42	3.01	0.87
Vegetable Oil	<i>NMR</i>	0.27	0.62	0.11	4.05	1.86
	<i>FAC-IDEAL (Ref)</i>	0.26	0.61	0.13	4.05	1.83
	<i>FAC-IDEAL (R=3)</i>	0.26	0.65	0.10	4.18	1.94
In Vivo		SFA	PUFA	MUFA	UD	PUD
Axillary Adipose Tissue	<i>NMR</i>	0.36 ± 0.04	0.39 ± 0.07	0.25 ± 0.04	3.10 ± 0.29	1.18 ± 0.17
	<i>FAC-IDEAL (Ref)</i>	0.37 ± 0.07	0.45 ± 0.03	0.18 ± 0.03	3.34 ± 0.25	1.37 ± 0.13
	<i>FAC-IDEAL (R=3)</i>	0.38 ± 0.06	0.43 ± 0.03	0.19 ± 0.03	3.16 ± 0.22	1.29 ± 0.11

Table 1: Phantom and in vivo validation of FAC-IDEAL from fully-sampled (Ref) and rate-3 accelerated (R=3) CS-DICT images vs NMR spectroscopy as a reference

EAT FAC mapping, EAT volume, and myocardial perfusion reserve in EPL-treated mice fed HFHSD

Figure 8A shows example EAT SFA and UD maps acquired using a prospectively rate-3 accelerated multi-echo gradient-echo sequence, reconstructed using CS-DICT, and mapped using FAC-IDEAL for an untreated HFHSD mouse and an EPL-treated HFHSD mouse, demonstrating a reduction of SFAs and increase UD with EPL treatment. Figure 8B-C summarizes the results from both groups of mice using both fully-sampled and rate-3 accelerated CS-DICT images. In EPL-treated vs untreated HFHSD mice (6 weeks of diet or diet and drug), the EAT SFA fraction was significantly reduced (0.26 ± 0.09 vs 0.41 ± 0.07 , $p < 0.01$, fully-sampled; 0.27 ± 0.09 vs 0.39 ± 0.07 , $p < 0.05$, accelerated). UD was significantly increased (4.49 ± 0.42 vs 3.44 ± 0.53 , $p < 0.01$, fully-sampled; 4.37 ± 0.32 vs 3.69 ± 0.58 , $p < 0.05$, accelerated). In addition, EAT volume was reduced in EPL-treated vs untreated mice (11.4 ± 0.7 mg vs 8.1 ± 0.6 mg, $p < 0.01$). PUFA, MUFA, and PUD results (Table S1) as well as Bland-Altman analysis comparing rate-3 accelerated and fully-sampled EAT FAC mapping (Figure S1) are provided in the supplemental data. The PUFA, MUFA, and PUD results also support the finding that EPL treatment promotes a shift toward increasing EAT unsaturation compared to untreated HFHSD mice.

Figure 9A shows rest and adenosine-stress myocardial perfusion results at baseline and 6-weeks post-diet in both groups of mice measured using ASL. Stress perfusion trended lower than baseline in both untreated and EPL-treated mice 6 weeks after initiating HFHSD, but the reduction was not statistically significant. Figure 9B shows that MPR was reduced at 6 weeks post-diet compared to baseline (before

HFHSD) in untreated (1.61 ± 0.17 vs 2.09 ± 0.22 , $p < 0.01$) and EPL-treated mice (1.83 ± 0.15 vs 2.06 ± 0.19 , $p < 0.05$), and MPR was improved post-diet in EPL-treated vs untreated mice (1.83 ± 0.15 vs 1.61 ± 0.17 , $p < 0.05$), indicating that EPL improves coronary microvascular function in mice fed HFHSD.

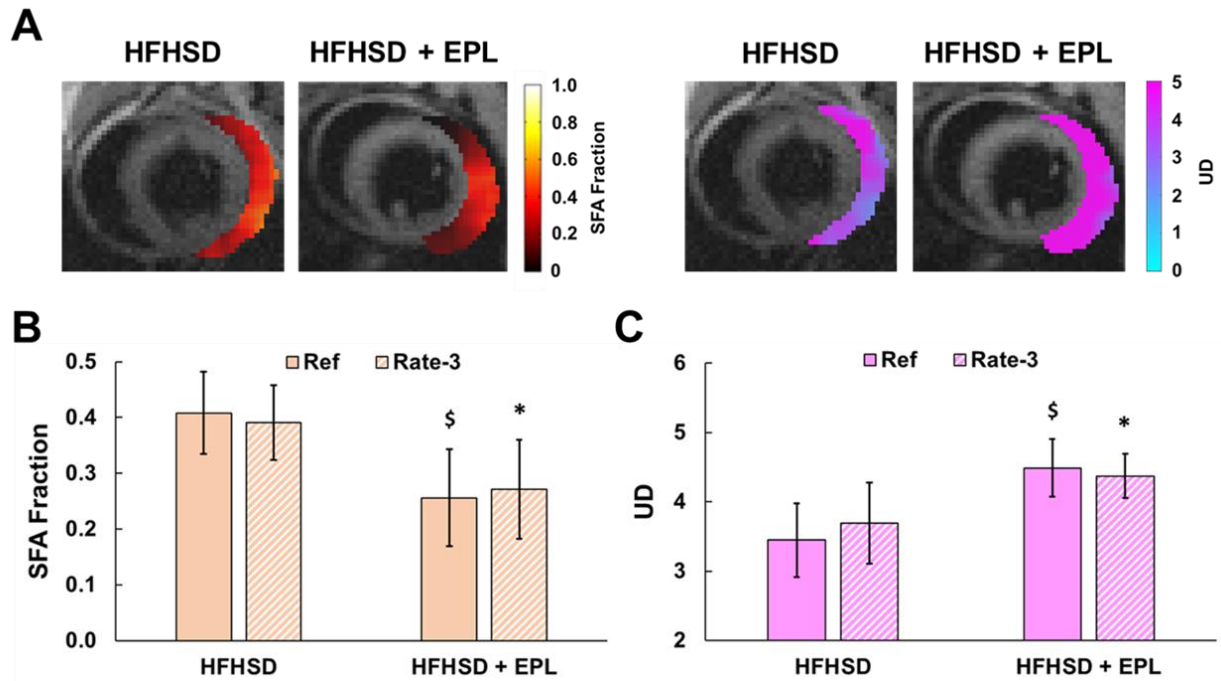


Figure 8: (A) Example FAC-IDEAL SFA and UD maps from rate-3 accelerated CS-DICT reconstructed images in untreated (HFHSD) and EPL-treated (HFHSD + EPL) mice showing a shift toward reduced SFAs and an increased UD in EPL-treated mice. EPL significantly altered the EAT FAC as (B) SFAs were significantly reduced and (C) UD was significantly elevated after 6 weeks of HFHSD compared to untreated mice fed HFHSD ($n=10/\text{group}$). There were no significant differences in the SFA and UD estimates when comparing FAC-IDEAL of fully-sampled (Ref) and rate-3 accelerated CS-DICT images.

* $p < 0.05$ vs HFHSD

\$ $p < 0.01$ vs HFHSD

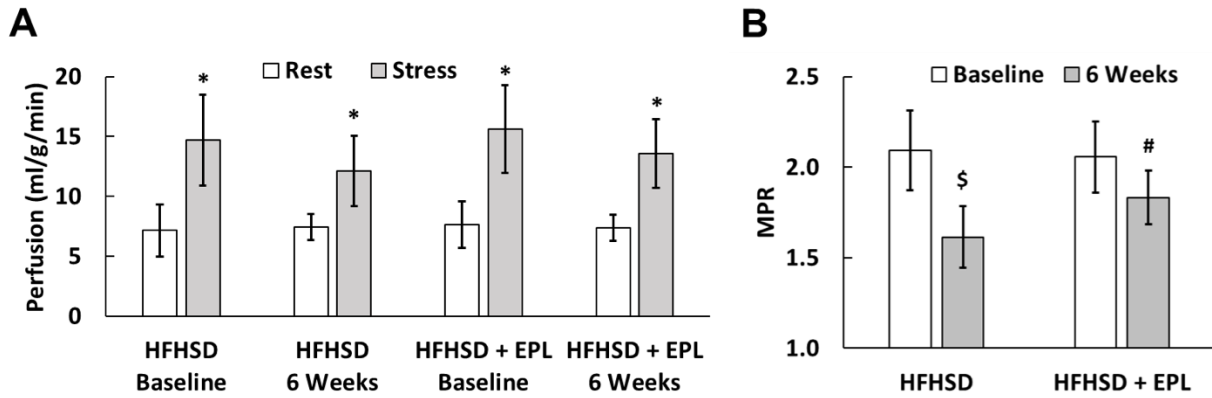


Figure 9: (A) Rest and adenosine-stress myocardial perfusion and (B) myocardial perfusion reserve (MPR) measurements in untreated and EPL-treated mice at baseline and 6-weeks post-diet (n=8/group).

* p < 0.01 vs Rest

\$ p < 0.01 vs HFHSD Baseline

p < 0.05 vs HFHSD + EPL Baseline & p < 0.05 vs HFHSD 6-weeks

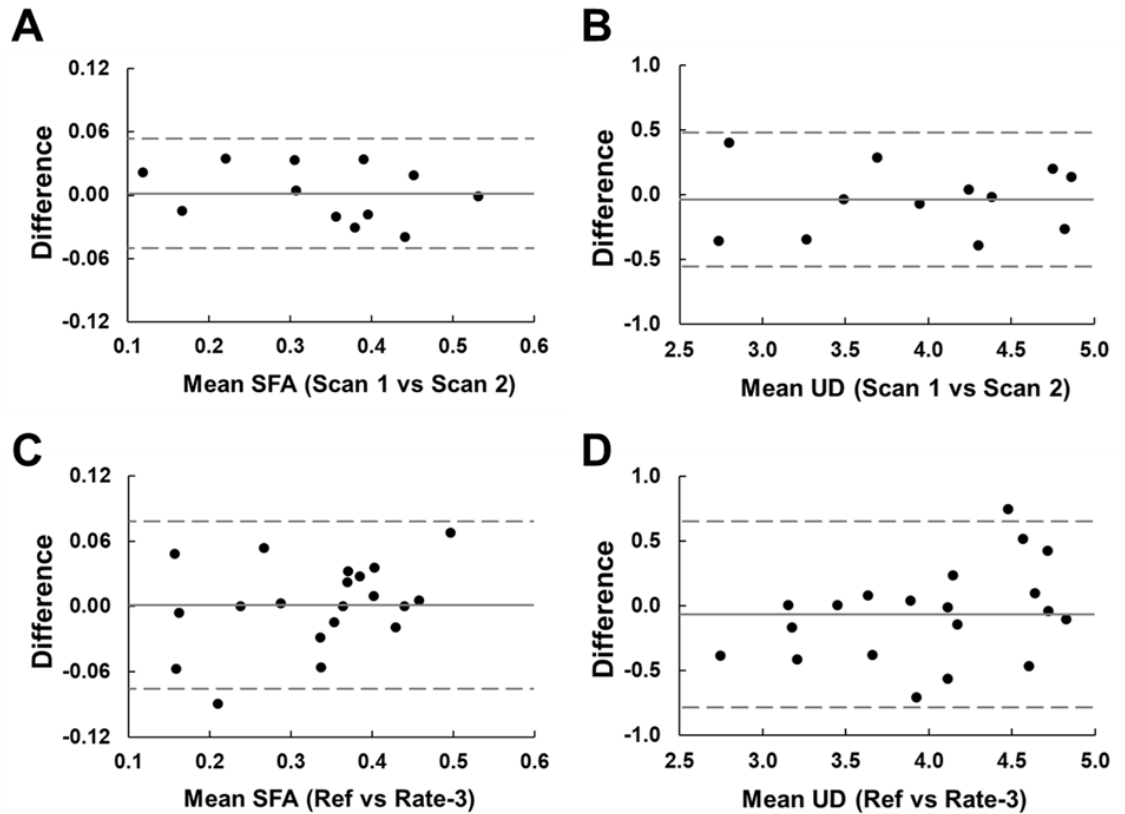


Figure S1: (A,B) Bland-Altman plots showing the interscan variability of imaging-based estimates of EAT SFA fraction and UD from fully-sampled data sets (n=12). (C,D) Bland-Altman plots comparing fully-sampled (Ref) and rate-3 accelerated imaging-based estimates of EAT SFA fractions and UD (n=20). The bias (solid line) and limits of agreement (dashed lines) for each FAC parameter are shown. For interscan variability of FAC-IDEAL using fully-sampled images, there was essentially no bias for estimates of SFAs (-0.00 ± 0.03) and UD (-0.04 ± 0.26). The upper and lower confidence limits for SFAs and UD were 0.05 to -0.05 and 0.56 to -0.48, respectively. Similarly, for FAC-IDEAL applied to accelerated images, compared to fully-sampled, there was essentially no bias for estimates of SFAs (0.00 ± 0.04) and UD (-0.06 ± 0.36). The upper and lower confidence limits for SFAs and UD were 0.08 to -0.07 and 0.65 to -0.78, respectively.

Mice		SFA	PUFA	MUFA	UD	PUD
HFHSD EAT	<i>Fully-sampled</i>	0.41 ± 0.07	0.53 ± 0.09	0.06 ± 0.06	3.44 ± 0.53	1.67 ± 0.38
	<i>Rate-3</i>	0.39 ± 0.07	0.57 ± 0.09	0.04 ± 0.05	3.69 ± 0.58	1.84 ± 0.40
HFHSD+EPL EAT	<i>Fully-sampled</i>	0.26 ± 0.09**	0.70 ± 0.05**	0.05 ± 0.04	4.49 ± 0.42**	2.26 ± 0.29**
	<i>Rate-3</i>	0.27 ± 0.09*	0.68 ± 0.04**	0.05 ± 0.06	4.37 ± 0.32*	2.18 ± 0.21*
HFHSD AAT	<i>Fully-sampled</i>	0.37 ± 0.07	0.45 ± 0.03	0.18 ± 0.03	3.34 ± 0.25	1.37 ± 0.13
	<i>Rate-3</i>	0.38 ± 0.06	0.43 ± 0.03	0.19 ± 0.03	3.16 ± 0.22	1.29 ± 0.11
HFD VAT ¹	<i>Fully-sampled</i>	0.37 ± 0.04	0.18 ± 0.03	0.45 ± 0.04	2.44 ± 0.19	0.54 ± 0.09
	-					
Humans		SFA	PUFA	MUFA	UD	PUD
Obese Male SCAT ²	<i>Fully-sampled</i>	0.41 ± 0.07	0.31 ± 0.05	0.28 ± 0.07	2.72 ± 0.31	0.94 ± 0.16
	-					
Obese Male VAT ³	<i>Fully-sampled</i>	0.43 ± 0.03	0.28 ± 0.05	0.29 ± 0.04	2.53 ± 0.21	0.84 ± 0.14
	-					

Table S1: Summary of FAC-MRI measurements of obese mice and patients in epicardial (EAT), axillary (AAT), visceral (VAT), and subcutaneous adipose tissue (SCAT). Dark shaded rows indicate our measurements, whereas lighter shaded rows indicate values from the literature.

3.5 Discussion and Conclusions

To the best of our knowledge, the present results represent the first application of FAC MRI to epicardial adipose tissue, the first demonstration of undersampling/acceleration applied to FAC MRI, and the first use of MRI to show that a drug shifts the FAC of adipose tissue to achieve a reduction of SFAs and increases in UD. Based on the knowledge that SFAs are proinflammatory, FAC MRI to quantify a reduction in SFAs and an increase in UD may represent a new imaging biomarker for detecting proinflammatory vs. anti-inflammatory EAT. Further, our finding that EPL treatment shifts the EAT FAC toward reduced SFAs and higher UD and that these effects are associated with an improvement in coronary microvascular function as measured by adenosine MPR suggests that these MRI methods may probe the EAT as it functions as a transducer of metabolic inflammation to the coronary microvessels.

Accelerated FAC imaging

Because FAC MRI of EAT is time consuming (e.g., requiring ~25 minutes using an unaccelerated protocol for mouse imaging), we investigated acceleration using undersampling with randomness and image reconstruction using CS-DICT. Using a rate-3 undersampled sequence, the FAC MRI scan time was reduced from ~25 minutes to ~8 minutes while maintaining high SSM and low RMSE. While the present sequence used Cartesian sampling, in the future an undersampled radial k-space trajectory could potentially further shorten the scan time. Furthermore, while we chose to use a double-echo sequence with flyback gradients, another possible choice would be a three-echo sequence with bipolar readout gradients. However, this approach would likely require an additional phase correction. We chose the flyback approach for simplicity.

The specific undersampling pattern and CS-DICT framework used in this study were extensions of methods from Liu et al.¹³⁶ with modifications. First, Liu et al. used the same undersampling mask for each echo because blip gradients can induce phase errors and inaccurate model estimations; however, their sampling pattern did not provide incoherence along the echo-time dimension. With 2 echoes per acquisition, we did not encounter significant problems related to the phase errors described by Liu, thus we varied the undersampling pattern along the echo-time dimension, facilitating the exploitation of sparsity in that dimension. Second, since Liu's work involved fat fraction imaging and not FAC imaging, their dictionary consisted of three parameters (fat fraction, ψ , and R_2^*), rather than the six needed for FAC (F_1 , F_2 , F_3 , F_4 , ψ , and R_2^*). Accordingly, Liu required just one element in α and one round of OMP, whereas we used four elements in α and four rounds of OMP. Also, for parameter mapping, Liu et al. performed a final round of OMP, whereas we applied FAC-IDEAL after the CS-DICT reconstruction due to the fairly coarse step sizes of our dictionary.

One limitation of the present study is that we did not develop autocalibration methods to compute sensitivity maps, as our protocol involved the acquisition of additional fully-sampled images from which we could generate sensitivity maps. In the future, we will develop autocalibration methods to overcome this limitation. A limitation of CS-DICT was that the reconstruction time for one dataset was approximately 10

minutes (using a system with a 3.4 GHz Intel(R)i7 CPU and 24 GB RAM), where the most computationally expensive step was OMP. Strategies such as K-singular value decomposition to condense the dictionary and reduce computation times could help address this issue²⁴¹.

FAC MRI optimization

In our study, the Cramér-Rao analysis showed low FAC parameter variances using 10 echoes, an echo spacing of 0.3ms, and an initial TE of 2.0ms, which was shortest TE possible using a pixel bandwidth of 390 Hz/pixel and the default RF excitation pulse. These parameters led to an echo train length of 2.7ms, which is shorter than the 6.5ms recommended by Berglund at 7T. However, B0 inhomogeneity due to heart-lung interfaces at 7T²³⁶ precludes the use of echo times longer than approximately 5ms for cardiac imaging in mice, as they lead to signal loss and image distortion in gradient echo images. The echo train length that we used of 2.7ms facilitated both good quality gradient-echo images and low FAC variances. In the future a shorter RF pulse could be used.

In this study we acquired data using a uniform echo spacing. Prior studies using Cramer-Rao bounds for T1 and T2 mapping showed that the optimal sampling scheme yielded a distribution concentrated at certain points rather than uniform sampling^{44,45}. A non-uniform sampling pattern could potentially be more optimal for FAC MRI with the caveat that echo times would also need to be optimized to prevent spectral aliasing, and such methods may be investigated in the future.

Validation

FAC-IDEAL estimates of all parameters (SFA, PUFA, MUFA, UD and PUD) agreed closely with NMR spectroscopy for sesame, olive, and vegetable oil. For axillary adipose tissue, FAC-IDEAL estimates of SFA, and UD agreed closely with NMR spectroscopy; however, the agreement with NMR spectroscopy for PUFAs, MUFAs and PUD was not as well correlated. Specifically, PUFAs were overestimated by 15-24%, MUFAs were underestimated 20-30%, and PUD was overestimated 8-21%. One potential explanation for the discrepancies may be PUFA to MUFA oxidation during the interim between euthanization, EAT extraction, and NMR spectroscopy²⁴⁴.

While we used FAC MRI to measure SFA and UD values of 0.41 and 3.44, respectively, in the EAT of mice fed a HFHSD, using FAC MRI others have measured SFA and UD values of 0.41 and 2.72 and 0.43 and 2.53 in subcutaneous adipose tissue (SCAT) and visceral adipose tissue (VAT), respectively, in obese male patients²²⁸. In VAT of mice fed a high fat diet (HFD), these values were 0.37 and 2.44²³¹. Compared to other fat depots, our EAT data show good agreement for SFA, but UD values in EAT were higher. This may be related to the heart's use of EAT as a reservoir of fatty acids for ATP generation with a preference toward unsaturated fatty acids²⁴⁵. We also measured significant differences in PUFA fractions, MUFA fractions, and PUD in EAT vs. other fat depots. Specifically, our estimates of PUFAs and PUD were higher and MUFAs were lower compared to the other depots (Table S1). One possible explanation

to the discrepancy is that our measurements of PUFA and MUFA in the EAT contain errors related to the FAC-IDEAL methodology. There may be a significant amount of unsaturated free fatty acids without a corresponding triglyceride backbone in EAT²⁴⁵ that leads to an overestimation of PUFAs using FAC-IDEAL²⁴⁶. A second limitation to the FAC-IDEAL model is that while it accounts for triglyceride fatty acid chains with 0, 1, or 2 double bonds, fatty acid chains with more than two double bonds, which should not be neglected in adipose tissue^{247,248}, would manifest as an overestimated F₄ value corresponding to incorrectly high PUFA and low MUFA value. At present, we have higher confidence in our FAC-MRI estimates of SFA and UD for the in vivo assessment of EAT in mice, and lower confidence in the measurements of EAT PUFA, MUFA, and PUD. For SFA and UD, our phantom and in vivo axillary adipose tissue data show close agreement with NMR spectroscopy and the values are similar to in vivo values in other adipose tissue depots as reported by others. Understanding why estimates of EAT PUFA, MUFA and PUD disagree with other adipose depots warrants further investigation in the future.

Role of EAT in coronary microvascular dysfunction

In obese mice treated with EPL, we measured a reduction in EAT volume, a shift in EAT FAC toward greater unsaturation with decreased SFAs and an increased UD, and an improvement in adenosine MPR, reflecting improved coronary microvascular function. Various studies have linked pro-inflammatory EAT to the development of cardiovascular diseases including coronary microvascular disease and heart failure with preserved ejection fraction^{102,118–120}. In addition, mineralocorticoid receptor (MLR) activation drives adipose tissue inflammation^{155,249} while MLR antagonism has shown promise to reduce adipose inflammation in obesity^{175,250}. In this study, we also measured a reduced EAT volume in EPL treated mice consistent with prior studies in HFD fed mice^{156,175}. The role of SFAs to promote adipogenesis²⁵¹ and macrophage polarization through TLR4 signaling¹¹¹, the capacity of UFAs in limiting adipose cell and tissue size²⁵¹, and the correlation between EAT volume, inflammation, and risk of developing cardiovascular diseases¹²⁶ are all well documented. Together, these results support the hypotheses that a) a highly saturated EAT can adversely influence the coronary vasculature potentially by promoting EAT hypertrophy and acting as a transducer of metabolic inflammation, and b) the SFA fraction and degree of unsaturation of EAT may represent biomarkers and potential therapeutic targets for the treatment of coronary microvascular disease.

There were some additional limitations to our study. FAC-IDEAL was validated in oil phantoms as well as axillary adipose tissue but not in EAT. Validation of EAT using NMR spectroscopy, gas chromatography, or mass spectrometry could further substantiate our results; however, the very small volume of EAT in mice (10-15mg) prevented our ability to make these measurements. In the future, we also plan to do experiments to associate EAT FAC with macrophage markers and cytokine arrays.

Conclusion

In conclusion, rate-3 accelerated FAC MRI enables quantification of the EAT SFA and UD in mice with acquisition times of approximately 8 minutes per slice. The acceleration methods we employed should apply to any adipose tissue depot. Our results demonstrate that these methods can detect shifts in EAT FAC toward presumably anti-inflammatory states with certain drug treatments, and that the shift is associated with improvements in coronary microvascular function. Future work toward mapping EAT FAC in human subjects may build upon the methods and results that we presented.

**Chapter 4 – Role of Mineralocorticoid Receptor Blockade and
Cell Specific Deletion on the Prevention of Diet-Induced
Coronary Microvascular Disease**

4.1 Abstract

Background: Coronary microvascular disease (CMD), measured by an impaired adenosine myocardial perfusion reserve (MPR), is a risk factor for major adverse cardiac events and mortality, and it is central to heart failure with preserved ejection fraction (HFpEF). However, there is limited knowledge of the mechanisms underlying CMD. In addition, treatments trials for CMD have been largely inconclusive and have shown gender-specific differences in outcomes. Using cardiac MRI applied to a mouse model of CMD, we elucidated the effects of mineralocorticoid receptor (MLR) inhibition via eplerenone (EPL), and smooth muscle cell (SMC) and endothelial cell (EC) MLR deletion for the prevention of CMD.

Methods: Male and female wild-type (WT) mice were fed either a high-fat, high-sucrose diet (HFHSD) or HFHSD+EPL for 18 weeks beginning at 10 weeks of age. Additionally, male SMC MLR^{-/-}, EC MLR^{-/-}, and Cre^{-/-} controls were fed a HFHSD on the same timeline to understand mechanisms. Glucose tolerance testing, blood pressure telemetry, and cardiac MRI to assess MPR, myocardial oxidative stress, left ventricular structure, and systolic function, were performed at baseline and 18 weeks post-diet. At 20 weeks post-diet, ex-vivo coronary arteriole vasoreactivity was performed on all groups of mice.

Results: MPR was impaired in all groups of mice post-HFHSD ($p < 0.01$), and eplerenone provided partial improvements in MPR ($p < 0.05$) in both male and female WT mice, however, SMC and EC MLR^{-/-} had no effect on MPR post-HFHSD. MPR results were supported by vasoreactivity results. In addition, eplerenone reduced weight gain, glucose intolerance, myocardial oxidative stress, and improved cardiac function in both male and female WT mice which were otherwise impaired due to a HFHSD, though there were some gender-specific differences. SMC MLR^{-/-} showed partial improvements in oxidative stress and strain post-HFHSD compared to controls, whereas EC MLR^{-/-} showed no improvement in any parameter.

Conclusions: Systemic MLR activation has an important role in the development of CMD, and our results supports the beneficial effect of MLR blockers on CMD, and potentially HFpEF, regardless of gender.

4.2 Introduction

Coronary microvascular disease (CMD) plays a pathophysiological role in numerous cardiovascular disease states including myocardial ischemia and heart failure with preserved ejection fraction (HFpEF)^{10,252}. CMD can be caused by impairments in both endothelial-independent and endothelial-dependent vasodilatory responses, however, the endothelial-independent impairment is associated with greater left ventricular diastolic dysfunction and increased mortality²¹, and it accounts for a majority of the data relating to CMD to outcomes and HFpEF²⁵³. Endothelial-independent CMD is typically assessed by coronary flow reserve (CFR) testing with intracoronary adenosine or myocardial perfusion reserve (MPR) imaging using rest and adenosine stress PET⁷ or MRI²⁵⁴. Comorbidities for CMD include obesity and diabetes which can lead to systemic oxidative stress, chronic metabolic inflammation, and ultimately microvascular dysfunction^{8,16,252}. However, while CMD has been identified as a key player in different clinical phenotypes, there is limited knowledge in the specific mechanisms underlying CMD, and there are no validated therapeutic strategies targeting CMD^{8,252}.

Adenosine increases coronary blood flow and myocardial perfusion through dilation of the coronary resistance vessels, thus, impaired adenosine CFR and MPR mainly reflect underlying coronary arteriole dysfunction. Considering the potential role of oxidative stress and metabolic inflammation in exacerbating microvascular impairment, we hypothesized that the mineralocorticoid receptor (MLR) plays an important role in CMD. MLRs are intracellular transcription factors which have a complex role in the cardiovascular system involving several mechanisms including vascular oxidative stress and inflammation¹⁴⁰. More specifically, activation of the smooth muscle cell (SMC) and endothelial cell (EC) MLRs have been implicated in hypertension¹⁴⁷, cellular proliferation²⁵⁵, fibrosis²⁵⁶, vascular stiffening^{148,257}, and coronary dysfunction¹⁴⁹, thus, chronic MLR activation could be major contributor to the development of CMD.

Mineralocorticoid receptor antagonists (MRAs), such as eplerenone (EPL) and spironolactone, have been associated with reductions in oxidative stress and inflammation, and an improvement in coronary blood flow in animal model of heart disease^{173,174}. In small clinical studies of patients with CMD, both eplerenone⁴⁷ and spironolactone⁴⁶ improved coronary microvascular function, as indicated by MPR, demonstrating the therapeutic potential of MRAs to treat CMD. However, small studies examining the relationship between MRA treatment and gender found that improvements in CFR were lower¹⁷⁶ or absent⁴⁸ in women. In addition, results from the “Treatment of Preserved Cardiac Function Heart Failure with an Aldosterone Antagonist” (TOPCAT) trial were negative, though, the results may have been hampered by broad inclusion criteria resulting in a heterogeneous patient population that could mask specific patient subgroups that may preferentially benefit from MLR antagonism^{177,178}. Thus, while MRAs may have potential as a treatment for CMD, sex differences may have an impact on MRA treatment.

We and others have developed arterial spin labeling (ASL) MRI methods enabling reproducible quantification of rest and adenosine stress myocardial perfusion and MPR in mice⁴⁰. We have also shown that mice fed a high fat diet or a high fat high

sucrose diet (HFHSD) develop an impaired adenosine-stress MPR and represent a model of CMD without obstructive coronary artery disease^{62,258}. In addition to MPR assessment, cardiac MRI in mice also enables a comprehensive noninvasive evaluation of cardiac structure, function, and oxidative stress, all of which are important parameters for the evaluation of the role of MLRs in CMD due to diabetes and obesity. In the present study we employed cardiac MRI and other methods in mice fed a HFHSD to (a) test the hypothesis that EPL can prevent CMD in male and female mice fed a HFHSD, and (b) determine the roles of the SMC and EC MLRs in the development of CMD.

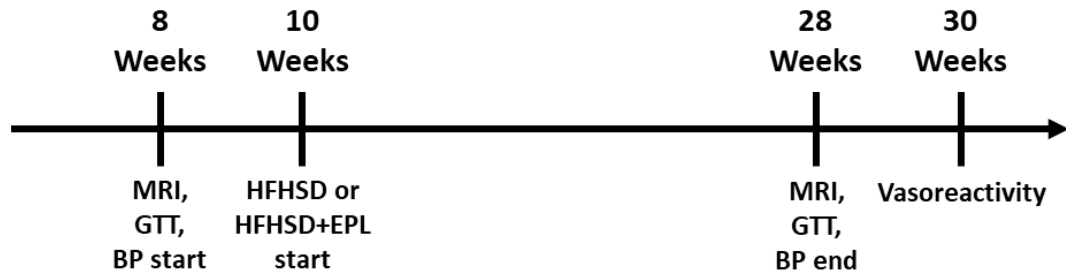
4.3 Methods

All animal studies were performed in accordance with protocols that conformed to the Declaration of Helsinki as well as the Guide for Care and Use of Laboratory Animals (NIH publication no. 85-23, revised 1996) and were approved by the Animal Care and Use Committee at the University of Virginia.

Experiments were performed using mice fed a HFHSD for 18 weeks as a model for CMD to (a) test whether EPL treatment can preserve coronary microvascular function and (b) demonstrate the role of SMC and EC MLRs in CMD. For the former objective, mice were obtained from the Jackson Laboratories (Bar Harbor, Maine). Four groups of mice ($n = 15/\text{group}$) were studied: male and female C57Bl/6J wild type (WT) mice fed a HFHSD (40% kcal fat, 40% kcal sucrose, Diet 12327, Research Diets Inc., New Brunswick, NJ), and male and female WT mice fed a HFHSD + EPL (100 mg/kg/day in diet, Mylan Pharmaceuticals Inc.). Either diet was initiated at 10 weeks of age and was continued for 18 weeks. For the latter objective, investigating the roles of SMC and EC MLRs in CMD, three groups of mice ($n = 10/\text{group}$) were bred at the University of Virginia and studied: (a) SMC MLR^{-/-} (NRC2^{fl/fl}/SM-MHC Cre-ERT2+), (b) EC MLR^{-/-} (NR3C2^{fl/fl}/CDH5 Cre-ERT2+), and (c) Cre^{-/-} control mice. All mice were backcrossed for at least 7 generations on a C57Bl/6J background. Since ERT2+ mice have inducible Cre recombinases, all mice received tamoxifen injection (1 mg/kg in peanut oil) for 10 days starting at 6 weeks old. Mice were fed a HFHSD for 18 weeks and initiated at 10 weeks of age.

Timelines for both experiments are shown in Figure 1. All mice underwent multiparametric MRI at baseline (8 weeks of age) and 18 weeks post-diet. The multiparametric MRI protocol at all time points included (a) ASL at rest and with adenosine vasodilation to quantify rest and stress myocardial blood flow and MPR, (b) dynamic nitroxide-enhanced MRI to assess oxidative stress²⁵⁹, (c) cine displacement encoding with stimulated echoes (DENSE) imaging to measure myocardial strain^{196,200}, and (d) cine imaging covering the entire left ventricle (LV) to measure end-diastolic volume (EDV), end-systolic volume (ESV), ejection fraction (EF), and LV mass (LVM). Body weight was recorded for all animals at the beginning of each imaging study. Glucose tolerance tests (GTTs) were performed at baseline and 18 weeks post-diet. After 20 weeks on diet, subgroups of mice ($n = 5/\text{group}$) were euthanized to assess coronary arteriolar vasoreactivity. Separately, radiotelemetry blood pressure measurements were recorded in WT male mice ($n = 4/\text{group}$) from baseline to 18 weeks post-HFHSD and post-HFHSD+EPL.

A HFHSD vs HFHSD+EPL (Male vs Female)



B Cre^{-/-} vs SMC MLR^{-/-} vs EC MLR^{-/-} (Male only)

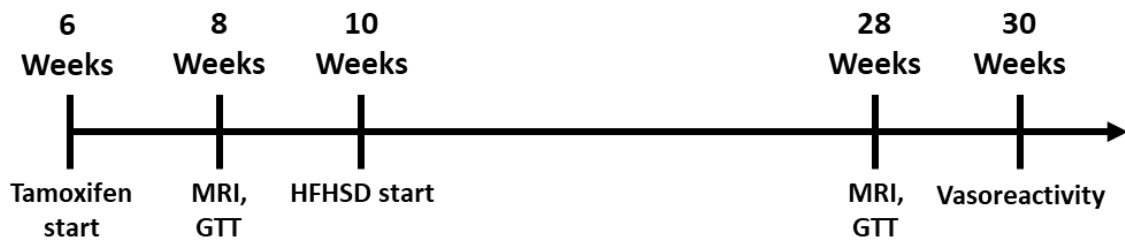


Figure 1. Experimental protocols. (A) Eight-week-old WT mice underwent cardiac MRI, glucose tolerance testing (GTT), and start of radiotelemetry blood pressure (BP) monitoring two weeks before starting a high-fat high-sucrose diet (HFHSD) or a HFHSD + eplerenone (HFHSD+EPL). Eighteen weeks after initiation of either diet, at 28 weeks of age, mice again underwent cardiac MRI and GTT, and ended radiotelemetry BP monitoring. Coronary arteriole vasoreactivity measurements were performed at 30 weeks of age. **(B)** Six-week-old male Cre^{-/-}, SMC MLR^{-/-}, and EC MLR^{-/-} mice underwent tamoxifen injections. At eight weeks of age, mice underwent cardiac MRI and GTT two weeks before starting a high-fat high-sucrose diet (HFHSD). Cardiac MRI and GTTs were repeated after eighteen weeks of HFHSD. Coronary arteriole vasoreactivity measurements were performed at 30 weeks of age.

MRI protocol

All MRI studies were performed using a 7T system (Clinscan, Bruker, Ettlingen, Germany) and a 35-mm-diameter birdcage radiofrequency coil. During MRI, an indwelling tail vein catheter was inserted to deliver a nitroxide contrast agent, 3-Carbamoyl-PROXYL (3CP, Sigma–Aldrich, 1.2 mmol/kg), and an intraperitoneal catheter was established to deliver adenosine (Sigma–Aldrich, 300 mg/kg/min). The electrocardiogram, body temperature, and respiration were monitored during imaging (SA Instruments, Stony Brook, NY). Mice were anesthetized with 1.25% isoflurane and maintained at 36 ± 0.5°C using circulating warm water. The full MRI protocol for each mouse was performed over two sessions separated by 2-3 days. Scout imaging was performed to establish long-axis and mid-ventricular short-axis localizer images. On day

1, cine DENSE strain imaging was performed on a long-axis slice as previously described^{196,197}. Rest perfusion imaging of a mid-ventricular short-axis slice was then performed using ASL³⁹. Thereafter, adenosine was infused i.v. (300 mg/kg/min, 5 μ l/min) and 10 minutes later ASL was repeated. Imaging parameters for ASL included: echo time (TE) = 2.5ms, repetition time (TR) = 10.0 ms, field of view (FOV) = 38 x 38 mm², matrix size = 128 x 128, flip angle = 7 degrees, slice thickness = 1 mm, saturation band thickness = 10 mm, and number of averages = 9. On day 2, black-blood cine MRI was performed²³⁹. Six - eight short-axis slices were acquired covering the entire LV from base to apex. Imaging parameters included: TR=5.7ms, TE = 2.0ms, temporal resolution = 5.7 ms, FOV = 25.6 x 25.6 mm², matrix size = 128 x 128, flip angle = 15 degrees, slice thickness = 1 mm, and number of averages = 4. Finally, to quantify oxidative stress, dynamic nitroxide-enhanced MRI with the nitroxide contrast agent, 3-carbamoyl-PROXYL (3CP), was performed on a mid-ventricular short-axis slice as previously described²⁵⁹.

Analysis of MR images

All image analysis was performed in MATLAB 2021a (Mathworks, Natick, MA). For perfusion quantification, rest and adenosine stress perfusion images were analyzed using methods previously described³⁹. Myocardial perfusion reserve (MPR) was calculated as stress perfusion / rest perfusion. For dynamic nitroxide-enhanced images, blood and myocardial signal intensities were converted to 3CP concentrations and fit to a 2-compartmental exchange and reduction model (2CXRm) to quantify oxidative stress via the nitroxide reduction rate, K_{red} , as previously described²⁵⁹. Strain analysis of cine DENSE images was performed using the DENSE analysis tool^{196,197}. Global longitudinal strain was measured as a metric of systolic function. Cine images were analyzed using the Segment v2.0 R3683 package (<http://segment.heiberg.se>)²⁶⁰. Specifically, the end-diastolic and end-systolic frames were identified, and thereafter, the endocardial and epicardial contours were manually drawn on these frames for all the slices. Using the software, EDV, ESV, EF, and LV mass were calculated.

Glucose tolerance tests

For GTTs, mice (n = 10/group) were injected intraperitoneally with glucose (8 g/kg) in milli-Q water after overnight fasting for 15–16 hours. A tail vein blood sample was taken before injection of glucose to measure the fasting blood glucose and at 10, 30, 60, 90, and 120 minutes after injection of the glucose solution. The area under the curve (AUC) was calculated using the trapezoidal rule to evaluate glucose tolerance⁶².

Radiotelemetric blood pressure measurements

Eight-week-old male mice (n = 4/group) were anesthetized with isoflurane (1.5%) and radiotelemetry catheters (TA11PA-C10, Data Sciences International, St. Paul, MN) were implanted in their left carotid arteries. Each catheter was tunneled through to the

radiotransmitter, which was placed in a subcutaneous pouch along the flank. Before arterial pressure measurements were initiated, mice were allowed to recover for seven days after surgery to regain normal circadian rhythms. Continuous blood pressure measurements were performed using Dataquest A.R.T. 20 software (Data Sciences International, St. Paul, MN), as described previously^{261,262}. Baseline systolic, diastolic, and mean arterial pressures (MAP) were recorded continuously (at 1-min intervals) over 96 hours following the recovery period. The values over four days (6 AM to 6 PM) and four nights (6 PM to 6 AM) were averaged to obtain the baseline pressures. Afterward, mice were placed on either a HFHSD or HFHSD+EPL and the same blood pressure protocol was performed every two weeks for 18 weeks.

Coronary arteriole vascular reactivity

After 20 weeks on diet, a subgroup of each group of mice as well as a control group of age-matched mice fed a standard chow diet (SD) (n = 5/group) was euthanized, and coronary arterioles from the second arborized branches off the left coronary artery were isolated. The arterioles were freed of the surrounding cardiac myocytes and were placed in an arteriography system (Danish MyoTechnology, DMT, Ann Harbor, MI), where they were cannulated at both ends and pressurized to 40 mmHg as previously described^{263–265}. Cumulative dose-responses to adenosine and sodium nitroprusside (SNP), a SMC specific vasodilator, were measured as previously described^{263–265}. Measurements were reported as a percent dilation of the initial vessel diameter.

Statistics

All measurements were reported as mean \pm standard deviation. Statistical analysis was performed using SigmaPlot (Systat Software Inc., Point Richmond, CA). One-way and two-way ANOVAs with post-hoc Tukey's HSD tests for multiple comparisons were used to detect differences in rest perfusion, stress perfusion, MPR, K_{red} , longitudinal strain, body weight, EDV, ESV, EF, LVM, blood glucose levels, GTT-AUC, blood pressure, and vascular reactivity between mouse groups, time points, and diet.

4.4 Results

Protective role of eplerenone on obesity and glucose intolerance due to a HFHSD

Both male and female WT mice had significant weight gain and developed significant glucose intolerance after 18 weeks of HFHSD (Figure 2A-B). Male mice treated with eplerenone also had significant weight gain and glucose intolerance compared to baseline ($p < 0.01$), however compared to untreated mice post-diet, EPL-treated mice showed partial reductions in weight gain and glucose intolerance ($p < 0.01$, Figure 2A-B). In female mice, eplerenone treatment had no effect on weight gain post-HFHSD, however, glucose tolerance was completely preserved in EPL-treated mice compared to baseline (Figure 2A-B). GTT curves for male (Figure 2C) and female (Figure 2D) mice at baseline and post-HFHSD or post-HFHSD+EPL are shown as reference.

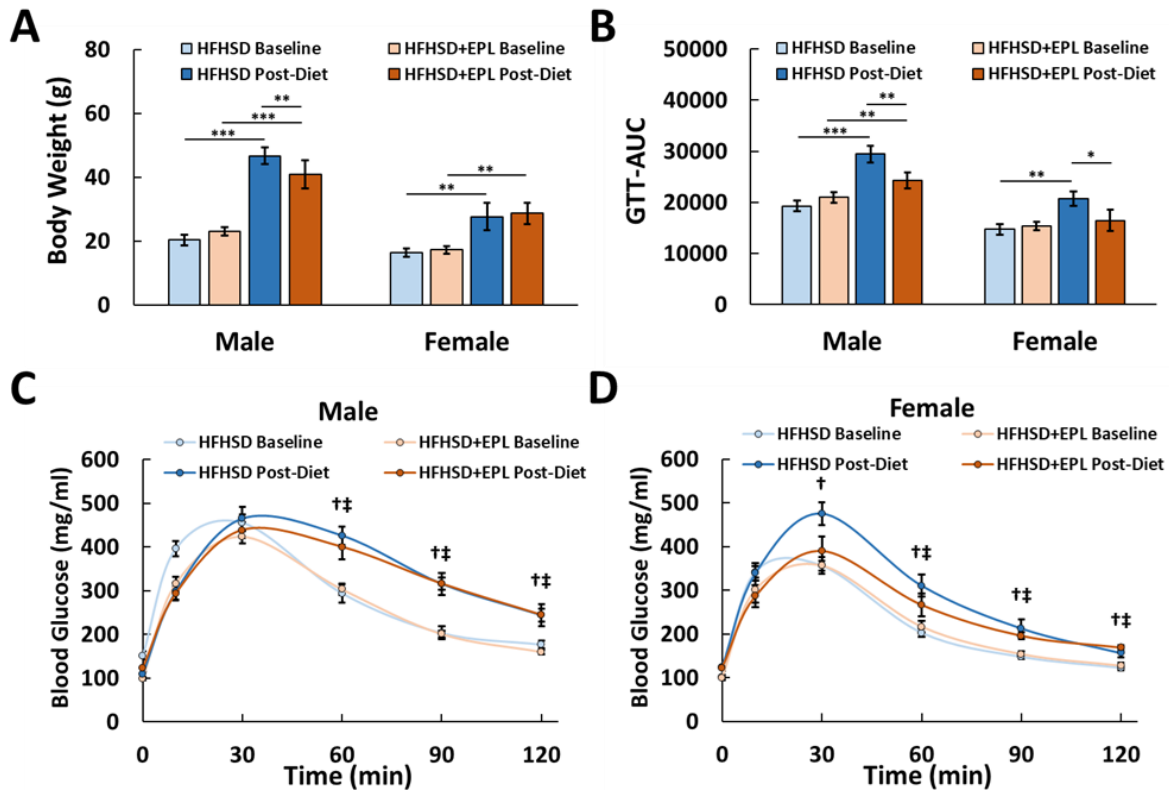


Figure 2. Body weight and glucose tolerance testing. (A) Body weight measurements in grams (g) for male and female WT mice at baseline and 18 weeks post high-fat high-sucrose diet (HFHSD) or HFHSD + eplerenone (HFHSD+EPL). **(B)** Glucose tolerance test area-under-curve (GTT-AUC) measurements for male and female mice at baseline and 18 weeks post HFHSD or HFHSD+EPL. **(C,D)** Example glucose tolerance curves for male and female mice at baseline and post-HFHSD or post-HFHSD+EPL. * $p < 0.05$, ** $p < 0.01$, *** $p < 0.001$, † $p < 0.05$ HFHSD Baseline vs Post-Diet, ‡ $p < 0.05$ HFHSD+EPL Baseline vs Post-Diet

HFHSD induces an impaired adenosine myocardial perfusion reserve, and the impairment is partially prevented in eplerenone treated mice

To investigate changes in MPR, we performed rest and adenosine-induced stress ASL myocardial perfusion mapping of male and female mice at baseline and after 18 weeks of HFHSD or HFHSD+EPL. We observed no differences in rest perfusion between male and female mice either at baseline or post-diet (Figure 3A); however, after 18 weeks of HFHSD there was a significant reduction of stress perfusion in all mice compared to baseline ($p < 0.01$) while stress perfusion was preserved in all EPL-treated mice compared to baseline and significantly improved compared to untreated mice post-HFHSD ($P < 0.05$, Figure 3B). Moreover, MPR was reduced similarly in male and female mice post-HFHSD compared to baseline ($p < 0.01$) and post-HFHSD+EPL compared to baseline ($p < 0.05$), but MPR was significantly improved in all EPL-treated vs untreated mice post-HFHSD ($p < 0.05$, Figure 3C). The findings showed that EPL partially prevented the development of impaired stress perfusion and MPR due to a HFHSD equally in both male and female mice.

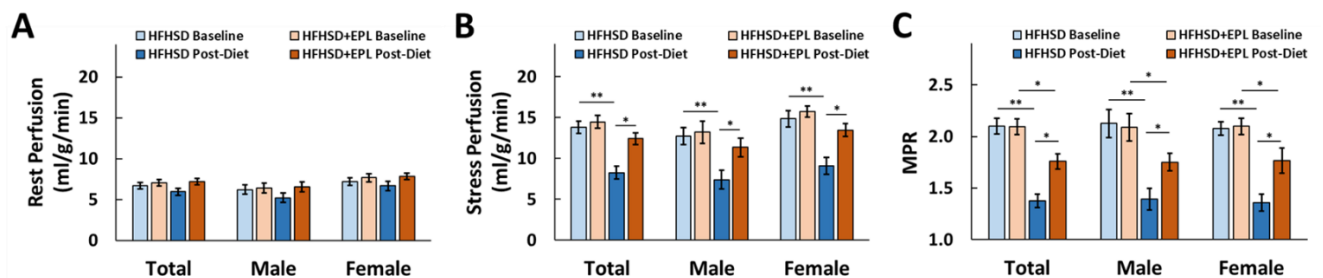


Figure 3. Myocardial perfusion and myocardial perfusion reserve (MPR). (A) Rest and (B) stress perfusion measurements in milliliters/gram/minute (ml/g/min) for all WT mice, and male and female mice separately at baseline and 18-weeks post high-fat, high-sucrose diet (HFHSD) or HFHSD + eplerenone (HFHSD+EPL). (C) MPR measurements for same groups of mice at baseline and post-HFHSD or post-HFHSD+EPL. * $p < 0.05$, ** $p < 0.01$

HFHSD mice treated with eplerenone have an improved coronary arteriolar vasoreactivity

Impaired vasoreactivity is a hallmark of impaired perfusion reserve and therefore we investigated coronary arteriolar reactivity in untreated and EPL-treated mice. We performed cumulative dose-response curves of isolated coronary arteriole dilation in response to adenosine and SNP on male and female mice fed either a HFHSD or HFHSD+EPL for 20 weeks and age-matched mice fed a SD as references. Considering SD mice as a control group, untreated male and female mice show a markedly reduced adenosine response, while EPL-treated mice demonstrate a significantly improved adenosine dilation compared to untreated mice ($p < 0.05$, Figure 4A-C). Similarly, untreated male and female mice show a blunted SNP response, and it is significantly improved in EPL-treated mice (Figure 4D-F). Like MPR, the findings showed that EPL

protected against the development of impaired coronary arteriolar vasoreactivity equivalently in male and female mice.

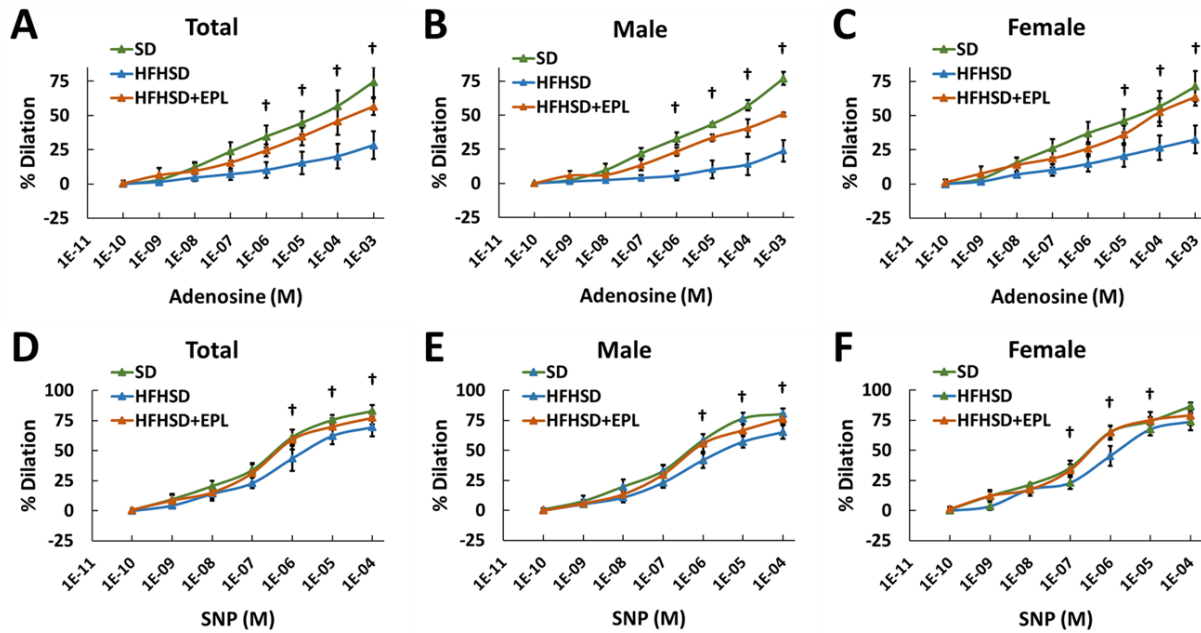


Figure 4. Coronary arteriole vasoreactivity. Cumulative arteriolar dose-response curves to (A) adenosine and (B) sodium nitroprusside (SNP) are shown for all WT mice, and male and female mice separately at 20-weeks post high-fat, high-sucrose diet (HFHSD) or HFHSD + eplerenone (HFHSD+EPL). Cumulative arteriolar dose-response curves for mice fed a standard chow diet (SD) are shown as a reference. Vasodilator concentrations are reported in moles/liter (M). † $p < 0.05$ HFHSD vs HFHSD+EPL

Eplerenone treated mice have reduced myocardial oxidative stress

To examine the extent of HFHSD-induced myocardial oxidative stress, dynamic nitroxide-enhanced MRI was performed at baseline and 18 weeks post-diet. K_{red} , the nitroxide reduction rate and metric of oxidative stress, at 18 weeks post-HFHSD was elevated compared to baseline in both male and female mice ($p < 0.001$, Figure 5). EPL treatment completely preserved myocardial oxidative stress post-diet compared to baseline in both male and female mice and showed significant reductions post-diet compared to untreated mice ($p < 0.01$, Figure 5). Again, like MPR, EPL protected against the development of myocardial oxidative stress similarly in both male and female mice.

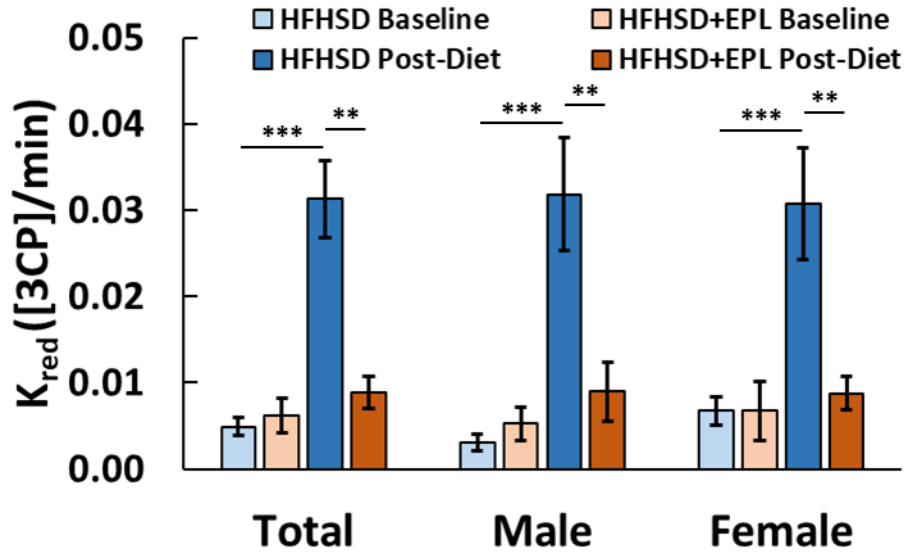


Figure 5. Cardiovascular oxidative stress. To quantify oxidative stress, dynamic nitroxide-enhanced MRI with the nitroxide contrast agent, 3-carbamoyl-PROXYL (3CP), was performed on a mid-ventricular, short-axis slice. The 3CP reduction rate, K_{red} , the MRI metric of oxidative stress, is shown for all WT mice, and male and female mice separately at baseline and 18-weeks post high-fat, high-sucrose diet (HFHSD) or HFHSD + eplerenone (HFHSD+EPL). * $p < 0.05$, ** $p < 0.01$, *** $p < 0.001$

Eplerenone protects from HFHSD-induced impairments in left ventricular structure and systolic strain

During the course of HFHSD administration, LV mass and EDV increased proportionally with age in untreated mice (Table 1). ESV was significantly increased ($p < 0.05$) and consequently, EF was significantly reduced ($p < 0.05$) post-HFHSD compared to baseline (Table 1). EPL-treatment protected mice from significant increases in ESV and the corresponding reduction in EF (Table 1), however, there were some sex-specific differences. Untreated male mice trended towards larger increases in LV mass, EDV, and ESV compared to female mice, but the reduction in EF remained consistent in both male and females (Table 2). EPL-treated male mice showed a similar increase in LV mass and trended towards reductions in EDV and ESV and improvements in EF compared to untreated mice whereas EPL-treated female mice showed no increases in LV mass, EDV, and ESV compared to baseline and each of those parameters were significantly reduced compared to female untreated mice post-HFHSD ($p < 0.05$, Table 2). In addition, female EPL-treated mice showed a significant increase in EF compared to female untreated mice post-HFHSD ($p < 0.05$, Table 2).

	Mass	EDV	ESV	EF
HFHSD Baseline	68 ± 7	37 ± 6	12 ± 3	68 ± 6
HFHSD Post-Diet	81 ± 9 †	45 ± 9	18 ± 6 †	59 ± 8 †
HFHSD+EPL Baseline	66 ± 5	36 ± 4	12 ± 2	67 ± 6
HFHSD+EPL Post-Diet	76 ± 15	40 ± 9	15 ± 5	64 ± 6

Table 1. Left ventricular structure and function (all mice). HFHSD denotes high-fat, high-sucrose diet; EPL eplerenone; EDV end-diastolic volume; ESV end-systolic volume; EF ejection fraction. † p<0.05 HFHSD Baseline vs Post-Diet

	Mass	EDV	ESV	EF
(M) HFHSD Baseline	68 ± 6	36 ± 6	11 ± 3	69 ± 7
(M) HFHSD Post-Diet	85 ± 6 †	49 ± 8 †	20 ± 4 †	60 ± 3 †
(M) HFHSD+EPL Baseline	67 ± 5	37 ± 4	12 ± 2	66 ± 5
(M) HFHSD+EPL Post-Diet	87 ± 7 †	43 ± 11	16 ± 6	62 ± 7
(F) HFHSD Baseline	69 ± 5	37 ± 5	12 ± 3	68 ± 5
(F) HFHSD Post-Diet	78 ± 10 †	42 ± 5 †	17 ± 3 †	59 ± 5 †
(F) HFHSD+EPL Baseline	63 ± 3	36 ± 4	11 ± 3	69 ± 7
(F) HFHSD+EPL Post-Diet	63 ± 4 ‡	35 ± 3 ‡	12 ± 2 ‡	65 ± 6 ‡

Table 2. Left ventricular structure and function (male vs female). HFHSD denotes high-fat, high-sucrose diet; EPL eplerenone; EDV end-diastolic volume; ESV end-systolic volume; EF ejection fraction. † p<0.05 same gender same diet Baseline vs Post-Diet, ‡ p<0.05 same gender post-diet HFHSD vs HFHSD+EPL

Next, we evaluated end-systolic longitudinal strain from DENSE MRI. The end-systolic longitudinal strain was impaired post-HFHSD compared to baseline in both male and female mice (p<0.001), however, EPL-treatment had a greater effect in males compared to females (Figure 6). EPL-treated male mice post-HFHSD had significantly greater LV strain compared to untreated mice (p<0.01) and showed nearly complete preservation of LV strain compared to baseline (Figure 6B). EPL-treated female mice post-HFHSD also had a significantly greater LV strain compared to untreated mice

($p < 0.05$), but only showed partial improvements in strain and was still significantly lower compared to baseline ($p < 0.05$, Figure 6C). Together, these results indicate that eplerenone imparts sex-specific improvements in LV structure and function which are otherwise impaired due to a HFHSD.

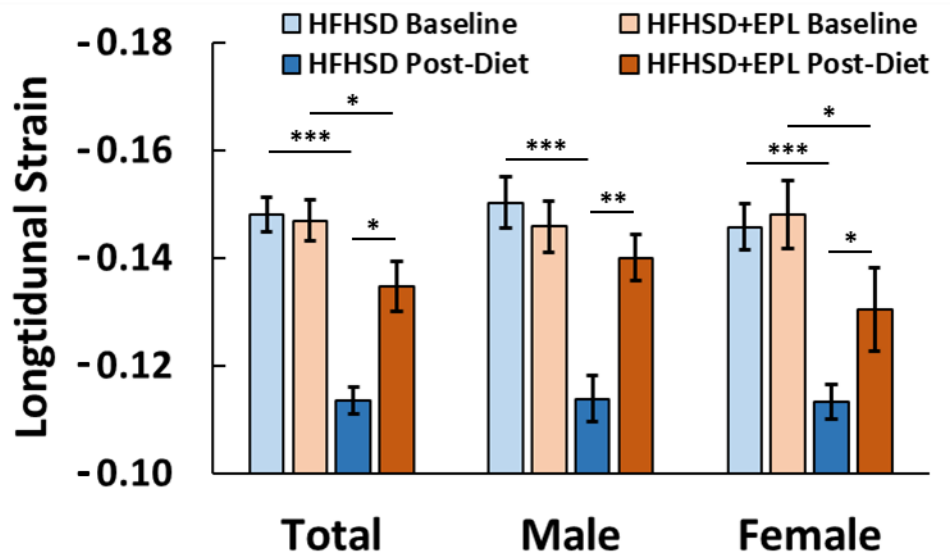


Figure 6. Longitudinal strain. Longitudinal strain measurements for all WT mice, and male and female mice separately at baseline and 18-weeks post high-fat, high-sucrose diet (HFHSD) or HFHSD + eplerenone (HFHSD+EPL). * $p < 0.05$, ** $p < 0.01$, *** $p < 0.001$

HFHSD induces blood pressure increases regardless of eplerenone treatment

Blood pressure results in male mice are summarized in Table 3. The HFHSD increased blood pressure equally in both untreated and EPL-treated mice. Diastolic and MAP were significantly increased post-HFHSD compared to baseline ($p < 0.05$) and there was a trend towards an increase in systolic blood pressure as well (Table 3) demonstrating that the effects of EPL are blood pressure-independent in male mice.

	Systolic	Diastolic	MAP
HFHSD Baseline	127 ± 4	93 ± 2	111 ± 3
HFHSD Post-Diet	133 ± 5	106 ± 8 †	120 ± 1 †
HFHSD+EPL Baseline	125 ± 4	91 ± 3	109 ± 1
HFHSD+EPL Post-Diet	134 ± 8	103 ± 6 ‡	119 ± 6 ‡

Table 3. Radiotelemetric blood pressure. HFHSD denotes high-fat, high-sucrose diet; EPL eplerenone; MAP mean arterial pressure. † p<0.05 HFHSD Baseline vs Post-Diet, ‡ p<0.05 HFHSD+EPL Baseline vs Post-Diet

Genetic deletion of SMC and EC MLRs has a minimal effect on the progression of HFHSD-induced CMD

Since global pharmacological inhibition of MLRs partially prevented impairments in MPR, we next investigated if SMC or EC MLR deletion in male mice could also prevent MPR impairment due to a HFHSD with Cre^{-/-} mice as controls. After 18 weeks on HFHSD, all groups of mice developed similar levels of obesity (Figure 7A) and glucose intolerance (Figure 7B) post-HFHSD compared to baseline. In addition, MPR was impaired in all groups of mice post-HFHSD compared to baseline (p<0.001) with no significant improvements between controls and SMC MLR^{-/-} or EC MLR^{-/-} mice post-HFHSD (Figure 8A). These results were consistent with adenosine and SNP coronary arteriole vasoreactivity showing no significant improvements in arteriole vasodilation between Cre^{-/-} and either MLR^{-/-} mice (Figure 8B-C). Also, SMC and EC MLR^{-/-} had no effect on LV structure; LV EDV and ESV were significantly greater, and consequently, EF was reduced post-HFHSD compared to baseline in all groups of mice (p<0.05, Table 4).

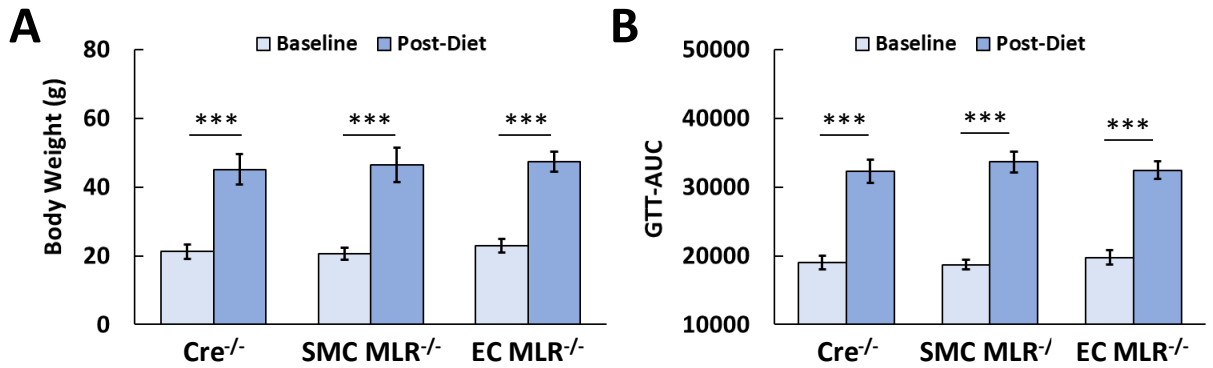


Figure 7. MLR^{-/-} Body weight and glucose tolerance testing. (A) Body weight measurements in grams (g) and **(B)** Glucose tolerance test area-under-curve (GTT-AUC) measurements for Cre^{-/-}, smooth muscle cell (SMC) mineralocorticoid receptor knockout (MLR^{-/-}), and endothelial cell (EC) MLR^{-/-} mice at baseline and 18 weeks post high-fat high-sucrose diet (HFHSD). * p<0.05, ** p<0.01, *** p<0.001

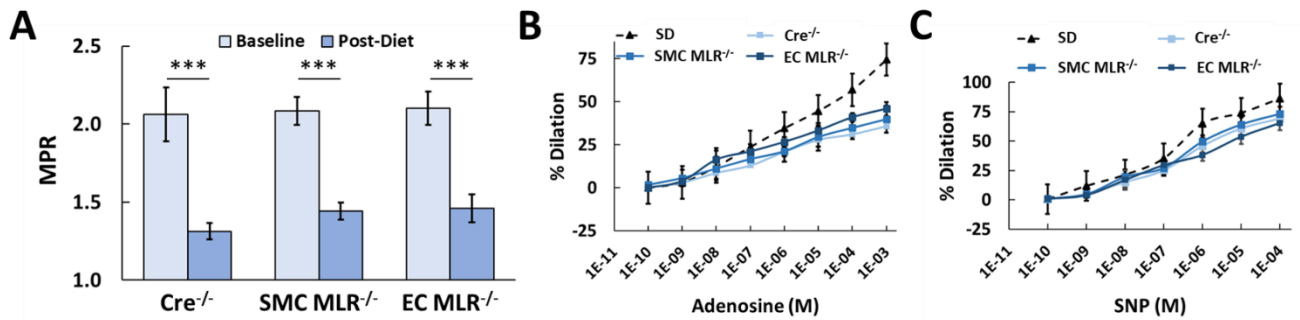


Figure 8. MLR^{-/-} Perfusion reserve and coronary arteriole vasoreactivity. (A) Myocardial perfusion reserve (MPR) measurements for Cre^{-/-}, and smooth muscle cell (SMC) and endothelial cell (EC) mineralocorticoid receptor knockout (MLR^{-/-}) mice at baseline and 18 weeks post high-fat high-sucrose diet (HFHSD). Cumulative arteriolar dose-response curves to **(B)** Adenosine and **(C)** sodium nitroprusside (SNP) cumulative arteriolar dose-response curves for all groups of mice at 20-weeks post-HFHSD, and wild-type mice fed a standard chow diet (SD) as a reference. Vasodilator concentrations are reported in moles/liter (M). * p<0.05, ** p<0.01, *** p<0.001

Though MLR^{-/-} had no significant effect on MPR post-HFHSD, there were a few differences between SMC MLR^{-/-}, EC MLR^{-/-}, and Cre^{-/-} control mice. Myocardial oxidative stress was significantly elevated in all groups of mice post-HFHSD compared to baseline (p<0.01), however, SMC MLR^{-/-} mice post-HFHSD did however show partial reductions in oxidative stress compared to controls and EC MLR^{-/-} mice post-HFHSD (p<0.05, Figure 9A). Similarly, longitudinal strain was impaired in all groups of mice post-HFHSD compared to baseline, and again, SMC MLR^{-/-} mice post-HFHSD showed partial improvements in strain compared to controls and EC MLR^{-/-} mice post-HFHSD (p<0.05, Figure 9B).

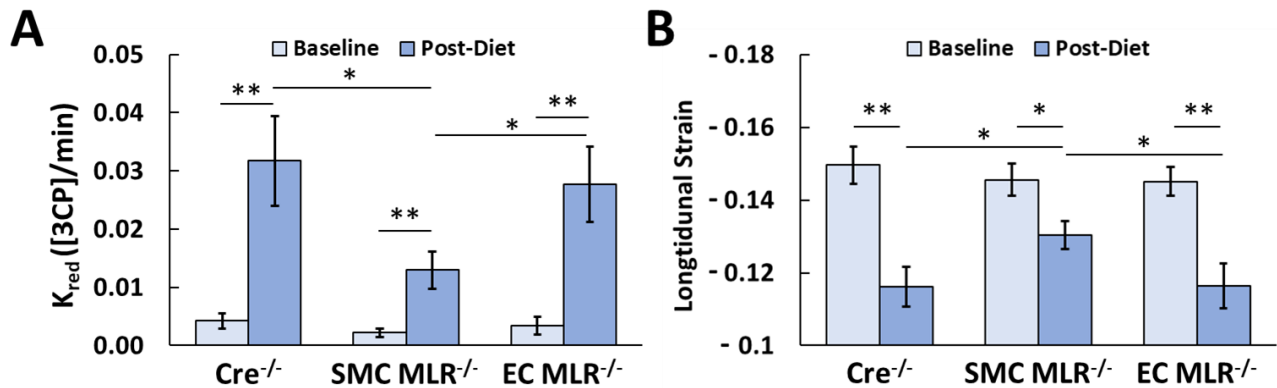


Figure 9. MLR^{-/-} Oxidative stress and longitudinal strain. (A) Oxidative stress and (B) longitudinal strain measurements for Cre^{-/-}, smooth muscle cell (SMC) mineralocorticoid receptor knockout (MLR^{-/-}), and endothelial cell (EC) MLR^{-/-} mice at baseline and 18 weeks post high-fat high-sucrose diet (HFHSD). * p<0.05, ** p<0.01, *** p<0.001

	Mass	EDV	ESV	EF
Cre^{-/-} Baseline	71 ± 11	40 ± 6	14 ± 2	66 ± 5
Cre^{-/-} Post-Diet	81 ± 7	50 ± 12 †	21 ± 7 †	59 ± 8 †
SMC MLR^{-/-} Baseline	73 ± 14	41 ± 9	14 ± 5	65 ± 6
SMC MLR^{-/-} Post-Diet	83 ± 12	52 ± 6 †	22 ± 5 †	59 ± 8 †
EC MLR^{-/-} Baseline	71 ± 9	40 ± 4	13 ± 2	66 ± 3
EC MLR^{-/-} Post-Diet	84 ± 6 †	52 ± 8 †	20 ± 3 †	60 ± 6 †

Table 4. MLR^{-/-} LV structure and function. SMC smooth muscle cell; EC endothelial cell; MLR^{-/-} mineralocorticoid receptor knockout; EDV end-diastolic volume; ESV end-systolic volume; EF ejection fraction. † p<0.05 same mouse group Baseline vs Post-Diet

4.5 Discussion and Conclusions

Main findings summary

The major findings of this study are that a) MLR blockade via EPL provides partial preservation of coronary arteriole and myocardial perfusion responses to adenosine, which are otherwise impaired in mice fed a HFHSD for 18 weeks, and the associated obesity, glucose intolerance, oxidative stress, and longitudinal strain, b) the effect of EPL on coronary arteriole function is consistent in both male and female mice, and c) SMC and EC MLR deletion in male mice did not significantly improve coronary arteriole function and MPR, though SMC MLR^{-/-} did show improvements in oxidative stress and longitudinal strain.

Model of diet-induced CMD

Prior studies have used rodent and murine models with various specific diet compositions and experimental timelines to study the effects of obesity and diabetes on microvascular function^{266,267}. Diets vary in terms of percentage of calories from fat (30–78%), and in the amounts of carbohydrate, protein, fatty acids, and sugar. Diets may also include additional compounds to alter cellular signal transduction^{266,268}. Experimental timelines may vary from 7 days to more than 24 weeks, and the specific protocol can alter the degree of microvascular pathophysiology and yield conflicting results and outcomes^{266,268}. The relatively long duration and high content of fat and sucrose in our diet suggests that our model may lead to relatively severe CMD.

MRAs in treatment of CMD and HFpEF

Our finding that global MLR blockade via EPL improves coronary arteriole function both in vivo and ex vivo is consistent with results from prior clinical studies^{46,47} and from preclinical studies in obese and diabetic rats^{269,270}. In addition, we found no sex-specific differences in improvements of MPR in eplerenone treated mice. Clinically, studies have shown no sex-specific differences in role of MRAs for the treatment of heart failure^{271–274}, and evidence surrounding sex-specific differences in MRA treatment of HFpEF specifically has been widely debated^{173,177,178,275}. While there may be distinct sex-specific differences between mice and humans in phenotypes of CMD and HFpEF and responses to MRAs, our results add to the evidence that MRAs can be beneficial for the treatment of CMD and HFpEF regardless of gender.

Sex-specific differences in MRA treatment

While there were no sex-specific differences in primary outcome of MPR in both the untreated and EPL-treated mice, there were differences in weight gain and glucose intolerance. Similar to prior studies, we showed that HFHSD fed male mice gained significantly more weight compared to females in mouse models of diet-induced obesity^{276,277}, and eplerenone treatment reduced weight gain in males but not

females^{69,175}. Also, HFHSD fed male mice developed a significantly greater glucose intolerance compared to females²⁷⁷, however, eplerenone only partially improved glucose tolerance in males whereas it was completely preserved in females. It is well established that MRAs improve glucose tolerance in both male and female mouse models of diet-induced obesity^{155,175,278,279}, however to the best of our knowledge, this is the first study showing a sex-specific difference of MRA treatment on diet-induced glucose intolerance in mice.

Our results also indicated trends toward sex-specific differences in perfusion, strain, and LV structure. Female mice trended towards a greater rest and adenosine-stress perfusion compared to males similar to clinical trends²⁸⁰. Eplerenone treatment showed trends towards greater improvements in longitudinal strain in male mice, but greater improvements in EF in female mice. Also, eplerenone prevented increases in LV mass, wall thickness, EDV, and ESV in female but not male mice. Together these results indicate that MRA treatment may impart some sex-specific cardiovascular phenotypes and warrant further studies to explore these relationships.

Mechanisms of CMD

Obesity, diabetes, and the metabolic syndrome are comorbidities which induce a systemic proinflammatory state and can eventually lead to CMD and HFpEF²⁷. While global MLR blockade provided improvements in adenosine MPR in WT mice, SMC and EC specific MLR deletion showed only minor, but insignificant, improvements in MPR after 18 weeks of HFHSD. We also showed that global MLR blockade reduces weight gain and glucose intolerance in HFHSD-fed WT mice, however, SMC and EC MLR deletion had no effect. Recent studies have demonstrated pathophysiological roles of macrophage and adipose MLRs in exacerbating microvascular dysfunction^{152,160,281}, and an important role of adipose MLRs in diet-induced weight gain and insulin resistance¹⁵⁵⁻¹⁵⁷. Together, these results indicate that CMD can be attributed to systemic, not only vascular, MLR activation, and further studies are needed to determine the order of the cascade of events.

Many studies have shown that MLR activation in SMCs and ECs increases NADPH oxidase expression and the generation of reactive oxygen species, thus promoting oxidative stress-related injury²⁸². Surprisingly, we showed that only SMC MLR^{-/-} mice had reduced myocardial oxidative stress compared to controls after 18 weeks of HFHSD. In addition, only SMC MLR^{-/-} mice showed improvements in longitudinal strain, however, one limitation is that we only studied male MLR^{-/-} mice. A recent study by Davel et al. showed that the effects of EC MLRs in obesity-induced vascular injury are sexually dimorphic as they showed that only female EC MLR^{-/-} prevented oxidative stress due to obesity²⁸³. Thus, oxidative stress and the cardiac dysfunction may be SMC MLR driven in males and EC MLR driven in females, and additional studies are warranted to understand the connection between cell-specific MLRs and sex in the progression of CMD.

Limitations

The present study had several limitations. First, while we show that the effects of EPL are blood pressure-independent in WT males, blood pressure telemetry was not performed on female WT mice or SMC and EC MLR^{-/-} mice. Prior studies on MRA treatment in diet-induced obese female mice showed that MRAs did not improve blood pressure and imparted blood pressure-independent effects in females as well^{69,284}. However, studies on MLR mechanisms have implicated the SMC¹⁴⁷ and EC MLR^{147,285} in diet-induced hypertension. A second limitation is that we did not evaluate endothelial dysfunction in our mouse model, although, our group has previously shown that microvascular endothelial dysfunction precedes CMD in diet-induced obese mice²⁸⁶. Future studies may seek to further understand the contributions of MLRs and MRAs in HFHSD-induced hypertension and endothelial dysfunction. Lastly, while we detected impairments in microvascular function, oxidative stress, and strain in mice after 18 weeks of a HFHSD, we did not determine the time of onset of each event, thus, future longitudinal studies may seek to determine the cascade of mechanisms underlying HFHSD-induced CMD.

Conclusions

In conclusion, adenosine stress MPR imaging, nitroxide-enhanced oxidative stress MRI, and LV structure and function MRI along with other methods applied in a HFHSD mouse model show an important role of MLRs and MLR blockade in CMD related to obesity, diabetes, and metabolic inflammation. These results add to the body of preclinical and clinical work demonstrating a key role of MLRs in the development of CMD and supports a beneficial effect of MRAs on CMD, and potentially HFpEF, regardless of gender.

Chapter 5 – Conclusions and Future Directions

5.1 Conclusions

In this dissertation, two MRI methods were developed to assess and quantify biomarkers of CMD in mice. DNE-MRI probes cardiovascular oxidative stress and accelerated EAT FAC MRI probes the FAC of EAT as a potential surrogate of the inflammatory profile of EAT. These new techniques along with traditional MRI methods were used to study the molecular mechanisms of MLRs and EPL, an MRA, on the development of CMD in a mouse model of HFHSD-induced CMD.

5.1.1 Nitroxide-enhanced MRI of cardiovascular oxidative stress

We developed 3CP DNE-MRI and a 2CXR to quantify the 3CP reduction rate as a metric of cardiovascular oxidative stress in mice, and we validated this technique in three mouse models of heart disease: ANGII infusion, MI, and HFHSD-induced obesity. To our knowledge, this was the first MRI method to quantify cardiovascular oxidative stress. As oxidative stress plays a vital role in numerous heart diseases, DNE-MRI can be one component of a multiparametric preclinical cardiac MRI protocol for investigations into mechanisms of heart disease and to test therapies aiming at decreasing oxidative stress.

5.1.2 Accelerated fatty acid composition MRI of epicardial adipose tissue

Here, we were the first group to develop FAC MRI and FAC-IDEAL localized to the heart to quantify the EAT FAC. We also applied pseudo-random undersampling with a CS-DICT reconstruction to achieve a total of rate-3 acceleration for EAT FAC MRI which we validated in oil phantoms and various adipose depots. Using this technique, we showed that EPL shifted the EAT towards a reduction in SFAs, increased unsaturation in a mouse model of HFHSD-induced CMD and was associated with an improvement in coronary microvascular function. Because an overabundance of SFAs in adipose tissues is regarded as proinflammatory, MRI to quantify the EAT FAC may represent a biomarker of proinflammatory vs. anti-inflammatory EAT and potentially an early biomarker of CMD.

5.1.3 Role of mineralocorticoid receptors in CMD

Using multiparametric MRI along with *ex vivo* techniques, we showed that EPL provides partial protection from the development of CMD in both male and female mice. However, we also showed that cell specific deletion of SMC or EC MLRs alone does not protect mice from the development of CMD. These results add to current preclinical and clinical data demonstrating a significant role of systemic MLR activation in CMD and MRAs as a potential therapy for CMD regardless of gender.

5.2 Future Directions

5.2.1 Nitroxide-enhanced MRI

For our DNE-MRI studies we used the nitroxide 3CP, however, other nitroxide contrast agents may be better suited to measure oxidative stress. For example, the nitroxide, 23c, has been shown to provide strong myocardial signal enhancement and may have a signal decay rate faster than that of 3CP. Other groups have also shown the effectiveness of DNE-MRI using the nitroxides TEMPO and Mito-TEMPO. Future work may compare the various nitroxides for detecting cardiovascular oxidative stress with DNE-MRI. Second, while our work focused on the evaluation of cardiovascular oxidative stress, DNE-MRI can be extrapolated to multiple other areas of preclinical studies including neurodegenerative disorders such as Alzheimer's or Parkinson's, cancers, chronic kidney disease, or alcoholic liver disease where oxidative stress plays an important role. Lastly, while nitroxides have not been tested in humans, DNE-MRI could be applied to humans as these compounds have the sufficient safety profiles. DNE-MRI could be an alternative to first-pass gadolinium-enhanced MRI to simultaneously assess perfusion and oxidative stress.

5.2.2 MRI of epicardial adipose tissue

Similar to oxidative stress imaging, we developed FAC MRI for a specific organ system which in this case was EAT, however, FAC imaging should not be limited to adipose depots. In addition to EAT FAC, myocardial FAC is also of interest in disease processes. Studies have linked myocardial FAC metabolism and cardiomyocyte FAC to an increased risk in contractile dysfunction, heart failure, and MI. The main challenge with myocardial FAC imaging is that the bulk protons in the myocardium are from water and the total fat signal is low which can lead to incorrect IDEAL fitting. Future work may incorporate increased SNR or water saturation for the quantification of myocardial FAC.

Second, in this study, we only developed an IDEAL-based method to quantify FAC, however, an IDEAL reconstruction also provides tissue R_2^* values, which may be related to iron deposition. In adipose tissues, iron is a critical regulator of energy metabolism and iron overload is tightly connected with metabolic disorders. Also, like oxidative stress imaging, R_2^* imaging can be important in neurodegenerative diseases related to excessive iron deposition, most notably Parkinson's and Alzheimer's. The main challenge with R_2^* imaging is that a different Cramer-Rao bound is needed because a longer echo train is required to accurately measure to estimate R_2^* than we currently use. To overcome this issue, we could modify our model to incorporate bipolar, as opposed to unipolar, readouts to acquire more than two echoes per acquisition and acquire a longer echo train without changing total acquisition time. Thus, future studies may modify the acquisitions parameters of FAC MRI to also correlate R_2^* to iron deposition for various diseases state.

Lastly, a main goal of this study was to show that acceleration of FAC MRI is possible, and while we achieved rate-3 acceleration, both the acceleration rate and reconstruction method could be further improved. Ultimately, the goal is to translate this method for human FAC imaging to acquire FAC maps and EAT FAC quantification within a single breath hold. The use of non-cartesian sampling patterns (e.g., radial or

spiral) or adding additional terms in the reconstruction model (e.g., total variation) could provide a greater acceleration rate. For human imaging, a multiecho segmented radial acquisition with rate-4 to -6 acceleration could be used to obtain FAC maps and estimation in <16 heart beats. In addition, a cardiologist would also want to see these maps in real time on the scanner, thus accelerating the reconstruction as well is of interest. Recently, Siemens has developed “FIRE” which is a system which exports the raw data of a scan to a separate server where offline reconstruction can be performed and subsequently imported back to the scanner. Currently, the whole process of CS-DICT with FAC-IDEAL of a 128x128 image may take up to 15 minutes, however we would like to achieve a reconstruction in <1 minute. In terms of CS-DICT, K-SVD could be used to compress the dictionary and reduce total reconstruction time. Also, a machine learning algorithm could be used for direct fatty acid composition mapping without the need for iterative reconstructions. Overall, additional refinement of FAC imaging, acceleration, and imaging can allow single breath-hold, fast reconstruction, and in total, an efficient method for human EAT FAC quantification.

5.2.3 Mechanisms and treatments for CMD

For the studies examining the role of MLRs and MRAs on CMD, there are a multitude of interesting follow up studies which could be done to more completely understand MLRs in CMD. First, we showed that SMC and EC MLR^{-/-} had very little effect on suppressing the development of CMD. The more interesting MLRs may in fact be the adipose and macrophage MLRs as both promote coronary microvascular inflammation. Also, recent studies have shown gender-dependent mechanisms of obesity-induced microvascular dysfunction. While in this study, we only looked at male MLR^{-/-}, female mice may be more prone to EC MLR induced CMD. Thus, future studies many study the roles of adipose and macrophage MLR^{-/-} as well as the gender specific MLR mechanistic differences on the progression of CMD.

In addition, our entire study revolved around endothelial-independent CMD, however endothelial-dependent CMD is continuing to gain recognition. Endothelial-dependent vasodilators such as acetylcholine could simply be added to our multiparametric MRI protocol. It would be interesting to study whether MLR^{-/-} or MRAs have a greater role in endothelial-dependent CMD.

Furthermore, aside from coronary vasoreactivity, we did not conduct any ex vivo experiments such as immunostaining, immunoassays, blood draws, western blotting, etc. For example, understanding where MLR expression is upregulated in HFHSD mice could help facilitate MLR^{-/-} studies. Similarly, macrophage or cytokine profiles of the blood, heart, and EAT would strengthen the hypothesis that a proinflammatory EAT is an important cause of CMD.

Finally, while we show that systemic MLR activation has a significant role in the progression of CMD, our study along with the body of preclinical and clinical data suggests that MRAs alone are not enough to protect against CMD and that there may be numerous other mechanisms involved. Because mouse models can allow for a large flexibility in studying the genetics and mechanisms underlying CMD as well as potential therapies, future studies can utilize our multiparametric MRI methods to understand other pathways related to CMD. For example, in [Appendix A](#), we demonstrate the role

of iNOS and iNOS inhibitors on the development of CMD. In addition, current preclinical and clinical studies are investigating the efficacy of SGLT2 inhibitors (e.g., Empagliflozin, Dapagliflozin) as a treatment for CMD. Future works should be directed to fully elucidate the mechanisms underlying CMD in order to develop a targeted treatment for CMD.

**Appendix A – Role of iNOS in Preventing and Reversing
Coronary Microvascular Disease Due to a High-Fat High-
Sucrose Diet**

A.1 Abstract

Background: Coronary microvascular disease (CMD), measured by an impaired adenosine myocardial perfusion reserve (MPR), is a risk factor for major cardiac events and mortality and central to heart failure with preserved ejection fraction (HFpEF). However, the mechanisms underlying CMD are not fully understood. Using cardiac MRI applied to a mouse model of CMD, we elucidated the effects of iNOS knockout (iNOS^{-/-}) and iNOS inhibition via 1400W in reducing and reversing CMD.

Methods: Wild-type (WT) and iNOS^{-/-} mice were fed either a standard diet (SD) or high-fat, high-sucrose diet (HFHSD) for 18 weeks beginning at 10 weeks of age. To study CMD reversal, 1400W treatment was initiated at 10 weeks post-HFHSD and continued for 8 weeks. Glucose tolerance testing, blood pressure telemetry, and cardiac MRI to assess MPR, myocardial oxidative stress, left ventricular structure, and systolic and diastolic function, were performed at baseline and 18 weeks post-diet. For 1400W-treated mice, cardiac MRI was also performed 10 weeks post-diet, prior to 1400W administration. At 20 weeks post-diet, ex-vivo coronary arteriole vasoreactivity was performed on all groups of mice.

Results: All groups of mice had weight gain and glucose intolerance after 18 weeks of HFHSD. MPR was reduced in WT mice post-HFHSD vs. baseline (1.39 ± 0.10 vs 2.19 ± 0.16 , $p < 0.01$). In contrast, MPR was maintained in iNOS^{-/-} mice post-HFHSD compared to baseline (1.97 ± 0.12 vs 2.07 ± 0.14), and the MPR results were supported by vasoreactivity results. Oxidative stress was reduced ($p = 0.02$) and systolic ($p = 0.03$) and diastolic ($p = 0.04$) function were improved in iNOS^{-/-} vs. WT mice post-HFHSD. For CMD reversal studies, 1400W treatment improved MPR from 10 to 18 weeks post-HFHSD (1.49 ± 0.10 vs 1.70 ± 0.07 , $p = 0.04$), improved MPR compared to untreated mice post-HFHSD (1.70 ± 0.07 vs 1.39 ± 0.10 , $p = 0.03$) and was confirmed by vasoreactivity. Oxidative stress was reduced ($p < 0.01$) and systolic function was improved ($p = 0.01$) in 1400W-treated mice from 10 to 18 weeks post-HFHSD and in treated vs. untreated mice post-HFHSD.

Conclusions: iNOS plays a central role in CMD, and therapies aimed at reducing iNOS activity warrant investigation as potential therapies for CMD.

A.2 Clinical Perspective

What is new

- iNOS is a central mediator of impaired MPR, myocardial oxidative stress, and systolic and diastolic function in mice fed a high-fat, high-sucrose diet
- The genetic ablation of iNOS prevented and the pharmacological inhibition of iNOS reversed CMD in mice fed a high-fat, high-sucrose diet

Clinical Implications

- Obesity, insulin resistance, and diabetes are increasingly prevalent in industrialized countries and predispose patients to CMD, characterized by impaired endothelial-independent coronary microvascular reactivity
- CMD imparts a high risk of cardiac events and mortality, even in the absence of epicardial CAD, and current treatments are ineffective
- The inhibition of iNOS reverses impaired MPR and improves cardiac function in a model of obesity-induced diabetes, revealing that iNOS may potentially serve as a therapeutic target in CMD

A.3 Introduction

Coronary microvascular disease (CMD) is an important cause of ischemic heart disease²⁸⁷, a central mechanism underlying heart failure with preserved ejection fraction (HFpEF)¹⁰, and a risk factor for major adverse cardiac events and mortality²⁵³. While CMD can refer to both endothelial-dependent and endothelial-independent impairments of microvascular reactivity, the endothelial-independent impairment, typically probed using adenosine, has stronger associations with adverse outcomes and diastolic dysfunction²¹ and accounts for most of the data relating CMD to outcomes and HFpEF²⁵³. Endothelial-independent CMD is typically assessed by coronary flow reserve (CFR) testing with intracoronary adenosine or myocardial perfusion reserve (MPR) imaging using rest and adenosine stress PET⁷ or MRI²⁵⁴. Comorbidities including obesity and diabetes that lead to metabolic inflammation are associated with CMD, and chronic metabolic inflammation is widely regarded as a major contributor to CMD^{16,288}. While the clinical significance of CMD is increasingly recognized, the specific mechanisms that cause CMD remain incompletely understood.

Because adenosine increases coronary blood flow and myocardial perfusion through its actions dilating the coronary resistance vessels, in the absence of epicardial coronary artery disease (CAD), impaired adenosine CFR and MPR mainly reflect underlying coronary arteriolar dysfunction. While endothelial NOS and neuronal NOS are constitutively expressed, iNOS is expressed only when induced by certain stressors such as occur in obesity and diabetes. For this reason, we hypothesized that inducible nitric oxide synthase (iNOS) may play a major role in CMD due to obesity and diabetes.

Vascular smooth muscle cells (VSMCs) and macrophages are predominant sources of iNOS expression²⁸⁹, and prior data show that a high-fat diet and obesity induce vascular expression of iNOS^{290,291}. Consistent with animal data, recent data from diabetic patients showed upregulation of splenic artery VSMC iNOS²⁹². A high-fat diet is also known to increase macrophage M1 polarization and iNOS expression²⁹³, and M1 polarized macrophages are known to accumulate in the walls of blood vessels where they contribute to local inflammation and oxidative stress²⁹⁴. Moreover, iNOS was recently found to play a central role in a mouse model of HFpEF⁶⁷. To our knowledge, no prior studies have investigated the role of iNOS in adenosine-mediated coronary arteriolar dysfunction or imaging-based, adenosine-mediated MPR.

We and others have developed arterial spin labeling (ASL) MRI methods that enable the reproducible quantification of rest and adenosine stress myocardial perfusion and MPR in mice⁴⁰. We have also shown that mice fed a high-fat diet or a high-fat, high-sucrose diet (HFHSD) develop impaired adenosine-stress MPR, and, since these mice do not develop atherosclerosis, represent a model of CMD without CAD^{62,258}. In addition to ASL, cardiac MRI in mice enables a comprehensive noninvasive evaluation of cardiac structure, function, perfusion, and oxidative stress, all of which are important parameters for the evaluation of heart disease due to diabetes and obesity. In the present study we employed cardiac MRI and other methods in mice fed a HFHSD to test the hypotheses that impaired adenosine MPR would be reduced in iNOS knockout (iNOS^{-/-}) mice and that established CMD could be partially reversed by iNOS inhibition.

A.4 Methods

Experimental design

All animal studies were performed in accordance with protocols that conformed to the Declaration of Helsinki as well as the Guide for Care and Use of Laboratory Animals (NIH publication no. 85-23, revised 1996) and were approved by the Animal Care and Use Committee at the University of Virginia.

Experiments were performed to: (1) demonstrate the central role of iNOS in CMD resulting from 18 weeks of HFHSD, and (2) test whether iNOS inhibition can partially reverse established CMD resulting from 10 weeks of HFHSD. All mice were obtained from the Jackson Laboratories (Bar Harbor, Maine). For the first objective, four groups of mice ($n = 12/\text{group}$) were studied: (a) wild type (WT) male C57Bl/6J mice fed a HFHSD (40% kcal fat, 40% kcal sucrose, Diet 12327, Research Diets Inc., New Brunswick, NJ), (b) WT mice fed a standard chow diet (SD), (c) iNOS^{-/-} mice (stock no. 002596 - B6.129P2-*Nos2*^{tm1Lau/J}) fed a HFHSD, and (d) iNOS^{-/-} mice fed a SD. Either diet was initiated at 10 weeks of age and was continued for 18 weeks. For the second objective, investigating reversal of established CMD, two groups of mice ($n = 10/\text{group}$) were studied: (a) WT mice fed HFHSD, where the diet was initiated at 10 weeks of age and continued for 18 weeks, and (b) WT mice fed HFHSD for 18 weeks, where the diet was initiated at 10 weeks of age, and where iNOS inhibition was initiated 10 weeks after beginning the HFHSD. iNOS inhibition was delivered using implanted osmotic minipumps (AZLET model 1004, DURECT Comp, Cupertino, CA) loaded with 1400W (Sigma-Aldrich, 30 mg/kg/day²⁹⁵), a highly selective iNOS inhibitor.

Timelines for both experiments are shown in Figure 1. All mice underwent multiparametric MRI at baseline (8 weeks of age) and 18 weeks post-diet. 1400W-treated mice and associated control mice also underwent MRI 10 weeks post-diet, prior to treatment initiation. The multiparametric MRI protocol at all time points included: (a) arterial spin labeling (ASL) at rest and with adenosine vasodilation to quantify myocardial blood flow and MPR, (b) dynamic nitroxide-enhanced MRI to assess oxidative stress²⁵⁹, (c) cine displacement encoding with stimulated echoes (DENSE) imaging to measure myocardial strain^{196,200}, and (d) cine imaging covering the entire left ventricle (LV) to measure end-diastolic volume (EDV), end-systolic volume (ESV), ejection fraction (EF), and LV mass (LVM). Body weight was recorded for all animals at the beginning of each imaging study. Glucose tolerance tests (GTTs) were performed at baseline and 18 weeks post-diet. After 20 weeks on diet, subgroups of mice ($n = 5/\text{group}$) were euthanized to assess coronary arteriolar reactivity. Separately, radiotelemetric blood pressure measurements were recorded in parallel groups of mice ($n = 4/\text{group}$) from baseline to 18 weeks post-diet.

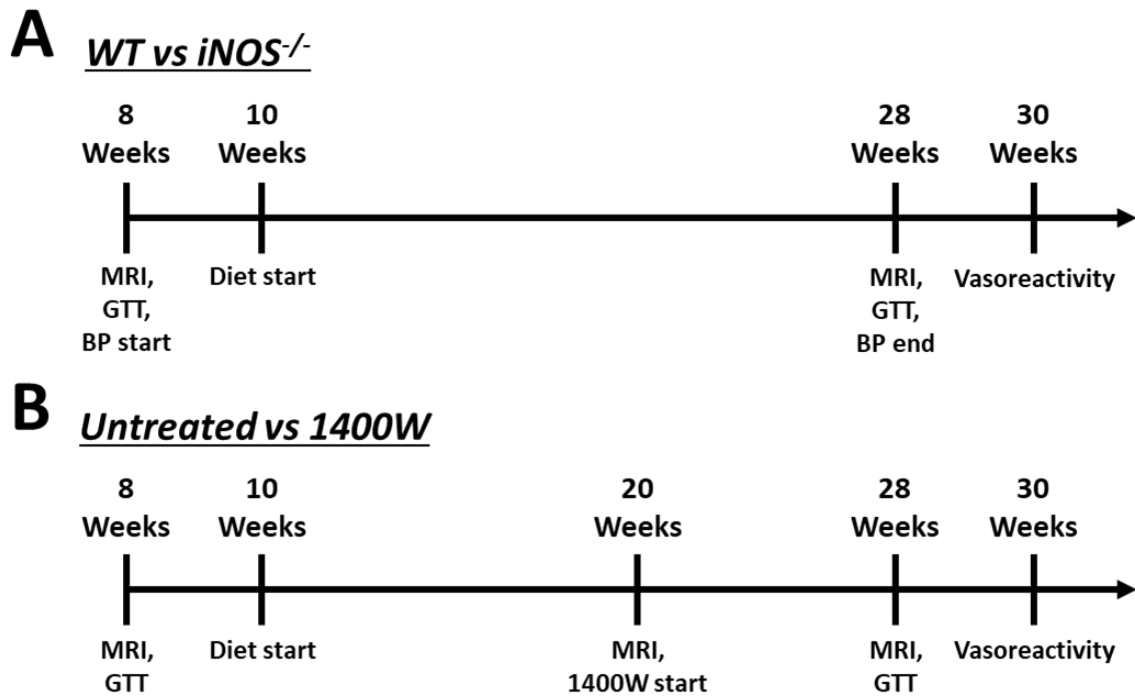


Figure 1. Experimental protocols. (A) Eight-week-old *iNOS*^{-/-} (B6.129P2-*Nos2*^{tm1Lau/J}) and WT (C57Bl/6J) mice underwent cardiac MRI, glucose tolerance testing (GTT), and start of radiotelemetry blood pressure (BP) monitoring two weeks before starting a high-fat high-sucrose diet (HFHSD) or standard chow diet (SD). Eighteen weeks after each diet, at 28 weeks of age, mice again underwent cardiac MRI and GTT, and ended radiotelemetry BP monitoring. Coronary arteriole vasoreactivity measurements were performed at 30 weeks of age. **(B)** Eight-week-old WT (C57Bl/6J) mice underwent cardiac MRI and GTT two weeks before starting a high-fat high-sucrose diet (HFHSD). The mice also underwent cardiac MRI after 10 weeks of HFHSD, and thereafter were randomized to 1400W treatment or no treatment and continued HFHSD for eight weeks. Cardiac MRI and GTTs were repeated after eight weeks of 1400W treatment or no treatment. Coronary arteriole vasoreactivity measurements were performed at 30 weeks of age.

MRI protocol

All MRI studies were performed using a 7T system (Clinscan, Bruker, Ettlingen, Germany) and a 35-mm-diameter birdcage radiofrequency coil. During MRI, an indwelling tail vein catheter was inserted to deliver a nitroxide contrast agent, 3-Carbamoyl-PROXYL (3CP, Sigma–Aldrich, 1.2 mmol/kg), and an intraperitoneal catheter was established to deliver adenosine (Sigma–Aldrich, 300 mg/kg/min). The electrocardiogram, body temperature, and respiration were monitored during imaging (SA Instruments, Stony Brook, NY). Mice were anesthetized with 1.25% isoflurane and maintained at 36 ± 0.5°C using circulating warm water. The full MRI protocol for each mouse was performed over two sessions separated by 2-3 days. Scout imaging was

performed to acquire long-axis and mid-ventricular short-axis localizer images. On day 1, cine DENSE strain imaging was performed on a four-chamber long-axis slice as previously described²⁰. Rest perfusion imaging of a mid-ventricular short-axis slice was then performed using ASL³⁹. Thereafter, adenosine was infused i.p. (300 mg/kg/min, 5 ul/min) and 10 minutes later ASL was repeated. Imaging parameters for ASL included: echo time (TE) = 2.5 ms, repetition time (TR) = 10.0 ms, field of view (FOV) = 38 x 38 mm², matrix size = 128 x 128, flip angle = 7 degrees, slice thickness = 1 mm, saturation band thickness = 10 mm, and number of averages = 9. On day 2, black-blood cine MRI was performed²³⁹. Six - eight short-axis slices were acquired covering the entire LV from base to apex. Imaging parameters included: TR=5.7ms, TE = 2.0ms, temporal resolution = 5.7 ms, FOV = 25.6 x 25.6 mm², matrix size = 128 x 128, flip angle = 15 degrees, slice thickness = 1 mm, and number of averages = 4. Finally, to quantify oxidative stress, dynamic nitroxide-enhanced MRI with the nitroxide contrast agent, 3CP, was performed on a mid-ventricular short-axis slice as previously described²⁵⁹.

Analysis of MR images

All image analysis was performed in MATLAB 2021a (Mathworks, Natick, MA). For perfusion quantification, rest and adenosine stress perfusion images were analyzed using methods previously described³⁹. Myocardial perfusion reserve (MPR) was calculated as stress perfusion / rest perfusion. For dynamic nitroxide-enhanced images, blood and myocardial signal intensities were converted to 3CP concentrations and fit to a 2-compartment exchange and reduction model (2CXRm) to quantify oxidative stress via the nitroxide reduction rate, K_{red} , as previously described²⁵⁹. Strain analysis of DENSE images was performed using the DENSE analysis tool (<https://github.com/dense-analysis>)²⁰⁰. Global longitudinal strain and diastolic strain rate¹⁹⁷ were measured as metrics of systolic and diastolic function, respectively. Cine images were analyzed using the Segment v2.0 R3683 package (<http://segment.heiberg.se>)²⁶⁰. Specifically, the end-diastolic and end-systolic frames were identified and thereafter the endocardial and epicardial contours were manually drawn on these frames for all the slices. Using the software, EDV, ESV, EF, and LV mass were calculated.

Glucose tolerance tests

For GTTs, mice (n = 10/group) were injected intraperitoneally with glucose (8 g/kg) in deionized water after overnight fasting for 15–16 hours. Tail vein blood samples were taken before injection of glucose to measure the fasting blood glucose and at 10, 30, 60, 90, and 120 minutes after injection of the glucose solution. The area under the curve (AUC) was calculated using the trapezoidal rule to evaluate glucose tolerance⁶².

Radiotelemetric blood pressure measurements

Eight-week-old mice (n = 4/group) were anesthetized with isoflurane (1.5%) and radiotelemetry catheters (TA11PA-C10, Data Sciences International, St. Paul, MN) were implanted in their left carotid arteries. Each catheter was tunneled through to the radiotransmitter, which was placed in a subcutaneous pouch along the flank. Before arterial pressure measurements were initiated, mice were allowed to recover for seven

days after surgery to regain normal circadian rhythms. Continuous blood pressure measurements were acquired on a radiotelemetry receiver and analyzed using Dataquest A.R.T. 20 software (Data Sciences International, St. Paul, MN), as described previously^{261,262}. Baseline systolic, diastolic, and mean arterial pressures (MAP) were recorded continuously (at 1-min intervals) over 96 hours following the recovery period. The values over four days (6 AM to 6 PM) and four nights (6 PM to 6 AM) were averaged to obtain the baseline pressures. Afterward, mice were placed either on a SD or HFHSD and the same blood pressure protocol was performed every two weeks for 18 weeks.

Vascular reactivity

After 20 weeks on diet, a subgroup of each group of mice (n = 5/group) were euthanized and coronary arterioles from the second arborized branches off the left coronary artery were isolated. The arterioles were freed of the surrounding cardiac myocytes and were placed in an arteriography system (Danish MyoTechnology, DMT, Ann Harbor, MI), where they were cannulated at both ends and pressurized to 40 mmHg as previously described^{263–265}. Cumulative dose-responses to adenosine and sodium nitroprusside (SNP), a VSMC-specific vasodilator, were measured as previously described^{263–265}. Measurements are reported as a percent dilation of the initial vessel diameter.

Statistics

Statistical analyses were performed using SigmaPlot (Systat Software Inc., Point Richmond, CA). Two-way ANOVAs with post-hoc Tukey's HSD tests for multiple comparisons were used to detect differences in rest perfusion, stress perfusion, MPR, K_{red} , longitudinal strain, diastolic strain rate, body weight, EDV, ESV, EF, LVM, blood glucose levels, GTT-AUC, blood pressure, and vascular reactivity between mouse groups, time points, and diets. A two-tailed t-test was used to detect differences in the vascular reactivities of untreated and 1400W-treated mice.

A.5 Results

WT and iNOS^{-/-} mice develop similar degrees of weight gain and glucose intolerance

Since iNOS expression is induced by certain stressors such as occur in obesity and diabetes and contributes to HFpEF, we hypothesized that the inhibition of iNOS would prevent, and possibly reverse, MPR impairment in a HFHSD mouse model of obesity-induced diabetes. Both iNOS^{-/-} and control (WT) mice were placed on standard chow diet (SD) or a HFHSD for 18 weeks (Figure 1A). All groups of mice had significant weight gain after 18 weeks of SD or HFHSD compared to baseline, and WT and iNOS^{-/-} mice post-HFHSD had a significantly greater weight gain compared to their post-SD counterparts (Figure 2A). The increase in weight for SD mice was consistent with prior data on mouse growth from 10 – 28 weeks of age²⁹⁶. GTT curves for WT (Figure 2B) and iNOS^{-/-} (Figure 2C) mice and GTT-AUC measurements for all groups (Figure 2D) at baseline and post-diet showed that HFHSD WT and HFHSD iNOS^{-/-} mice develop similar degrees of glucose intolerance.

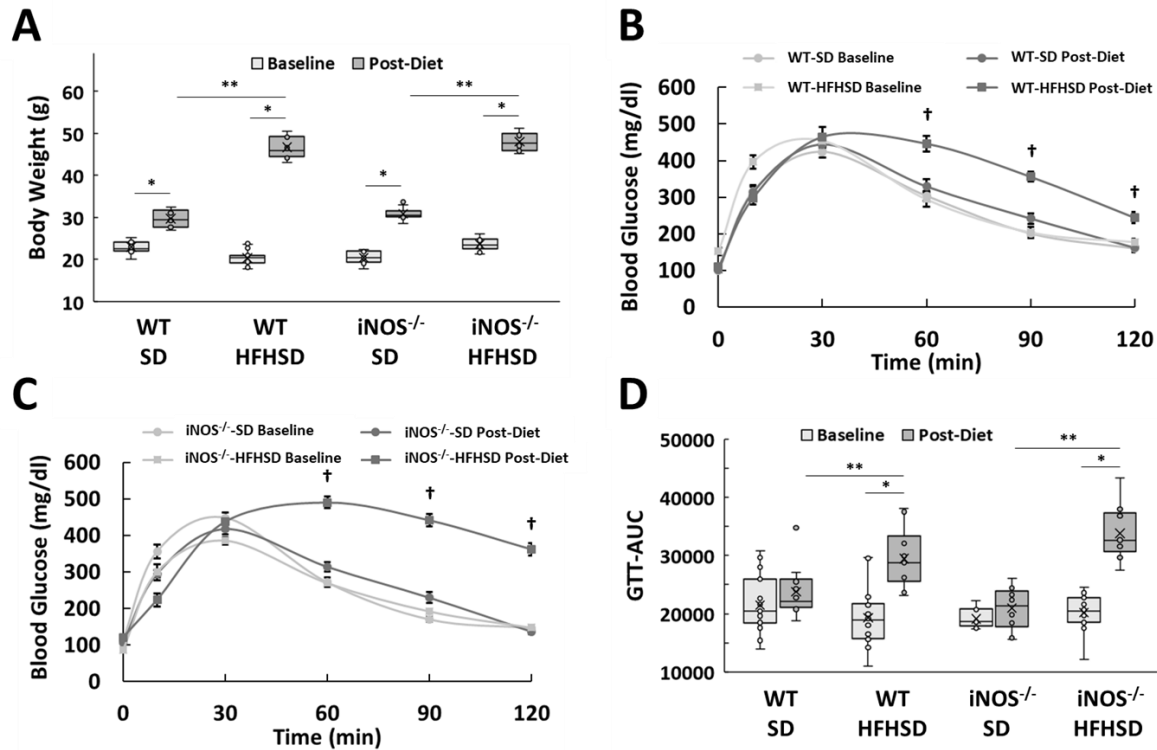


Figure 2. Body weight and Glucose Tolerance Testing. (A) Body weight measurements in grams (g) for wild-type C57Bl/6J (WT) and *iNOS*^{-/-} mice at baseline and 18 weeks post standard chow diet (SD) or high-fat high-sucrose diet (HFHSD). (B,C) Example glucose tolerance curves for WT and *iNOS*^{-/-} mice at baseline and post-SD or post-HFHSD. (D) Glucose tolerance test area-under-curve (GTT-AUC) measurements for WT and *iNOS*^{-/-} mice at baseline and 18 weeks post standard chow diet (SD) or high-fat high-sucrose diet (HFHSD). Box and whisker plots show the interquartile ranges (IQR), values within 1.5*IQR (whiskers), data from individual animals (open circles), and the mean value (X). Data in line graphs are shown as mean ± standard deviation. P-values were calculated by two-way ANOVA with post-hoc Tukey tests for multiple comparisons (n = 12/group). * p < 0.05 for indicated groups, ** p < 0.01 for indicated groups, † p < 0.01 HFHSD Post-Diet vs HFHSD Baseline & SD Post-Diet.

HFHSD induced impaired adenosine myocardial perfusion reserve by MRI and the impairment is prevented in *iNOS*^{-/-} mice

To investigate changes in MPR, we performed rest and adenosine-induced stress ASL myocardial perfusion mapping of the WT and *iNOS*^{-/-} mice at baseline and after a SD or HFHSD. Figure 3A shows example rest and adenosine-stress ASL myocardial perfusion maps obtained from a SD WT mouse. We observed no differences in rest perfusion between WT and *iNOS*^{-/-} mice either at baseline or post-diet (Figure 3B); however, after 18 weeks of HFHSD there was a significant reduction of stress perfusion in WT mice while stress perfusion was fully preserved in *iNOS*^{-/-} mice (Figure 3C). Moreover, MPR was reduced in WT mice post-HFHSD compared to baseline (1.39

± 0.10 vs 2.19 ± 0.16 , $p < 0.01$), while MPR was maintained in $iNOS^{-/-}$ mice post-HFHSD compared to baseline (1.97 ± 0.12 vs 2.07 ± 0.14) (Figure 3D). The findings showed that the genetic ablation of $iNOS$ prevented the development of impaired MPR under conditions of a HFHSD.

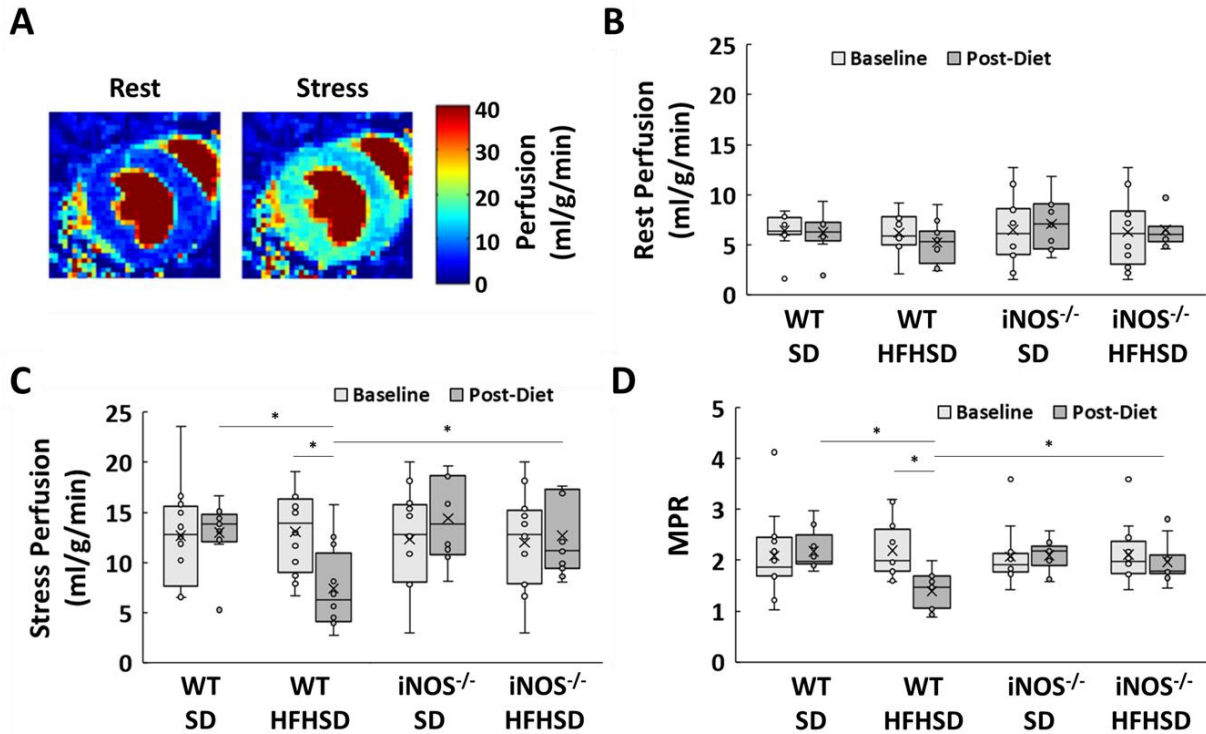


Figure 3. Myocardial Perfusion and Myocardial Perfusion Reserve (MPR). (A) Example arterial spin labeling (ASL) myocardial perfusion maps acquired at rest and during adenosine-induced stress in a mid-ventricular slice of a wild-type (WT) mouse heart at baseline. (B) Rest and (C) stress perfusion measurements in milliliters/gram/minute (ml/g/min) for WT and $iNOS^{-/-}$ mice at baseline and 18-weeks post standard chow diet (SD) or post high-fat, high-sucrose diet (HFHSD). (D) Myocardial perfusion reserve measurements for WT and $iNOS^{-/-}$ mice at baseline and post-SD or post-HFHSD. Box and whisker plots show the interquartile ranges (IQR), values within $1.5 \times IQR$ (whiskers), data from individual animals (open circles), and the mean value (X). P-values were calculated by two-way ANOVA with post-hoc Tukey tests for multiple comparisons ($n = 12/\text{group}$). * $p < 0.05$ for indicated groups, ** $p < 0.01$ for indicated groups.

$iNOS^{-/-}$ mice fed a HFHSD have preserved coronary arteriolar reactivity

Impaired vasoreactivity is a hallmark of impaired perfusion reserve and therefore we investigated coronary arteriolar reactivity in WT and $iNOS^{-/-}$ mice. We performed cumulative dose-response curves of isolated coronary arteriole dilation in response to adenosine from WT and $iNOS^{-/-}$ mice fed either a SD or HFHSD for 20 weeks. Considering SD WT mice as a control group, WT HFHSD mice show a markedly

reduced adenosine response ($p < 0.05$, Figure 4A). In contrast, *iNOS*^{-/-} mice fed HFHSD for 20 weeks have a coronary arteriolar adenosine response that is nearly identical to that of the SD WT group. The other control group, SD *iNOS*^{-/-} mice, demonstrated normal adenosine dilation. Cumulative dose-response curves to SNP, an endothelial-independent VSMC specific vasodilator, indicated that HFHSD *iNOS*^{-/-} mice had less of an impaired response than HFHSD WT mice at the higher SNP concentrations ($p < 0.05$, Figure 4B). The *ex vivo* results of adenosine coronary arteriole vasoreactivity reinforced the *in vivo* MRI data and supported the result that genetic ablation of *iNOS* prevented coronary arteriole impairment under conditions of a HFHSD.

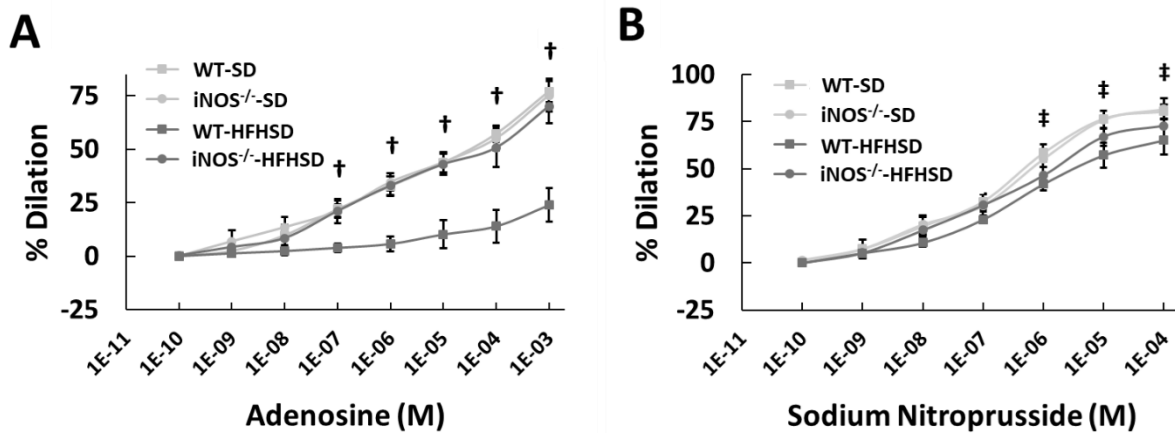


Figure 4. Coronary arteriole vasoreactivity. After 20 weeks on a standard chow diet (SD) or high-fat, high-sucrose diet (HFHSD), subgroups of wild-type (WT) and *iNOS*^{-/-} mice ($n = 5/\text{group}$) were euthanized and coronary arterioles from the second arborized branches off the left coronary artery were isolated. The arterioles were freed of the surrounding cardiac myocytes and were placed in an arteriography system (Danish MyoTechnology, DMT, Ann Harbor, MI), cannulated at both ends and pressurized to 40 mmHg. Cumulative arteriolar dose-response curves to **(A)** adenosine and **(B)** sodium nitroprusside are shown for WT and *iNOS*^{-/-} mice at 20 weeks post-SD and post-HFHSD. Vasodilator concentrations are reported in moles/liter (M). Measurements are reported as a percent dilation of the initial vessel diameter and shown as mean \pm standard deviation. P-values were calculated by two-way ANOVA with post-hoc Tukey tests for multiple comparisons. † $p < 0.01$ WT-HFHSD vs WT-SD & *iNOS*^{-/-}-HFHSD, ‡ $p < 0.01$ WT-HFHSD vs WT-SD & $p < 0.05$ WT-HFHSD vs *iNOS*^{-/-}-HFHSD.

***iNOS*^{-/-} mice on a HFHSD have reduced oxidative stress by nitroxide-enhanced MRI**

Oxidative stress and dysregulated nitric oxide signaling are major drivers of cardiac pathophysiology and have been implicated in the untoward sequelae of diet-induced obesity. To examine the extent of oxidative stress induced in the model, myocardial dynamic nitroxide-enhanced saturation-recovery gradient-echo imaging was

performed (Figure 5). The initial myocardial signal enhancement caused by injection of 3CP decays over time because 3CP reacts with reactive oxygen species. The rate of decay provides a measurement to quantify tissue reactive oxygen species. As shown in the example in Figure 5, manually-demarcated contours of the blood pool and myocardial tissue (Figure 5B) are used to measure [3CP] data for the blood pool (C_V) and myocardial tissue (C_T), and the 2CXRM provides good fits for control mice at baseline and post-diet (Figure 5C). K_{red} , the nitroxide reduction rate in the 2CXRM, at 18 weeks post-HFHSD was elevated compared to baseline in both WT (0.0318 ± 0.0065 vs 0.0014 ± 0.0010 [3CP]/min, $p < 0.01$) and $iNOS^{-/-}$ mice (0.0084 ± 0.0023 vs 0.0006 ± 0.0007 [3CP]/min, $p < 0.01$, $p = 0.02$), however, K_{red} was significantly reduced post-HFHSD in $iNOS^{-/-}$ mice compared to WT mice ($p = 0.02$) (Figure 5D).

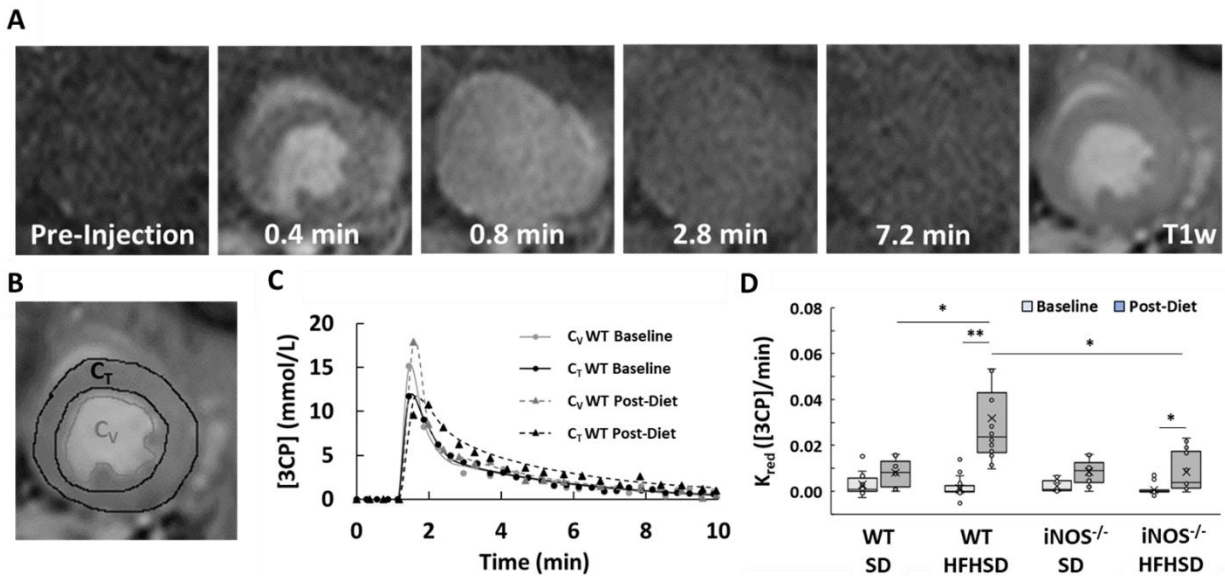


Figure 5. Nitroxide enhanced MRI of cardiovascular oxidative stress. To quantify oxidative stress, dynamic nitroxide-enhanced MRI with the nitroxide contrast agent, 3-carbamoyl-PROXYL (3CP), was performed on a mid-ventricular, short-axis slice. **(A)** Example dynamic nitroxide-enhanced MR images before and after injection of 3CP demonstrate signal enhancement kinetics in a wild-type (WT) mouse at baseline. Also shown is a T1-weighted image (T1w) used to visualize myocardial borders. **(B)** Example contours of the LV blood pool and myocardium used to estimate vascular and tissue 3CP concentrations, C_V and C_T , respectively. **(C)** Example $C_V(t)$ fit and two-compartment exchange and reduction model (2CXRM) fitting of $C_T(t)$ of a WT mouse at baseline and 18 weeks post-HFHSD. **(D)** The 3CP reduction rate, K_{red} , a 2CXRM metric of oxidative stress, in WT and $iNOS^{-/-}$ mice at baseline and post standard chow diet (SD) or post high-fat, high-sucrose diet (HFHSD). Box and whisker plots show the interquartile ranges (IQR), values within 1.5*IQR (whiskers), data from individual animals (open circles), and the mean value (X). P-values were calculated by two-way ANOVA with post-hoc Tukey tests for multiple comparisons ($n = 12$ /group). * $p < 0.05$ for indicated groups, ** $p < 0.01$ for indicated groups.

Deletion of iNOS ameliorates HFHSD-induced changes in systolic and diastolic strain

During the course of diet administration, LV mass increased similarly in all groups of mice post-diet by approximately 25%, corresponding proportionally to the approximately 25% increase in body weight that occurred as SD mice increase in age from 10 to 28 weeks (Table 1). No differences in LV mass related to diet or knockout of iNOS were observed. LV EDV and ESV similarly increased proportionally with age and growth in all groups of mice. While LV ESV was elevated in all groups post-diet, there was a further increase in LV ESV in WT and iNOS^{-/-} mice fed a HFHSD compared to SD ($p < 0.05$). Additionally, HFHSD WT and HFHSD iNOS^{-/-} mice had reduced EFs compared to SD mice ($p < 0.05$). Specifically, HFHSD WT and iNOS^{-/-} mice had EF values of approximately 60%, representing a mild degree of LV systolic dysfunction as compared to reference EF values of approximately 68%.

	Mass	EDV	ESV	EF
WT-SD Baseline	73 ± 5	37 ± 4	12 ± 2	68 ± 5
WT-SD Post-Diet	93 ± 8 *	48 ± 6 *	16 ± 4 *	69 ± 5
WT-HFHSD Baseline	77 ± 6	36 ± 6	11 ± 3	69 ± 7
WT-HFHSD Post-Diet	96 ± 6 *	49 ± 8 *	20 ± 4 *†	60 ± 3 *†
iNOS^{-/-}-SD Baseline	73 ± 14	39 ± 9	12 ± 5	67 ± 6
iNOS^{-/-}-SD Post-Diet	98 ± 6 *	51 ± 9 *	15 ± 3 *	70 ± 4
iNOS^{-/-}-HFHSD Baseline	70 ± 7	36 ± 5	11 ± 2	70 ± 3
iNOS^{-/-}-HFHSD Post-Diet	91 ± 9 *	48 ± 9 *	19 ± 5 *‡	61 ± 7 *‡

Table 1. Left ventricular structure and function. WT denotes wild-type mice; iNOS^{-/-} inducible nitric oxide synthase knockout mice; SD standard diet; HFHSD high-fat, high-sucrose diet; EDV end-diastolic volume; ESV end-systolic volume; EF ejection fraction. P-values were calculated by two-way ANOVA with post-hoc Tukey tests for multiple comparisons ($n = 12$ /group). * $p < 0.05$ same group Baseline, † $p < 0.05$ WT-SD Post-Diet, ‡ $p < 0.05$ iNOS^{-/-}-SD Post-Diet.

Next, we evaluated end-systolic longitudinal strain from DENSE MRI. An example strain map of a WT mouse at baseline and after 18 weeks of HFHSD is shown in Figure 6A. The end-systolic longitudinal strain was impaired post-HFHSD in both WT (-0.114 ± 0.004 vs -0.150 ± 0.005 , $p < 0.01$) and iNOS^{-/-} mice (-0.132 ± 0.006 vs $-0.154 \pm$

0.003, $p=0.02$); however, the longitudinal strain impairment was lower in $iNOS^{-/-}$ mice vs WT mice post-HFHSD ($p=0.03$) (Figure 6B).

In addition to impaired systolic strain, the diastolic strain rate was reduced in WT mice after 18 weeks of HFHSD (1.19 ± 0.10 vs 1.82 ± 0.09 s^{-1} , $p<0.01$) but it was preserved in $iNOS^{-/-}$ mice post-HFHSD compared to baseline (1.44 ± 0.06 vs 1.58 ± 0.15 s^{-1}) (Figure 6C). When comparing diastolic strain rate between HFHSD $iNOS^{-/-}$ and WT mice, there was a trend toward a higher value in $iNOS^{-/-}$ mice ($p=0.09$). Collectively, strain MRI indicated that the deletion of $iNOS$ mitigates HFHS-induced changes in systolic strain and diastolic strain rate.

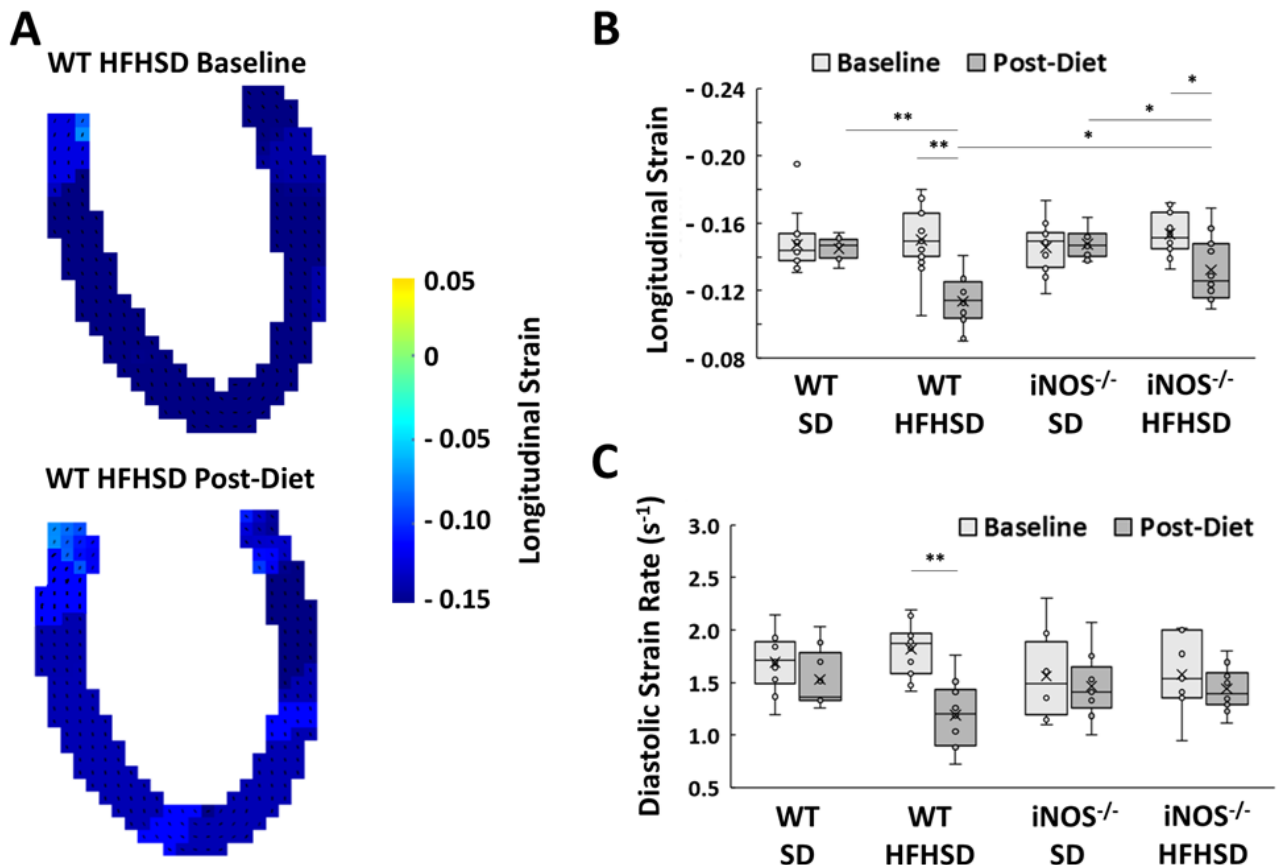


Figure 6. Systolic strain and diastolic strain rate. (A) Example DENSE long-axis longitudinal strain maps in a wild-type (WT) mouse at baseline and 18 weeks post- high-fat, high-sucrose diet (HFHSD) showing an impairment in contractile function. **(B)** Longitudinal strain measurements in WT and $iNOS^{-/-}$ mice at baseline and post-standard chow diet (SD) or post-HFHSD. **(C)** Diastolic strain rate measurements (s^{-1}) in WT and $iNOS^{-/-}$ mice at baseline and post-SD or post-HFHSD. Box and whisker plots show the interquartile ranges (IQR), values within $1.5 \times IQR$ (whiskers), data from individual animals (open circles), and the mean value (X). P-values were calculated by two-way ANOVA with post-hoc Tukey tests for multiple comparisons ($n = 12/\text{group}$). * $p < 0.05$ for indicated groups, ** $p < 0.01$ for indicated groups.

HFHSD induced similar blood pressure increases in *iNOS*^{-/-} and WT mice

Blood pressure results are summarized in Table 2. No differences were found between WT and *iNOS*^{-/-} mice, or between pre- and post-diet for SD mice. However, for HFHSD WT and *iNOS*^{-/-} mice, significantly higher diastolic and MAP pressures were observed after 18 weeks of diet compared to baseline and SD ($p < 0.05$).

	Systolic	Diastolic	MAP
SD-WT Baseline	129 ± 2	97 ± 1	113 ± 1
SD-WT Post-Diet	126 ± 2	98 ± 5	112 ± 3
HFHSD-WT Baseline	127 ± 4	93 ± 2	111 ± 3
HFHSD-WT Post-Diet	133 ± 5	106 ± 6 †	120 ± 1 †
SD-<i>iNOS</i>^{-/-} Baseline	128 ± 1	95 ± 2	111 ± 1
SD-<i>iNOS</i>^{-/-} Post-Diet	125 ± 2	90 ± 4	107 ± 2
HFHSD-<i>iNOS</i>^{-/-} Baseline	125 ± 3	91 ± 2	109 ± 3
HFHSD-<i>iNOS</i>^{-/-} Post-Diet	131 ± 4	114 ± 5 ‡	122 ± 4 ‡

Table 2. Radiotelemetric blood pressure. WT denotes wild-type mice; *iNOS*^{-/-} inducible nitric oxide synthase knockout mice; SD standard diet; HFHSD high-fat high-sucrose diet; MAP mean arterial pressure. P-values were calculated by two-way ANOVA with post-hoc Tukey tests for multiple comparisons ($n = 4/\text{group}$). † $p < 0.05$ vs SD-WT Post-Diet & HFHSD-WT Baseline, ‡ $p < 0.05$ vs SD-*iNOS*^{-/-} Post-Diet & HFHSD-*iNOS*^{-/-} Baseline.

The pharmacological inhibition of *iNOS* largely reverses HFHSD-induced impairments in MPR, cardiac function and coronary arteriolar reactivity

Since the genetic ablation of *iNOS* prevented impaired MPR in mice fed a HFHSD, we next investigated if impaired MPR could be reversed with 1400W, a highly selective *in vivo* inhibitor of *iNOS*. C57Bl/6J mice were fed a HFHSD for 10 weeks to establish impaired MPR and then treated with 1400W for 8 weeks while remaining on HFHSD (Figure 1B). The control group remained on the same duration of HFHSD without 1400W treatment. Both untreated and 1400W-treated mice had similar levels of weight gain 10 and 18 weeks after HFHSD (Figure 7A) and both developed similar levels of glucose intolerance (Figure 6B). After 18 weeks of HFHSD, MPR was higher in 1400W-treated compared to untreated mice (1.70 ± 0.07 vs 1.39 ± 0.10 , $p=0.03$) and MPR after 8 weeks of *iNOS* inhibition (and 18 weeks of HFHSD) was greater than MPR prior to the initiation of *iNOS* inhibition (after 10 weeks of HFHSD) (1.70 ± 0.07 vs 1.49 ± 0.10 , $p=0.04$), demonstrating partial recovery of coronary microvascular function (Figure

7C). Of note, MPR was still lower than baseline after 8 weeks of iNOS inhibition (1.70 ± 0.07 vs 2.12 ± 0.17 , $p=0.04$). Oxidative stress was greatly reduced in 1400W-treated mice compared to untreated mice at 18 weeks post-HFHSD (0.0004 ± 0.0022 vs 0.0318 ± 0.0065 [3CP]/min, $p<0.01$) and compared to 10 weeks post-HFHSD (0.0004 ± 0.0022 vs 0.0250 ± 0.0072 [3CP]/min, $p=0.01$) (Figure 7D). EF decreased between weeks 10 and 18 in untreated mice fed HFHSD, and treatment with 1400W prevented such a decrease (Table 3). Similarly, longitudinal strain analyses showed worsening systolic function between weeks 10 and 18 in untreated mice fed HFHSD, and treatment with 1400W prevented the deterioration in systolic strain between weeks 10 and 18, such that 1400W-treated mice have greater longitudinal shortening at week 18 than untreated mice (-0.130 ± 0.006 vs -0.114 ± 0.004 , $p=0.02$). However, longitudinal strain at week 18 was still impaired in 1400W-treated mice compared to baseline (-0.130 ± 0.006 vs -0.150 ± 0.005 , $p=0.01$) (Figure 7E). Similarly, the diastolic strain rate trended towards reduction at week 10 and was significantly reduced 18 weeks post-HFHSD in untreated mice ($p=0.03$), while treatment with 1400W prevented diastolic strain rate deterioration between weeks 10 and 18; however, there was not a significant difference in diastolic strain rate between untreated and 1400W-treated mice at week 18 post-HFHSD ($p=0.21$) (Figure 7F).

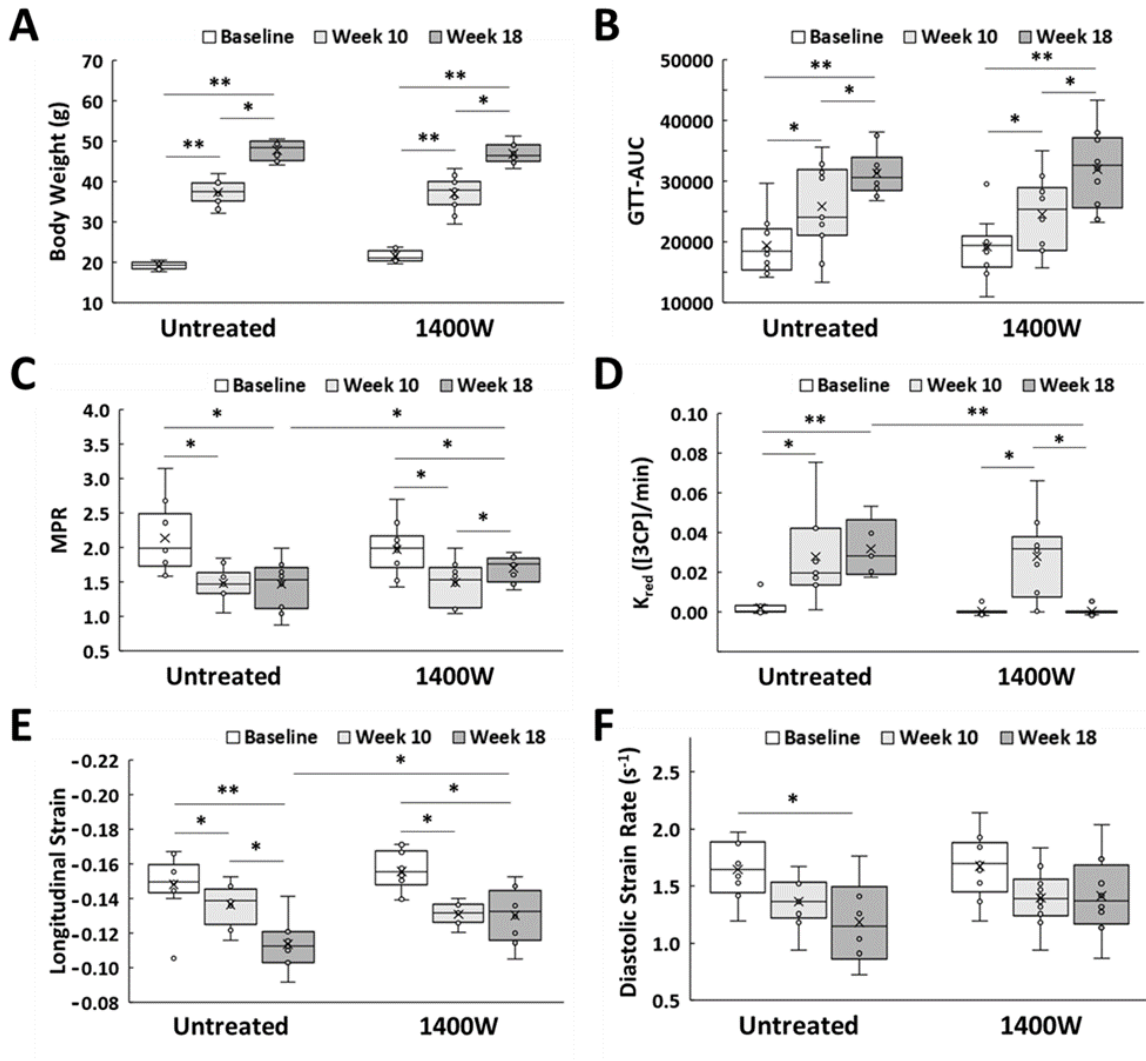


Figure 7. Untreated vs 1400W-treated mice. (A) Body weight, **(B)** glucose tolerance test area-under-curve (GTT-AUC), **(C)** myocardial perfusion reserve, **(D)** oxidative stress as measured by K_{red} , **(E)** longitudinal strain, and **(F)** diastolic strain rate measurements in untreated and 1400W-treated wild-type mice at baseline, 10-weeks post- high-fat, high-sucrose diet (HFHSD), and 18-weeks post-HFHSD. Box and whisker plots show the interquartile ranges (IQR), values within 1.5*IQR (whiskers), data from individual animals (open circles), and the mean value (X). P-values were calculated by two-way ANOVA with post-hoc Tukey tests for multiple comparisons ($n = 10/\text{group}$). * $p < 0.05$ for indicated groups, ** $p < 0.01$ for indicated groups.

Similar to the MPR results, the cumulative dose-response curves of coronary arteriolar reactivity demonstrated partial recovery of the adenosine response in 1400W-treated mice compared to untreated mice ($p < 0.01$) (Figure 8A). 1400W treatment also resulted in a significant recovery in SNP-induced vasodilation ($p < 0.01$ vs untreated) (Figure 8B).

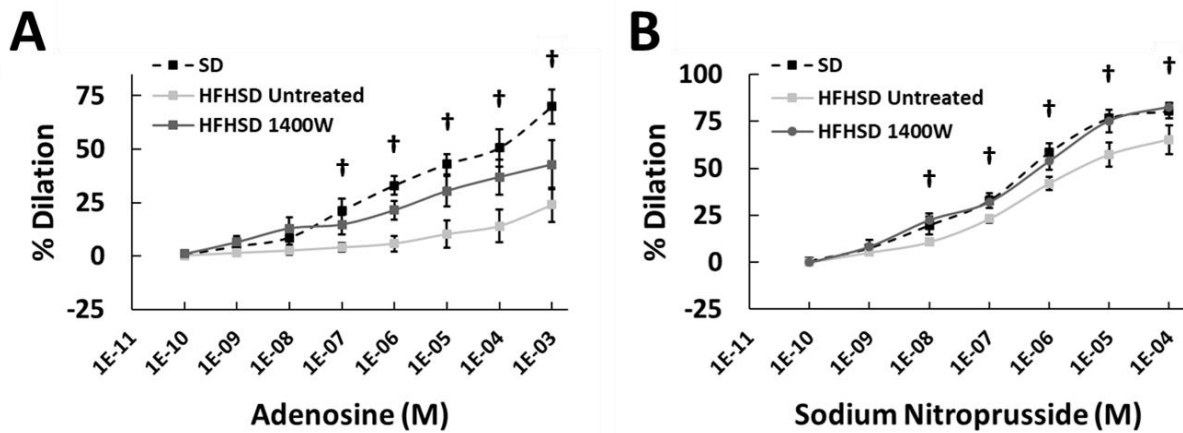


Figure 8. Coronary arteriole vasoreactivity in untreated vs 1400W-treated mice. Cumulative arteriolar dose-response curves to (A) adenosine and (B) sodium nitroprusside are shown for untreated and 1400W-treated wild-type (WT) mice at 20 weeks post- high-fat, high-sucrose diet (HFHSD). Results from age-matched WT mice fed a standard chow diet (SD) are also shown for reference. Vasodilator concentrations are reported in moles/liter (M). Measurements are reported as a percent dilation of the initial vessel diameter and shown as mean \pm standard deviation. P-values were calculated by two-tailed t-tests ($n = 5/\text{group}$). † $p < 0.01$ Untreated vs 1400W.

A.6 Discussion and Conclusions

Oxidative/nitrosative stress is a major contributor to CMD related to obesity, diabetes, and hypertension^{27,297}, and our results indicate that iNOS is critical to obesity-induced impaired MPR. Specifically, we identified that iNOS deletion provided essentially complete preservation of the coronary arteriolar and myocardial perfusion responses to adenosine that are otherwise impaired due to a HFHSD and the associated obesity, glucose intolerance, metabolic inflammation, and oxidative stress. Moreover, iNOS inhibition by 1400W treatment after establishment of impaired MPR can partially reverse CMD due to HFHSD. In addition to complete preservation of the vascular/perfusion adenosine response, longitudinal strain was also higher in iNOS^{-/-} vs. WT mice fed HFHSD, consistent with a protective effect of iNOS deletion on myocardial function. The inhibition of iNOS by 1400W beginning after 10 weeks of HFHSD prevented the decrease in EF that occurred in untreated HFHSD mice between weeks 10-18 (see Table 3).

The *in vivo* MRI data from rest and adenosine ASL were supported by *ex vivo* experiments measuring adenosine reactivity of isolated coronary arterioles. The correspondence between adenosine stress perfusion imaging in mice and adenosine reactivity data of isolated coronary arterioles is important because stress perfusion imaging in mice recapitulates clinical adenosine stress perfusion imaging, which is used to assess CMD in human patients, the relationships between CMD and adverse events, and the relationships between CMD and HFpEF.

Our findings that iNOS is a critical regulator of CMD are consistent with those of Schiattarella et al., who showed a central role of iNOS and nitrosative stress in a mouse model of HFpEF⁶⁷. In the present study we used noninvasive nitroxide-enhanced MRI of the heart to quantify oxidative/nitrosative stress. Although nitroxide-enhanced MRI is not widely used, the method derives from well-established electron spin resonance (ESR) methods^{95,298} and both the ESR and MRI methods are well validated^{97,99,259}. Noninvasive nitroxide-enhanced MRI of the heart has the advantages that it can be used for serially investigating groups of mice over the course of a treatment and interrogating the oxidative/nitrosative stress under *in vivo* physiological conditions. Additionally, the assessment of oxidative/nitrosative stress is quantitative when using a tracer kinetic model. We quantified oxidative/nitrosative stress at baseline, after 10 weeks of diet, and after 8 weeks of continued diet and iNOS inhibition, making use of the ability to measure changes in oxidative/nitrosative stress on mice over time and due to treatment.

CMD is estimated to be present in approximately 75% of human HFpEF¹⁰, and the present study of iNOS and oxidative/nitrosative stress in the adenosine coronary arteriolar and myocardial perfusion responses (i.e., CMD) is supportive of the work of Schiattarella et al. who discovered the central role of iNOS and oxidative/nitrosative stress in HFpEF⁶⁷. The mouse model described by Schiattarella et al. used 15 weeks of HFD and chronic administration of L-NAME while our model utilized 18 weeks of HFHSD. Both models produced obesity, glucose intolerance, metabolic inflammation, oxidative/nitrosative stress, diastolic dysfunction, and impaired systolic longitudinal strain. We detected a mild decrease in LV EF by MRI in the HFHSD model; however,

the EF did not decrease as measured by echocardiography in the HFD + L-NAME model. The difference is likely related to the imaging methods. Both models led to increased blood pressure; however, we used radiotelemetry while Schiattarella et al. used the tail cuff method, therefore a comparison of blood pressure values measured between studies is difficult. Finally, Schiattarella et al. used ultrasound to measure coronary flow reserve (CFR) with isoflurane as the vasodilator and showed impaired CFR in the HFD + L-NAME model; however they did not use adenosine which is typically used in clinical practice to investigate impaired CFR²⁹⁹ and central to the diagnosis of CMD, and they did not assess CFR in HFD + L-NAME iNOS^{-/-} mice. Both models, HFD + L-NAME and HFHSD, are relevant to investigation of CMD and HFpEF, and the clinical implication of our study is the same as that of Schiattarella et al., which is that therapies that reduce iNOS activation should be pursued as potential treatments for CMD and HFpEF.

From a microvascular reactivity perspective, our work is in alignment with Daneva et al. that demonstrates a central role for iNOS in systemic resistance arteries during obesity³⁰⁰. As reported in third order mesenteric arteries on a prolonged high fat diet, the coronary arteries from our mice on the HFHSD lacking iNOS genetically or having iNOS inhibited with 1400W demonstrated a resiliency to vasodilation. The exact cell type responsible for the change in vasodilatory functions was not identified, however, previous work from Sato et al. points to a role for smooth muscle cells after adenosine-mediated dilation with SNP-mediated dilations tending to support this conclusion³⁰¹. It is also possible that other cell types with significant iNOS, such as macrophages, may be involved.

Notably, our data show that CMD due to obesity and diabetes is partially reversible. Previously, two clinical studies showed improved adenosine PET CFR using mineralocorticoid receptor antagonists^{46,47}. To our knowledge, the present study is the first report of reversal of CMD as assessed by adenosine MPR in an animal model. Adenosine reactivity of isolated coronary arterioles confirmed the *in vivo* MRI finding of reversal of CMD with iNOS inhibition. Along with the reversal of CMD in 1400W-treated mice, better LV systolic function was also measured at 18 weeks post-HFHSD in the treated vs. untreated mice, and strain-rate imaging showed a trend toward better diastolic function.

In conclusion, adenosine stress myocardial perfusion imaging, nitroxide-enhanced MRI, cine imaging, and strain MRI along with other methods applied in a HFHSD mouse model show a central role of iNOS and oxidative/nitrosative stress in CMD related to obesity, diabetes, and metabolic inflammation. These results are consistent with similar recent findings regarding a central role of iNOS and oxidative/nitrosative stress in a HFpEF mouse model. Due to the prognostic importance of CMD and its causative role in HFpEF, therapies aimed at reducing iNOS activation warrant further investigation.

Appendix B – Molecular Mechanisms of Adenosine Stress T1 Mapping

Note: The content in Chapter 2 has formally been published in *Circulation: Cardiovascular Imaging*

Shah SA, Reagan CE, French BA, Epstein FH. Molecular mechanisms of adenosine stress T1 mapping. Circulation: Cardiovascular Imaging. 2021 Mar;14(3):e011774.

B.1 Abstract

Background: Adenosine stress T1 mapping is an emerging MRI method to investigate coronary vascular function and myocardial ischemia without application of a contrast agent. Using gene-modified mice and two vasodilators, we elucidated and compared the mechanisms of adenosine myocardial perfusion imaging and adenosine T1 mapping.

Methods: Wild-type (WT), adenosine A_{2A} ($A_{2A}AR^{-/-}$), A_{2B} ($A_{2B}AR^{-/-}$), and A_3 receptor knockout ($A_3AR^{-/-}$), and endothelial nitric oxide synthase receptor knockout ($eNOS^{-/-}$) mice underwent rest and stress perfusion MRI (n=8) and T1 mapping (n=10) using either adenosine, regadenoson (a selective $A_{2A}AR$ agonist), or saline. Myocardial blood flow and T1 were computed from perfusion imaging and T1 mapping, respectively, at rest and stress to assess myocardial perfusion reserve (MPR) and T1 reactivity ($\Delta T1$). Changes in heart rate (ΔHR) for each stress agent were also calculated. Two-way ANOVA was used to detect differences in each parameter between the different groups of mice.

Results: MPR was significantly reduced only in $A_{2A}AR^{-/-}$ compared to WT mice using adenosine (1.06 ± 0.16 vs 2.03 ± 0.52 , $p < 0.05$) and regadenoson (0.98 ± 0.26 vs 2.13 ± 0.75 , $p < 0.05$). In contrast, adenosine $\Delta T1$ was reduced compared to WT mice (3.88 ± 1.58) in both $A_{2A}AR^{-/-}$ (1.63 ± 1.32 , $p < 0.05$) and $A_{2B}AR^{-/-}$ (1.55 ± 1.35 , $p < 0.05$). Furthermore, adenosine $\Delta T1$ was halved in $eNOS^{-/-}$ (1.76 ± 1.46 , $p < 0.05$) vs WT mice. Regadenoson $\Delta T1$ was approximately half of adenosine $\Delta T1$ in WT mice (1.97 ± 1.50 , $p < 0.05$), and additionally, it was significantly reduced in $eNOS^{-/-}$ mice (-0.22 ± 1.46 , $p < 0.05$). Lastly, ΔHR was two times greater using regadenoson vs. adenosine in all groups except $A_{2A}AR^{-/-}$, where heart rate remained constant.

Conclusions: The major findings are that: (a) while adenosine MPR is mediated through the A_{2A} receptor, adenosine $\Delta T1$ is mediated through the A_{2A} and A_{2B} receptors, (b) adenosine MPR is endothelial-independent while adenosine $\Delta T1$ is partially endothelial-dependent, and (c) $\Delta T1$ mediated through the A_{2A} receptor is endothelial-dependent while $\Delta T1$ mediated through the A_{2B} receptor is endothelial-independent.

B.2 Clinical Perspective

The results of the present study show that there are differences in the adenosine receptor subtypes that mediate adenosine myocardial perfusion imaging and adenosine T1 reactivity imaging. Adenosine myocardial perfusion is mediated solely through the A_{2A} adenosine receptor (AR), while adenosine T1 reactivity is mediated through both the A_{2A} AR and the A_{2B} AR. Furthermore, while adenosine increases myocardial perfusion through eNOS-independent mechanisms, adenosine increases myocardial blood volume and T1 reactivity partly through eNOS-dependent mechanisms. Due to these differences, while adenosine myocardial perfusion imaging and adenosine T1 reactivity imaging may both be used clinically for ischemia detection, they are not equivalent and should not be considered interchangeable in their clinical interpretation. The two techniques have fundamental differences in their underlying molecular mechanisms, and their clinical applications and the resulting clinical interpretation and performance may reflect these different underlying mechanisms.

B.3 Introduction

Adenosine stress T1 mapping is an emerging MRI method to interrogate coronary vascular function and myocardial ischemia without the use of contrast agents³⁰². In this method, adenosine-induced coronary vasodilation leads to an increase in myocardial blood volume (MBV), and since the T1 of blood is greater than the T1 of myocardium, the increase in MBV is reflected as an increase in the aggregate T1 of heart tissue, an effect referred to as adenosine T1 reactivity. Initial clinical evaluations have detected reduced adenosine T1 reactivity in patients with coronary microvascular disease due to type 2 diabetes³⁰³ and in ischemic regions in patients with coronary artery disease (CAD)³⁰⁴. A study in dogs with acute coronary stenoses suggested that MBV may better differentiate between moderate and severe coronary stenoses than myocardial blood flow (MBF)³⁰⁵, and that it may be a more comprehensive global marker of ischemia as it represents the total blood volume of the coronary macro- and microcirculation^{305–307}. Also, adenosine T1 reactivity imaging may be particularly useful in patients with contraindications to gadolinium unable to undergo adenosine contrast-enhanced myocardial perfusion imaging, such as those with end stage renal disease³⁰⁸. While data suggest the potential clinical utility of adenosine T1 reactivity imaging, the molecular mechanisms underlying adenosine T1 reactivity have yet to be carefully elucidated, potentially limiting the ability to fully understand and interpret adenosine T1 reactivity findings.

Adenosine mediates vascular dilation, increased MBF, and increased MBV through interactions with cell surface receptors on coronary vascular smooth muscle cells (VSMCs) and endothelial cells (ECs). There are four adenosine receptor (AR) subtypes, namely A₁, A_{2A}, A_{2B}, and A₃, and all four are expressed in the coronary vasculature. The A_{2A}AR is expressed on VSMCs and ECs and is the subtype that predominantly controls MBF by relaxing arteriolar vascular smooth muscle, leading to decreased coronary resistance³⁰⁹. With these properties, the A_{2A}AR would be expected to play an important role in mediating MBV and adenosine T1 reactivity. The A_{2B}AR is also present on coronary VSMCs and ECs, and studies have shown its role in mediating MBF³¹⁰, albeit with a much smaller effect than that of the A_{2A}AR, suggesting the possibility of a role for the A_{2B}AR in MBV and T1 reactivity. The A₃AR and A₁AR are also present on coronary VSMCs, and both have been shown, to a relatively small degree, to negatively modulate coronary vasodilation mediated by activation of other adenosine receptor subtypes^{311,312}, suggesting the potential for modest opposing effects on MBV and T1 reactivity. Finally, whether the vasodilatory effects of adenosine on MBF and MBV are endothelial-dependent or endothelial-independent remains incompletely understood, and elucidating these mechanisms would be important to the clinical interpretation of adenosine myocardial perfusion and T1-reactivity imaging studies.

Using gene-modified mice, adenosine or the selective A_{2A}AR agonist, regadenoson, and small-animal MRI for quantitative myocardial perfusion imaging and myocardial T1 mapping, we investigated the roles of the A_{2A}AR, the A_{2B}AR, and the A₃AR in both adenosine myocardial perfusion imaging and myocardial T1 reactivity. We also utilized endothelial nitric oxide synthase (eNOS) knockout mice to investigate

whether adenosine myocardial perfusion and myocardial T1 reactivity are endothelial-dependent or -independent.

B.4 Methods

Experimental Design

We first sought to determine the contributions of the A_{2A}, A_{2B}, and A₃ ARs to the increases in myocardial perfusion and T1 after vasodilation using adenosine or regadenoson. For these studies, we performed myocardial perfusion MRI (n=8 per group) and T1 mapping (n=10 per group) before and 10 minutes after injection of vasodilator in 8-12-week-old male wild-type (WT), A_{2A}AR knockout (A_{2A}AR^{-/-}), A_{2B}AR knockout (A_{2B}AR^{-/-}), and A₃AR receptor knockout (A₃AR^{-/-}) mice, all on a C57Bl/6 background.

Next, we examined whether the changes in myocardial perfusion and T1 during vasodilation are attributable to endothelial-independent or dependent pathways. For these studies, we performed the same MRI protocol as above in 8-12-week-old male eNOS knockout (eNOS^{-/-}) mice to evaluate MBF and T1 reactivity.

Animal Handling

All animal studies were performed in accordance with protocols that conformed to the Declaration of Helsinki as well as the Guide for Care and Use of Laboratory Animals (NIH publication no. 85-23, revised 1996) and that were approved by the Animal Care and Use Committee at the University of Virginia. WT mice, A_{2A}AR^{-/-} mice (stock no. 010685), and eNOS^{-/-} mice (stock no. 002684) were obtained from The Jackson Laboratories (Bar Harbor, ME). A_{2B}AR^{-/-} mice and A₃AR^{-/-} mice were generated by Dr. Katya Ravid of Boston University (Boston, MA) and Merck Research Laboratories (West Point, PA), respectively, and were bred at the University of Virginia. During MRI, mice were anesthetized with 1.25% isoflurane and maintained at 36±0.5°C, and the electrocardiogram, body temperature, and respiration were monitored. An intraperitoneal (IP) catheter was established for delivery of vasodilatory agents.

MRI Acquisition and Analysis

MRI was performed using a 7T system (Clinscan, Bruker, Ettlingen, Germany) with a 35-mm diameter birdcage RF coil and an MR-compatible physiological monitoring and gating system for mice (SA Instruments, Inc., Stony Brook, NY). The MRI protocol began with localizer imaging to select a mid-ventricular short-axis slice. Next, as shown in Figure 1, T1 mapping and perfusion imaging were performed at rest. Thereafter, adenosine (Sigma–Aldrich, St. Louis, MO, 250 mg/kg/min³¹³, IP infusion), regadenoson (Sigma–Aldrich, St. Louis, MO, 0.1 mg/kg²⁵⁸, IP bolus), or saline was given and after 10 minutes, both T1 mapping and perfusion imaging were repeated. The total infusion or injection volume ranged from 80 to 100 µl. Heart rate (HR) measurements were taken before and 10 minutes after administration of the vasodilator. All image reconstructions and analyses were performed offline using MATLAB (Mathworks, Natick, MA). Regions of interest (ROIs) for the myocardium were drawn manually and included the entire left

Statistical Analysis

Statistical analysis was performed using SigmaPlot (Systat Software Inc., Point Richmond, CA). Two-way ANOVA with a post-hoc Tukey's HSD test was used to detect specific group-to-group differences in MBF, T1, MPR, $\Delta T1$, and heart rate between different mouse strains and vasodilator types.

B.5 Results

ASL and T1 mapping repeatability

Bland-Altman plots showing the intersession repeatability of ASL and T1 mapping are shown in Figure 2. For ASL, the mean MBF difference was 0.1 ml/g/min and the 95% confidence interval was -3.0 to 3.2 ml/g/min. The ICC and COV for ASL were 0.90 and 20.4 ± 8.6 %. For the T1 mapping sequence, the mean difference was 0.4 and the 95% confidence interval was -43.9 to 44.7 ms. The ICC and COV for T1 mapping were 0.94 and 1.7 ± 0.1 %.

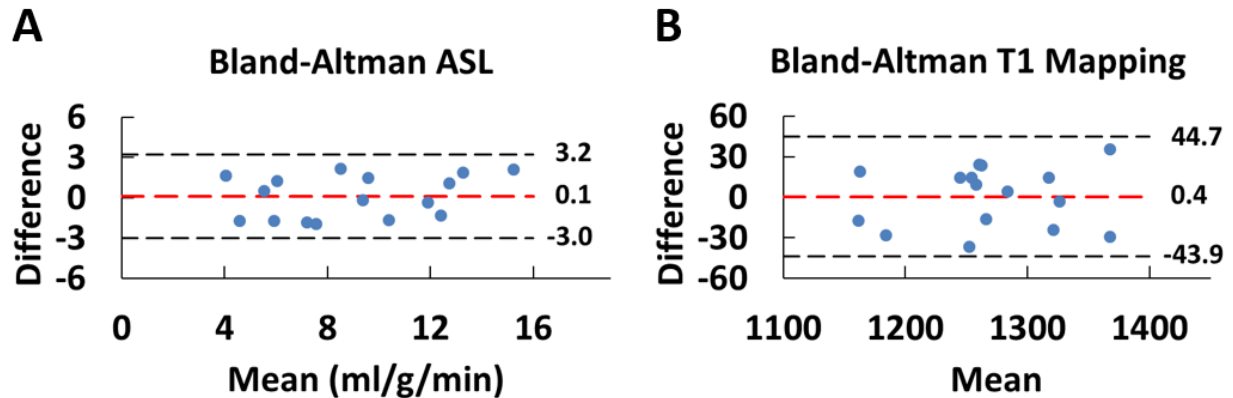


Figure 2. Bland-Altman plots for the (A) ASL and (B) T1 mapping MRI sequences demonstrating small average differences and narrow limits of agreement between the two measurements of each MRI sequence.

Adenosine-induced increases in myocardial perfusion are mediated solely through the $A_{2A}AR$

Figure 3A shows example myocardial perfusion maps acquired at rest and during adenosine-induced vasodilation using ASL in WT and $A_{2A}AR^{-/-}$ mice, demonstrating the effect of adenosine on increasing MBF in WT mice but not in $A_{2A}AR^{-/-}$ mice. The results summarizing the pre- and post-adenosine, pre- and post-regadenoson, and pre- and post-saline perfusion imaging studies using WT, $A_{2A}AR^{-/-}$, $A_{2B}AR^{-/-}$, and $A_{3}AR^{-/-}$ are presented in Table 1 and Figure 3B. In WT control mice, MBF at rest and with adenosine were 6.3 ± 2.3 and 12.1 ± 3.7 respectively, leading to a reference MPR value of 2.1 ± 0.5 . In contrast, MPR due to adenosine was reduced to approximately unity in $A_{2A}AR^{-/-}$ mice, demonstrating a central role of the $A_{2A}AR$ in mediating the increase in MBF. Perfusion imaging of $A_{2B}AR^{-/-}$ and $A_{3}AR^{-/-}$ mice show that MBF at rest and MBF with adenosine are not significantly different than the results in WT mice (Table 1), and that MPR is not significantly different than that of WT mice (Figure 3B). MBF and MPR results measured using regadenoson in the various groups of mice were not significantly different than those measured using adenosine. These results indicate that the increase in perfusion due to either vasodilator is mediated through the $A_{2A}AR$.

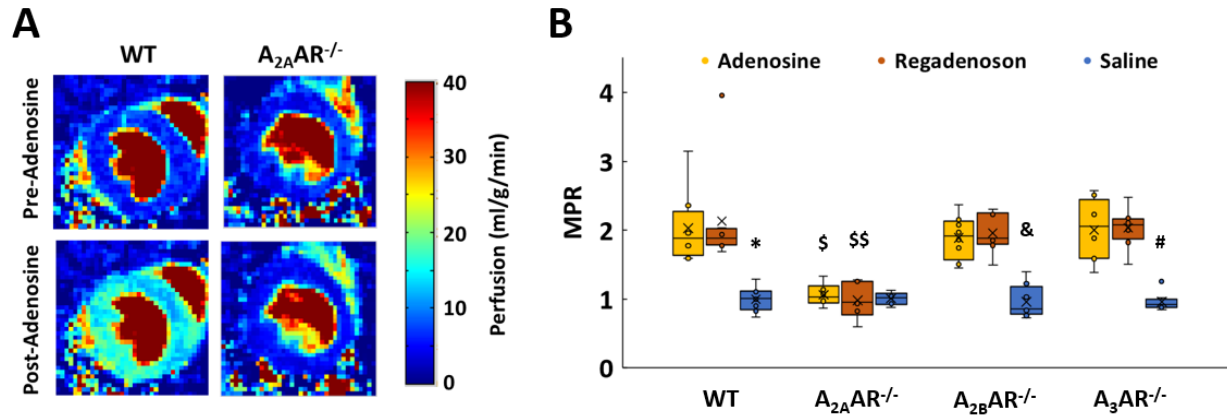


Figure 3. A. Example ASL perfusion maps before and after adenosine vasodilation in wild type (WT) and $A_{2A}AR^{-/-}$ mice. **B.** Adenosine, regadenoson, and saline myocardial perfusion reserve (MPR) measurements for WT and adenosine receptor subtype knockout mice. MPR in response to adenosine and regadenoson was reduced in $A_{2A}AR^{-/-}$ mice as compared to all other groups of mice. * p<0.001 vs WT adenosine and WT regadenoson, \$ p<0.001 vs adenosine in all other mouse groups, \$\$ p<0.001 vs regadenoson in all mouse groups, & p<0.001 vs $A_{2B}AR^{-/-}$ adenosine and $A_{2B}AR^{-/-}$ regadenoson, # p<0.001 vs $A_{3}AR^{-/-}$ adenosine and $A_{3}AR^{-/-}$ regadenoson.

	Adenosine		Regadenoson		Saline	
	Rest	Stress	Rest	Stress	Rest	Stress
WT	6.3 ± 2.3	12.1 ± 3.7 *	6.2 ± 1.3	12.8 ± 3.6 *	6.3 ± 2.3	6.2 ± 2.2 ‡
$A_{2A}AR^{-/-}$	6.7 ± 2.1	7.3 ± 3.4 †	8.0 ± 1.6	7.9 ± 2.8 †	6.7 ± 2.1	6.7 ± 2.1
$A_{2B}AR^{-/-}$	7.2 ± 1.2	13.5 ± 2.5 *	7.3 ± 2.1	14.2 ± 3.7 *	7.2 ± 1.2	6.7 ± 0.9 ‡
$A_{3}AR^{-/-}$	7.8 ± 2.4	15.2 ± 4.9 *	7.0 ± 1.5	14.1 ± 2.2 *	7.8 ± 2.4	7.5 ± 2.3 ‡

Table 1. Myocardial blood flow ($ml \cdot g^{-1} \cdot min^{-1}$) at rest and stress in response to adenosine, regadenoson, and saline in WT and adenosine receptor subtype knockout mice (mean ± stdev).

* p<0.001 vs same vasodilator rest perfusion in same group of mice

† p<0.001 vs same vasodilator stress perfusion in all other groups of mice

‡ p<0.001 vs adenosine and regadenoson stress perfusion in same group of mice

Adenosine-induced myocardial T1 reactivity is mediated through both the A_{2A}AR and the A_{2B}AR

Example T1 relaxation curves computed from Look-Locker images acquired before and after adenosine vasodilation in a WT mouse and regadenoson vasodilation in an A_{2A}AR^{-/-} mouse are shown in Figure 4A and 4B. Table 2 and Figure 4C summarize the pre- and post- adenosine, regadenoson, and saline T1 and ΔT1 data from WT, A_{2A}AR^{-/-}, A_{2B}AR^{-/-}, and A₃AR^{-/-} mice. T1 reactivity due to adenosine is reduced by approximately a factor of 2 in both A_{2A}AR^{-/-} and A_{2B}AR^{-/-} mice compared to WT mice, while there is no significant difference in adenosine T1 reactivity between WT and A₃AR^{-/-} mice. These results demonstrate that A_{2A}AR and A_{2B}AR agonism each account for about half of adenosine T1 reactivity, and the A₃AR does not have a significant role in adenosine T1 reactivity. As shown in Table 2, we also observed that T1 values are lower in A_{2B}AR^{-/-} and A₃AR^{-/-} mice than in WT and A_{2A}AR^{-/-} mice.

	Adenosine		Regadenoson		Saline	
	Rest	Stress	Rest	Stress	Rest	Stress
WT	1236 ± 43	1284 ± 41 *	1255 ± 69	1280 ± 79	1242 ± 55	1236 ± 58
A_{2A}AR^{-/-}	1213 ± 53	1232 ± 47	1254 ± 67	1252 ± 62	1253 ± 61	1251 ± 58
A_{2B}AR^{-/-}	1098 ± 65 †	1113 ± 70 †	1149 ± 37 †	1172 ± 45 †	1158 ± 44 †	1157 ± 58 †
A₃AR^{-/-}	1107 ± 72 †	1154 ± 64 ‡	1164 ± 45 †	1184 ± 45 †	1168 ± 75 †	1169 ± 64 †

Table 2. Myocardial T1 at rest and stress in response to adenosine, regadenoson, and saline in WT and adenosine receptor subtype knockout mice (mean ± stdev).

* p=0.026 vs WT adenosine rest T1

† p<0.01 vs same treatment WT and A_{2A}AR^{-/-} mice

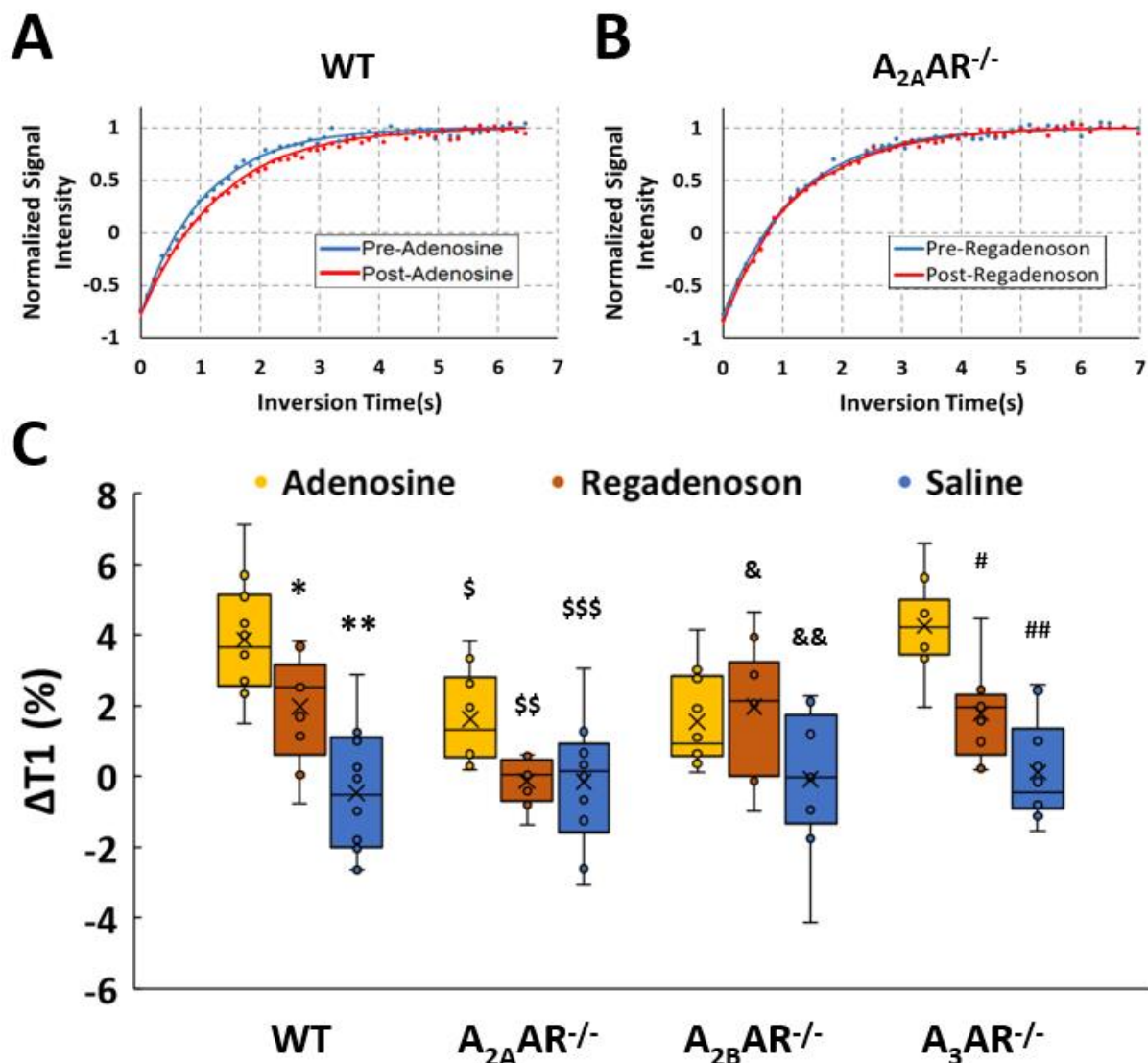


Figure 4. **A.** Example myocardial T1 relaxation curves before and after adenosine in a WT mouse and **(B)** regadenoson in an $A_{2A}AR^{-/-}$ mouse. **C.** Adenosine, regadenoson, and saline T1 reactivity ($\Delta T1$) measurements in WT and adenosine receptor subtype knockout mice. Adenosine $\Delta T1$ was significantly reduced in both $A_{2A}AR^{-/-}$ and $A_{2B}AR^{-/-}$ mice. Regadenoson $\Delta T1$ was approximately half of adenosine $\Delta T1$ in WT mice and was nullified in $A_{2A}AR^{-/-}$ mice. * $p=0.030$ vs WT adenosine, ** $p<0.001$ vs WT adenosine and WT regadenoson, \$ $p=0.045$ vs WT adenosine, $p=0.037$ vs $A_{3}AR^{-/-}$ adenosine, \$\$ $p=0.032$ vs $A_{2A}AR^{-/-}$ adenosine, $p=0.039$ vs WT regadenoson, $p=0.044$ vs $A_{2B}AR^{-/-}$ regadenoson, $p=0.048$ $A_{3}AR^{-/-}$ regadenoson, \$\$\$ $p=0.027$ vs $A_{2A}AR^{-/-}$ adenosine, & $p=0.044$ vs WT adenosine, $p=0.036$ vs $A_{3}AR^{-/-}$ adenosine, && $p=0.031$ vs $A_{2B}AR^{-/-}$ adenosine, $p=0.022$ vs $A_{2B}AR^{-/-}$ regadenoson, # $p=0.021$ vs $A_{3}AR^{-/-}$ adenosine, ## $p<0.001$ vs $A_{3}AR^{-/-}$ adenosine, $p=0.050$ vs $A_{3}AR^{-/-}$ regadenoson.

Adenosine, a nonselective adenosine receptor agonist, provides greater myocardial T1 reactivity compared to regadenoson, a selective A_{2A}AR agonist

Table 2 and Figure 4C also show that adenosine T1 reactivity in WT mice is about two times greater than T1 reactivity due to regadenoson. In A_{2B}AR^{-/-} mice, adenosine and regadenoson T1 reactivity are similar and approximately half of the value measured in WT mice. Regadenoson T1 reactivity is similar in WT, A_{2B}AR^{-/-} and A₃AR^{-/-} mice and is substantially reduced in A_{2A}AR^{-/-} mice. Further, the amount of regadenoson-induced T1 reactivity in all but the A_{2A}AR^{-/-} mice corresponds to about half of the adenosine-induced T1 reactivity measured in WT mice. These results demonstrate that adenosine agonizes both the A_{2A}AR and A_{2B}AR and that each contribute to T1 reactivity, whereas regadenoson agonizes only the A_{2A}AR, and thereby contributes to about half of the adenosine-induced T1 reactivity.

Adenosine- and regadenoson-induced increases in myocardial perfusion are eNOS-independent

In our second set of experiments, we performed rest and vasodilator ASL and T1 mapping in eNOS^{-/-} mice. Table 3 and Figure 5A summarize the perfusion data before and after injection of each stress agent, showing no significant difference in MBF or MPR between WT and eNOS^{-/-} mice using either vasodilator, indicating that both adenosine- and regadenoson-induced increases in myocardial perfusion are eNOS independent.

	Adenosine		Regadenoson		Saline	
	Rest	Stress	Rest	Stress	Rest	Stress
WT	6.3 ± 2.3	12.1 ± 3.7 *	6.2 ± 1.3	12.8 ± 3.6 †	6.3 ± 2.3	6.2 ± 2.2 ‡
eNOS^{-/-}	5.5 ± 1.0	10.7 ± 1.3 §	6.7 ± 4.3	13.9 ± 7.9	5.5 ± 1.0	5.3 ± 1.0

Table 3. Myocardial blood flow (ml*g⁻¹*min⁻¹) at rest and stress in response to adenosine, regadenoson, and saline in WT and eNOS^{-/-} mice (mean ± stdev).

* p=0.004 vs WT adenosine rest

† p= 0.002 vs WT regadenoson rest

‡ p=0.003 vs WT adenosine stress, p<0.001 vs WT regadenoson stress

§ p<0.001 vs eNOS^{-/-} adenosine rest

|| p<0.001 vs eNOS^{-/-} adenosine stress, p=0.03 vs eNOS^{-/-} regadenoson stress

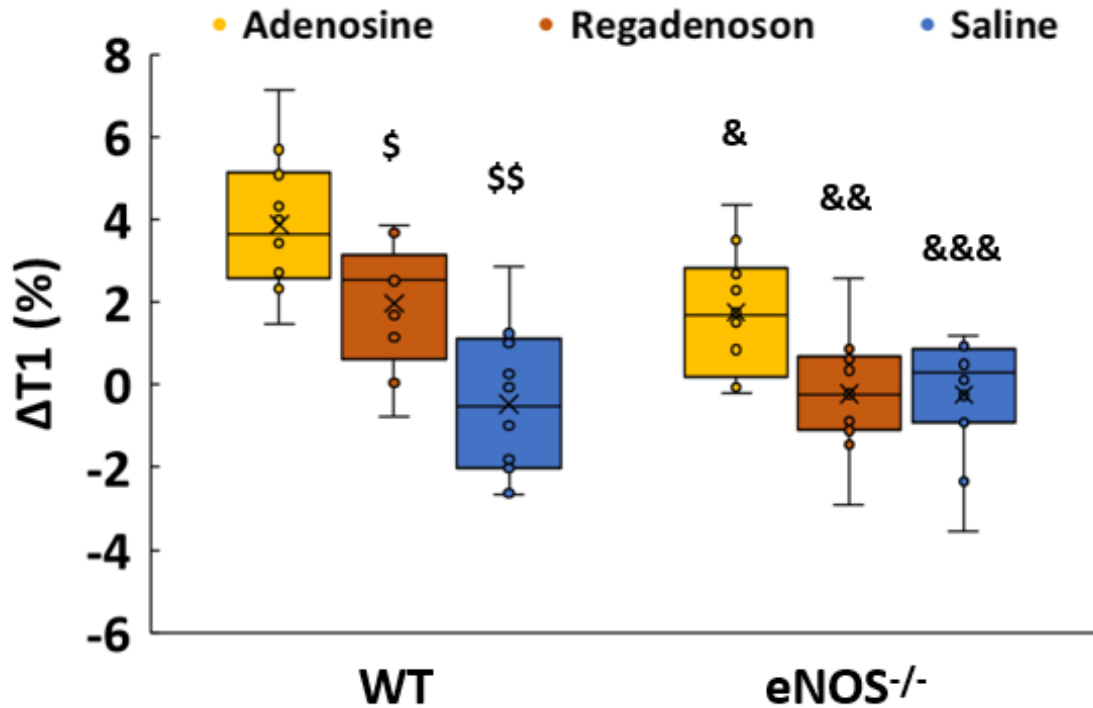


Figure 5. Adenosine, regadenoson, and saline (A) MPR and (B) $\Delta T1$ measurements for WT and $eNOS^{-/-}$ mice. There was no difference in MPR between adenosine and regadenoson MPR in WT vs $eNOS^{-/-}$ mice. However, adenosine $\Delta T1$ was significantly lower in $eNOS^{-/-}$ mice and regadenoson $\Delta T1$ was nullified in $eNOS^{-/-}$ mice. * $p=0.003$ vs WT adenosine, $p=0.001$ vs WT regadenoson, ** $p=0.009$ vs $eNOS^{-/-}$ adenosine, $p=0.001$ vs $eNOS^{-/-}$ regadenoson, \$ $p=0.030$ vs WT adenosine, \$\$ $p<0.001$ vs WT adenosine, $p=0.003$ vs WT regadenoson, & $p=0.014$ vs WT adenosine, && $p=0.036$ vs $eNOS^{-/-}$ adenosine, $p=0.012$ vs WT regadenoson, &&& $p=0.028$ vs $eNOS^{-/-}$ adenosine

	Adenosine		Regadenoson		Saline	
	Rest	Stress	Rest	Stress	Rest	Stress
WT	1236 ± 43	1284 ± 41 *	1255 ± 69	1280 ± 79	1242 ± 55	1236 ± 58
$eNOS^{-/-}$	1250 ± 83	1272 ± 92	1200 ± 52	1198 ± 56	1256 ± 72	1253 ± 68

Table 4. Myocardial T1 at rest and stress in response to adenosine, regadenoson, and saline in WT and $eNOS^{-/-}$ mice (mean ± stdev).

* $p=0.04$ vs WT adenosine rest

A_{2A}AR-mediated myocardial T1 reactivity is eNOS dependent while A_{2B}AR-mediated myocardial T1 reactivity is eNOS independent

Figure 5B and Table 4 show the myocardial T1 and $\Delta T1$ results from WT and eNOS^{-/-} mice treated with adenosine, regadenoson, or saline. For adenosine T1 reactivity, eNOS^{-/-} mice have approximately half the $\Delta T1$ response as WT mice. Using the selective A_{2A}AR agonist regadenoson, eNOS^{-/-} T1 reactivity was substantially reduced. Together, these results suggest that A_{2A}AR-mediated myocardial T1 reactivity is eNOS dependent and that A_{2B}AR-mediated myocardial T1 reactivity is eNOS independent. All T1 reactivity and absolute change in T1 values are shown in Table I and II in the Data Supplement.

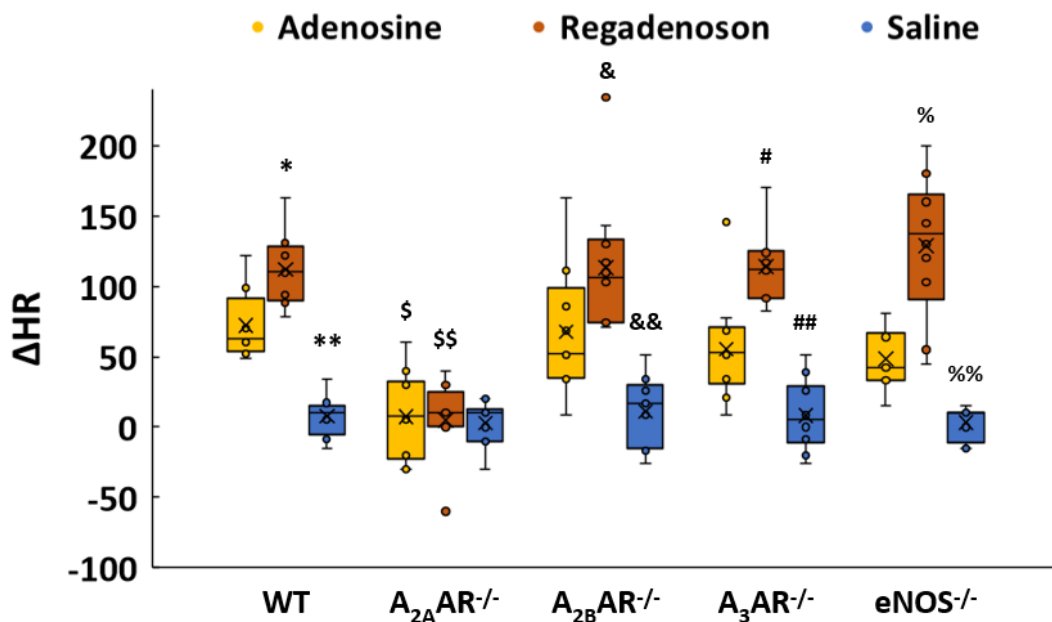


Figure 6. Adenosine, regadenoson, and saline heart rate response post-administration in all groups of mice. The change in heart rate (ΔHR) with regadenoson was about twice that of adenosine in all groups of mice except A_{2A}AR^{-/-} where ΔHR was essentially eliminated. * p=0.025 vs WT adenosine, ** p=0.009 vs WT adenosine, p<0.001 vs WT regadenoson, \$ p=0.004 vs WT adenosine, p=0.007 vs A_{2B}AR^{-/-} adenosine, p=0.033 vs A₃AR^{-/-} adenosine, p=0.039 vs eNOS^{-/-} adenosine, \$\$ p<0.001 vs regadenoson in all other mouse groups, & p=0.046 vs A_{2B}AR^{-/-} adenosine, && p=0.021 vs A_{2B}AR^{-/-} adenosine, # p=0.011 vs A₃AR^{-/-} adenosine, ## p=0.044 vs A₃AR^{-/-} adenosine, p<0.001 vs A₃AR^{-/-} regadenoson, % p<0.001 vs eNOS^{-/-} adenosine, %% p=0.031 vs eNOS^{-/-} adenosine, p<0.001 vs eNOS^{-/-} regadenoson

Heart rate responses to adenosine and regadenoson

Figure 6 summarizes the heart rate responses to each vasodilator for the different groups of mice. For both adenosine and regadenoson, the increases in HR were not significantly different for WT, A_{2B}AR^{-/-}, A₃AR^{-/-}, and eNOS^{-/-} mice, and changes in heart rate are minimal in A_{2A}AR^{-/-} mice. Regadenoson provides an approximately two-fold greater heart rate increase compared to adenosine in all groups except A_{2A}AR^{-/-} mice.

B.6 Discussion and Conclusions

The major findings of this study, as show in Figure 7, are: (a) while adenosine myocardial perfusion reserve is mediated solely through the A_{2A}AR, adenosine myocardial T1 reactivity is mediated through both the A_{2A}AR and the A_{2B}AR, (b) while adenosine increases MBF through eNOS-independent mechanisms, adenosine increases MBV and T1 reactivity partly through eNOS-dependent mechanisms, and (c) specifically, the increase in MBV and T1 reactivity mediated through the A_{2A}AR is eNOS-dependent, while the increase in MBV and T1 reactivity mediated through the A_{2B}AR is eNOS-independent.

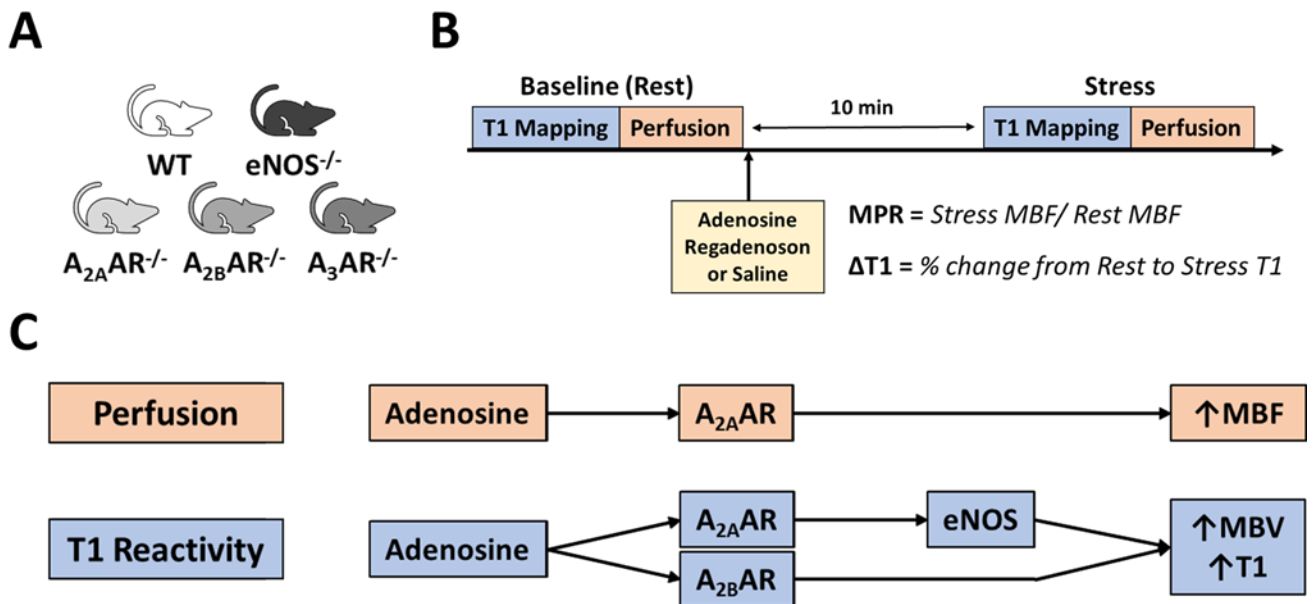


Figure 7. (A,B) Five groups of mice underwent rest and stress perfusion and T1 mapping MRI using adenosine, regadenoson, or saline. The output parameters were myocardial perfusion reserve (MPR) and T1 reactivity (ΔT1). **C.** We found that adenosine increases myocardial blood flow (MBF) via endothelial-independent activation of the A_{2A}AR. In contrast, adenosine increases myocardial blood volume (MBV) and subsequently T1 via both endothelial-dependent activation of the A_{2A}AR and endothelial-independent activation of the A_{2B}AR.

The differential effects of the adenosine receptor subtypes and eNOS on MPR and T1 reactivity may be explained by considering the different sections of the coronary vasculature tree that primarily control MBF and MBV. Increased MPR requires primarily dilation of the resistance vessels, which are predominantly the coronary arterioles^{301,315–317}. Our results suggest that the increase in MBF secondary to vasodilation of the coronary arterioles is entirely A_{2A}AR-dependent and endothelial-independent, and these results are consistent with prior studies^{301,318–321}. Adenosine has also been implicated in capillary recruitment^{322,323} and dilation³²⁴, and as the terminal arterioles and capillaries

with diameters $<10\mu\text{m}$ contain the majority of MBV, this may be the main mechanism of myocardial adenosine T1 reactivity. Our results show an endothelial-dependent role of the $A_{2A}AR$ and an endothelial-independent role of the $A_{2B}AR$ in modulating MBV. The $A_{2A}AR$ may directly stimulate eNOS^{325–327} or may indirectly stimulate eNOS through flow-mediated dilation^{264,328}, whereas the $A_{2B}AR$ may directly stimulate VMSCs on the terminal arteriole vessels^{321,329} resulting in increased capillary recruitment and MBV. Flow-mediated dilation may also occur upstream of the coronary arterioles, however, the effect of the upstream vessels on MBV and T1 reactivity is likely overshadowed by the downstream terminal arterioles and capillaries. Overall, our results demonstrate that adenosine T1 reactivity imaging interrogates different aspects of coronary vascular function than adenosine perfusion imaging and suggests that some of the change in MBV occurs downstream of changes in MBF.

Our results in mice are not entirely consistent with published results of adenosine and regadenoson myocardial T1 reactivity measurements in human subjects. First, for MRI of the heart at 7T, our myocardial T1 values are low. While our fully-sampled spiral Look-Locker method provides accurate myocardial T1 values²¹⁵, the accelerated version of the method causes an underestimation of T1²⁸⁶. While not ideal, reproducibility remains high, and the four-fold faster scan facilitates the acquisition of ASL and T1 mapping during a single adenosine stress session. We also report an adenosine T1 reactivity in WT mice of $3.9 \pm 1.5\%$, while adenosine T1 reactivity in healthy humans is generally reported to be approximately 6% ^{302–304}. Differences in T1 and T1 reactivity may be related to the use of different pulse sequences. For example, Kuijpers et al. reported an adenosine T1 reactivity of $4.3 \pm 2.8\%$ in patients using a breathhold modified Look-Locker inversion recovery (MOLLI) sequence as opposed to the $6.2 \pm 1.0\%$ reported using the standard breathhold shortened MOLLI (shMOLLI) sequence³³⁰. For mouse MRI, we used a low-rank accelerated segmented Look-Locker acquisition method which may yield different T1 reactivity values than other sequences. Furthermore, as myocardial T1 is affected by changes in MBV, there may be inter-species differences in MBV between mice and humans that may affect T1 and T1 reactivity. Third, we report a significantly reduced regadenoson T1 reactivity vs. the T1 reactivity due to adenosine whereas Van Dijk et al. reported a regadenoson T1 reactivity of $5.4 \pm 2.4\%$ which was not significantly different than adenosine $\Delta T1$ in healthy patients³³¹. A possible explanation for this discrepancy is that the distribution of adenosine receptors along the coronary artery tree may vary from species to species³⁰⁹, potentially altering the T1 reactivity mechanisms of mice compared to humans.

Prior studies have shown a small vasoconstrictive role for the A_3AR that occurs in response to $A_{2A}AR$ and $A_{2B}AR$ mediated vasodilation^{312,332}. Our results may be consistent with these studies as we observed a 10% increase in adenosine T1 reactivity in $A_3AR^{-/-}$ compared to that of WT mice (although the increase was not statistically significant), potentially reflecting a small vasoconstrictive role for the A_3AR . Future studies may utilize IB-MECA, an A_3AR agonist, and CAY10498 or PSB11, A_3AR antagonists, in combination with gene-knockout mice to further elucidate a potential effect of the A_3AR on adenosine T1 reactivity.

In WT mice, our rest and stress perfusion measurements of 6.3 and 12.1 ml/g/min, respectively, and MPR measurement of 2.1 are consistent with prior studies^{39,40,258}.

However, there is conflicting evidence regarding the role of the endothelium in the adenosine-induced increase in MBF. Multiple studies have suggested that adenosine imparts an endothelial-independent increase in MBF^{301,318-321}, however, PET perfusion studies have demonstrated a 21-25% reduction in stress MBF after inhibition of eNOS^{333,334}. While the role of the endothelium is controversial, our results add to the evidence that the adenosine-induced increase in MBF is endothelial-independent.

Prior studies have shown roles of the A_{2A}AR and A₁AR in modulating heart rate^{309,335,336}, and, in particular, Schindler et al demonstrated that A_{2A}AR activation in the central nervous system elevates heart rate while A₁AR activation in the peripheral nervous system decreases heart rate³³⁶. Our results are consistent with these studies as regadenoson increased heart rate in mice about 60 beats per minute more than adenosine. Our results further suggest that A₁AR activation may act to suppress heart rate in parallel with an A_{2A}AR-mediated increase, as there was no change in heart rate in A_{2A}^{-/-} mice due to adenosine. As a related point, we previously demonstrated that spiral Look-Locker MRI with cardio-respiratory gating and fuzzy clustering measures myocardial T1 independent of heart rate²¹⁵. Heart rate independent T1 mapping was particularly important in this study because we required precise T1 mapping in a setting where different vasodilators applied in various gene-modified mice led to a variety of heart rates.

A limitation of our study is that we did not include A₁AR^{-/-} mice. Similar to the A₃AR, pharmacological studies have indicated that A₁AR activation may induce coronary vasoconstriction, and thus may negatively modulate T1 reactivity to a small degree^{337,338}. Future studies may investigate a potential role for the A₁AR in adenosine myocardial T1 reactivity. A second limitation is that our study was performed using male mice; however, there are sex-dependent differences in MBF and MBV and their response to adenosine²⁸⁰. Thus, future studies will be required to determine whether these findings can be reproduced in female mice. Furthermore, there are sex differences in coronary vascular disease, including coronary macrovascular and microvascular disease^{17,339,340}. Whether our results hold or may be modified, potentially in a sex-dependent manner, in various disease contexts may also be investigated in future studies.

B.7 Data Supplement

	Adenosine		Regadenoson		Saline	
	<i>T1 reactivity</i>	<i>Absolute T1 change</i>	<i>T1 reactivity</i>	<i>Absolute T1 change</i>	<i>T1 reactivity</i>	<i>Absolute T1 change</i>
WT	3.9 ± 0.4	48 ± 5	2.0 ± 0.4 *	25 ± 5 *	-0.5 ± 0.5 †	-6 ± 7 †
A_{2A}AR^{-/-}	1.6 ± 0.4 ‡	19 ± 5 ‡	-0.1 ± 0.2 §	-2 ± 3 §	-0.1 ± 0.6	-2 ± 7
A_{2B}AR^{-/-}	1.6 ± 0.4 #	17 ± 5 #	2.0 ± 0.6	23 ± 7	-0.1 ± 0.7 **	-1 ± 6 **
A₃AR^{-/-}	4.3 ± 0.4	47 ± 5	1.8 ± 0.4 ††	21 ± 5 ††	0.1 ± 0.5 ††	1 ± 5 ††

Table I. T1 reactivity and absolute change from rest to stress T1 values for wild type (WT) and adenosine receptor knockout mice with adenosine, regadenoson and saline. All values are shown as mean ± standard error.

* p<0.05 vs WT adenosine

† p<0.001 vs WT adenosine, p<0.01 vs WT regadenoson

‡ p<0.05 vs WT adenosine, p<0.05 vs A₃AR^{-/-} adenosine

§ p<0.05 vs A_{2A}AR^{-/-} adenosine, p<0.05 vs WT regadenoson, p<0.05 vs A_{2B}AR^{-/-} regadenoson, p<0.05 A₃AR^{-/-} regadenoson

|| p<0.05 vs A_{2A}AR^{-/-} adenosine

p<0.05 vs WT adenosine, p<0.05 vs A₃AR^{-/-} adenosine

** p<0.05 vs A_{2B}AR^{-/-} adenosine, p<0.05 vs A_{2B}AR^{-/-} regadenoson

†† p<0.05 vs A₃AR^{-/-} adenosine

†† p<0.001 vs A₃AR^{-/-} adenosine, p<0.05 vs A₃AR^{-/-} regadenoson

	Adenosine		Regadenoson		Saline	
	<i>T1 reactivity</i>	<i>Absolute T1 change</i>	<i>T1 reactivity</i>	<i>Absolute T1 change</i>	<i>T1 reactivity</i>	<i>Absolute T1 change</i>
WT	3.9 ± 0.4	48 ± 5	2.0 ± 0.4 *	25 ± 5 *	-0.5 ± 0.5 †‡	-6 ± 7 †‡
eNOS^{-/-}	1.8 ± 0.4 *	22 ± 5 *	-0.2 ± 0.4 §	-3 ± 5 §	-0.2 ± 0.4 §	-3 ± 6 §

Table II. T1 reactivity and absolute change from rest to stress T1 values for wild type (WT) and eNOS^{-/-} mice with adenosine, regadenoson and saline. All values are shown as mean ± standard error.

* p<0.05 vs WT Adenosine

† p<0.001 vs WT Adenosine

‡ p<0.01 vs WT Regadenoson

§ p<0.05 vs eNOS^{-/-} Adenosine

|| p<0.05 vs WT Regadenoson

Appendix C – Awards and Publications

C.1 Awards

- SCMR Early Career Award in Translation Science, *SCMR 2022*
- ISMRM Magna Cum Laude Merit Award, *ISMRM 2020*
- AHA Predoctoral Fellowship 19PRE34380163, *Jan 2019 – Dec 2020*
- NIH Cardiovascular Research Training Grant T32 HL007284, *Jul 2018 – Jun 2019*

C.2 First Author Manuscripts

Shah S., Reagan C., French B., & Epstein F. Molecular mechanisms of adenosine T1 mapping. *Circulation: Cardiovascular Imaging*. 2021. 14(3); e011774.

Shah S., Cui S., Waters C., Sano S., Wang Y., Doviak H., Leor J., Walsh., French B., & Epstein F. Nitroxide-enhanced magnetic resonance imaging of cardiovascular oxidative stress. *NMR in Biomedicine*. 2020. 33(9); e4359.

Shah S., Echols J., Wolf M., & Epstein F. Accelerated fatty acid composition MRI of epicardial adipose tissue: development and application to eplerenone treatment in a mouse model of obesity-induced coronary microvascular disease. *Magnetic Resonance in Medicine - Under Review*.

Shah S., Reagan C., Bresticker J., Billcheck H., Bradley L., Wolf M., Isakson B., French B., & Epstein F. Deletion or inhibition of iNOS prevents or reverses coronary microvascular disease due to a high-fat high-sucrose diet. *Circulation – Under Review*.

Shah S., Reagan C., Billcheck H., Bradley L., Wolf M., Isakson B., French B., & Epstein F. Role of mineralocorticoid receptor blockade and cell-specific deletion on coronary microvascular disease due to obesity. *Manuscript Preparation*.

C.3 Other Manuscripts

Daneva Z., Ottolini M., Chen Y., Klimentova E., Kuppusamy M., **Shah S.**, Minshall R., Seye C., Laubach V., Isakson B., & Sonkusare S. Endothelial Pannexin 1–TRPV4 channel signaling lowers pulmonary arterial pressure in mice. *Elife*. 2021. 10; e67777.

Daneva Z., Ottolini M., Chen Y., Klimentova E., **Shah S.**, Minshall R., Seye C., Laubach V., Isakson B., & Sonkusare S. Endothelial Pannexin 1–TRPV4 channel signaling lowers pulmonary arterial pressure. *BioRxiv*. 2021.

Nagalakshmi V., Li M., **Shah S.**, Gigliotti J., Klibanov A., Epstein F., ... & Sequeira-Lopez M. Changes in cell fate determine the regenerative and functional capacity of the developing kidney before and after release of obstruction. *Clinical Science*. 2018. 132(23); 2519-2545.

C.4 First Author Oral Abstracts

Shah S., Wolf M., & Epstein F. Eplerenone promotes anti-inflammatory epicardial adipose tissue and preserves coronary microvascular function in mice fed a high-fat high-sucrose diet. SCMR. 2022. 25; 000227. ***SCMR Early Career Award in Translational Science***

Shah S., French B., Wolf M., & Epstein F. Cardiac MRI detects a reduced volume and anti-inflammatory fatty acid composition of epicardial adipose tissue in eplerenone-treated obese mice. ISMRM. 2021. 29; 1264.

Shah S., Reagan C., French B., & Epstein F. Molecular mechanisms of myocardial adenosine stress T1 mapping. SCMR. 2021. 24; 942614.

Shah S., Reagan C., French B., Isakson B., Wolf M., & Epstein F. INOS deletion prevents coronary microvascular disease in mice fed a high fat high sucrose diet. SCMR. 2021. 24; 943276.

Shah S., Wang Y., Waters C., Chen L., French B., & Epstein F. Tracer kinetic modeling of nitroxide-enhanced MRI to quantify oxidative stress in mouse models of heart disease. ISMRM. 2020. 28; 1949. ***ISMRM Magna Cum Laude Merit Award***

Shah S., Reagan C., Roy R., Bradley L., Billcheck H., French B., Isakson B., Wolf M., Kramer C., & Epstein F. Eplerenone protects against myocardial oxidative stress and preserves perfusion reserve in high fat high sucrose fed mice. SCMR. 2020. 23; 751068.

Shah S., Reagan C., Roy R., French B., & Epstein F. Molecular mechanisms of adenosine and regadenoson T1 mapping. SCMR. 2020. 23; 748814.

Shah S., Waters C., Chen L., Roy R., French B., & Epstein F. Dynamic Nitroxide-Enhanced MRI detects the development and decline of oxidative stress. SCMR. 2019. 22; 537649.

C.5 First Author Poster Presentations

Shah, S., Sun C., & Epstein F. Accelerated MRI of epicardial adipose tissue fatty acid composition in mice using a compressed-sensing and dictionary-based reconstruction. ISMRM. 2022. 31; 4292.

Shah, S., Sun C., & Epstein F. Multiband CINE MRI of the mouse heart using the phase-offset multiplanar (POMP) method. SCMR. 2020. 23; 748825.

Shah, S., Cui S., Waters C., Chen L., Roy R., French B., & Epstein F. Dynamic nitroxide-enhanced MRI detects oxidative stress in MI. ISMRM. 2018. 26; 5042.

Acknowledgements

There are several UVA faculty members, staff, and students I would like to thank for their contributions and efforts guiding me through my time at UVA.

My advisor and full dissertation committee – Dr. Fred Epstein, Dr. Brent French, Dr. Shayn Peirce-Cottler, Dr. Matt Wolf, Dr. Craig Meyer, and Dr. Michael Salerno

Epstein Lab – Dr. Fred Epstein, Dr. Daniel Auger, Dr. Sophia Cui, Dr. Xiaoying Cai, Dr. Changyu Sun, Dr. Sona Ghadimi, Claire Reagan, Yu Wang, Jack Echols, and Julia Bresticker

French Lab – Dr. Brent French, Lanlin Chen, and Christopher Waters

Wolf Lab – Dr. Matt Wolf, Leigh Bradley, and Helen Billcheck

Isakson Lab – Dr. Brant Isakson, Dr. Miranda Good, Abigail Antoine, Angela Best, and Edgar Macal

Walsh Lab – Dr. Ken Walsh, Heather Doviak, Soichi Sano, and Ying Wang

Leor Lab – Dr. Jonathan Leor and Nir Lewis

7T MRI Core – Dr. Stuart Berr and Jack Roy

NMR Core – Dr. Jeffrey Ellena

UVA BME Staff

MR4 and MR6 Vivarium Staff

References

1. Safdar, B. *et al.* Prevalence and characteristics of coronary microvascular dysfunction among chest pain patients in the emergency department. *European Heart Journal: Acute Cardiovascular Care* **9**, 5–13 (2018).
2. Selker, H. P. *et al.* Use of the acute cardiac ischemia time-insensitive predictive instrument (ACI-TIPI) to assist with triage of patients with chest pain or other symptoms suggestive of acute cardiac ischemia: a multicenter, controlled clinical trial. *Annals of Internal Medicine* **129**, 845–855 (1998).
3. Farrehi, P. M. *et al.* Frequency of negative coronary arteriographic findings in patients with chest pain is related to community practice patterns. *American Journal of Managed Care* **8**, 643–652 (2002).
4. Bradley, S. M. *et al.* Normal coronary rates for elective angiography in the Veterans Affairs Healthcare System: insights from the VA CART program (veterans affairs clinical assessment reporting and tracking). *Journal of the American College of Cardiology* **63**, 417–426 (2014).
5. Radico, F., Cicchitti, V., Zimarino, M. & De Caterina, R. Angina pectoris and myocardial ischemia in the absence of obstructive coronary artery disease: practical considerations for diagnostic tests. *JACC: Cardiovascular Interventions* **7**, 453–463 (2014).
6. Jespersen, L. *et al.* Stable angina pectoris with no obstructive coronary artery disease is associated with increased risks of major adverse cardiovascular events. *European heart journal* **33**, 734–744 (2012).
7. Murthy, V. L. *et al.* Association between coronary vascular dysfunction and cardiac mortality in patients with and without diabetes mellitus. *Circulation* **126**, 1858–1868 (2012).
8. Taqueti, V. R. & Di Carli, M. F. Coronary microvascular disease pathogenic mechanisms and therapeutic options: JACC state-of-the-art review. *Journal of the American College of Cardiology* **72**, 2625–2641 (2018).
9. Sara, J. D. *et al.* Prevalence of coronary microvascular dysfunction among patients with chest pain and nonobstructive coronary artery disease. *JACC: Cardiovascular Interventions* **8**, 1445–1453 (2015).
10. Sinha, A., Rahman, H., Webb, A., Shah, A. M. & Perera, D. Untangling the pathophysiologic link between coronary microvascular dysfunction and heart failure with preserved ejection fraction. *European Heart Journal* **42**, 4431–4441 (2021).
11. Murthy, V. L. *et al.* Effects of sex on coronary microvascular dysfunction and cardiac outcomes. *Circulation* **129**, 2518–2527 (2014).
12. Pepine, C. J. *et al.* Coronary microvascular reactivity to adenosine predicts adverse outcome in women evaluated for suspected ischemia: results from the National Heart, Lung and Blood Institute WISE (Women's Ischemia Syndrome Evaluation) study. *Journal of the American College of Cardiology* **55**, 2825–2832 (2010).

13. Taqueti, V. R. & Di Carli, M. F. Clinical significance of noninvasive coronary flow reserve assessment in patients with ischemic heart disease. *Current opinion in cardiology* **31**, 662–669 (2016).
14. Johnson, B. D. *et al.* Prognosis in women with myocardial ischemia in the absence of obstructive coronary disease: results from the National Institutes of Health–National Heart, Lung, and Blood Institute–Sponsored Women’s Ischemia Syndrome Evaluation (WISE). *Circulation* **109**, 2993–2999 (2004).
15. Olson, M. B. *et al.* Symptoms, myocardial ischaemia and quality of life in women: results from the NHLBI-sponsored WISE Study. *European heart journal* **24**, 1506–1514 (2003).
16. Crea, F., Camici, P. G. & Bairey Merz, C. N. Coronary microvascular dysfunction: an update. *European heart journal* **35**, 1101–1111 (2014).
17. Dean, J., Cruz, S. D., Mehta, P. K. & Merz, C. N. B. Coronary microvascular dysfunction: sex-specific risk, diagnosis, and therapy. *Nature Reviews Cardiology* **12**, 406–414 (2015).
18. Jones, E., Eteiba, W. & Merz, N. B. Cardiac syndrome X and microvascular coronary dysfunction. *Trends in cardiovascular medicine* **22**, 161–168 (2012).
19. McHugh, K. *et al.* Heart failure with preserved ejection fraction and diabetes: JACC state-of-the-art review. *Journal of the American College of Cardiology* **73**, 602–611 (2019).
20. Taqueti, V. R. *et al.* Coronary microvascular dysfunction and future risk of heart failure with preserved ejection fraction. *European heart journal* **39**, 840–849 (2018).
21. Yang, J. H. *et al.* Endothelium-dependent and independent coronary microvascular dysfunction in patients with heart failure with preserved ejection fraction. *European journal of heart failure* **22**, 432–441 (2020).
22. Mahfouz, R. A., Gouda, M. & Abdelhamid, M. Relation of microvascular dysfunction and exercise tolerance in patients with heart failure with preserved ejection fraction. *Echocardiography* **37**, 1192–1198 (2020).
23. Nelson, M. D., Wei, J. & Merz, C. N. B. Coronary microvascular dysfunction and heart failure with preserved ejection fraction as female-pattern cardiovascular disease: the chicken or the egg? *European heart journal* **39**, 850 (2018).
24. Wei, J. *et al.* Myocardial steatosis as a possible mechanistic link between diastolic dysfunction and coronary microvascular dysfunction in women. *American Journal of Physiology-Heart and Circulatory Physiology* **310**, H14–H19 (2016).
25. Nelson, M. D. *et al.* Myocardial tissue deformation is reduced in subjects with coronary microvascular dysfunction but not rescued by treatment with ranolazine. *Clinical cardiology* **40**, 300–306 (2017).
26. Nelson, M. D. *et al.* Diastolic dysfunction in women with signs and symptoms of ischemia in the absence of obstructive coronary artery disease: a hypothesis-generating study. *Circulation: Cardiovascular Imaging* **7**, 510–516 (2014).

27. Paulus, W. J. & Tschöpe, C. A novel paradigm for heart failure with preserved ejection fraction: comorbidities drive myocardial dysfunction and remodeling through coronary microvascular endothelial inflammation. *Journal of the American College of Cardiology* **62**, 263–271 (2013).
28. Bairey Merz, C. N. *et al.* Ischemia and no obstructive coronary artery disease (INOCA) developing evidence-based therapies and research agenda for the next decade. *Circulation* **135**, 1075–1092 (2017).
29. Crea, F. *et al.* The parallel tales of microvascular angina and heart failure with preserved ejection fraction: a paradigm shift. *European heart journal* **38**, 473–477 (2017).
30. Camici, P. G. & Crea, F. Coronary microvascular dysfunction. *New England Journal of Medicine* **356**, 830–840 (2007).
31. Chilian, W. M. Coronary microcirculation in health and disease: summary of an NHLBI workshop. *Circulation* **95**, 522–528 (1997).
32. Ong, P. *et al.* International standardization of diagnostic criteria for microvascular angina. *International Journal of Cardiology* **250**, 16–20 (2018).
33. Egashira, K. *et al.* Impaired coronary blood flow response to acetylcholine in patients with coronary risk factors and proximal atherosclerotic lesions. *The Journal of clinical investigation* **91**, 29–37 (1993).
34. Lee, J. M. *et al.* Coronary flow reserve and microcirculatory resistance in patients with intermediate coronary stenosis. *Journal of the American College of Cardiology* **67**, 1158–1169 (2016).
35. Valenta, I., Dilsizian, V., Quercioli, A., Ruddy, T. D. & Schindler, T. H. Quantitative PET/CT measures of myocardial flow reserve and atherosclerosis for cardiac risk assessment and predicting adverse patient outcomes. *Current cardiology reports* **15**, 1–10 (2013).
36. Wöhrle, J. *et al.* Myocardial perfusion reserve in cardiovascular magnetic resonance: correlation to coronary microvascular dysfunction. *Journal of Cardiovascular Magnetic Resonance* **8**, 781–787 (2006).
37. Feher, A. & Sinusas, A. J. Quantitative assessment of coronary microvascular function: dynamic single-photon emission computed tomography, positron emission tomography, ultrasound, computed tomography, and magnetic resonance imaging. *Circulation: Cardiovascular Imaging* **10**, e006427 (2017).
38. Liu, A. *et al.* RETRACTED: Diagnosis of Microvascular Angina Using Cardiac Magnetic Resonance. (2018).
39. Troalen, T., Capron, T., Cozzone, P. J., Bernard, M. & Kober, F. Cine-ASL: A steady-pulsed arterial spin labeling method for myocardial perfusion mapping in mice. Part I. Experimental study. *Magnetic Resonance in Medicine* **70**, 1389–1398 (2013).
40. Naresh, N. K. *et al.* Repeatability and variability of myocardial perfusion imaging techniques in mice: Comparison of arterial spin labeling and first-pass contrast-enhanced MRI. *Magn Reson Med* **75**, 2394–2405 (2016).
41. Shah, S. A., Reagan, C. E., French, B. A. & Epstein, F. H. Molecular mechanisms of adenosine stress T1 mapping. *Circulation: Cardiovascular Imaging* **14**, e011774 (2021).

42. Doyle, M. *et al.* Prognostic Value of Global MR Myocardial Perfusion Imaging in Women With Suspected Myocardial Ischemia and No Obstructive Coronary Disease: Results From the NHLBI–Sponsored WISE (Women’s Ischemia Syndrome Evaluation) Study. *JACC: Cardiovascular Imaging* **3**, 1030–1036 (2010).
43. Vogel, R. *et al.* The quantification of absolute myocardial perfusion in humans by contrast echocardiography: algorithm and validation. *Journal of the American College of Cardiology* **45**, 754–762 (2005).
44. Youn, H.-J. & Foster, E. Demonstration of coronary artery flow using transthoracic Doppler echocardiography. *Journal of the American Society of Echocardiography* **17**, 178–185 (2004).
45. Marinescu, M. A. *et al.* Coronary microvascular dysfunction, microvascular angina, and treatment strategies. *JACC: Cardiovascular imaging* **8**, 210–220 (2015).
46. Garg, R. *et al.* Mineralocorticoid receptor blockade improves coronary microvascular function in individuals with type 2 diabetes. *Diabetes* **64**, 236–242 (2015).
47. Joffe, H. V. *et al.* Beneficial effects of eplerenone versus hydrochlorothiazide on coronary circulatory function in patients with diabetes mellitus. *The Journal of Clinical Endocrinology & Metabolism* **92**, 2552–2558 (2007).
48. Bavry, A. A. *et al.* Aldosterone inhibition and coronary endothelial function in women without obstructive coronary artery disease: An ancillary study of the National Heart, Lung, and Blood Institute–sponsored Women’s Ischemia Syndrome Evaluation. *American heart journal* **167**, 826–832 (2014).
49. Denardo, S. J. *et al.* Effect of phosphodiesterase type 5 inhibition on microvascular coronary dysfunction in women: a Women’s Ischemia Syndrome Evaluation (WISE) ancillary study. *Clinical cardiology* **34**, 483–487 (2011).
50. Egashira, K., Hirooka, Y., Kuga, T., Mohri, M. & Takeshita, A. Effects of L-arginine supplementation on endothelium-dependent coronary vasodilation in patients with angina pectoris and normal coronary arteriograms. *Circulation* **94**, 130–134 (1996).
51. Gellman, J. *et al.* L-arginine ameliorates the abnormal sympathetic response of the dysfunctional human coronary microvasculature. *Angiology* **55**, 1–8 (2004).
52. Houghton, J. L. *et al.* Cholesterol lowering with pravastatin improves resistance artery endothelial function: report of six subjects with normal coronary arteriograms. *Chest* **118**, 756–760 (2000).
53. Zhang, X. *et al.* Effects of combination of statin and calcium channel blocker in patients with cardiac syndrome X. *Coronary artery disease* **25**, 40–44 (2014).
54. Eshtehardi, P. *et al.* Effect of intensive atorvastatin therapy on coronary atherosclerosis progression, composition, arterial remodeling, and microvascular function. *The Journal of invasive cardiology* **24**, 522–529 (2012).

55. Caliskan, M. *et al.* Effects of atorvastatin on coronary flow reserve in patients with slow coronary flow. *Clinical Cardiology: An International Indexed and Peer-Reviewed Journal for Advances in the Treatment of Cardiovascular Disease* **30**, 475–479 (2007).
56. Bairey Merz, C. N., Pepine, C. J., Shimokawa, H. & Berry, C. Treatment of coronary microvascular dysfunction. *Cardiovascular research* **116**, 856–870 (2020).
57. Takahashi, J. & Shimokawa, H. Treatment of Coronary Microvascular Dysfunction. in *Coronary Vasomotion Abnormalities* 139–155 (Springer, 2021).
58. Yutzey, K. E. & Robbins, J. Principles of genetic murine models for cardiac disease. *Circulation* **115**, 792–799 (2007).
59. Zaragoza, C. *et al.* Animal models of cardiovascular diseases. *Journal of Biomedicine and Biotechnology* **2011**, (2011).
60. Aoqui, C. *et al.* Microvascular dysfunction in the course of metabolic syndrome induced by high-fat diet. *Cardiovascular Diabetology* **13**, 1–11 (2014).
61. Kwiatkowski, G., Bar, A., Jasztal, A. & Chłopicki, S. MRI-based in vivo detection of coronary microvascular dysfunction before alterations in cardiac function induced by short-term high-fat diet in mice. *Scientific Reports* **11**, 1–13 (2021).
62. Naresh, N. K. *et al.* Cardiovascular magnetic resonance detects the progression of impaired myocardial perfusion reserve and increased left-ventricular mass in mice fed a high-fat diet. *Journal of Cardiovascular Magnetic Resonance* **18**, 1–11 (2016).
63. Piek, A. *et al.* Pharmacological myeloperoxidase (MPO) inhibition in an obese/hypertensive mouse model attenuates obesity and liver damage, but not cardiac remodeling. *Scientific reports* **9**, 1–12 (2019).
64. Reddy, S. S., Agarwal, H. & Barthwal, M. K. Cilostazol ameliorates heart failure with preserved ejection fraction and diastolic dysfunction in obese and non-obese hypertensive mice. *Journal of Molecular and Cellular Cardiology* **123**, 46–57 (2018).
65. Gaspari, T. *et al.* Molecular and cellular mechanisms of glucagon-like peptide-1 receptor agonist-mediated attenuation of cardiac fibrosis. *Diabetes and Vascular Disease Research* **13**, 56–68 (2016).
66. Withaar, C., Lam, C. S., Schiattarella, G. G., de Boer, R. A. & Meems, L. M. Heart failure with preserved ejection fraction in humans and mice: embracing clinical complexity in mouse models. *European heart journal* **42**, 4420–4430 (2021).
67. Schiattarella, G. G. *et al.* Nitrosative stress drives heart failure with preserved ejection fraction. *Nature* **568**, 351–356 (2019).
68. Stokes, K. Y. *et al.* Dietary nitrite prevents hypercholesterolemic microvascular inflammation and reverses endothelial dysfunction. *American Journal of Physiology-Heart and Circulatory Physiology* **296**, H1281–H1288 (2009).

69. Bostick, B. *et al.* Mineralocorticoid receptor blockade prevents Western diet-induced diastolic dysfunction in female mice. *American Journal of Physiology-Heart and Circulatory Physiology* **308**, H1126–H1135 (2015).
70. Abdesselam, I. *et al.* Time course of cardiometabolic alterations in a high fat high sucrose diet mice model and improvement after GLP-1 analog treatment using multimodal cardiovascular magnetic resonance. *Journal of Cardiovascular Magnetic Resonance* **17**, 95 (2015).
71. Aroor, A. R. *et al.* Dipeptidyl peptidase-4 (DPP-4) inhibition with linagliptin reduces western diet-induced myocardial TRAF3IP2 expression, inflammation and fibrosis in female mice. *Cardiovascular diabetology* **16**, 1–15 (2017).
72. Bostick, B. *et al.* Daily exercise prevents diastolic dysfunction and oxidative stress in a female mouse model of western diet induced obesity by maintaining cardiac heme oxygenase-1 levels. *Metabolism* **66**, 14–22 (2017).
73. Alex, L., Russo, I., Holoborodko, V. & Frangogiannis, N. G. Characterization of a mouse model of obesity-related fibrotic cardiomyopathy that recapitulates features of human heart failure with preserved ejection fraction. *American Journal of Physiology-Heart and Circulatory Physiology* **315**, H934–H949 (2018).
74. Choi, S.-K. *et al.* Poly (ADP-ribose) polymerase 1 inhibition improves coronary arteriole function in type 2 diabetes mellitus. *Hypertension* **59**, 1060–1068 (2012).
75. Moien-Afshari, F. *et al.* Exercise restores coronary vascular function independent of myogenic tone or hyperglycemic status in db/db mice. *American Journal of Physiology-Heart and Circulatory Physiology* **295**, H1470–H1480 (2008).
76. DelloStritto, D. J. *et al.* Differential regulation of TRPV1 channels by H₂O₂: implications for diabetic microvascular dysfunction. *Basic research in cardiology* **111**, 1–16 (2016).
77. Van den Bergh, A., Flameng, W. & Herijgers, P. Type II diabetic mice exhibit contractile dysfunction but maintain cardiac output by favourable loading conditions. *European journal of heart failure* **8**, 777–783 (2006).
78. Broderick, T. L., Wang, D., Jankowski, M. & Gutkowska, J. Unexpected effects of voluntary exercise training on natriuretic peptide and receptor mRNA expression in the ob/ob mouse heart. *Regulatory peptides* **188**, 52–59 (2014).
79. Christoffersen, C., Bartels, E. & Nielsen, L. Heart specific up-regulation of genes for B-type and C-type natriuretic peptide receptors in diabetic mice. *European journal of clinical investigation* **36**, 69–75 (2006).
80. Manolescu, D.-C. *et al.* All-trans retinoic acid stimulates gene expression of the cardioprotective natriuretic peptide system and prevents fibrosis and apoptosis in cardiomyocytes of obese ob/ob mice. *Applied Physiology, Nutrition, and Metabolism* **39**, 1127–1136 (2014).
81. Clément, K. Genetics of human obesity. *Comptes rendus biologiques* **329**, 608–622 (2006).

82. Xu, X., Gao, X., Potter, B. J., Cao, J.-M. & Zhang, C. Anti-LOX-1 rescues endothelial function in coronary arterioles in atherosclerotic ApoE knockout mice. *Arteriosclerosis, thrombosis, and vascular biology* **27**, 871–877 (2007).
83. Gödecke, A., Ziegler, M., Ding, Z. & Schrader, J. Endothelial dysfunction of coronary resistance vessels in apoE^{-/-} mice involves NO but not prostacyclin-dependent mechanisms. *Cardiovascular research* **53**, 253–262 (2002).
84. Förstermann, U. Nitric oxide and oxidative stress in vascular disease. *Pflügers Archiv-European Journal of Physiology* **459**, 923–939 (2010).
85. Valko, M., Rhodes, C., Moncol, J., Izakovic, M. & Mazur, M. Free radicals, metals and antioxidants in oxidative stress-induced cancer. *Chemico-biological interactions* **160**, 1–40 (2006).
86. Valko, M., Morris, H. & Cronin, M. Metals, toxicity and oxidative stress. *Current medicinal chemistry* **12**, 1161–1208 (2005).
87. Elahi, M. M., Naseem, K. M. & Matata, B. M. Nitric oxide in blood: the nitrosative–oxidative disequilibrium hypothesis on the pathogenesis of cardiovascular disease. *The FEBS journal* **274**, 906–923 (2007).
88. Ridnour, L. A. *et al.* The chemistry of nitrosative stress induced by nitric oxide and reactive nitrogen oxide species. Putting perspective on stressful biological situations. (2004).
89. Niemann, B. *et al.* Oxidative stress and cardiovascular risk: obesity, diabetes, smoking, and pollution: part 3 of a 3-part series. *Journal of the American college of cardiology* **70**, 230–251 (2017).
90. Crea, F., Lanza, G. A. & Camici, P. G. Mechanisms of coronary microvascular dysfunction. in *Coronary microvascular dysfunction* 31–47 (Springer, 2014).
91. Severino, P. *et al.* Myocardial ischemia and diabetes mellitus: role of oxidative stress in the connection between cardiac metabolism and coronary blood flow. *Journal of diabetes research* **2019**, (2019).
92. Severino, P. *et al.* Diabetes mellitus and ischemic heart disease: the role of ion channels. *International Journal of Molecular Sciences* **19**, 802 (2018).
93. Soule, B. P. *et al.* The chemistry and biology of nitroxide compounds. *Free Radical Biology and Medicine* **42**, 1632–1650 (2007).
94. Kuppusamy, P. *et al.* Noninvasive imaging of tumor redox status and its modification by tissue glutathione levels. *Cancer research* **62**, 307–312 (2002).
95. Elas, M., Ichikawa, K. & Halpern, H. J. Oxidative stress imaging in live animals with techniques based on electron paramagnetic resonance. *Radiation research* **177**, 514–523 (2012).
96. Hyodo, F. *et al.* Assessment of tissue redox status using metabolic responsive contrast agents and magnetic resonance imaging. *Journal of Pharmacy and Pharmacology* **60**, 1049–1060 (2008).

97. Matsumoto, K. *et al.* High-resolution mapping of tumor redox status by magnetic resonance imaging using nitroxides as redox-sensitive contrast agents. *Clinical cancer research* **12**, 2455–2462 (2006).
98. Matsumoto, K. *et al.* Brain contrasting ability of blood-brain-barrier-permeable nitroxyl contrast agents for magnetic resonance redox imaging. *Magnetic Resonance in Medicine* **76**, 935–945 (2016).
99. Zhelev, Z., Gadjeva, V., Aoki, I., Bakalova, R. & Saga, T. Cell-penetrating nitroxides as molecular sensors for imaging of cancer in vivo, based on tissue redox activity. *Molecular BioSystems* **8**, 2733–2740 (2012).
100. Zhelev, Z. *et al.* Tissue redox activity as a sensing platform for imaging of cancer based on nitroxide redox cycle. *European Journal of Cancer* **49**, 1467–1478 (2013).
101. Lazarova, D. *et al.* Nitroxide-enhanced magnetic resonance imaging of kidney dysfunction in vivo based on redox-imbalance and oxidative stress. *General Physiology and Biophysics* **38**, 191–204 (2019).
102. Packer, M. Epicardial adipose tissue may mediate deleterious effects of obesity and inflammation on the myocardium. *Journal of the American College of Cardiology* **71**, 2360–2372 (2018).
103. Iacobellis, G. & Bianco, A. C. Epicardial adipose tissue: emerging physiological, pathophysiological and clinical features. *Trends in Endocrinology & Metabolism* **22**, 450–457 (2011).
104. Antonopoulos, A. S. *et al.* Mutual regulation of epicardial adipose tissue and myocardial redox state by PPAR- γ /adiponectin signalling. *Circulation research* **118**, 842–855 (2016).
105. Teijeira-Fernandez, E., Eiras, S., Somoza, A. S. & Gonzalez-Juanatey, J. R. Baseline epicardial adipose tissue adiponectin levels predict cardiovascular outcomes: a long-term follow-up study. *Cytokine* **60**, 674–680 (2012).
106. Patel, V. B., Shah, S., Verma, S. & Oudit, G. Y. Epicardial adipose tissue as a metabolic transducer: role in heart failure and coronary artery disease. *Heart failure reviews* **22**, 889–902 (2017).
107. Şengül, C. & Özveren, O. Epicardial adipose tissue: a review of physiology, pathophysiology, and clinical applications. *Anadolu Kardiyol Derg* **13**, 261–5 (2013).
108. Hayes, K. Dietary fat and heart health: in search of the ideal fat. *Asia Pacific journal of clinical nutrition* **11**, S394–S400 (2002).
109. Lopaschuk, G. D. Metabolic abnormalities in the diabetic heart. *Heart failure reviews* **7**, 149–159 (2002).
110. Iozzo, P. Metabolic toxicity of the heart: insights from molecular imaging. *Nutrition, Metabolism and Cardiovascular Diseases* **20**, 147–156 (2010).
111. McKernan, K., Varghese, M., Patel, R. & Singer, K. Role of TLR4 in the induction of inflammatory changes in adipocytes and macrophages. *Adipocyte* **9**, 212–222 (2020).
112. Liberale, L., Dallegri, F., Montecucco, F. & Carbone, F. Pathophysiological relevance of macrophage subsets in atherogenesis. *Thrombosis and haemostasis* **26**, 07–18 (2017).

113. Wen, H. *et al.* Fatty acid–induced NLRP3–ASC inflammasome activation interferes with insulin signaling. *Nature immunology* **12**, 408–415 (2011).
114. Calder, P. C. Omega-3 fatty acids and inflammatory processes: from molecules to man. *Biochemical Society Transactions* **45**, 1105–1115 (2017).
115. Robblee, M. M. *et al.* Saturated fatty acids engage an IRE1 α -dependent pathway to activate the NLRP3 inflammasome in myeloid cells. *Cell reports* **14**, 2611–2623 (2016).
116. Cikim, A. S. *et al.* Epicardial adipose tissue, hepatic steatosis and obesity. *Journal of endocrinological investigation* **30**, 459–464 (2007).
117. Iacobellis, G., Malavazos, A. E. & Corsi, M. M. Epicardial fat: from the biomolecular aspects to the clinical practice. *The international journal of biochemistry & cell biology* **43**, 1651–1654 (2011).
118. Parsaei, M. S. *et al.* Relationship between epicardial fat and coronary microvascular dysfunction. *Kardiologia Polska (Polish Heart Journal)* **72**, 417–424 (2014).
119. Sade, L. E. *et al.* Relation between epicardial fat thickness and coronary flow reserve in women with chest pain and angiographically normal coronary arteries. *Atherosclerosis* **204**, 580–585 (2009).
120. Alam, M. S., Green, R., de Kemp, R., Beanlands, R. S. & Chow, B. J. Epicardial adipose tissue thickness as a predictor of impaired microvascular function in patients with non-obstructive coronary artery disease. *Journal of Nuclear Cardiology* **20**, 804–812 (2013).
121. Gaborit, B. *et al.* Epicardial fat volume is associated with coronary microvascular response in healthy subjects: a pilot study. *Obesity* **20**, 1200–1205 (2012).
122. Le Jemtel, T. H., Samson, R., Ayinapudi, K., Singh, T. & Oparil, S. Epicardial adipose tissue and cardiovascular disease. *Current Hypertension Reports* **21**, 1–11 (2019).
123. Nakanishi, K. *et al.* Relationships between periventricular epicardial adipose tissue accumulation, coronary microcirculation, and left ventricular diastolic dysfunction. *Canadian Journal of Cardiology* **33**, 1489–1497 (2017).
124. Rabkin, S. W. Is reduction in coronary blood flow the mechanism by which epicardial fat produces left ventricular diastolic dysfunction? *Canadian Journal of Cardiology* **33**, 1459–1461 (2017).
125. Yudkin, J. S., Eringa, E. & Stehouwer, C. D. “Vasocrine” signalling from perivascular fat: a mechanism linking insulin resistance to vascular disease. *The Lancet* **365**, 1817–1820 (2005).
126. Ansaldo, A. M., Montecucco, F., Sahebkar, A., Dallegri, F. & Carbone, F. Epicardial adipose tissue and cardiovascular diseases. *International journal of cardiology* **278**, 254–260 (2019).
127. Dixon, W. T. Simple proton spectroscopic imaging. *Radiology* **153**, 189–194 (1984).
128. Glover, G. & Schneider, E. Three-point Dixon technique for true water/fat decomposition with B0 inhomogeneity correction. *Magnetic resonance in medicine* **18**, 371–383 (1991).
129. Homsj, R. *et al.* 3D-Dixon MRI based volumetry of peri-and epicardial fat. *The international journal of cardiovascular imaging* **32**, 291–299 (2016).

130. Ren, J., Dimitrov, I., Sherry, A. D. & Malloy, C. R. Composition of adipose tissue and marrow fat in humans by ¹H NMR at 7 Tesla. *Journal of lipid research* **49**, 2055–2062 (2008).
131. Hernando, D. *et al.* Joint estimation of water/fat images and field inhomogeneity map. *Magnetic Resonance in Medicine: An Official Journal of the International Society for Magnetic Resonance in Medicine* **59**, 571–580 (2008).
132. Reeder, S. B. *et al.* Multicoil Dixon chemical species separation with an iterative least-squares estimation method. *Magnetic Resonance in Medicine: An Official Journal of the International Society for Magnetic Resonance in Medicine* **51**, 35–45 (2004).
133. Reeder, S. B. *et al.* Iterative decomposition of water and fat with echo asymmetry and least-squares estimation (IDEAL): application with fast spin-echo imaging. *Magnetic Resonance in Medicine: An Official Journal of the International Society for Magnetic Resonance in Medicine* **54**, 636–644 (2005).
134. Berglund, J., Ahlström, H. & Kullberg, J. Model-based mapping of fat unsaturation and chain length by chemical shift imaging—phantom validation and in vivo feasibility. *Magnetic resonance in medicine* **68**, 1815–1827 (2012).
135. Peterson, P., Trinh, L. & Månsson, S. Quantitative ¹H MRI and MRS of fatty acid composition. *Magnetic Resonance in Medicine* **85**, 49–67 (2021).
136. Liu, D., Steingoetter, A., Parker, H. L., Curcic, J. & Kozerke, S. Accelerating MRI fat quantification using a signal model-based dictionary to assess gastric fat volume and distribution of fat fraction. *Magnetic resonance imaging* **37**, 81–89 (2017).
137. Fuller, P. J. & Young, M. J. Mechanisms of mineralocorticoid action. *Hypertension* **46**, 1227–1235 (2005).
138. Rossier, B. C., Baker, M. E. & Studer, R. A. Epithelial sodium transport and its control by aldosterone: the story of our internal environment revisited. *Physiological reviews* **95**, 297–340 (2015).
139. Gomez-Sanchez, E. P. The mammalian mineralocorticoid receptor: tying down a promiscuous receptor. *Experimental physiology* **95**, 13–18 (2010).
140. Buonafine, M., Bonnard, B. & Jaisser, F. Mineralocorticoid receptor and cardiovascular disease. *American journal of hypertension* **31**, 1165–1174 (2018).
141. Davel, A. P., Anwar, I. J. & Jaffe, I. Z. The endothelial mineralocorticoid receptor: mediator of the switch from vascular health to disease. *Current opinion in nephrology and hypertension* **26**, 97 (2017).
142. Biennvenu, L. A., Reichelt, M. E., Delbridge, L. M. & Young, M. J. Mineralocorticoid receptors and the heart, multiple cell types and multiple mechanisms: a focus on the cardiomyocyte. *Clinical Science* **125**, 409–421 (2013).
143. Biennvenu, L. A. *et al.* Cardiomyocyte mineralocorticoid receptor activation impairs acute cardiac functional recovery after ischemic insult. *Hypertension* **66**, 970–977 (2015).
144. Rickard, A. J. *et al.* Cardiomyocyte mineralocorticoid receptors are essential for deoxycorticosterone/salt-mediated inflammation and cardiac fibrosis. *Hypertension* **60**, 1443–1450 (2012).

145. Fraccarollo, D. & Bauersachs, J. Cardiomyocyte mineralocorticoid receptor function post myocardial infarction. *Trends in cardiovascular medicine* **21**, 42–47 (2011).
146. Nagase, M. *et al.* Oxidative stress causes mineralocorticoid receptor activation in rat cardiomyocytes: role of small GTPase Rac1. *Hypertension* **59**, 500–506 (2012).
147. McCurley, A. *et al.* Direct regulation of blood pressure by smooth muscle cell mineralocorticoid receptors. *Nature medicine* **18**, 1429–1433 (2012).
148. Kim, S. K. *et al.* Smooth muscle cell–mineralocorticoid receptor as a mediator of cardiovascular stiffness with aging. *Hypertension* **71**, 609–621 (2018).
149. Gueret, A. *et al.* Vascular smooth muscle mineralocorticoid receptor contributes to coronary and left ventricular dysfunction after myocardial infarction. *Hypertension* **67**, 717–723 (2016).
150. McCurley, A., McGraw, A., Pruthi, D. & Jaffe, I. Z. Smooth muscle cell mineralocorticoid receptors: role in vascular function and contribution to cardiovascular disease. *Pflügers Archiv-European Journal of Physiology* **465**, 1661–1670 (2013).
151. Jia, G. *et al.* Endothelial mineralocorticoid receptor mediates diet-induced aortic stiffness in females. *Circulation research* **118**, 935–943 (2016).
152. Jia, G., Aroor, A. R. & Sowers, J. R. The role of mineralocorticoid receptor signaling in the cross-talk between adipose tissue and the vascular wall. *Cardiovascular Research* **113**, 1055–1063 (2017).
153. Lothar, A. *et al.* Deoxycorticosterone Acetate/Salt-Induced Cardiac But Not Renal Injury Is Mediated By Endothelial Mineralocorticoid Receptors Independently From Blood Pressure. *Hypertension* **67**, 130–138 (2016).
154. DuPont, J. J. & Jaffe, I. Z. 30 YEARS OF THE MINERALOCORTICOID RECEPTOR: The role of the mineralocorticoid receptor in the vasculature. *J Endocrinol* **234**, T67–T82 (2017).
155. Hirata, A. *et al.* Blockade of mineralocorticoid receptor reverses adipocyte dysfunction and insulin resistance in obese mice. *Cardiovascular research* **84**, 164–172 (2009).
156. Wada, T. *et al.* Eplerenone prevented obesity-induced inflammasome activation and glucose intolerance. *Journal of Endocrinology* **235**, 179–191 (2017).
157. Urbanet, R. *et al.* Adipocyte mineralocorticoid receptor activation leads to metabolic syndrome and induction of prostaglandin D2 synthase. *Hypertension* **66**, 149–157 (2015).
158. Lehrke, M. & Lazar, M. A. Inflamed about obesity. *Nature medicine* **10**, 126–127 (2004).
159. Nguyen Dinh Cat, A. *et al.* Adipocyte-specific mineralocorticoid receptor overexpression in mice is associated with metabolic syndrome and vascular dysfunction: role of redox-sensitive PKG-1 and Rho kinase. *Diabetes* **65**, 2392–2403 (2016).
160. Usher, M. G. *et al.* Myeloid mineralocorticoid receptor controls macrophage polarization and cardiovascular hypertrophy and remodeling in mice. *The Journal of clinical investigation* **120**, 3350–3364 (2010).

161. Martín-Fernández, B. *et al.* Aldosterone induces renal fibrosis and inflammatory M1-macrophage subtype via mineralocorticoid receptor in rats. *PLoS One* **11**, e0145946 (2016).
162. Shen, Z.-X. *et al.* Mineralocorticoid receptor deficiency in macrophages inhibits atherosclerosis by affecting foam cell formation and efferocytosis. *Journal of Biological Chemistry* **292**, 925–935 (2017).
163. Shen, J. Z. *et al.* Cardiac tissue injury and remodeling is dependent upon MR regulation of activation pathways in cardiac tissue macrophages. *Endocrinology* **157**, 3213–3223 (2016).
164. Li, C. *et al.* Myeloid mineralocorticoid receptor deficiency inhibits aortic constriction-induced cardiac hypertrophy in mice. *PLoS one* **9**, e110950 (2014).
165. Bene, N. C., Alcaide, P., Wortis, H. H. & Jaffe, I. Z. Mineralocorticoid receptors in immune cells: emerging role in cardiovascular disease. *Steroids* **91**, 38–45 (2014).
166. Herrada, A. A. *et al.* Aldosterone promotes autoimmune damage by enhancing Th17-mediated immunity. *The Journal of Immunology* **184**, 191–202 (2010).
167. Montecucco, F. *et al.* The role of inflammation in cardiovascular outcome. *Current atherosclerosis reports* **19**, 1–9 (2017).
168. Parviz, Y. *et al.* Emerging cardiovascular indications of mineralocorticoid receptor antagonists. *Trends in Endocrinology & Metabolism* **26**, 201–211 (2015).
169. Iqbal, J. *et al.* Selection of a mineralocorticoid receptor antagonist for patients with hypertension or heart failure. *European Journal of Heart Failure* **16**, 143–150 (2014).
170. Struthers, A., Krum, H. & Williams, G. H. A comparison of the aldosterone-blocking agents eplerenone and spironolactone. *Clinical Cardiology: An International Indexed and Peer-Reviewed Journal for Advances in the Treatment of Cardiovascular Disease* **31**, 153–158 (2008).
171. Fagart, J. *et al.* A new mode of mineralocorticoid receptor antagonism by a potent and selective nonsteroidal molecule. *Journal of Biological Chemistry* **285**, 29932–29940 (2010).
172. Martín-Fernández, B. *et al.* Beneficial effects of proanthocyanidins in the cardiac alterations induced by aldosterone in rat heart through mineralocorticoid receptor blockade. *PLoS one* **9**, e111104 (2014).
173. Bauersachs, J., Jaisser, F. & Toto, R. Mineralocorticoid receptor activation and mineralocorticoid receptor antagonist treatment in cardiac and renal diseases. *Hypertension* **65**, 257–263 (2015).
174. Fraccarollo, D. *et al.* Additive improvement of left ventricular remodeling and neurohormonal activation by aldosterone receptor blockade with eplerenone and ACE inhibition in rats with myocardial infarction. *Journal of the American College of Cardiology* **42**, 1666–1673 (2003).
175. Vecchiola, A. *et al.* Eplerenone implantation improved adipose dysfunction averting RAAS activation and cell division. *Frontiers in Endocrinology* **11**, 223 (2020).
176. Haas, A. V. *et al.* Sex differences in coronary microvascular function in individuals with type 2 diabetes. *Diabetes* **68**, 631–636 (2019).

177. Shah, A. M. *et al.* Cardiac structure and function in heart failure with preserved ejection fraction: baseline findings from the echocardiographic study of the Treatment of Preserved Cardiac Function Heart Failure with an Aldosterone Antagonist trial. *Circulation: Heart Failure* **7**, 104–115 (2014).
178. Pitt, B. *et al.* Spironolactone for heart failure with preserved ejection fraction. *N Engl J Med* **370**, 1383–1392 (2014).
179. Costa, R. R. *et al.* High fat diet induces central obesity, insulin resistance and microvascular dysfunction in hamsters. *Microvascular research* **82**, 416–422 (2011).
180. Singer, G., Stokes, K. Y. & Neil Granger, D. Reactive oxygen and nitrogen species in sepsis-induced hepatic microvascular dysfunction. *Inflammation Research* **62**, 155–164 (2013).
181. Münzel, T. *et al.* Impact of oxidative stress on the heart and vasculature: part 2 of a 3-part series. *Journal of the American College of Cardiology* **70**, 212–229 (2017).
182. Duilio, C. *et al.* Neutrophils are primary source of O₂ radicals during reperfusion after prolonged myocardial ischemia. *American Journal of Physiology-Heart and Circulatory Physiology* **280**, H2649–H2657 (2001).
183. Furukawa, S. *et al.* Increased oxidative stress in obesity and its impact on metabolic syndrome. *The Journal of clinical investigation* **114**, 1752–1761 (2017).
184. Münzel, T., Gori, T., Keaney, J. F., Jr, Maack, C. & Daiber, A. Pathophysiological role of oxidative stress in systolic and diastolic heart failure and its therapeutic implications. *European Heart Journal* **36**, 2555–2564 (2015).
185. Davis, R. M. *et al.* A novel nitroxide is an effective brain redox imaging contrast agent and in vivo radioprotector. *Free Radical Biology and Medicine* **51**, 780–790 (2011).
186. Landmesser, U. *et al.* Role of p47 phox in vascular oxidative stress and hypertension caused by angiotensin II. *Hypertension* **40**, 511–515 (2002).
187. Higashi, M. *et al.* Long-term inhibition of Rho-kinase suppresses angiotensin II-induced cardiovascular hypertrophy in rats in vivo: effect on endothelial NAD (P) H oxidase system. *Circulation research* **93**, 767–775 (2003).
188. Feillet-Coudray, C. *et al.* Oxidative stress in rats fed a high-fat high-sucrose diet and preventive effect of polyphenols: Involvement of mitochondrial and NAD (P) H oxidase systems. *Free Radical Biology and Medicine* **46**, 624–632 (2009).
189. Yokoyama, H., Tada, M., Itoh, O. & Fukui, K. Reaction kinetics analysis to estimate in vivo decay rate of EPR signals of a nitroxide radical in the brain and the inferior vena cava of rats. *Applied Magnetic Resonance* **25**, 217 (2003).
190. Barnes, S. L., Whisenant, J. G., Loveless, M. E. & Yankeelov, T. E. Practical dynamic contrast enhanced MRI in small animal models of cancer: data acquisition, data analysis, and interpretation. *Pharmaceutics* **4**, 442–478 (2012).

191. Ross, A. J. *et al.* Serial MRI evaluation of cardiac structure and function in mice after reperfused myocardial infarction. *Magnetic Resonance in Medicine: An Official Journal of the International Society for Magnetic Resonance in Medicine* **47**, 1158–1168 (2002).
192. Naresh, N. K. *et al.* Monocyte and/or macrophage infiltration of heart after myocardial infarction: MR imaging by using T1-shortening liposomes. *Radiology* **264**, 428–435 (2012).
193. Vandervelde, S. *et al.* Increased inflammatory response and neovascularization in reperfused vs. nonreperfused murine myocardial infarction. *Cardiovascular Pathology* **15**, 83–90 (2006).
194. Li, H., He, G., Deng, Y., Kuppusamy, P. & Zweier, J. L. In vivo proton electron double resonance imaging of the distribution and clearance of nitroxide radicals in mice. *Magnetic Resonance in Medicine: An Official Journal of the International Society for Magnetic Resonance in Medicine* **55**, 669–675 (2006).
195. Voros, S. *et al.* Interaction between AT1 and AT2 receptors during postinfarction left ventricular remodeling. *American Journal of Physiology-Heart and Circulatory Physiology* **290**, H1004–H1010 (2006).
196. Kim, D., Gilson, W. D., Kramer, C. M. & Epstein, F. H. Myocardial tissue tracking with two-dimensional cine displacement-encoded MR imaging: development and initial evaluation. *Radiology* **230**, 862–871 (2004).
197. Vandsburger, M. H., French, B. A., Kramer, C. M., Zhong, X. & Epstein, F. H. Displacement-encoded and manganese-enhanced cardiac MRI reveal that nNOS, not eNOS, plays a dominant role in modulating contraction and calcium influx in the mammalian heart. *American Journal of Physiology-Heart and Circulatory Physiology* **302**, H412–H419 (2012).
198. Zhong, X., Spottiswoode, B. S., Meyer, C. H., Kramer, C. M. & Epstein, F. H. Imaging three-dimensional myocardial mechanics using navigator-gated volumetric spiral cine DENSE MRI. *Magnetic resonance in medicine* **64**, 1089–1097 (2010).
199. Epstein, F. H. *et al.* MR tagging early after myocardial infarction in mice demonstrates contractile dysfunction in adjacent and remote regions. *Magnetic Resonance in Medicine: An Official Journal of the International Society for Magnetic Resonance in Medicine* **48**, 399–403 (2002).
200. Spottiswoode, B. S. *et al.* Tracking myocardial motion from cine DENSE images using spatiotemporal phase unwrapping and temporal fitting. *IEEE transactions on medical imaging* **26**, 15–30 (2006).
201. Spottiswoode, B. S. *et al.* Motion-guided segmentation for cine DENSE MRI. *Medical image analysis* **13**, 105–115 (2009).
202. Cernicanu, A. & Axel, L. Theory-based signal calibration with single-point T1 measurements for first-pass quantitative perfusion MRI studies. *Academic radiology* **13**, 686–693 (2006).
203. Zielonka, J. & Kalyanaraman, B. Hydroethidine-and MitoSOX-derived red fluorescence is not a reliable indicator of intracellular superoxide formation: another inconvenient truth. *Free Radical Biology and Medicine* **48**, 983–1001 (2010).
204. Schindelin, J. *et al.* Fiji: an open-source platform for biological-image analysis. *Nature methods* **9**, 676–682 (2012).

205. Troalen, T., Capron, T., Bernard, M. & Kober, F. In vivo characterization of rodent cyclic myocardial perfusion variation at rest and during adenosine-induced stress using cine-ASL cardiovascular magnetic resonance. *Journal of cardiovascular magnetic resonance* **16**, 1–12 (2014).
206. Giordano, F. J. Oxygen, oxidative stress, hypoxia, and heart failure. *The Journal of clinical investigation* **115**, 500–508 (2005).
207. Takimoto, E. & Kass, D. A. Role of oxidative stress in cardiac hypertrophy and remodeling. *Hypertension* **49**, 241–248 (2007).
208. Jeong, E.-M. *et al.* Metabolic stress, reactive oxygen species, and arrhythmia. *Journal of molecular and cellular cardiology* **52**, 454–463 (2012).
209. Octavia, Y. *et al.* Doxorubicin-induced cardiomyopathy: from molecular mechanisms to therapeutic strategies. *Journal of molecular and cellular cardiology* **52**, 1213–1225 (2012).
210. Sonta, T. *et al.* In vivo imaging of oxidative stress in the kidney of diabetic mice and its normalization by angiotensin II type 1 receptor blocker. *Biochemical and biophysical research communications* **330**, 415–422 (2005).
211. Bačić, G., Pavićević, A. & Peyrot, F. In vivo evaluation of different alterations of redox status by studying pharmacokinetics of nitroxides using magnetic resonance techniques. *Redox biology* **8**, 226–242 (2016).
212. Manintveld, O. C. *et al.* Cardiac effects of postconditioning depend critically on the duration of index ischemia. *American Journal of Physiology-Heart and Circulatory Physiology* **292**, H1551–H1560 (2007).
213. Obana, M. *et al.* Therapeutic administration of IL-11 exhibits the postconditioning effects against ischemia-reperfusion injury via STAT3 in the heart. *American Journal of Physiology-Heart and Circulatory Physiology* **303**, H569–H577 (2012).
214. Epstein, F. H. MR in mouse models of cardiac disease. *NMR in Biomedicine: An International Journal Devoted to the Development and Application of Magnetic Resonance In vivo* **20**, 238–255 (2007).
215. Vandsburger, M. H. *et al.* Improved arterial spin labeling after myocardial infarction in mice using cardiac and respiratory gated look-locker imaging with fuzzy C-means clustering. *Magn Reson Med* **63**, 648–657 (2010).
216. Nagy, E., Jermendy, A. L., Merkely, B. & Maurovich-Horvat, P. Clinical importance of epicardial adipose tissue. *Archives of medical science: AMS* **13**, 864 (2017).
217. Matloch, Z., Kotulák, T. & Haluzík, M. The role of epicardial adipose tissue in heart disease. *Physiological research* **65**, 23 (2016).
218. Gaborit, B., Sengenès, C., Ancel, P., Jacquier, A. & Dutour, A. Role of epicardial adipose tissue in health and disease: a matter of fat? *Comprehensive physiology* **7**, 1051–1082 (2011).
219. Cheng, K. *et al.* Adipocytokines and proinflammatory mediators from abdominal and epicardial adipose tissue in patients with coronary artery disease. *International journal of obesity* **32**, 268–274 (2008).

220. Gruzdeva, O. *et al.* Adipokine and cytokine profiles of epicardial and subcutaneous adipose tissue in patients with coronary heart disease. *Bulletin of experimental biology and medicine* **163**, 608–611 (2017).
221. Patel, V. B., Basu, R. & Oudit, G. Y. ACE2/Ang 1-7 axis: a critical regulator of epicardial adipose tissue inflammation and cardiac dysfunction in obesity. *Adipocyte* **5**, 306–311 (2016).
222. Bambace, C. *et al.* Inflammatory profile in subcutaneous and epicardial adipose tissue in men with and without diabetes. *Heart and vessels* **29**, 42–48 (2014).
223. Pezeshkian, M. *et al.* Fatty Acid Composition of Epicardial and Subcutaneous Human Adipose Tissue. *Metabolic Syndrome and Related Disorders* **7**, 125–132 (2009).
224. Pezeshkian, M. & Mahtabipour, M.-R. Epicardial and subcutaneous adipose tissue Fatty acids profiles in diabetic and non-diabetic patients candidate for coronary artery bypass graft. *Bioimpacts* **3**, 83–89 (2013).
225. Petrini, M. *et al.* Epicardial adipose tissue volume in patients with coronary artery disease or non-ischaemic dilated cardiomyopathy: evaluation with cardiac magnetic resonance imaging. *Clinical radiology* **74**, 81-e1 (2019).
226. Flüchter, S. *et al.* Volumetric assessment of epicardial adipose tissue with cardiovascular magnetic resonance imaging. *Obesity* **15**, 870–878 (2007).
227. Peterson, P. & Månsson, S. Simultaneous quantification of fat content and fatty acid composition using MR imaging. *Magnetic resonance in medicine* **69**, 688–697 (2013).
228. Leporq, B., Lambert, S. A., Ronot, M., Vilgrain, V. & Van Beers, B. E. Quantification of the triglyceride fatty acid composition with 3.0 T MRI. *NMR in Biomedicine* **27**, 1211–1221 (2014).
229. Nemeth, A. *et al.* 3D chemical shift-encoded MRI for volume and composition quantification of abdominal adipose tissue during an overfeeding protocol in healthy volunteers. *Journal of Magnetic Resonance Imaging* **49**, 1587–1599 (2019).
230. Schneider, M. *et al.* Accurate fatty acid composition estimation of adipose tissue in the abdomen based on bipolar multi-echo MRI. *Magnetic resonance in medicine* **81**, 2330–2346 (2019).
231. Leporq, B. *et al.* Hepatic fat fraction and visceral adipose tissue fatty acid composition in mice: Quantification with 7.0 T MRI. *Magnetic resonance in medicine* **76**, 510–518 (2016).
232. Martel, D. *et al.* Chemical shift-encoded MRI for assessment of bone marrow adipose tissue fat composition: pilot study in premenopausal versus postmenopausal women. *Magnetic resonance imaging* **53**, 148–155 (2018).
233. Martel, D. *et al.* 3T chemical shift-encoded MRI: Detection of altered proximal femur marrow adipose tissue composition in glucocorticoid users and validation with magnetic resonance spectroscopy. *Journal of Magnetic Resonance Imaging* **50**, 490–496 (2019).
234. Yu, H. *et al.* Multiecho reconstruction for simultaneous water-fat decomposition and T2* estimation. *Journal of Magnetic Resonance Imaging: An Official Journal of the International Society for Magnetic Resonance in Medicine* **26**, 1153–1161 (2007).

235. Pineda, A. R., Reeder, S. B., Wen, Z. & Pelc, N. J. Cramér–Rao bounds for three-point decomposition of water and fat. *Magnetic Resonance in Medicine: An Official Journal of the International Society for Magnetic Resonance in Medicine* **54**, 625–635 (2005).
236. Beyers, R. J. *et al.* T2-weighted MRI of post-infarct myocardial edema in mice. *Magnetic resonance in medicine* **67**, 201–209 (2012).
237. Lin, F., Kwong, K. K., Belliveau, J. W. & Wald, L. L. Parallel imaging reconstruction using automatic regularization. *Magnetic Resonance in Medicine: An Official Journal of the International Society for Magnetic Resonance in Medicine* **51**, 559–567 (2004).
238. Walsh, D. O., Gmitro, A. F. & Marcellin, M. W. Adaptive reconstruction of phased array MR imagery. *Magnetic Resonance in Medicine: An Official Journal of the International Society for Magnetic Resonance in Medicine* **43**, 682–690 (2000).
239. Berr, S. S. *et al.* Black blood gradient echo cine magnetic resonance imaging of the mouse heart. *Magnetic Resonance in Medicine: An Official Journal of the International Society for Magnetic Resonance in Medicine* **53**, 1074–1079 (2005).
240. Cui, X. & Epstein, F. (advisor). Development of MRI Methods to Assess Coronary Microvascular Function in Mice. (University of Virginia, Biomedical Engineering - School of Engineering and Applied Science, PHD (Doctor of Philosophy), 2018, 2018).
241. Aharon, M., Elad, M. & Bruckstein, A. K-SVD: An algorithm for designing overcomplete dictionaries for sparse representation. *IEEE Transactions on signal processing* **54**, 4311–4322 (2006).
242. Jones, J., Hodgkinson, P., Barker, A. & Hore, P. Optimal sampling strategies for the measurement of spin–spin relaxation times. *Journal of Magnetic Resonance, Series B* **113**, 25–34 (1996).
243. Akçakaya, M., Weingärtner, S., Roujol, S. & Nezafat, R. On the selection of sampling points for myocardial T1 mapping. *Magnetic resonance in medicine* **73**, 1741–1753 (2015).
244. Li, L. *et al.* Recent development on liquid chromatography-mass spectrometry analysis of oxidized lipids. *Free Radical Biology and Medicine* **144**, 16–34 (2019).
245. Rajabi, M., Kassiotis, C., Razeghi, P. & Taegtmeyer, H. Return to the fetal gene program protects the stressed heart: a strong hypothesis. *Heart failure reviews* **12**, 331–343 (2007).
246. Sacks, H. S. & Fain, J. N. Human epicardial adipose tissue: a review. *American heart journal* **153**, 907–917 (2007).
247. Lunati, E. *et al.* Polyunsaturated fatty acids mapping by 1H MR-chemical shift imaging. *Magnetic Resonance in Medicine: An Official Journal of the International Society for Magnetic Resonance in Medicine* **46**, 879–883 (2001).
248. Hudgins, L. C., Hirsch, J. & Emken, E. A. Correlation of isomeric fatty acids in human adipose tissue with clinical risk factors for cardiovascular disease. *The American journal of clinical nutrition* **53**, 474–482 (1991).

249. Guo, C. *et al.* Williams, GH and Adler, GK (2008) Mineralocorticoid Receptor Blockade Reverses Obesity-Related Changes in Expression of Adiponectin, Peroxisome Proliferator-Activated Receptor- γ , and Proinflammatory Adipokines. *Circulation* **117**, 2253–2261 (32).
250. Rafeh, R., Viveiros, A., Oudit, G. Y. & El-Yazbi, A. F. Targeting perivascular and epicardial adipose tissue inflammation: therapeutic opportunities for cardiovascular disease. *Clinical Science* **134**, 827–851 (2020).
251. Garaulet, M., Hernandez-Morante, J., Lujan, J., Tebar, F. & Zamora, S. Relationship between fat cell size and number and fatty acid composition in adipose tissue from different fat depots in overweight/obese humans. *International journal of obesity* **30**, 899–905 (2006).
252. Del Buono, M. G. *et al.* Coronary microvascular dysfunction across the spectrum of cardiovascular diseases: JACC State-of-the-Art Review. *Journal of the American College of Cardiology* **78**, 1352–1371 (2021).
253. Gdowski, M. A. *et al.* Association of isolated coronary microvascular dysfunction with mortality and major adverse cardiac events: a systematic review and meta-analysis of aggregate data. *Journal of the American Heart Association* **9**, e014954 (2020).
254. Zorach, B. *et al.* Quantitative cardiovascular magnetic resonance perfusion imaging identifies reduced flow reserve in microvascular coronary artery disease. *Journal of Cardiovascular Magnetic Resonance* **20**, 14 (2018).
255. Pruthi, D. *et al.* Aldosterone promotes vascular remodeling by direct effects on smooth muscle cell mineralocorticoid receptors. *Arteriosclerosis, thrombosis, and vascular biology* **34**, 355–364 (2014).
256. Yan, Y. *et al.* Mineralocorticoid receptor antagonism protects the aorta from vascular smooth muscle cell proliferation and collagen deposition in a rat model of adrenal aldosterone-producing adenoma. *Journal of physiology and biochemistry* **74**, 17–24 (2018).
257. Galliche, G. *et al.* Smooth Muscle Cell Mineralocorticoid Receptors Are Mandatory for Aldosterone–Salt to Induce Vascular Stiffness. *Hypertension* **63**, 520–526 (2014).
258. Naresh, N. K. *et al.* Accelerated dual-contrast first-pass perfusion MRI of the mouse heart: Development and application to diet-induced obese mice. *Magnetic Resonance in Medicine* **73**, 1237–1245 (2015).
259. Shah, S. A. *et al.* Nitroxide-enhanced MRI of cardiovascular oxidative stress. *NMR in Biomedicine* e4359 (2020).
260. Heiberg, E. *et al.* Design and validation of Segment-freely available software for cardiovascular image analysis. *BMC medical imaging* **10**, 1 (2010).
261. Billaud, M. *et al.* A molecular signature in the pannexin1 intracellular loop confers channel activation by the α 1 adrenoceptor in smooth muscle cells. *Science signaling* **8**, ra17–ra17 (2015).
262. Biwer, L. A. *et al.* Non–Endoplasmic Reticulum–Based Calr (Calreticulin) Can Coordinate Heterocellular Calcium Signaling and Vascular Function. *Arteriosclerosis, thrombosis, and vascular biology* **38**, 120–130 (2018).

263. Billaud, M. *et al.* Characterization of the thoracodorsal artery: morphology and reactivity. *Microcirculation* **19**, 360–372 (2012).
264. Kuo, L., Davis, M. J. & Chilian, W. M. Endothelium-dependent, flow-induced dilation of isolated coronary arterioles. *American Journal of Physiology-Heart and Circulatory Physiology* **259**, H1063–H1070 (1990).
265. Stapleton, P. A. *et al.* Impairment of coronary arteriolar endothelium-dependent dilation after multi-walled carbon nanotube inhalation: a time-course study. *International journal of molecular sciences* **13**, 13781–13803 (2012).
266. Sorop, O. *et al.* Experimental animal models of coronary microvascular dysfunction. *Cardiovascular Research* **116**, 756–770 (2020).
267. Picchi, A. *et al.* Coronary microvascular dysfunction in diabetes mellitus: a review. *World Journal of Cardiology* **2**, 377 (2010).
268. Hariri, N. & Thibault, L. High-fat diet-induced obesity in animal models. *Nutrition research reviews* **23**, 270–299 (2010).
269. Bender, S. B. *et al.* Mineralocorticoid receptor antagonism treats obesity-associated cardiac diastolic dysfunction. *Hypertension* **65**, 1082–1088 (2015).
270. Brown, S. M., Meuth, A. I., Davis, J. W., Rector, R. S. & Bender, S. B. Mineralocorticoid receptor antagonism reverses diabetes-related coronary vasodilator dysfunction: a unique vascular transcriptomic signature. *Pharmacological research* **134**, 100–108 (2018).
271. Williams, B. *et al.* 2018 ESC/ESH Guidelines for the management of arterial hypertension: The Task Force for the management of arterial hypertension of the European Society of Cardiology (ESC) and the European Society of Hypertension (ESH). *European heart journal* **39**, 3021–3104 (2018).
272. Rossello, X. *et al.* Sex differences in mineralocorticoid receptor antagonist trials: a pooled analysis of three large clinical trials. *European Journal of Heart Failure* **22**, 834–844 (2020).
273. Hu, L., Chen, Y., Deng, S., Du, J. & She, Q. Additional use of an aldosterone antagonist in patients with mild to moderate chronic heart failure: a systematic review and meta-analysis. *British journal of clinical pharmacology* **75**, 1202–1212 (2013).
274. Ezekowitz, J. A. & McAlister, F. A. Aldosterone blockade and left ventricular dysfunction: a systematic review of randomized clinical trials. *European heart journal* **30**, 469–477 (2009).
275. Solomon, S. D. *et al.* Influence of ejection fraction on outcomes and efficacy of spironolactone in patients with heart failure with preserved ejection fraction. *European heart journal* **37**, 455–462 (2016).
276. Hwang, L. *et al.* Sex differences in high-fat diet-induced obesity, metabolic alterations and learning, and synaptic plasticity deficits in mice. *Obesity* **18**, 463–469 (2010).
277. Victorio, J. A., Guizoni, D. M., Freitas, I. N., Araujo, T. R. & Davel, A. P. Effects of High-Fat and High-Fat/High-Sucrose Diet-Induced Obesity on PVAT Modulation of Vascular Function in Male and Female Mice. *Frontiers in pharmacology* 2252 (2021).

278. Armani, A. *et al.* Mineralocorticoid receptor antagonism induces browning of white adipose tissue through impairment of autophagy and prevents adipocyte dysfunction in high-fat-diet-fed mice. *The FASEB Journal* **28**, 3745–3757 (2014).
279. Guo, C. *et al.* Mineralocorticoid receptor blockade reverses obesity-related changes in expression of adiponectin, peroxisome proliferator-activated receptor- γ , and proinflammatory adipokines. *Circulation* **117**, 2253–2261 (2008).
280. Nickander, J. *et al.* Females have higher myocardial perfusion, blood volume and extracellular volume compared to males—an adenosine stress cardiovascular magnetic resonance study. *Scientific Reports* **10**, 1–9 (2020).
281. Manrique-Acevedo, C. *et al.* Mineralocorticoid receptor in myeloid cells mediates angiotensin II-induced vascular dysfunction in female mice. *Frontiers in Physiology* **12**, 276 (2021).
282. Barrera-Chimal, J. & Jaisser, F. Vascular mineralocorticoid receptor activation and disease. *Experimental Eye Research* **188**, 107796 (2019).
283. Davel, A. P. *et al.* Sex-specific mechanisms of resistance vessel endothelial dysfunction induced by cardiometabolic risk factors. *Journal of the American Heart Association* **7**, e007675 (2018).
284. DeMarco, V. G. *et al.* Low-dose mineralocorticoid receptor blockade prevents Western diet-induced arterial stiffening in female mice. *Hypertension* **66**, 99–107 (2015).
285. Faulkner, J. L. & Belin de Chantemèle, E. J. Mineralocorticoid receptor and endothelial dysfunction in hypertension. *Current hypertension reports* **21**, 1–5 (2019).
286. Cui, S. X. & Epstein, F. H. MRI assessment of coronary microvascular endothelial nitric oxide synthase function using myocardial T(1) mapping. *Magn Reson Med* **79**, 2246–2253 (2018).
287. Kaski, J.-C., Crea, F., Gersh, B. J. & Camici, P. G. Reappraisal of ischemic heart disease: fundamental role of coronary microvascular dysfunction in the pathogenesis of angina pectoris. *Circulation* **138**, 1463–1480 (2018).
288. Recio-Mayoral, A. *et al.* Chronic inflammation and coronary microvascular dysfunction in patients without risk factors for coronary artery disease. *European heart journal* **30**, 1837–1843 (2009).
289. Hecker, M., Cattaruzza, M. & Wagner, A. H. Regulation of inducible nitric oxide synthase gene expression in vascular smooth muscle cells. *General Pharmacology: The Vascular System* **32**, 9–16 (1999).
290. Costa, R. R. *et al.* High fat diet induces central obesity, insulin resistance and microvascular dysfunction in hamsters. *Microvascular research* **82**, 416–422 (2011).
291. Virdis, A. *et al.* Vascular generation of tumor necrosis factor- α reduces nitric oxide availability in small arteries from visceral fat of obese patients. *Journal of the American College of Cardiology* **58**, 238–247 (2011).
292. Zhang, M. *et al.* iNOS-derived peroxynitrite mediates high glucose-induced inflammatory gene expression in vascular smooth muscle cells through promoting KLF5 expression and nitration. *Biochimica et Biophysica Acta (BBA)-Molecular Basis of Disease* **1863**, 2821–2834 (2017).

293. Lumeng, C. N., Bodzin, J. L. & Saltiel, A. R. Obesity induces a phenotypic switch in adipose tissue macrophage polarization. *The Journal of clinical investigation* **117**, 175–184 (2007).
294. Khoury, M. K., Yang, H. & Liu, B. Macrophage biology in cardiovascular diseases. *Arteriosclerosis, Thrombosis, and Vascular Biology* **41**, e77–e81 (2021).
295. Beyers, R. J., Xu, Y., Roy, R. J., Epstein, F. H. & French, B. A. Selective Inhibition of iNOS Alone Offers Protection Against Left Ventricular Remodeling Similar to the Combination of ACE-Inhibition and Beta-Blockade in a Murine Model of Reperfused Myocardial Infarction: A Cardiac MR Study. *Circulation* **114**, 3773 (2006).
296. Jax Mice and Services. *Body Weight Information for C57BL/6J (000664)*. <https://www.jax.org/jax-mice-and-services/strain-data-sheet-pages/body-weight-chart-000664>.
297. Pérez-Torres, I., Manzano-Pech, L., Rubio-Ruíz, M. E., Soto, M. E. & Guarner-Lans, V. Nitrosative stress and its association with cardiometabolic disorders. *Molecules* **25**, 2555 (2020).
298. Sano, T., Umeda, F., Hashimoto, T., Nawata, H. & Utsumi, H. Oxidative stress measurement by in vivo electron spin resonance spectroscopy in rats with streptozotocin-induced diabetes. *Diabetologia* **41**, 1355–1360 (1998).
299. Zhou, X., Abboud, W., Manabat, N. C., Salem, R. M. & Crystal, G. J. Isoflurane-induced dilation of porcine coronary arterioles is mediated by ATP-sensitive potassium channels. *The Journal of the American Society of Anesthesiologists* **89**, 182–189 (1998).
300. Daneva, Z. *et al.* Caveolar peroxynitrite formation impairs endothelial TRPV4 channels and elevates pulmonary arterial pressure in pulmonary hypertension. *Proceedings of the National Academy of Sciences* **118**, (2021).
301. Sato, A. *et al.* Mechanism of vasodilation to adenosine in coronary arterioles from patients with heart disease. *American Journal of Physiology-Heart and Circulatory Physiology* **288**, H1633–H1640 (2005).
302. Mahmood, M. *et al.* Adenosine stress native T1 mapping in severe aortic stenosis: evidence for a role of the intravascular compartment on myocardial T1 values. *Journal of Cardiovascular Magnetic Resonance* **16**, 92 (2014).
303. Levelt, E. *et al.* Adenosine stress CMR T1-mapping detects early microvascular dysfunction in patients with type 2 diabetes mellitus without obstructive coronary artery disease. *Journal of Cardiovascular Magnetic Resonance* **19**, 81 (2017).
304. Liu, A. *et al.* Adenosine Stress and Rest T1 Mapping Can Differentiate Between Ischemic, Infarcted, Remote, and Normal Myocardium Without the Need for Gadolinium Contrast Agents. *JACC: Cardiovascular Imaging* **9**, 27 (2016).
305. McCommis, K. S. *et al.* Roles of myocardial blood volume and flow in coronary artery disease: an experimental MRI study at rest and during hyperemia. *European radiology* **20**, 2005–2012 (2010).
306. Wacker, C. M. & Bauer, W. R. Myocardial Microcirculation in Humans-New Approaches Using MRI. *Herz* **28**, 74–81 (2003).

307. Piechnik, S. K., Chiarelli, P. A. & Jezzard, P. Modelling vascular reactivity to investigate the basis of the relationship between cerebral blood volume and flow under CO₂ manipulation. *Neuroimage* **39**, 107–118 (2008).
308. Poli, F. E. *et al.* The reliability and feasibility of non-contrast adenosine stress cardiovascular magnetic resonance T1 mapping in patients on haemodialysis. *Journal of Cardiovascular Magnetic Resonance* **22**, 43 (2020).
309. Mustafa, S. J., Morrison, R. R., Teng, B. & Pelleg, A. Adenosine Receptors and the Heart: Role in Regulation of Coronary Blood Flow and Cardiac Electrophysiology. in *Adenosine Receptors in Health and Disease* (eds. Wilson, C. N. & Mustafa, S. J.) 161–188 (Springer Berlin Heidelberg, 2009). doi:10.1007/978-3-540-89615-9_6.
310. Morrison, R. R., Talukder, M. A. H., Ledent, C. & Mustafa, S. J. Cardiac effects of adenosine in A_{2A} receptor knockout hearts: uncovering A_{2B} receptors. *American Journal of Physiology-Heart and Circulatory Physiology* **282**, H437–H444 (2002).
311. Tawfik, H. E., Teng, B., Morrison, R. R., Schnermann, J. & Mustafa, S. J. Role of A₁ adenosine receptor in the regulation of coronary flow. *American Journal of Physiology-Heart and Circulatory Physiology* **291**, H467–H472 (2006).
312. Talukder, M. A. H. *et al.* Targeted deletion of adenosine A₃ receptors augments adenosine-induced coronary flow in isolated mouse heart. *American Journal of Physiology-Heart and Circulatory Physiology* **282**, H2183–H2189 (2002).
313. Cochet, H. *et al.* In Vivo MR Angiography and Velocity Measurement in Mice Coronary Arteries at 9.4 T: Assessment of Coronary Flow Velocity Reserve. *Radiology* **254**, 441–448 (2010).
314. Chen, X., Salerno, M., Yang, Y. & Epstein, F. H. Motion-compensated compressed sensing for dynamic contrast-enhanced MRI using regional spatiotemporal sparsity and region tracking: block low-rank sparsity with motion-guidance (BLOSM). *Magn Reson Med* **72**, 1028–1038 (2014).
315. Silver, P. J., Walus, K. & DiSalvo, J. Adenosine-mediated relaxation and activation of cyclic AMP-dependent protein kinase in coronary arterial smooth muscle. *Journal of Pharmacology and Experimental Therapeutics* **228**, 342–347 (1984).
316. White, T. D. & Angus, J. A. Relaxant effects of ATP and adenosine on canine large and small coronary arteries in vitro. *European journal of pharmacology* **143**, 119–126 (1987).
317. Müller, B. *et al.* High-resolution tomographic imaging of microvessels. in vol. 7078 70780B (International Society for Optics and Photonics, 2008).
318. Cerqueira, M. D. The future of pharmacologic stress: selective A_{2A} adenosine receptor agonists. *The American journal of cardiology* **94**, 33–40 (2004).
319. Reiss, A. B. *et al.* Adenosine and the cardiovascular system. *American Journal of Cardiovascular Drugs* 1–16 (2019).

320. Christiansen, J. P., Karamitsos, T. D., Myerson, S. G., Francis, J. M. & Neubauer, S. Stress perfusion imaging using cardiovascular magnetic resonance: a review. *Heart, Lung and Circulation* **19**, 697–705 (2010).
321. Thengchaisri, N., Miriel, V. A. & Rivers, R. J. Multiple receptor subtypes and multiple mechanisms of dilation are involved in vascular network dilation caused by adenosine. *Microvascular research* **77**, 356–363 (2009).
322. Li, X., Springer Jr, C. S. & Jerosch-Herold, M. First-pass dynamic contrast-enhanced MRI with extravasating contrast reagent: evidence for human myocardial capillary recruitment in adenosine-induced hyperemia. *NMR in Biomedicine: An International Journal Devoted to the Development and Application of Magnetic Resonance In vivo* **22**, 148–157 (2009).
323. Overholser, K. A. & Harris, T. Effect of exogenous adenosine on resistance, capillary permeability-surface area and flow in ischemic canine myocardium. *Journal of Pharmacology and Experimental Therapeutics* **229**, 148–153 (1984).
324. Kiyooka, T. *et al.* Direct observation of epicardial coronary capillary hemodynamics during reactive hyperemia and during adenosine administration by intravital video microscopy. *American Journal of Physiology-Heart and Circulatory Physiology* **288**, H1437–H1443 (2005).
325. Olanrewaju, H. A. & Mustafa, S. J. Adenosine A2A and A2B receptors mediated nitric oxide production in coronary artery endothelial cells. *General Pharmacology: The Vascular System* **35**, 171–177 (2000).
326. Watts, S. W., Florian, J. A. & Monroe, K. M. Dissociation of angiotensin II-stimulated activation of mitogen-activated protein kinase kinase from vascular contraction. *Journal of Pharmacology and Experimental Therapeutics* **286**, 1431–1438 (1998).
327. Hasan, A. A., Abebe, W. & Mustafa, S. J. Antagonism of coronary artery relaxation by adenosine A2A-receptor antagonist ZM241385. *Journal of cardiovascular pharmacology* **35**, 322–325 (2000).
328. Kuo, L., Chilian, W. M. & Davis, M. J. Interaction of pressure-and flow-induced responses in porcine coronary resistance vessels. *American Journal of Physiology-Heart and Circulatory Physiology* **261**, H1706–H1715 (1991).
329. Berwick, Z. C. *et al.* Contribution of adenosine A2A and A2B receptors to ischemic coronary dilation: role of KV and KATP channels. *Microcirculation* **17**, 600–607 (2010).
330. Kuijpers, D. *et al.* Caffeine intake inverts the effect of adenosine on myocardial perfusion during stress as measured by T1 mapping. *The international journal of cardiovascular imaging* **32**, 1545–1553 (2016).
331. Van Dijk, R. *et al.* Effects of caffeine intake prior to stress cardiac magnetic resonance perfusion imaging on regadenoson-versus adenosine-induced hyperemia as measured by T1 mapping. *The International Journal of Cardiovascular Imaging* **33**, 1753–1759 (2017).
332. Ansari, H. R., Nadeem, A., Tilley, S. L. & Mustafa, S. J. Involvement of COX-1 in A3 adenosine receptor-mediated contraction through endothelium in mice aorta. *American Journal of Physiology-Heart and Circulatory Physiology* **293**, H3448–H3455 (2007).

333. Buus, N. H. *et al.* Influence of nitric oxide synthase and adrenergic inhibition on adenosine-induced myocardial hyperemia. *Circulation* **104**, 2305–2310 (2001).
334. Tawakol, A. *et al.* Homocysteine impairs coronary microvascular dilator function in humans. *Journal of the American College of Cardiology* **40**, 1051–1058 (2002).
335. Headrick, J. P., Gauthier, N. S., Morrison, R. R. & Matherne, G. P. Chronotropic and vasodilatory responses to adenosine and isoproterenol in mouse heart: effects of adenosine A1 receptor overexpression. *Clinical and Experimental Pharmacology and Physiology* **27**, 185–190 (2000).
336. Schindler, C. W. *et al.* Role of central and peripheral adenosine receptors in the cardiovascular responses to intraperitoneal injections of adenosine A1 and A2A subtype receptor agonists. *British journal of pharmacology* **144**, 642–650 (2005).
337. Tawfik, H. E., Schnermann, J., Oldenburg, P. J. & Mustafa, S. J. Role of A1 adenosine receptors in regulation of vascular tone. *American Journal of Physiology-Heart and Circulatory Physiology* **288**, H1411–H1416 (2005).
338. Tawfik, H. E., Teng, B., Morrison, R. R., Schnermann, J. & Mustafa, S. J. Role of A1 adenosine receptor in the regulation of coronary flow. *American Journal of Physiology-Heart and Circulatory Physiology* **291**, H467–H472 (2006).
339. Maric-Bilkan, C. Sex differences in micro-and macro-vascular complications of diabetes mellitus. *Clinical Science* **131**, 833–846 (2017).
340. Lyon, A., Jackson, E. A., Kalyani, R. R., Vaidya, D. & Kim, C. Sex-specific differential in risk of diabetes-related macrovascular outcomes. *Current diabetes reports* **15**, 85 (2015).